ABSTRACT

Title of dissertation: PNEUMATIC ARTIFICIAL MUSCLE DRIVEN
                           TRAILING EDGE FLAPS FOR ACTIVE ROTORS

                           Benjamin King Sutton Woods
                           Doctor of Philosophy, 2012

Dissertation directed   Professor Norman M. Wereley
by: Department of Aerospace Engineering

This research focuses on the development of an active rotor system capable of primary control and vibration reduction for rotorcraft. The objective is to investigate the feasibility of a novel Trailing Edge Flap (TEF) actuation system driven by Pneumatic Artificial Muscles (PAMs). A significant design effort led to a series of experimental apparatuses which tested various aspects of the performance of the actuators themselves and of TEF systems driven by them. Analytical models were developed in parallel to predict the quasistatic and dynamic behavior of these systems.

Initial testing of a prototype blade section with an integrated PAM driven TEF proved the viability of the concept through successful benchtop testing under simulated $M = 0.3$ loading and open jet wind tunnel tests under airspeeds up to $M = 0.13$. This prototype showed the ability of PAM actuators to generate significant flap deflections over the bandwidth of interest for primary control and vibration reduction on a rotorcraft. It also identified the importance of high pneumatic system mass flow rate for maintaining performance at higher operating frequencies.

Research into the development and improvement of PAM actuators centered around a new manufacturing technique which was invented to directly address the weaknesses of previous designs. Detailed finite element model (FEM) analysis of the design allowed for the mitigation of stress concentrations, leading to increased strength. Tensile testing of the swaged actuators showed a factor of safety over 5, and burst pressure testing showed a factor of safety of 3. Over 120,000,000 load cycles were applied to the actuators without failure. Characterization testing before, during, and after the fatigue tests showed no reduction in PAM performance.

Wind tunnel testing of a full scale Bell 407 blade retrofitted with a PAM TEF system showed excellent control authority. At the maximum wind tunnel test speed of $M = 0.3$ and a derated PAM operating pressure of 28 psi, 18.8° half-peak-to-peak flap deflections were achieved at 1/rev (7 Hz), and 17.1° of half-peak-to-peak flap deflection was still available at 5/rev (35 Hz). A quasistatic system model was developed which combined PAM forces, kinematics and flap aerodynamics to predict flap deflection amplitudes. This model agreed well with experimental data.

Whirl testing of a sub-span whirl rig under full scale loading conditions showed the ability of PAM TEF systems to operate under full scale levels of centrifugal (*CF*), aerodynamic, and inertia loading. A commercial pneumatic rotary union was used to provide air in the rotating frame. Extrapolation of the results to 100% of *CF* acceleration predicts 15.4° of half-peak-to-peak flap deflection at 1/rev (7 Hz), and 7.7° of half-peak-to-peak flap deflection at 5/rev (35 Hz).

A dynamic model was developed which successfully predicted the time domain behavior of the PAM actuators and PAM TEF system. This model includes control valve

dynamics, frictional tubing losses, pressure dynamics, PAM forces, mechanism kinematics, aerodynamic hinge moments, system stiffness, damping, and inertia to solve for the rotational dynamics of the flap.

Control system development led to a closed loop control system for PAM TEF systems capable of tracking complex, multi-sinusoid flap deflections representative of a combined primary control and vibration reduction flap actuation scheme.

This research shows the promise that PAM actuators have as drivers for trailing edge flaps on active helicopter rotors. The robustness, ease of integration, control authority and tracking accuracy of these actuators have been established, thereby motivating further research.

Pneumatic Artificial Muscle Driven Trailing Edge Flaps
For Active Rotors

by

Benjamin King Sutton Woods

Dissertation submitted to the Faculty of the Graduate School of the
University of Maryland, College Park, in partial fulfillment
Of the requirements for the degree of
Doctor of Philosophy
2012

Advisory Committee:
Dr. Norman Wereley, Chair/Advisor
Dr. Curt Kothera
Dr. Amr Baz
Dr. Roberto Celi
Dr. Inderjit Chopra
Dr. Alison Flatau

DEDICATION

This entire work is dedicated to my beautiful, sweet, and compassionate wife Jenna Katherine Miller. She was and is the best thing that has ever happened to me. She was my loving companion for seven years, and in that time she taught me how brilliant love can be. Her personal struggles made her an exceptionally compassionate woman, and drew her into a loving relationship with me that was marked by an intensity, depth, and purity unlike anything I have ever known. I could not help but love her with the same passion, completeness, and loyalty.

The beauty of her soul and kindness of her heart were clear to everyone who knew her, even if few people understood the pain and anxiety that she dealt with every day. She fought constantly with an eating disorder that she had developed at a very young age. Her eating disorder became her way of coping, and since she was so young when it started, she never developed healthy methods of dealing with stress. She fought particularly hard in the last years of her life to overcome this deeply ingrained component of her personality, and I am very proud of her for never giving up. We had a wonderful life together free of jealousy, blame, bitterness and all the other parasitic slag that so often grows between people and tarnishes their relationships. The crucible of our love continuously burned off such impurities. Of course we fought, but we lived by the simple creed of Daniel Johnston: "Don't let the sun go down on your grievances."

Her cruel death from a heart attack at the age of 26 on January 8th 2011 destroyed me and everyone who knew her. It was directly caused by her eating disorder. She had an earlier brush with death a year and a half before which I had been lucky enough to save her from. I was unable to save her the second time, but I am so grateful that she

died peacefully in my arms. She was in bed next to me and never awoke from her sleep that morning. I took her last breaths with her and though the intensity of that experience at first pained me beyond comprehension, I now see how lucky I was to be with her in her final moments as she drifted off into the ether.

Though our relationship was all too short, it burned with an intensity that I can still see when I close my eyes. I tell her I love her dozens of times every day and I still feel very close to her. I am living now for both of us and I strive to make her proud.

This dissertation marks the end of an important and formative chapter in my life, and though I am sad she is not here to celebrate this triumph with me, I can feel her love and excitement all the same. I will begin the next phase of my life with a postdoctoral research position overseas at Swansea University in Wales, where I will develop morphing structures for aircraft and wind turbines. I will be buoyed in my journey by the satisfaction of this accomplishment and my intense gratitude towards Jenna for all that she has given me. I am not moving on from her; I am moving forward with her.

I love you baby!

ACKNOWLEDGEMENTS

I would like to gratefully acknowledge the support of the broad community of people who helped make my PhD work a very productive and rewarding time in my life.

First and foremost are my advisors in this work. Here I include Dr. Wereley, Dr. Kothera, and the members of my committee, Dr. Chopra, Dr. Flatau, Dr. Baz, and Dr. Celi. Dr. Wereley is a remarkable professor. He gives his students the perfect mix of independence and timely support. He'll let you muck about for a while figuring things out yourself, and then be there with a rope right when the quicksand starts to get too deep. I consider this to be the ideal mentoring style, and I am grateful that he took a chance on me. Dr. Kothera has been my colleague and friend at Techno-Sciences throughout my time here. I have worked closely with him on most of what is presented here and on several other projects which are not within the scope of this work. He has worked tirelessly to ensure the success and continuation of the fascinating and captivating research projects we are involved in. He is also an excellent editor, and has gone through my writings with a fine toothed comb, much to their benefit. Dr. Chopra and I have developed a very nice relationship over the past few years. Working with him on the Human Powered Helicopter project has been incredibly fun, and Dr. Chopra's support of this effort and of me has been crucial. We have also had some good and interesting conversations. Dr. Flatau, Dr. Baz, and Dr. Celi are all delightful people to work with and talk to, and their support and guidance in my work are much appreciated.

I would also like to acknowledge the love and support of my family. My mother taught me very early the value of doing what you're good at. She has also given me a

steady, helpful push towards the finish line. Jenna's parents Laura and George and Tom have also been amazingly supportive and loving. What we have been through together has only drawn us closer.

I'd also like to thank all of my friends from the office who made work fun, and who didn't forget about me when I moved up to the "Nursing Home" to finish up my dissertation. Special thanks to Grum, Erica, Ted, Ami, Robbie, Andrew, Nick, Harinder, Ryan, Jürgen, and Greg (in no particular order).

TABLE OF CONTENTS

LIST OF FIGURES

xi

LIST OF TABLES

NOMENCLATURE

a	Lift curve slope
A_s	Braided sleeve filament cross-sectional area
b	Critical pressure ratio – transition point from subsonic to choked flow
B	Length of a single filament in braid
C	Sonic conductance of the spool valve
C_{01}	Mooney-Rivlin bladder elasticity parameter
C_{10}	Mooney-Rivlin bladder elasticity parameter
c_f	Flap chord
CF	Centrifugal
c_h	Total hinge moment coefficient
c_{ha}	Hinge moment coefficient due to angle of attack
c_{hf}	Hinge moment coefficient due to flap deflection
c_l	Section lift coefficient
E	Flap chord ratio
E_s	Braided sleeve filament elastic modulus
f	Actuation frequency
F	PAM actuator force
F_a	Active (agonist) PAM force
F_b	Bladder elastic energy force component
F_{bl}	Actuator blocked force
F_f	Friction force component
F_G	Gaylord force component
F_p	Passive (antagonist) PAM force
F_S	Sleeve elastic energy force component
H	Total hinge moment
h_{pp}	Half-peak-to-peak amplitude
k	Linear spring constant
k_f	PAM friction coefficient
k_δ	Flap deflection lift coefficient factor
L	Actuator length
L_0	PAM initial (unloaded) active length
l_a	Active PAM moment arm
L_i	Active length of PAM defined as span between fittings
$\widehat{L_\iota}$	Effective active length of PAM with end correction
l_p	Passive PAM moment arm
$\dot{m}$	Mass flow rate
M	Mach number
MA	PAM TEF system mechanical advantage

n	Number of filaments in braided sleeve
N	Number of turns that a single braid filament makes around the PAM
OD	Outer diameter
P	Internal PAM pressure
PAM	Pneumatic artificial muscle
p_i	Valve inlet absolute pressure
p_o	Valve outlet absolute pressure
q	Dynamic pressure
r	Actuator radius
R_b	Rotor bade radius
r_0	Initial PAM radius
r_1	Inboard end of trailing edge flap
r_2	Outboard end of trailing edge flap
r_i	Current PAM radius
S_f	Planform area of flap
SMA	Shape memory alloy
s_t	Arc length of end transition region
t_0	Initial bladder thickness
$T_{available}$	Torque available
TECO	Trailing edge close-out
TEF	Trailing edge flap
T_i	Absolute temperature of air at orifice inlet
t_i	Current bladder thickness
T_o	Absolute temperature of air at orifice outlet
T_{ref}	Standard air temperature (293.15 K)
TRF	Torsion Rod Flexure
V	Internal PAM volume
V_b	Bladder volume
V_s	Braided sleeve volume
x_t	Axial length of end transition region
α	Section angle of attack
β_{lam}	Pressure ratio at laminar flow
δ	Flap deflection angle, positive downwards
ΔL	Change in actuator length
ΔR	Change in actuator radius
$\Delta\theta$	Local blade twist
ε	Material or actuator strain
θ	Deflection angle of moment arm for spring loading setup
θ_o	Global blade pitch
λ	Contraction ratio

λ_0	Actuator free contraction
λ_1	First Mooney-Rivlin strain invariant
λ_2	Second Mooney-Rivlin strain invariant
λ_3	Third Mooney-Rivlin strain invariant
ρ	Density of air
ρ_{ref}	Air density at standard conditions (1.185 kg/m^3)

1. Introduction

1.1.   PROBLEM STATEMENT

Rotary wing aircraft are complicated machines that have inspired and challenged design engineers since the time of Leonardo da Vinci. As with fixed wing aircraft, success did not come until the early 20th century when a series of parallel advancements in materials, aerodynamics, structures, and engine technology coalesced around a gifted group of designers all over the world. Innovations and progress came quickly and constantly over the following decades as helicopters left the realm of experimental whirlygigs and began doing real, useful work. Successful military deployment at the end of World War II proved that the unique capabilities of the helicopter, stemming from their ability to hover, more than warranted the complexity, cost, and danger involved. For the next several decades, there was an explosive boom in the development of this powerful new platform. Many new models were put into service as rapid advancements were made in key metrics such as speed, range, payload, and operating ceiling. Additionally, there was a significant diversification of the fleet as the helicopter was found to excel in a broad range of applications including search and rescue, cargo carrying, troop transport, attack, anti-submarine warfare and reconnaissance, among others. During the Vietnam War, the entire operating doctrine of the US Army changed as the helicopter earned a place of preeminence as an incredibly effective tactical and logistical tool.

The golden era of helicopter development started to slow, however, as performance became increasingly limited by the manifold complications of edgewise

rotor flight. First and foremost are the aerodynamic limitations caused by unsymmetric flow over a rotor in forward flight. Advancing blade drag divergence and retreating blade stall create a significant impediment to high speed forward flight due to rapid increases in the power required and large rotor force and moment imbalances. These unsteady forces and moments lead to high levels of vibration well beyond what is considered acceptable in the fixed wing community. Designing blades to perform well over the wide range of operating conditions seen between hover, high Mach number advancing blade flight, and low speed retreating blade flight requires significant compromise in all areas. This very broad operating envelope means that a design innovation which might help one area of performance will often hurt another. Thus, the helicopter is beset with a host of competing design constraints that vastly complicate an engineer's ability to create significant leaps forward. The result of these challenges has been a plateau in the performance of conventional helicopters over the last three decades.

Attempts to address this stagnation have included serious consideration of a wide range of alternatives to the "conventional" configuration of a single main rotor controlled through a swashplate with a single tail rotor for anti-torque and yaw control. Concepts such as thrust compounding, lift compounding, tilt-rotors, rigid coaxial rotors, slowed and even stopped rotors, and variable diameter rotors have been designed, tested, and in some cases put into production. Starting in the 1990's, another approach was considered which allowed for retention of the conventional configuration while promising to reduce vibration, drag, power requirements, and potentially noise. The basic premise was to make the rotors active in a manner which allowed for each blade to be controlled individually. Envisioned as a replacement for the current swashplate based technology,

individual blade control via an effective active rotor system would provide reduced vibration, noise, pilot and passenger fatigue, and even significantly reduced drag and power requirements through the elimination of the swashplate and associated drag intensive control components. The promise of the active rotor concept is nothing short of a new generation of "jet smooth," quieter, higher speed helicopters.

Researchers have now been aggressively pursuing the active rotor concept for a decade and a half. Progress over this time has been significant. While there are still no certified commercial or military helicopters flying with active rotors, there has been a lot of research work into a wide range of potential active rotor configurations that has led to a multitude of sub scale rotor tests, several full scale whirl tests, full scale wind tunnel testing, and in at least one instance, successful flight testing.

The most successful systems to date have used smart material based actuators, specifically piezoelectric materials, to drive trailing edge flaps. Unfortunately, these systems have some inherent limitations due to the actuation technology chosen. They are all vibration and noise reduction systems, with no primary control capability. While benefitting from compactness, direct conversion of electricity into mechanical work, and excellent frequency bandwidth, piezoelectric materials do not appear at this point in time to offer sufficient control authority to become the primary control actuators of future rotorcraft. As a result, active rotors have yet to fulfill their full promise.

While many other alternative actuation technologies have been explored for active rotors, one that has not been given any previous consideration is a rather promising option: Pneumatic Artificial Muscles, also known as PAMs. These devices are very

lightweight and simple muscle-like actuators powered by compressed air. They generate incredible levels of force for their size, and the deflections achievable are much larger than any smart material. They have a number of advantages over both traditional actuator technologies (hydraulics and electromechanical actuators) and smart materials, and deserve proper consideration for this demanding problem.

The purpose of the research program described in this dissertation was therefore to explore the possibility of a PAM driven active rotor system. Specifically, a Trailing Edge Flap driven by PAMs (PAM TEF) is proposed as a servo type flap for individual blade control capable of primary control and vibration reduction. A wide range of concerns and research questions were present at the outset of this work, from the basic robustness of the actuators, all the way to the waveform tracking accuracy of pneumatically driven actuators at frequencies significantly higher than typical for compressible fluid drive systems. This dissertation therefore has a broad scope, examining as many aspects of the problem as possible.

1.2. ACTIVE ROTOR SYSTEMS

The background and motivation for making rotor blades active will be discussed in further detail. A brief discussion of the extensive research done to date will show the evolution and progressive down-selection of actuator technologies that has led to the current state-of-the-art.

1.2.1. BACKGROUND AND MOTIVATION

Active rotor technologies are being pursued to address several fundamental problems that exist with rotorcraft. This section will address the sources of these

problems and how active rotors can benefit. The high levels of vibration present in rotorcraft will first be discussed. The sources of vibratory loads will be overviewed, leading to a discussion of how active rotor systems, if driven at the proper frequencies, can mitigate vibration by directly canceling unsteady loads. The background of the primary control systems used in helicopters will then be discussed, including discussion of the limitations and drawbacks of current technology. The ability of an active rotor system to supplement or replace current technology will be established. The high levels of control authority, reliability, and long life required for this to happen will be recognized.

1.2.1.1. Helicopter Vibration

The sources of high vibration levels in helicopters are myriad. Unsteady aerodynamic forces couple with the high elasticity of the long and slender blades to create a complex, multi-component vibration problem. In forward flight, the edgewise orientation of the main rotor creates a time varying velocity vector on each part of the blades. On the advancing side of the rotor, the forward flight velocity adds to the rotational velocity. On the retreating side the forward flight velocity reduces the effective free-stream velocity. In between, when the blades are aligned with the direction of motion, forward flight creates a spanwise flow component. Since the forces generated by the blades are dependent on the square of the velocity over the blades, the change in velocity around the azimuth creates significant changes in forces and moments. The 1/rev and 2/rev velocity fluctuations give rise to steady, 1/rev, and higher harmonic air loads. This broad spectrum of forcing then excites various elastic modes in the blades. Motion of the blades also couples back with the aerodynamics, creating a complex

5

vibratory interaction. The rotor hub sums all of the loads, and transfers them into the airframe where they degrade the quality of flight for the operators, limit pilot endurance, and reduce the safe operating lifetime of components on the helicopter. In moving from the rotating frame to the fixed frame, a filtering effect occurs, leaving (for a balanced rotor) vibration energy at frequencies which are multiples of the blade passing frequency, which is denoted as N/rev, where N is the number of blades on the main. For example, the fuselage of a four bladed helicopter will vibrate primarily at 4/rev, with progressively lower levels of energy at increasing harmonics (8/rev, 12/rev, etc.). It is known through the mathematics of Fourier Coordinate Transformation that only the N/rev and N±1/rev loads in the rotating frame contribute to the N/rev fixed frame loads.

In order to reduce the level of vibration transmitted into the airframe, it is therefore necessary to generate counteracting loads at N/rev and N±1/rev that will directly cancel out the vibrations present at the hub. Active rotor systems accomplish this by creating time-varying, complex waveform blade deflections that induce the desired airloads. Historically, this has been accomplished primarily through active twisting of the blade, thereby changing the pitch angle distribution, or through trailing edge flaps that locally change the airfoil camber and thus aerodynamic coefficients.

1.2.1.2. Helicopter Primary Control

One of the greatest challenges that faced the early helicopter pioneers was how to control the thrust level and direction of flight of the craft. During the early decades of the 20$^{\text{th}}$ century many different approaches were tried. It was not until the invention of the swashplate that a reliable, relatively simple and scalable solution was found. The development of the swashplate can be traced through the patents of Crocco in 1906,

Yurev in 1910, and Hafner in 1922 (Leishman, 2006). This technology became the industry standard mechanism by which both the magnitude and orientation of the aerodynamic forces on the rotor are controlled. This device allows for independent control of the collective and cyclic pitch of the blades. Collective pitch control increases or decreases the pitch angle off all the blades simultaneously, thereby changing the overall level of thrust produced by the main rotor. Cyclic pitch induces a sinusoidal variation in blade pitch angle as the blade rotates through the azimuth. These cyclic pitch changes then excite cyclic blade flapping motions which tilt the tip-path-plane of the rotor disc about the hub. This creates a net directional force which is used to control the direction of flight. The design of the swashplate allows for motion in any direction in 3D space, or for no motion at all in the case of hover; which is what makes helicopters so useful and unique. Figure 1.1 shows a modern swashplate mechanism as realized in the AH-64 Apache attack helicopter. Note the mechanical complexity and poor aerodynamic geometry.
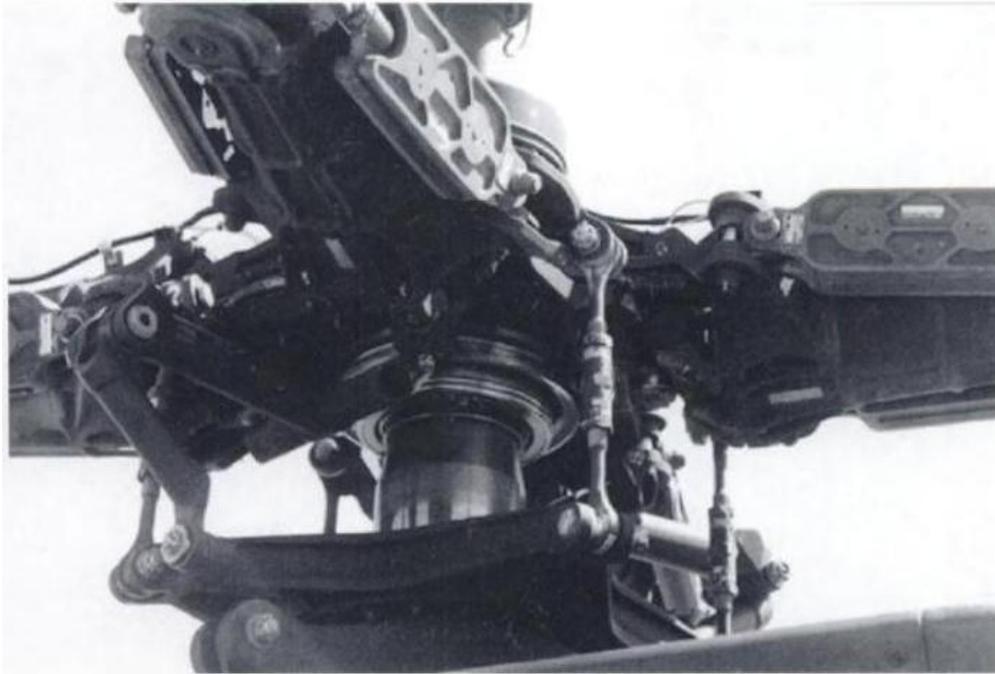
Figure 1.1. AH-64 Apache hub showing swashplate and associated components (Leishman 2006).

While the helicopter industry as a whole converged on the swashplate as the means of rotor control, there is one interesting and informative exception. Charles Kaman, one of the most brilliant and inventive engineers to work on rotorcraft, worked for Igor Sikorsky in the 1940's and helped design the breakthrough R-4 and R-5 helicopters. Frustrated that his new ideas were falling on deaf ears under Sikorsky's leadership, Kaman quit and started his own company. The designs he subsequently produced all use a significantly different approach to rotor control than the industry standard. Kaman paired torsionally soft rotor blades with servo-type trailing edge flaps to create a control system with all the authority of a swashplate mechanism but with several distinctly different traits. Since this approach is very similar to what is being proposed as a solution in this dissertation, it is useful to consider the relative merits of swashplate and trailing edge flap driven rotor systems:

1. Swashplates are a well-established technology with a long track record of good service. Trailing edge flap driven rotors also have a long service career, but at much lower numbers.

2. Swashplates drive the entire rotor blade directly by changing the pitch angle at the root. This givens good blade aerodynamics, but very poor hub aerodynamics (due to the size and shape of the components). This is a particularly important point due to the significant impact of hub drag on overall vehicle drag. Leishman estimates the hub, pitch links, pitch horns and other related components to be 30% of total equivalent flat plate area (Leishman 2006).

3. Swashplates are complex, heavy, and susceptible to several types of mechanical failure. They contribute a significant portion of the initial cost and recurring maintenance costs for a modern helicopter.

4. Servo type trailing edge flap rotors drive the blades indirectly: flap deflections generate large pitching moments which twist the torsionally soft blades. This approach uses energy in the airflow to affect control action, and so requires significantly lower control loads. The flap does incur a drag penalty, particularly if a separate flap mounted behind the blade is used, as in the Kaman designs. However, a significantly cleaner hub is realized, which may lead to an overall reduction in vehicle drag.

5. Current trailing edge flap designs still use swashplate mechanisms to transfer the collective and cyclic flap inputs from the fixed to rotating frames, so they are not free of the associated problems. Due to the reduced control loads

however, the swashplates used in the Kaman designs are much smaller, lighter, and simpler. Additionally, Kaman designs will typically embed the swashplates into the airframe, such that their effect on drag is minimal.

If these various design traits are considered together, the benefit of a trailing edge flap driven rotor coupled with active on-blade actuation to eliminate the need for a swashplate can be seen. Additionally, careful design of the flap system can lead to a substantially lower drag penalty. This can be achieved through the choice of an embedded plain flap as opposed to the Kaman style bracket mounted, discrete flap behind the airfoil.

It is important to note that the swashplates of current helicopters are flight critical components. Failures typically lead to a loss of aircraft control, which is clearly a very dangerous situation. Any system which would replace the swashplate for primary control would still be just as flight critical. Therefore the robustness, reliability, fatigue life and damage tolerance of any proposed active rotor primary control system must be thoroughly proven before success is possible. One potential advantage of active rotors is that multiple, redundant trailing edge flaps could be installed on each blade such that the loss of any one component would not be catastrophic. Swashplate mechanisms have not been able to be made mechanically redundant, and so will always provide a single point of failure for the entire vehicle.

1.2.2. ACTIVE ROTOR LITERATURE REVIEW

As mentioned above, there is a large body of literature extant on the subject of active rotor systems. For the purposes of this dissertation, which is really focused on the

actuation component of this multifaceted problem, previous work will be presented and organized based on the type of actuation technology used. Attempts to use the more well-established aerospace actuators such as hydraulic pistons and electric motor based devices, which are referred to as "traditional" technologies herein, will be discussed first. Subsequently, the development and use of smart materials as active rotor actuators will be shown.

1.2.2.1. Traditional Actuation Technologies

A series of analyses and experiments have been undertaken attempting to use hydraulic and electric motor based actuators for active rotor systems. One of the most extensive programs to-date involved retrofitting a full-scale UH-60A rotor system with hydraulically driven pitch links to supplement the swashplate inputs with higher harmonic control actuations. This was a joint effort between Sikorsky Aircraft Corporation, ZF Luftfahrttechnik GmbH (who manufactured the actuators), and the NASA Ames Research Center. This program culminated in a full-scale wind tunnel test in the 80 by 120 ft wind tunnel at Moffett Field, CA (Jacklin, Haber, de Simone, *et al.*, 2002). This testing showed effective reduction of 4/rev vibrations, and noise reduction using 2/rev inputs to push the blades out of the trailing wake of the blade in front of them; directly mitigating Blade Vortex Interaction (BVI) noise. The individual blade control (IBC) system was tested with blade pitch variations of up to 3.0°. The actuators were capable of larger dynamic pitch changes, but test time in the wind tunnel was limited. This testing program was more extensive than earlier related work using a BO-105 rotor system (Jacklin, Nguyen, Blaas, *et al.*, 1994).
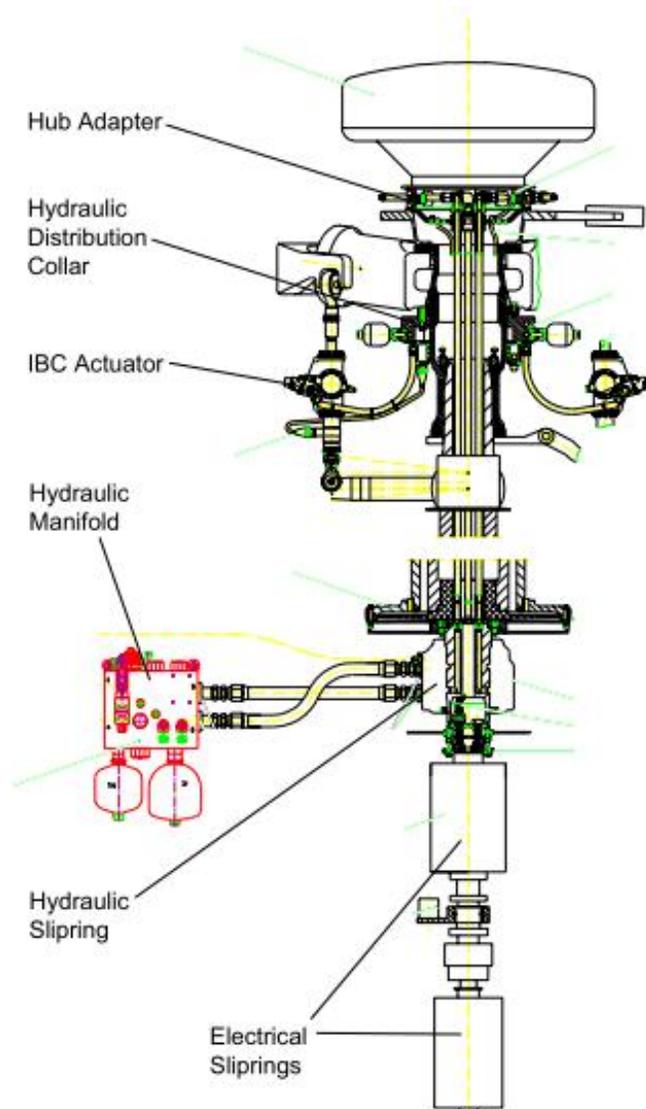
Figure 1.2. Hydraulically driven active pitch link system schematic (Haber, Jacklin, deSimone, 2002).

Figure 1.2 shows a schematic view of the hydraulic and electrical systems used in the Sikorsky/ZFL/NASA testing. The mechanical complexity of this system is apparent, and the use of hydraulic pistons in the rotating frame introduces a series of reliability and safety of flight issues. The hydraulic slip ring is a complex apparatus that must distribute four different fluid lines (in the case of a four bladed rotor) at very high pressure. Oil leaks and component malfunctions, while not noted in the discussions of the wind tunnel

testing, would be a concern for long term reliability. The effect of this system on aircraft drag would also be considerable given the large projected area of the active pitch links and the added hub components. Furthermore, this system was a supplement and not a replacement for the swashplate as the control authority of the active pitch links was insufficient for primary control.

An electromagnetic actuator was developed for use on active rotor systems by Diversified Technologies Inc., in collaboration with the US Army Aeroflightdynamics Directorate (Fink, Hawkey, Gaudreau, *et al.*, 2000). A trailing edge flap of 11.3% span, 46% chord centered at 91% of blade radius was retrofit into an OH-58 (Kiowa Warrior) rotor blade and hover tested. The configuration of this flap can be seen in Figure 1.3. While whirl testing showed fairly good performance levels of ±6° of flap deflection at 4.4/rev, 81% of dynamic loading, and 66% of centrifugal loading, testing on this concept appears to have ceased. An added weight of 9.6 pounds per flap is one concern, although the authors state that the weight was not optimized. Given the short span of each flap, multiple flaps per blade would likely be required to generate sufficient authority for primary control, compounding the system weight. The effect of adding at least 10 pounds to the tip of the blade on the centrifugal loads that must be reacted at the hub is considerable. At 91% span on an OH-58, the centrifugal acceleration is 925 *g*, so the 10 pounds of mass added to this point will add 9250 lb of centrifugal force to the attachment point of each blade.
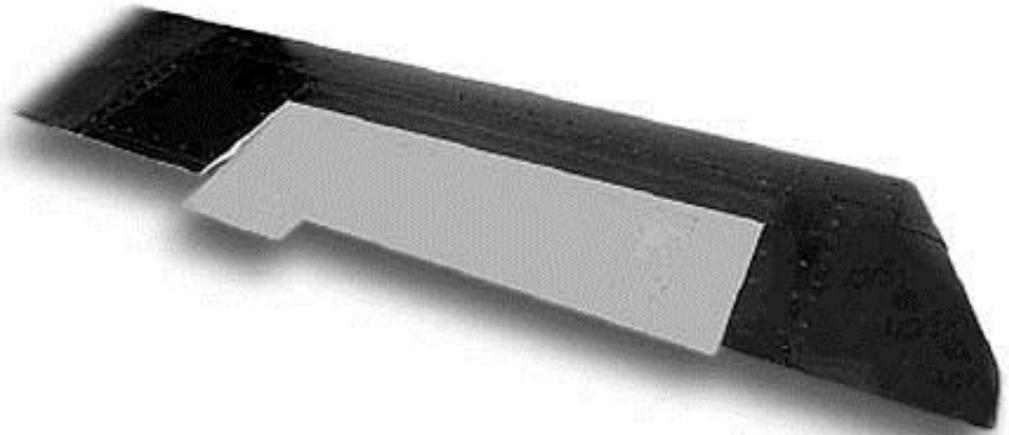
Figure 1.3. Heliflap electromagnetically driven TEF (Fink, Hawkey, Gaudreau, Wellman, *et al.*, 2000).

1.2.2.2. Smart Material Actuation Technologies

So called "Smart Materials" are a class of materials that exhibit induced strain under excitation from various types of fields. Most often this strain occurs due to reorientation of the atomic or crystalline microstructure. While materials exist in nature that exhibit such properties, the strains available from these are too small to make effective actuators. Over the last century, a series of advanced alloys have been developed which respond to electrical, magnetic, or thermal fields with significant levels of induced strain and stress. Piezoelectic materials, such as PZT, respond to electrical fields and can generate contraction/tension and extension/compression depending on the polarity of applied field. Shape Memory Alloys (SMAs), such as NiTiNol, create contraction/tension under the application of thermal fields. Temperature changes are often created in SMA by running current through them and generating resistive heating. Magnetostrictives, such as TerFeNol-D, and Magnetic Shape Memory Alloys (MSMA),

14

such as Ni_2MnGa, can extend or contract depending on the polarity of applied magnetic fields.

Uses of magnetostrictive/MSMA materials for active rotors have been limited. Couch (Couch, 2006) explored the possibility, but ultimately the weight and volume of the electromagnets required to generate the desired fields were prohibitive, and the work output of the Nickel Manganese Gallium alloy used was too small.

Liang, Davidson, Schetky, and Straub investigated the use of a torsional SMA actuator to produce elastic blade twisting in a V-22 Osprey blade (Liang, Davidson, Schetky, *et al.*, 1996). The intention was to create a low frequency actuator that would help mitigate the severe design compromises present in the tilt-rotor due to requirements for both edgewise and propeller mode flight. The system would be actuated as the aircraft converted from helicopter mode to airplane mode, allowing for better efficiency in both modes.

Singh, Sirohi, and Chopra developed an active blade tracking tab powered by SMA wires (Singh, Sirohi, and Chopra, 2003). The device was intended to provide in-flight tracking capability through low frequency flap deflections. This is not strictly an active rotor application as the control authority and bandwidth were too low to accommodate primary control and vibration reduction, but wind tunnel testing of the concept at low Mach numbers showed significant flap deflection levels and good closed-loop tracking.

Chandra investigated active twist rotors using sandwich beams constructed from SMA sheets and graphite-epoxy (Chandra, 2001). The concept used bending-torsion

composite coupling to generate twisting motion from axial displacements in the SMA layers.

A group of inventors from Italy have applied for a US Patent for an SMA driven multi-segment morphing trailing edge (Pecora, Iannuzzo, Riccio, *et al.*, 2010). The effectiveness of this device is not known, but the mechanisms shown in the patent application are mechanically fairly complex. One additional concern for Shape Memory Alloy systems is their relatively low fatigue life, as reported by (Casciati and Marzi, 2010).

By far the most successful smart material active rotor research to date has focused on the use of piezoelectric materials. The direct conversion of electricity into work that piezos provide makes them significantly easier to implement, allows for lighter weight solutions, and provides excellent response times, leading to high bandwidth capability. Piezoelectric TEF actuation systems were originally proposed by Hall and colleagues (Hall and Spangler, 1993; Hall and Wereley, 1993; Hall and Prechtl, 1996), and subsequently attracted substantial attention. They have typically been employed in reduced scale prototype demonstrations (Chopra, 2002). Many researchers over the last two decades have pursued this approach and performance has been progressively improved as a result of this work (Loewy, 1997; Giurgiutiu 2000; Chopra, 2000; Fulton, 2000; Niezrecki, Brei, Balakrishnan, *et al.,* 2001). Indeed, a full-scale whirl test (Straub *et al.* 2004), and the first flight test (Dieterich, Enenkl, and Roth, 2006) of a smart rotor equipped with piezoelectric actuator-based TEF systems were recently conducted. It is important to note that the work done to date with piezoelectrics has focused on vibration and noise reduction.

However, piezoelectric materials are known to suffer from some inherent limitations, including small actuation strains ($\varepsilon < 0.2\%$), material brittleness, and significant cost, among others (Giurgiutiu, 2000). They require very high excitation voltages, as well. Historically, bulky and heavy power amplifiers have been used, although advances in microelectronics have started to mitigate this problem. The main drawback of piezos as active rotor actuators is that they do not provide sufficient control authority for primary control of the helicopter. This is why research to date has focused on generating the smaller flap deflections required for vibration and noise reduction. Flap deflection amplitudes under full-scale loading have been limited to $\sim\pm6°$ (Straub, Kennedy, Stemple, *et al.* 2004). While it is possible that a significant breakthrough in material science or system design will allow for either more work output from piezoelectrics or more resultant system control authority, motivation clearly exists at this point in time to consider alternative actuation technologies if the true potential of active rotor systems is to be realized.

1.3.   PNEUMATIC ARTIFICIAL MUSCLE ACTUATORS

The actuation technology pursued in this dissertation will be introduced. A brief historical perspective will lead to a discussion of the operating mechanism of PAMs. Strong motivation for PAMs in active rotors will be established by consideration of a series of quantitative performance metrics, and through discussion of more qualitative concerns specific to the challenging active rotor problem.

Discussion of previous research on PAMs for aerospace applications will show that while others have considered related uses, the concept of a PAM TEF is novel. Review of the extensive body of literature relating to PAMs as actuators for orthotics and

robotics will establish the state-of-the-art in PAM performance, modeling and controller development.

1.3.1. BACKGROUND AND MOTIVATION

Pneumatic artificial muscles are an interesting class of actuators with a surprising mix of excellent performance but relative obscurity. Reportedly, the first true actuators of this type were developed in the 1930's by a Russian inventor named S. Garasiev (Marcinčin and Palko, 1993). Similar types of devices can be found in patents from the era including a rubber tube covered in a braided fiber exterior (Pierce, 1940), an actuator (Haven, 1949), and an elastic diaphragm covered in stiff fibers (Morin, 1953). It is Joseph McKibben though who is generally credited with the first true development of a pneumatic artificial muscle (Life, 1960). For this reason, these devices are often known as McKibben muscles in the literature. Many other names exist as well, including Pneumatic Muscle Actuators, Fluidic Flexible Matrix Composites, Fluidic Muscles, Braided Artificial Muscle, and the trademark name Rubbertuator® used by the Bridgestone rubber company. Pneumatic Artificial Muscle (PAM) is used throughout this work as it is the most relevant and accurate descriptor for the devices considered here.

PAMs possess many attractive characteristics for implementation in active rotor systems. They are simple, lightweight actuators that produce high levels of force and large, usable strokes at moderate actuation pressures (< 620 kPa). For example, a 16 mm diameter, 0.2 m long PAM can generate as much as 4450 N of blocked force at 620 kPa, and will have a maximum stroke of up to 40% of its initial active length. This PAM is 20 cm long, but has only 15 cm of active length (due to the end fitting lengths),

corresponding to a nominal maximum displacement of 6 cm, while having a mass of only 40 g. This PAM will therefore have a maximum specific force of over 100,000 N/kg, and a maximum specific work of 4000 J/kg.

The potential advantages of PAM actuators extend beyond their high performance levels. They are naturally compliant which makes them highly tolerant to misalignment and impulsive loading. PAMs use pressurized air as their operating fluid, which offers several distinct advantages over hydraulics, such as the ability to eliminate the return circuit, a significantly lower fluid density (air vs. oil), and no risk of fire or explosion. Also, because air can be distributed to PAMs via flexible, lightweight, low pressure tubing, PAMs are highly amenable to distributed actuation concepts.

PAMs consist of four basic parts: an inner elastomeric bladder (e.g., latex or silicone tubing); an outer helically braided sleeve; and a fitting at each end to seal the actuator and allow for transfer of the force and motion. The operating principle of PAM actuators is as follows. The inner bladder is inflated with air under pressure, causing an expansion of the bladder diameter. The braided sleeve around the bladder is thereby forced to expand radially; however, the fixed length of the stiff sleeve fibers generates a contractile force and displacement along the main axis of the PAM. This force and motion is transferred to the system via the end fittings. Figure 1.4 shows a PAM in both the relaxed (upper) and inflated (lower) stages.
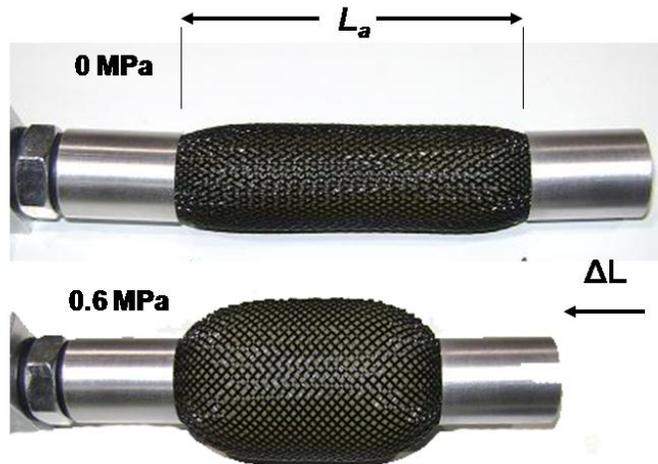
Figure 1.4. PAM geometry and operation.

In order to consider the performance of PAM actuators relative to other alternatives, Table 1.1 compares several key actuator performance metrics. This table is adapted from (Huber, Fleck, and Ashby, 1997) with representative data for electromechanical actuators and PAMs added. Active rotor applications require large forces and strokes to affect significant changes to aircraft performance. Here, the stroke of the actuators is normalized to their starting (resting) length to give actuator strain. Actuation stress is found by dividing the force available by the cross sectional area of a given actuator, which allows for more direct comparison of differently sized actuators. The actuator strain and stress can be combined to give a maximum work output of the actuator. Dividing this work by the mass of the actuator gives a very informative and useful specific work metric. It can be seen in Table 1.1 that the large strains and high actuation stresses of PAM actuators combine with their low weight to yield excellent specific work. They have significantly better performance in this respect than all of the smart material actuators with the exception of shape memory alloys (SMA). It can be

seen that the specific work of hydraulic actuators is very good, which helps to explain their current prominence, but as mentioned before, the need for high pressure oil complicates their use in active rotors.

Table 1.1. Comparison of actuator technologies. Adapted from (Huber, Fleck, and Ashby, 1997) with data from (Moog, 2011) and (Muirhead, 2011).

Actuation Technology	Max Strain	Actuation Stress (MPa)	Specific Work (J/kg)	Max Frequency (Hz)
Hydraulic	1	70	35000	100
Electomechanical	0.5	1	300	–
Solenoid	0.4	0.1	5	80
Piezoelectric	0.002	9	1	10^7
Magnetostrictive	0.002	200	20	10^7
Shape Memory Alloy (SMA)	0.07	700	4500	7
Pneumatic Cylinder	1	0.9	1200	100
UMD Pneumatic Artificial Muscle	0.4	16	4000	100

Another performance metric of interest, particularly for active rotor applications, is the operating bandwidth. In order to achieve the goal of vibration and noise mitigation, actuation frequencies on the order of 50 Hz (Yu, Gmelin, Splettstoesser, *et al.*, 1997) are typically required. SMA actuators in particular are unable to meet this requirement and are therefore not a contender for dynamic control in active rotors.

Due to their operating principle, PAMs are essentially a unidirectional actuator. Interestingly, they can be designed to generate either contraction or extension depending

on the initial helix angle of the braided sleeve. Generally, the forces created by contractile PAMs are much greater than those of a similar sized extensile PAM. Additionally, extensile PAMs are susceptible to buckling when actuated, especially with longer lengths. For these reasons the PAMs studied here are designed to be contractile. Contractile operation is also more analogous to natural muscle, allowing for biologically inspired configurations and architectures to be employed (Schulte, 1961). If bidirectional control is desired, as in the case of a helicopter TEF, a single PAM can be operated against a spring load. In this configuration, a bias pressure is required to center the output in the middle of the operating range. A second option is to replace the spring with another PAM, so that the two PAMs operate as a pair of agonist/antagonist muscles. Shown schematically in Figure 1.5, this approach is inspired by the operation of muscles in the human body (e.g., the biceps/triceps arrangement) and has the benefit of allowing for control of both rotation of an effector about a pivot point, as well as joint/hinge stiffness. In an antagonistic arrangement, motion in one direction is achieved by inflating the agonist PAM, while leaving its antagonist PAM vented to atmosphere. To move in the other direction, the roles of the agonist and antagonist are switched. The formerly agonist PAM is deflated and becomes the antagonist while the formerly antagonist muscle is pressurized to becomes the agonist. Antagonistic PAM configurations are the preferred choice for trailing edge flap systems because they have a neutral state (i.e., no pressure in either PAM) at the center of their output range, which creates a more graceful failure mode than the hard over neutral state of a PAM vs. spring configuration. Additionally, the antagonistic arrangement has the benefit of variable hinge stiffness by overlaying a bias pressure to both PAMs. Increasing pressure equally in both PAMs

increases the force in both without changing the output flap angle, causing an effective increase in hinge stiffness.
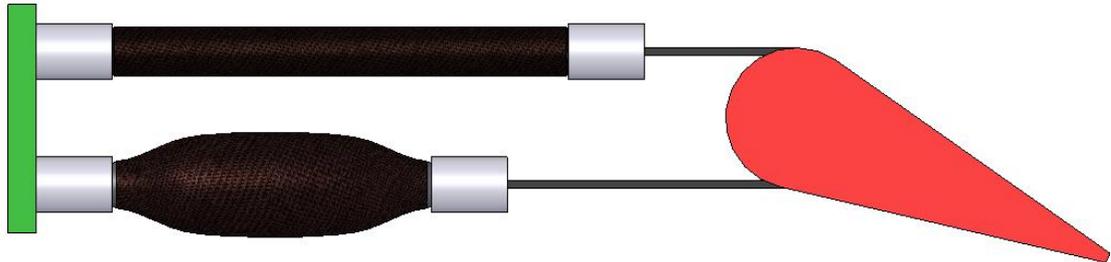
Figure 1.5. Schematic of antagonistic PAM pair driven trailing edge flap.

1.3.2. PAM LITERATURE REVIEW

The existing literature on PAM actuators will be discussed, focusing first on aerospace applications, and then expanding out to robotic, orthotic, and variable stiffness structure applications.

1.3.2.1. Aerospace Applications

To date the use of pneumatic artificial muscles for aerospace applications has been limited, with all of the research in the literature having occurred in the last six years.

The first aerospace related application was the use of large scale PAMs to provide a soft landing capability and steering for an active parachute system (Zhang, Accorsi, and Leonard, 2005). Chronologically, the next aerospace application in the literature is the prototype PAM TEF system developed here (Woods, Bubert, Kothera *et al.*, 2007), as described in detail in Chapter 2. PAM actuators were also used to drive a morphing aircraft demonstrator developed by this author and colleagues in (Bubert, Woods, Kothera, *et al.*, 2010).

Researchers at Texas A&M University-Kingsville have developed a morphing wing concept using PAMs (Peel, Mejia, Narvaez, *et al.*, 2009). This is the closest application in the literature to the concept proposed here, and so will be discussed in more detail. The actuators used in this study, seen in Figure 1.6, were manufactured via filament winding of carbon fiber tow impregnated with polyurethane elastomer over a steel mandrel. The ends of the carbon fibers were left dry to allow for subsequent bonding into the test model.

Figure 1.6. Filament wound carbon fiber/polyurethane PAMs fabricated in (Peel, Mejia, Narvaez, *et al.*, 2009).

Three of these PAMs (known here as Rubber Muscle Actuators, RMAs) were assembled into a short section of Clark Y airfoil which was designed to allow for leading edge droop and trailing edge camber morphing. The required motions in the skin were accommodated through a discontinuous sliding interface on the lower skin surface. The actuators were mounted to the bottom of the leading edge and the bottom of the trailing edge, such that the contraction during pressurization simultaneously drooped the leading edge and increased the camber of the trailing edge in a coupled manner, as can be seen in

Figure 1.7. The actuation is unidirectional, with elastic stiffness returning the airfoil to its original shape upon depressurization of the actuators.

(a) In resting state

(b) With PAMs pressurized
Figure 1.7. Morphing wing section (Peel, Mejia, Narvaez, *et al.*, 2009).

While this concept seems promising, to date no loaded testing on the prototype exists in the literature. Its performance on the benchtop, in the wind tunnel, or under rotation is unknown. The impact of the elastically driven deflected airfoil shape and the lower surface discontinuity on the aerodynamic coefficients has not been established. Similarly, the fatigue life of the actuators and mechanisms is unknown.

An actuated alternative to the variable stiffness structures, discussed in section 2.1.1.2 below, has been presented in two publications to date (Chou and Philen, 2008; Hinshaw, 2009). In this concept a matrix of PAMs (known here as Flexible Matrix

composites, FMCs) are embedded into a solid block of elastomer to form a morphing structure. Chou and Philen (2008) proposed a trailing edge morphing concept wherein differential actuation of the top and bottom layers of muscles would induce positive and negative camber changes. Analytical predictions of deflected shape under aerodynamic loading were shown.
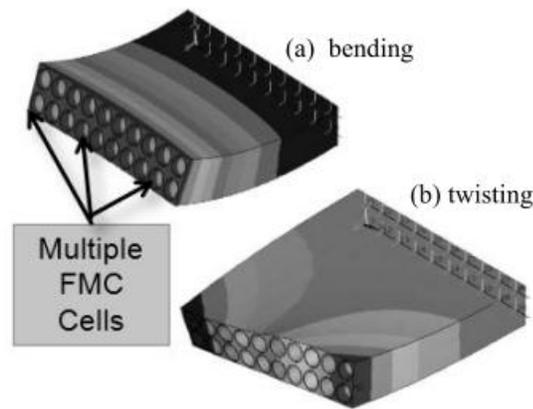
Figure 1.8. Embedded PAM morphing structure concept (Chou and Philen, 2008).

Hinshaw presented a morphing wingtip concept for a glider wherein thin skins made from PAMs embedded in elastomer were used to twist the airfoil structure, inducing changes in the angle of attack (Hinshaw, 2009). This concept is shown schematically in Figure 1.9. A detailed structural model was developed and combined with vortex panel method aerodynamic predictions to create a coupled FEA/CFD analysis. The structures were predicted to be able to induce tip angle changes of -6° to +2°. The developed model was then validated against results from commercially available software, NASTRAN for the structural component and XFOIL for the aerodynamics, with generally good agreement. However, no test articles have been built to date and no experimental results are shown.
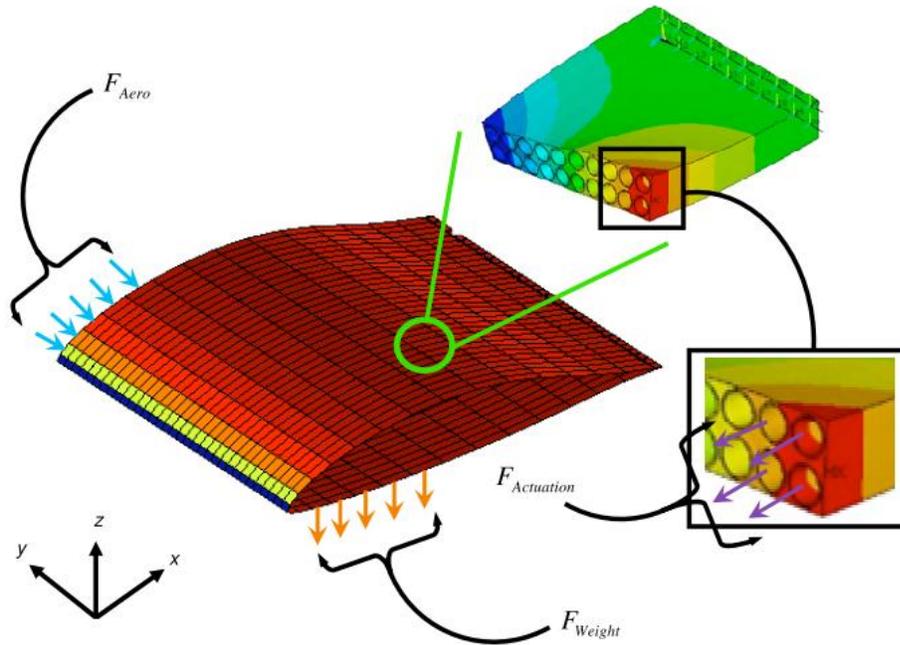
Figure 1.9. Finite element model of PAM driven morphing wing tip (Hinshaw, 2009).

A related type of pneumatic actuator, known as a bellow actuator, has been used as the driving mechanism for a wing sweep mechanism (de Marmier and Wereley, 2003). While they both are made from reinforced elastomer materials, pneumatic bellow actuators differ from PAMs in structure, geometry and operation; being extensile/compression type actuators. Experimental testing of a UAV scale test article showed the ability of the antagonistic actuation system to deploy and retract the wings through a 45 degree sweep range.

<div align="center">
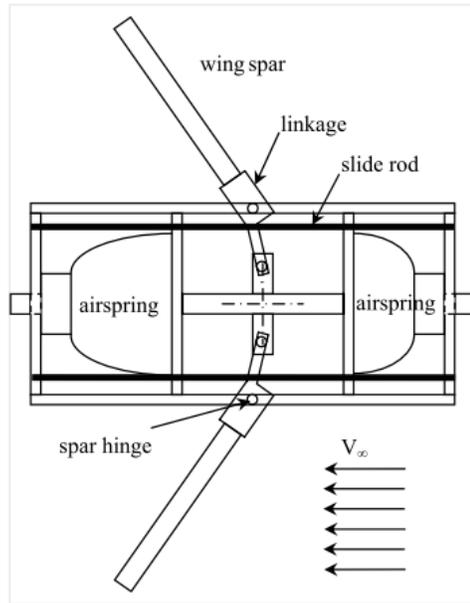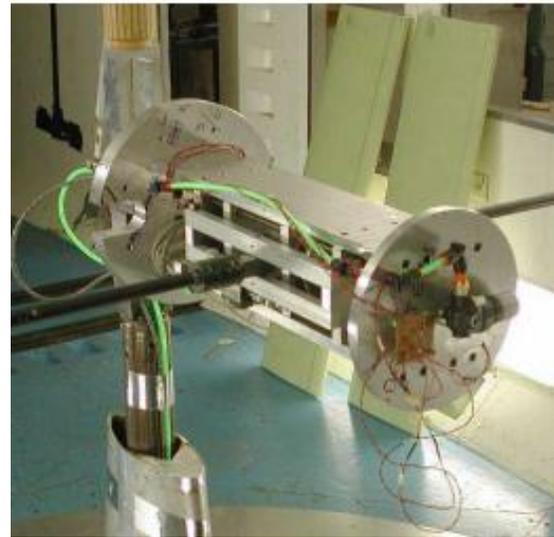
(a). design schematic   (b). prototype in wind tunnel

Figure 1.10. Bellow actuator driven wing sweep mechanism (de Marmier and Wereley, 2003).

</div>

1.3.2.2.   Orthotics/Robotics Applications

The primary use of PAM actuators to date has been as analogs to natural muscle in orthotics and robotics. Indeed, Joseph McKibben's pioneering use of the actuator in the 1950's was on devices for polio patient rehabilitation. Since then a wide array of related applications have been investigated, and much progress has been made in the areas of PAM performance, modeling, and control.

Schulte performed a combined analytical and experimental examination of PAM behavior (Schulte, 1961). This work developed a model of PAM force, and ran a series of characterization tests on five different PAM geometries. A PAM powered orthotic was shown, as seen in Figure 1.11, although the design and performance of this device were not discussed. An interesting comparison was made between the performance of natural human muscle and one of the developed actuators, with remarkable similarities in the shape of force evolution with displacement. Bharadwaj and colleagues developed a

<div align="center">

28

</div>

similar rehabilitative orthotic device that used a linear extension spring in addition to a PAM to provide a restoring torque (Bharadwaj, Hollander, Mathis, et al., 2004).
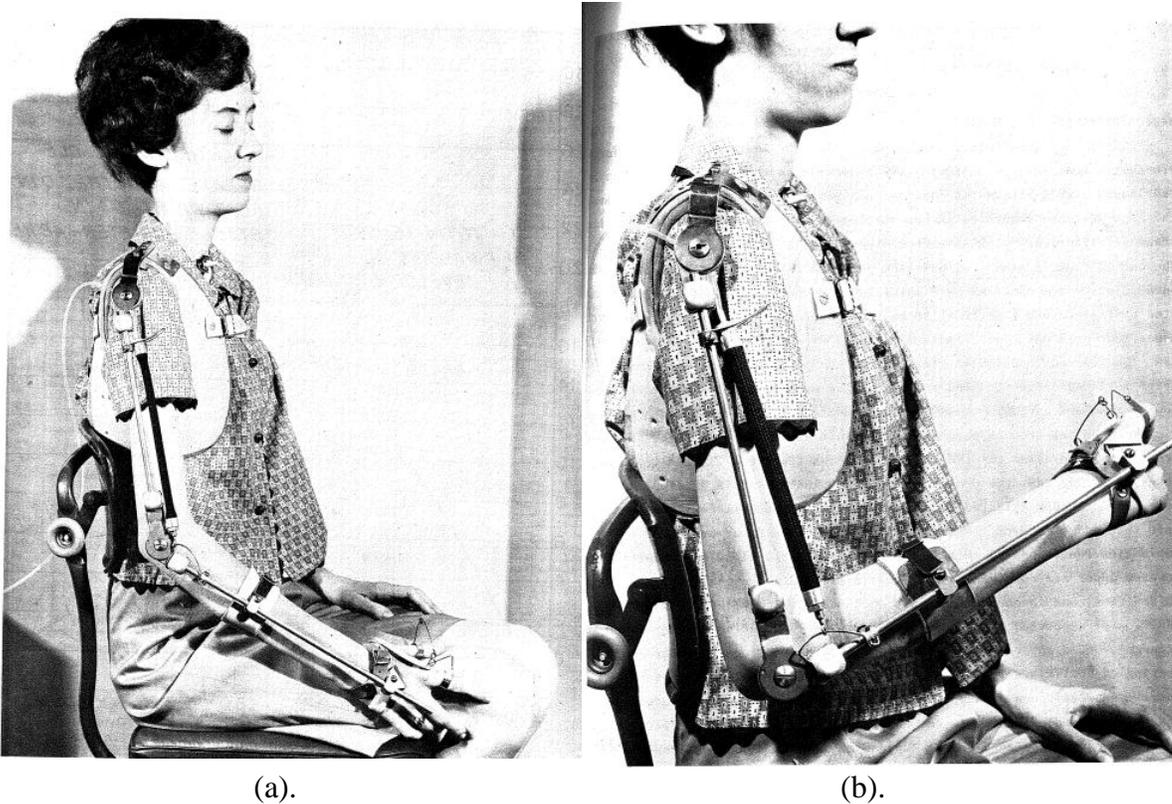
<div align="center">(a).   (b).</div>

Figure 1.11. Early PAM powered orthotic (a). relaxed and (b). contracted (Schulte, 1961).

Several different leg orthotics have been developed with varying levels of complexity and degrees of freedom, including an ankle-foot device (Ferris, Czerniecki and Hannaford, 2005), a knee-ankle-foot orthotic (Sawicki and Ferris, 2009), and a fully powered leg exoskeleton (Costa and Caldwell, 2006).

A lot of work has been done in the area of robotic devices and most of the PAM modeling and control work done to date has been in this area. In 1995, Caldwell *et al.* developed a robot arm with a 3 DOF shoulder joint, 3 DOF wrist, and 1 DOF elbow (Caldwell, Medrano-Cerda, and Goodwin, 1995). The shoulder joint was driven by

<div align="center">29</div>

electric motors mounted off of the arm, with the remaining joints being PAM driven. This device is pictured in Figure 1.12.
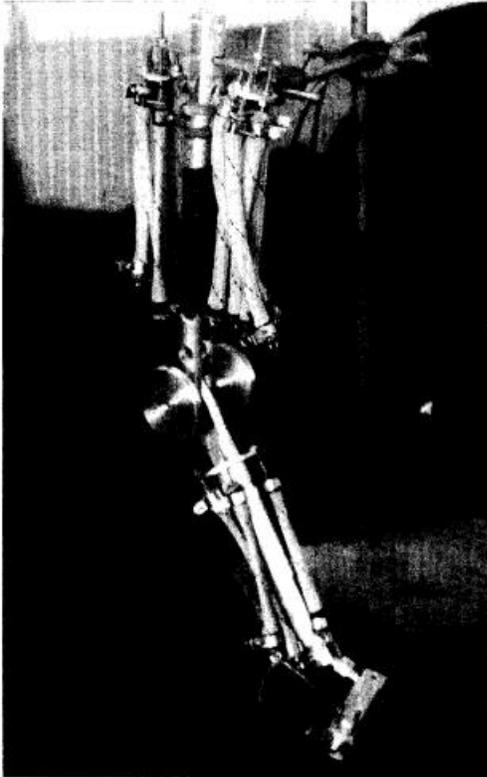
Figure 1.12. Seven DOF robot arm (Caldwell, Medrano-Cerda, and Goodwin, 1995).

Initial testing focused on the elbow joint, driven by 5 PAMs mounted in parallel as "biceps." System identification techniques were used to develop a system model for controller development. Tracking of sinusoidal commanded waveforms at frequencies up to 0.62 Hz signals showed significant lag in the system, and additionally the system was not able to achieve the desired displacement amplitudes, as seen in Figure 1.13.
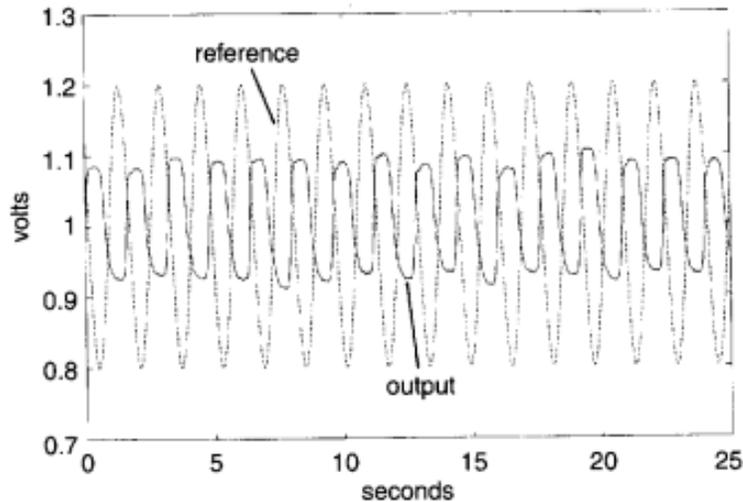
Figure 1.13. Closed-loop sinusoid tracking of elbow joint rotation @ 0.62 Hz (Caldwell, Medrano-Cerda, and Goodwin, 1995).

A bipedal walking robot driven by eight PAM actuators arranged into antagonistic pairs around four joints (a hip and knee joint in each leg) was built and tested for walking capability (Caldwell, Medrano-Cerda, and Bowler, 1997). Each actuator was driven by a solenoid valve through pulse width modulated commands from an adaptive controller. Frequency capability up to 5 Hz and position accuracies of better than 1% are claimed, although no results were shown. It was found that for short stride lengths the system was sufficiently stable, but larger stride lengths (over 15 cm), the robot experienced balance problems. An active balance system was recommended but not implemented in this work.

A 2 DOF robot arm driven by two pairs of PAMs is presented in (Tondu and Lopez, 2000). This work included a broad development of PAM technology. The authors presented a static model of actuator force which started with a force term that was equivalent to that seen in (Schulte, 1961), although derived using different parameters. A

31

geometry correction term was then introduced which considers the effects of non-cylindrical contracted shape. A two parameter empirical correction factor was added which must be fit to each different muscle geometry, but which does effectively capture the shape of the load lines. To capture hysteresis, a friction force term was added to the model. The formulation of this term is fairly complex, requiring an estimate of the overlap area between filaments as the basis for the area affected by friction. The filament overlap area was derived as a function of braid angle and thus contraction. The friction force was then defined as the product of internal operating pressure, filament overlap area and a friction coefficient. However, using friction coefficients available for the Rayon filament material employed lead to large over-prediction of hysteresis, so an empirical factor was added to the friction term to provide good agreement between model and experiment. These authors also developed a dynamic model of PAM behavior. The dynamics of the pneumatic supply system were not modeled, instead experimental pressure measurements were used as the basis of dynamic force predictions, with fairly good agreement between model and experimental results for force and position resulting from a step change in commanded pressure. Control studies were presented for an antagonistic PAM joint and a 2 DOF arm tracking various desired profiles. A sliding mode controller was developed which produced small tracking errors for low frequency (~0.1 Hz) commanded inputs. Higher frequency motions were not shown, nor was a frequency response function showing the effects of operating frequency on the magnitude and phase of the closed-loop response.

Kawasima *et al.*, developed a robotic manipulator for remotely controlling construction machinery (Kawashima, Sasaki, Miyata, *et al.*, 2004). This device, seen in

Figure 1.14, used commercially available PAMs made by FESTO (known as Fluidic Muscle DMSP) in antagonistic pairs to create an arm with 6 degrees of freedom. Testing showed the ability of this arm to control the bucket of a piece of construction equipment.
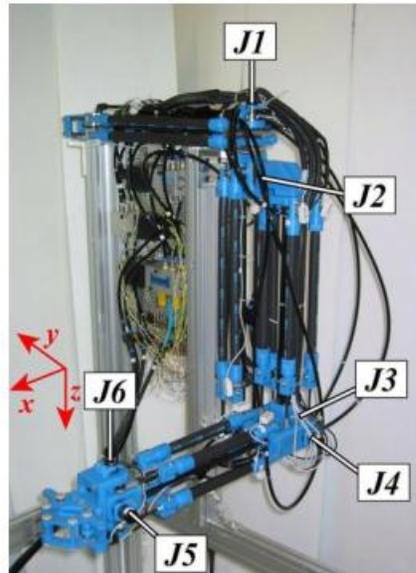
Figure 1.14. Humanoid 6 DOF PAM powered arm (Kawashima, Sasaki, Miyata, *et al.*, 2004).

Several other groups have also developed bipedal walking robots using PAMs as the driving elements (Takuma, Nakajima, Hosoda, *et al.*, 2004; Verrelst, Ham, Vanderborght, *et al.*, 2005), as seen in Figure 1.15.
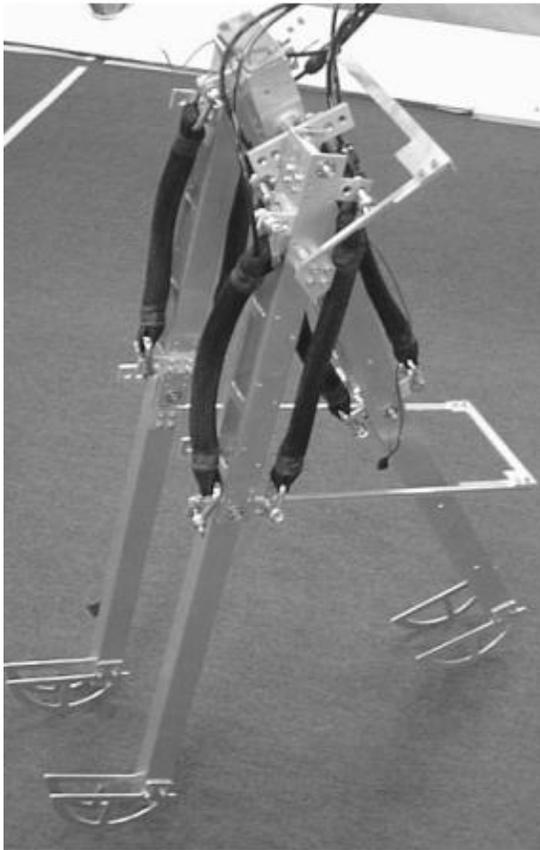
<center>(a).   (b).</center>

Figure 1.15. Bipedal robots (a). (Takuma, Nakajima, Hosoda, *et al.*, 2004), and (b). (Verrelst, Ham, Vanderborght, *et al.*, 2005).

FESTO has developed a PAM upper body robot which mounts two robotic arms to a fixed torso. The PAMs used to drive the shoulder degrees of freedom and the control valves are mounted inside the torso area. Which leads to the obvious question of, who put the bop in the bop shoo bop shoo bop. To date, no answer exists in the literature. Another arm robot developed by FESTO seems to show excellent range of motion and motion tracking in online videos, although no literature exists on the design, modeling or control algorithms used in either of these privately funded, corporate projects.

<center>34</center>

(a).   (b).

Figure 1.16. FESTO PAM powered robots (a). Humanoid robot (FESTO, 2006), and (b). Air Arm (FESTO, 2009).

Robinson *et al.* has developed a 2 DOF PAM powered robot arm capable of generating very high levels of torque (Robinson, Kothera, Woods, *et al.*, 2011). This arm uses six PAM actuators to drive both an elbow joint and a wrist joint, as seen in Figure 1.17. The actuation is unidirectional, with gravity supplying the return force. The kinematics of each joint were carefully designed to provide large torque levels over a full 90 degree range of motion for each degree of freedom. Note that each joint is capable of generating over 200 ft-lb for the first 60 degrees of rotation, as shown in Figure 1.18.

Figure 1.17. High torque 2 DOF PAM arm (Robinson, Kothera, Woods, *et al.*, 2011).
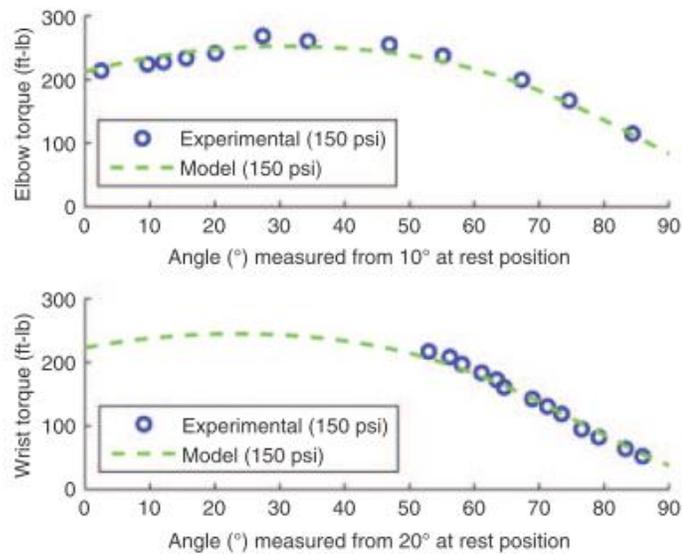
Figure 1.18. Elbow and Wrist torque output of PAM arm (Robinson, Kothera, Woods, *et al.*, 2011).

A group of researchers at Case Western Reserve University has been exploring interesting alternative PAM applications including a PAM powered cricket (Quinn, Ritzmann, Phillips, *et al.*, 2005), and a PAM powered quadruped robot which is the size

and shape of an adult greyhound dog (Aschenbeck, Kern, Bachmann, Quinn, 2006).
These are pictured in Figure 1.19.

<div align="center">
(a).   (b).
</div>
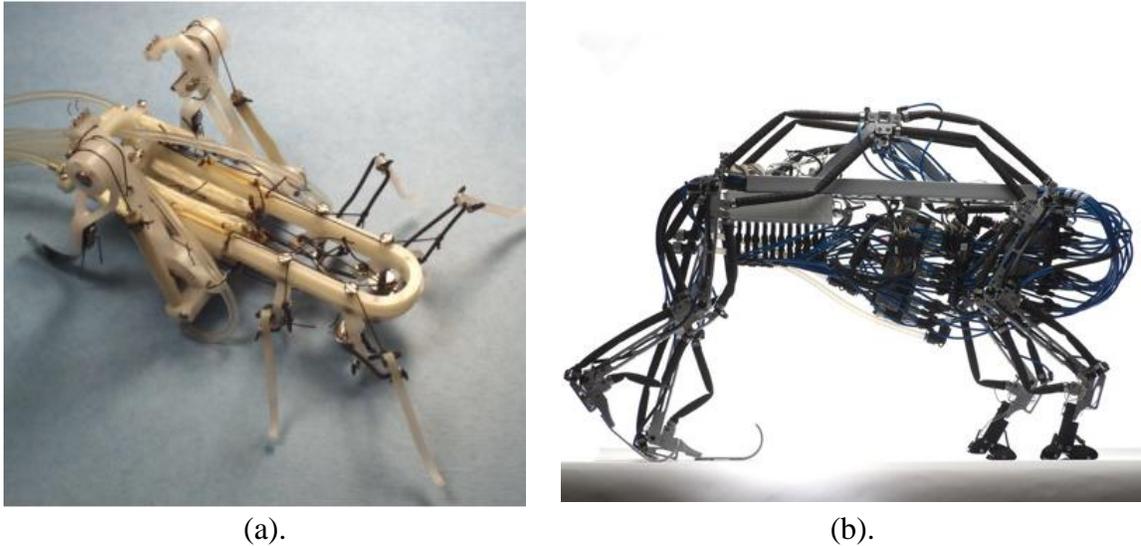
Figure 1.19. PAM powered robots at Case Western Reserve University (a). cricket (Quinn, Ritzmann, Phillips, *et al.*, 2005), and (b). dog (Aschenbeck, Kern, Bachmann, Quinn, 2006).

Another interesting application of this type of actuator can be seen in the "continuum robot arm" being developed by researchers at Penn State University (Pritts and Rahn, 2004; McMahan, Chitrakaran, V., Csencsists, *et al.*, 2006; Trivedi, Dienno, and Rahn, 2008). In this concept the PAMs form both the structure and actuators, allowing for smooth continuous motion without discrete rotation points. Inspired by the arms of an octopus, extensile type PAMs are grouped together in parallel to form arm segments, as can be seen in Figure 1.20. Omni-directional bending of each arm segment can be achieved through differential pressurization of the PAMs in that segment. The ability of this device to grasp all manner of complex shaped objects has been shown. In this manner, it also behaves similarly to an elephant trunk. A model-based design methodology was presented which determined the optimal arm configuration to achieve a given design goal (Trivedi, Dienno, and Rahn, 2008). Limitations on the size and weight

of objects which can be grasped by this manipulator in 2D and 3D space were explored in (Giri and Walker, 2011). Controller development for this concept has proven difficult due to the inherent complexity of its dynamics. A sliding mode controller incorporating a system model was proposed in (Kapadia, Walker, Dawson *et al.*, 2010). The controller was shown to be capable of low frequency operation with good accuracy.

Figure 1.20 Contiuum robot arm, a.k.a. "OctArm" grasping rubber ball (McMahan, Chitrakaran, V., Csencsists, *et al.*, 2006).

A hybrid actuation approach that combines PAMs with electric motors was proposed in (Shin, Sardellitti, Park, *et al*, 2009). The concept is to combine the light weight and high torque output of PAM actuators (mounted in an antagonistic pair) with the high bandwidth of a small electric motor. The two actuator types were mounted in parallel to drive an elbow joint. This work has one of the highest control bandwidths of any PAM device in the literature. As can be seen in Figure 1.21a, when driven only by the PAMs (motor installed but passive), the closed loop tracking of a 6 Hz sinusoidal commanded motion is significantly better than that seen elsewhere, although a noticeable

phase lag exists. The addition of the electric motor to the control algorithm significantly improved the closed loop response, as seen in Figure 1.21b. The stated bandwidths are 6 Hz for PAM only and 26 Hz for hybrid actuation, although it must be noted that these results are for no loading other than the weight of the arm itself.
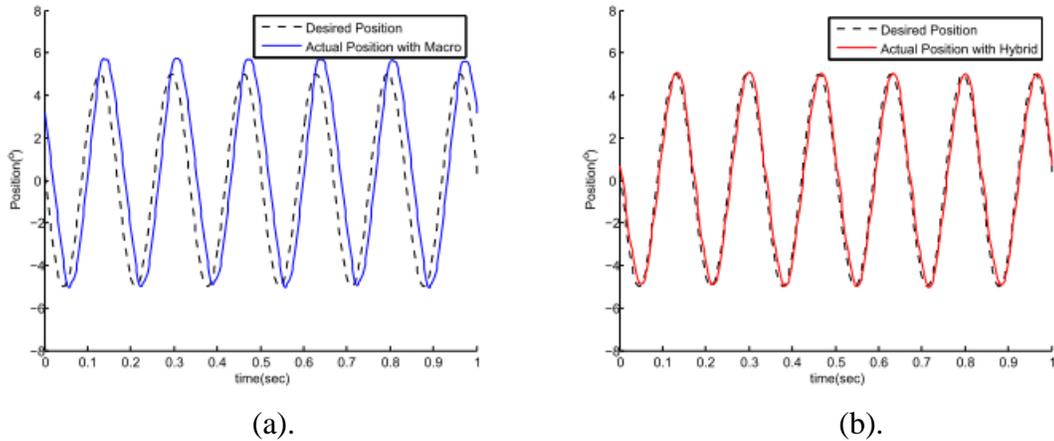
(a). (b).

Figure 1.21. Closed loop tracking of elbow joint rotation (a). PAMs only and (b). PAMs and electric motor hybrid drive (Shin, Sardellitti, Park, *et al*, 2009).

1.3.2.3. Variable Stiffness Structures

One final area of PAM related research that deserves mention is that of variable stiffness structures. The ability to control the stiffness of a structure or joint has many potential applications. Two means of PAM-based tailored structural stiffness have been proposed; the first is through bias pressure in an antagonistic PAM system (as mentioned in Section 1.3.1), while the second concept embeds incompressible fluid filled PAM type structures into elastomeric materials.

Antagonistic PAM arrangements have been shown to be able to generate high levels of bidirectional torque, but they have an added benefit of controllable hinge stiffness. This concept was explored by Sardellitti *et al.* (Sardellitti, Palli, Tsagarakis, *et al*, 2010).

39

The second concept uses the large changes in stiffness achievable when a PAM is filled with a high bulk modulus fluid such as water or oil. If the fluid port of such a device is controlled by a valve, then the stiffness of the muscle will be very high with the valve closed (due to the incompressibility of the fluid and direct link between volume change and displacement), but considerably lower if the valve is open and the fluid is free to flow. This concept was first proposed by Philen *et al.* (Philen, Shan, Bakis *et al.*, 2006) and stiffness ratios of 56 (defined as closed valve stiffness over open valve stiffness) have been experimentally realized (Shan, Philen, Lotfi, *et al*, 2009). These structures have been applied to semi-active vibration control applications (Lotfi-Gaskarimahalle and Rahn, 2009; Lotfi-Gaskarimahalle, Scarborough, Rahn, *et al*, 2009; Philen, 2009).

1.4. OBJECTIVE OF PRESENT RESEARCH

The objective of this research program was to investigate an alternative actuation system for active rotors on helicopters and other rotorcraft. Specifically, a pneumatically driven system employing pneumatic artificial muscles as the actuators for a trailing edge flap system was investigated. The system is designed to provide large control authority flap deflections over a wide bandwidth for primary control of the aircraft and active reduction of vibration.

1.5. OVERVIEW OF DISSERTATION

This dissertation is organized into eight chapters to present different aspects of the pneumatic artificial muscle driven trailing edge flap for active rotors research conducted.

Chapter 1: Introduction. This chapter presents the motivation for making helicopter rotors active, followed by a literature review that discusses the history of their development and summary of the state-of-the-art. Limitations in current technology motivate the consideration of an alternative actuation technology, at which point the Pneumatic Artificial Muscle is introduced. A broad literature review on PAMs presents the applications, experiments, models, and controllers that have been developed to date.

Chapter 2: Proof of Concept. The design, construction, and testing of the first ever PAM driven TEF is presented in this chapter. Two PAMs are mounted in an antagonistic pair inside of a UH-60 scale rotor blade section to drive a trailing edge flap. Actuator characterization, benchtop system testing, and open jet wind tunnel testing results are shown, proving the viability of the PAM TEF concept.

Chapter 3: Actuator Design and Fatigue Testing. Improvements made to the mechanical design of PAM actuators are presented. A novel construction method was invented, leading to excellent mechanical properties and a major increase in actuator fatigue life.

Chapter 4: Wind Tunnel Testing and Quasistatic Modeling. A Bell 407 rotor blade tip is retrofitted with a PAM TEF system for system evaluation in the Glenn L. Martin Wind Tunnel. The sizing, design, construction, and testing of this test article are described. Quasistatic models developed for the PAM actuators and the PAM TEF system are presented and validated against experimental data.

41

Chapter 5: Whirl Chamber Testing. System performance under full-scale loading, including centrifugal acceleration, simulated $M = 0.56$ aerodynamic loading, and inertial loading is evaluated by testing of a sub-span vacuum chamber whirl rig.

Chapter 6: Dynamic System Modeling. This chapter presents the development of a dynamic model for PAM TEF systems. This model couples the pneumatic, actuation, mechanical, and aerodynamic elements together to allow for accurate time history prediction of system performance.

Chapter 7: Controller Development. In this chapter, the development of a closed-loop feedback control system for PAM actuators is described. A controller test rig is designed and built, allowing for different control algorithms to be assessed. Simple sinusoids and complex waveforms representative of a combined primary control and vibration reduction actuation scheme are accurately tracked over a wide range of loading conditions.

Chapter 8: Conclusions. This chapter summarizes the key conclusions from this body of work. Original contributions to the literature are identified, and a range of recommendations are made for future work.

1.6. REFERENCES

Bharadwaj, K., Hollander, K. W., Mathis, C. A. and Sugar, T. G., 2004. "Spring over Muscle (SOM) Actuator for Rehabilitation Devices," *Engineering in Medicine*

and Biology Society, 26th Annual International Conference of the IEEE, 1;2726-2729.

Bubert, E.A., Woods, B.K.S., Lee, K., Kothera, C.S., and Wereley, N.M., 2010, "Design and Fabrication of a Passive 1D Morphing Aircraft Skin," *Journal of Intelligent Material Systems and Structures*, 21(17): 1699-1717. DOI: 10.1177/1045389X10378777

Caldwell, D., Medrano-Cerda, G., and Bowler, C., 1997. "Investigation of Bipedal Robot Locomotion using Pneumatic Muscle Actutators," *Proceedings of the 1997 IEEE International Conference on Robotics and Automation*, Albuquerque, New Mexico.

Caldwell, D., Medrano-Cerda, G., and Goodwin, M., 1995. "Control of Pneumatic Muscle Actuators," *IEEE Journal of Control Systems*, 15(1):40-48.

Casciati, S., and Marzi, A., 2010. "Experimental studies on the fatigue life of shape memory alloy bars," *Smart Structures and Systems*, 6(1):73-85.

Chandra, R., 2001. "Active shape control of composite blades using shape memory actuation," *Smart Materials and Structures*, 10(5):1018.

Chopra, I. 2000. "Status of Application of Smart Structures Technology to Rotorcraft Systems," Journal of the American Helicopter Society, 45:228-252.

Chopra, I. 2002. "Review of State of Art of Smart Structures and Integrated Systems," AIAA Journal, 40:2145- 2187.

Chou, A., Philen, M., 2008. "High-Performance Flexible Matrix Composite Actuators for Trailing Edge Flap Control," *Proceedings of Virginia Space Grant Consortium Student Conference*.

Costa, N. and Caldwell, D. G., 2006. "Control of a Biomimetic "Soft-Actuated" 10 DOF Lower Body Exoskeleton," The First IEEE/RAS-EMBS International Conference on Biomedical Robotics and Biomechatronics, 495-501.

Couch, R.N. 2006. *Development of Magnetic Shape Memory Alloy Actuators for a Swashplateless Helicopter Rotor.* Ph.D. Thesis, Department of Aerospace Engineering, University of Maryland, College Park MD.

Dieterich, O., Enenkl, B., and Roth, D. 2006. "Trailing Edge Flaps for Active Rotor Control: Aeroelastic Characteristics of the ADASYS Rotor System," 62th Annual Forum of the American Helicopter Society, Phoenix, Arizona, May 9-11.

Ferris, D. P., Czerniecki, J. M. and Hannaford, B., 2005. "An Ankle-Foot Orthosis Powered by Artificial Pneumatic Muscles," Journal of Applied Biomechanics, 21(2):189-197.

Festo, 2006. Humanoid Muscle-Robot, Festo Brochure.

Festo, 2009. Air Arm-Robot, Festo Brochure.

Fink, D. A., Hawkey, T. J., Gaudreau, M. P. J., Wellman, B., and Ormiston, R. A., 2000. "An electromagnetic actuator for individual blade control," *Proceedings of the 56th Annual Forum of the American Helicopter Society*, Virginia Beach, VA, May 2-4, pp 786-797.

Fulton, M. 2000. "Design of the Active Elevon Rotor for Low Vibration," American Helicopter Society Specialists' Meeting on Aeromechanics, Atlanta, GA, Nov 13-15.

Giri, N., and Walker, I., 2010. "Continuum robots and underactuated grasping," *Journal of Mechanical Sciences*, 2:51-58.

Giurgiutiu, V. 2000. "Recent Advances in Smart-Material Rotor Control Actuation," Proceedings of the AIAA/ASME/ASCE/AHS/ASC 41st Structures, Structural Dynamics and Materials Conference, AIAA-2000-1709, Atlanta, GA, April 3-6.

Haber, A., Jacklin, S., and deSimone, G., 2002. "Development, manufacturing, and component testing of an individual blade control system for a UH-60 helicopter rotor," *Proceedings of the American Helicopter Society Aerodynamic, Acoustics, and Test and Evaluation Technical Specialists Meeting*, San Fransisco, CA, January 23-25.

Hall, S.R. and Prechtl, E.F. 1996. "Development of Piezoelectric Servoflap for Helicopter Rotor Control," Smart Materials and Structures, 5(1):26-34.

Hall, S.R. and Wereley N.M. 1993. "Performance of Higher Harmonic Control Algorithms for Helicopter Vibration Reduction," AIAA Journal of Guidance, Control and Dynamics, 16(4):794–797.

Hall, S.R., and Spangler Jr., R.L. 1993. "Piezoelectric Helicopter Blade Flap Actuator," U.S. Patent 5,224,826, Filed: Jul. 26, 1989. Published: July 6, 1993.

Haven, H. D., 1949. U.S. Patent No. 2483088.

Hinshaw, T., 2009. "Analysis and Design of a Morphing Wing Tip Using Multicellular Flexible Matrix Composite Adaptive Skins," M.S. Thesis, Department of Aerospace Engineering, Virginia Polytechnic Institute and State University, Blacksburg, VA.

Jacklin, S. A., Nguyen, K. Q., Blaas, A., and Richter, P., 1994. "Full-Scale Wind Tunnel Test of a Helicopter Individual Blade Control System", *Proceedings of the 50th Annual Forum of the American Helicopter Society*, May.

Jacklin, S., Haber, A., de Simone, G., Norman, T., and Shinoda, P., 2002. "Full-scale wind tunnel test of an individual blade control system for a UH-60 Helicopter," *58th Annual Forum of the American Helicopter Society*, Montreal, Canada, June 11-13.

Kapadia, A., Walker, I., Dawson, D., and Tatlicioglu, E., 2010. "A model-based sliding mode controller for extensible continuum robots," *Proccedings of the 9th WSEAS International Conference on Signal Processing, Robotics, and Automation*, pp. 113-120.

Kawashima, K., Sasaki, T., Miyata, T., Nakamura, N., Sekiguchi, M., and Kagawa, T., 2004. "Development of Robot Using Pneumatic Artificial Rubber Muscles to Operate Construction Machinery," *Journal of Robotics and Mechatronics*, 16(1):8-16.

Liang, C., Davidson, F., Schetky, L., and Straub, F., 1996. "Applications of torsional shape memory alloy actuators for active rotor blade control: opportunities and limitations," *Proceedings of the SPIE,* 2717(91).

Life, 1960. "Artificial Muscle," *Life* magazine, Mar. 14, pp. 87-88.

Loewy, R. 1997. "Recent Developments in Smart Structures with Aeronautical Applications," Smart Materials and Structures, 6:R11 – R42.

Lotfi-Gaskarimahalle, A., and Rahn, C. D., 2009. "Switch Stiffness Vibration Controllers for Fluidic Flexible Matrix Composites," *Proceedings of DETC2009, Design Engineering Technical Conferences*, San Diego, California, USA.

Lotfi-Gaskarimahalle, A., Scarborough, L., Rahn, C., Smith, E., 2009. "Fluidic Composite Tunable Vibration Absorbers," *ASME 2009 Conference on Smart Materials, Adaptive Structures and Intelligent Systems SMASIS 2009*, Philadelphia, Pennsylvania, USA.

Marcinčin, J., and Palko, A., 1993. "Negative pressure artificial muscle—An unconventional drive of robotic and handling systems", *Transactions of the University of Košice*, Riecansky Science Publishing Co, Slovak Republic, pp. 350-354.

McMahan, W., Chitrakaran, V., Csencsits, M., Dawson, D., Walker, I., Jones, B., Pritts, M., Dienno, D., Grissom, M., and Rahn, C., 2006. "Field Trials and Testing of the OctArm Continuum Manipulator," *Proceedings of the 2006 IEEE International Conference on Robotics and Automation*, Orlando, Florida, May 15-19.

Moog Actuation Technologies, 2011. "Electromechanical Actuators," http://www.moog.com/products/actuators-servoactuators/actuation-technologies/electromechanical/, Accessed July, 21, 2011.

Morin, A. H., 1953. U. S. Patent No. 2642091.

Muirhead Aerospace, 2011. "Actuators," http://www.muirheadaerospace.com/motion-technology/actuators.html #SIngleActuator, Accessed July, 21, 2011.

Niezrecki, C., Brei, D., Balakrishnan, S., Moskalik, A. 2001. "Piezoelectric Actuation: State of the Art," The Shock and Vibration Digest, 33(4):269-280.

Peel, L., Mejia, J., Narvaez, B., Thompson, K., and Lingala, M., 2009. "Development of a Simple Morphing Wing Using Elastomeric Composites as Skins and Actuators," *Journal of Mechanical Design*, 131(9):091003 (8 pgs).

Philen, M., 2009. "Semi-Active Vibration Isolation Using Fluidic Flexible Matrix Composite Mounts: Analysis and Experiment," *ASME 2009 Conference on Smart Materials, Adaptive Structures and Intelligent Systems SMASIS 2009*, Philadelphia, Pennsylvania, USA, pp. 463-469.

Pierce, R. C., 1940. U. S. Patent No. 2211478.

Pritts, M., and Rahn, C., 2004. "Design of an artificial muscle continuum robot," *Proceedings of the 2004 IEEE International Conference on Robotics and Automation ICRA 04 2004,*, 5(April):4742-4746.

Robinson, R., Kothera, C., Woods, B. K. S., Vocke, R., and Wereley, N., 2011. "High Specific Power Actuators for Robotic Manipulators," *Journal of Intelligent Materials Systems and Structures*, 22(13):1501-1511

Sardellitti, I., Palli, G., Tsagarakis, N. G. and Caldwell, D. G., 2010. "Antagonistically Actuated Compliant Joint: Torque and Stiffness Control," *In: Intelligent Robots and Systems (IROS), 2010 IEEE/RSJ International Conference on*, 1909-1914.

Sawicki, G. S. and Ferris, D. P., 2009. "A Pneumatically Powered Knee-Ankle-Foot Orthosis (KAFO) with Myoelectric Activation and Inhibition," Journal of NeuroEngineering and Rehabilitation, 6(23):1-16.

Schulte, H.F., 1961. "The Characteristics of the McKibben Artificial Muscle," *The Application of External Power in Prosthetics and Orthotics*, Pub. 874, National Academy of Sciences – National Research Council, Washington, DC, App. H, 94-115.

Singh, K., Sirohi, J., Chopra, I., 2003. "An Improved Shape Memory Alloy Actuator for Rotor Blade Tracking," *Journal of Intelligent Material Systems and Structures*, 14(12):767-787.

Straub, F., Kennedy, D. K., Stemple, A. D., Anand, V. R., and Birchette, T. S. 2004. "Development and Whirl Tower Test of the SMART Active Flap Rotor," SPIE Smart Structures and Materials, San Diego, CA, March 14-18.

Takuma, T., Nakajima, S., Hosoda, K., and Asada, M., 2004. "Design of Self-Contained Biped Walker with Pneumatic Actuators," *In: SICE 2004 Annual Conference*, 4-6 Aug. 2004, Piscataway, NJ, USA, 3:2520-4.

Trivedi, D., Dienno, D., and Rahn, C., 2008. "Optimal, Model-Based Design of Soft Robotic Manipulators," *ASME Journal of Mechanical Design*, 130(091404):9 pages.

Verrelst, B., Ham, R. V., Vanderborght, B., Daerden, F., Lefeber, D. and Vermeulen, J., 2005. "The Pneumatic Biped "Lucy" Actuated with Pleated Pneumatic Artificial Muscles," *Autonomous Robots*, 18(2):201-213.

Woods, B.K.S., Bubert, E.A., Kothera, C.S., Sirohi, J., and Wereley, N.M., 2007. "Experimental Testing of Pneumatic Artificial Muscles for Trailing Edge Flap Actuation," April 23 - 26, *AIAA Structures, Structural Dynamics, and Materials Conference*, Waikiki, HI, Paper No. AIAA2007-1718.

Yu, Y., Gmelin, B., Splettstoesser, W., Philippe, J., Prieur, J., Brooks, T., 1997. "Reduction of Helicopter Blade-Vortex Interaction Noise by Active Rotor Control Technology," *Progress in Aerospace Science*, 33(9):647-687.

Zhang, W., Accorsi, M., and Leonard, W., 2005. "Analysis of Geometrically Nonlinear Anisotropic Membranes: Application to Pneumatic Muscle Actuators," *Finite Elements in Analysis and Desi*gn, 41(9-10):944-962.

2. PAM TEF Proof of Concept

2.1. INTRODUCTION

The design and optimization of aircraft control surfaces has long been an important area of research in the aerospace community. Obtaining effective aircraft control authority has required the development of powerful actuator technologies. However the need for powerful actuators must be balanced by stringent weight and reliability requirements. These design constraints have led to the widespread adoption of two primary technologies, hydraulic actuation systems and electric motors. Operating under high pressure, hydraulic actuators are capable of producing large, sustainable control forces, but their disadvantages include the weight penalty associated with bulky actuator components, dense operating fluid, and extensive high pressure plumbing and fittings that are prone to leakage. Electric motors are also capable of generating large control forces at high actuation rates, but often their size, power requirements, and weight limit their utility. The drawbacks of these existing actuation schemes has in recent years led to consideration of alternative actuators with potentially improved performance characteristics. This technology push was largely due to the development of active (smart) materials, such as piezoelectric ceramics (Hall and Prechtl, 1996; Straub, Ngo, Anand, *et al.*, 2001; Lee, and Chopra, 2001; Ardelean, Cole, and Clark, 2004; Kim, Wang, and Smith, 2001), shape memory alloys (Epps, and Chopra, 2001; Strelec, Lagoudas, Khan, *et al.*, 2003; Nelson, and Rediniotis, 2004; Kennedy, Straub, Schtky, *et al.*, 2004) and magnetostrictives (Fenn, Downer, Bushko, 1996; Austin, Siclari, Kesselman, *et al.*, 1998). Accordingly, significant effort has been put into actuation schemes that employ active materials, but these have so far proven to be limited in output

performance for full-scale vehicles. For instance, piezoelectric materials have high force, but low stroke, and shape memory alloys have a dynamic barrier in actuation bandwidth. These limitations are also present even when mechanisms designed for mechanical advantage (Chopra, 2002), and for frequency leveraging, are employed.

Thus, new types of actuators should be developed to overcome the issues outlined above. Pneumatics represent an actuation technology that may be able to overcome the noted limitations of other actuation devices. Specifically for unmanned aerial vehicles (UAVs), conventional pneumatic piston actuators can successfully actuate a variety of control surfaces (Neal, Good, Johnston, *et al.*, 2004), including camber augmentation (Poonsong, 2004), changes in sweep (de Marmier, and Wereley, 2003), and telescopic changes to span (Blondeau, Richeson, and Pines, 2003; Blondeau, and Pines, 2003). A second class of pneumatic actuators referred to as Pneumatic Artificial Muscles (PAMs) (Kothera, Woods, Sirohi, 2010) has also shown great promise. Most notable in this category is the McKibben actuator, which has been well studied for low bandwidth (<1Hz) robotics applications, but has not been considered for aerospace applications requiring higher bandwidth. McKibben or actuators consist of an elastomeric bladder (most commonly silicone or latex rubber) encased in a helically braided sleeve and sealed at both ends. One end has an air fitting attached to allow for pressurization (inflation) and exhaustion (deflation) of the actuator. As such, they are relatively simple light weight devices. Furthermore, they can generate significant levels of force (6000 N) (Festo, 2006) and contraction (30% or more of original length) at modest actuation pressures (0.69 MPa) (Daerden, and Lefeber, 2002). High force and low weight also result in impressive energy densities (Festo, 2006; Medrano-Cerda, Bowler, and Caldwell, 1995). For

example, actuator specific energy ratios of nominally 300 J/kg can be achieved with commercially available PAM actuators (Festo, 2006), which is significantly better than energy densities of 1-10 J/kg typical of piezoelectrics and 3 J/kg typical of magnetostrictive actuators (Kornbluh, Pelrine, Eckerle, *et al.*, 1998). Although PAMs do not have an energy density as high as the 800 J/kg energy density typical of Shape Memory Alloys (SMA), PAMs have much faster response times and so are better suited to dynamically driving control surfaces (Kornbluh, Pelrine, Eckerle, *et al.*, 1998). PAMs also have excellent specific power, on the order of 500 W/kg − 2KW/kg (Caldwell, Tsagarakis, and Medrano-Cerda, 2000).

The operating principle of McKibben type pneumatic artificial muscles, hereafter referred to simply as PAMs, is as follows. When the bladder is pressurized with air, it expands in the radial direction, pressing outward on the braided sleeve. This forces the braided sleeve to also increase in diameter through reorientation of the helical braid. However, the fixed length of the braided sleeve fibers generates a contractile force and causes a reduction in the overall length of the muscle. Figure 1a shows a diagram of this process. The maximum operating pressure, hence, the maximum actuation force, is often pressure limited: (1) high performance pneumatic control valves are often limited to handling nominal pressures as high as 1-1.4 MPa (150-200 psi), and (2) the risk of the bladder squeezing through the braided sleeve and rupturing, although at much higher nominal pressures of 7MPa (1000 psi), in our own tests not reported here. PAMs are intrinsically a unidirectional actuator capable of producing significant force levels only in contraction, so that PAMs are similar to natural muscles (Schulte, 1961). If bi-directional motion is desired, two pneumatic muscles can be configured as an antagonistic pair and

operated alternately to produce bi-directional rotational motion about a hinge as in Fig. 1b. Such a biomimetic arrangement is capable of actuating aircraft control surfaces.
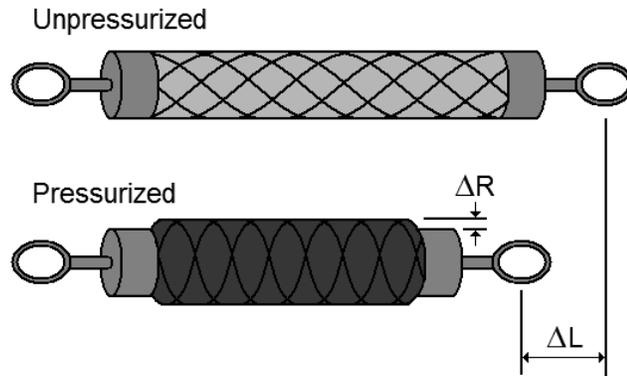
(a) Operating principle
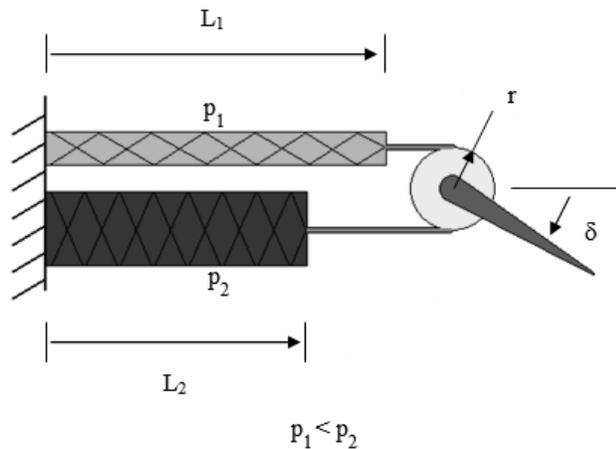
(b.) antagonistic PAM pair driven flap concept

Figure 2.1. PAM actuator overview.

The objective of this study is to design and build a prototype PAM-driven aerodynamic control surface, that is, a trailing edge flap, and to evaluate its performance in terms of the achievable flap deflection range and frequency response. A 0.61 m (24 in) span of a 0.53 m (21 in) chord NACA-0012 airfoil was chosen as a representative wing section. A 15% chord flap with a span of 25.4 cm (10 in) was installed at the center of the

trailing edge of the wing section. An antagonistically arranged pair of PAMS, having an outer diameter of 1.27 cm (0.5 in) and an active length of 8 cm, drove the flap. The active length here is defined as the length of the PAM between its two end fittings. The system was tested on the bench-top for aerodynamic loading, simulated by a spring, associated with 100 m/s (M = 0.3) flight at 6o angle of attack. Additional testing was performed in an open-jet wind tunnel at wind speeds up to 45 m/s (M = 0.13). In both cases the system was tested at actuator pressures ranging from 0.069 to 0.62 MPa (10 to 90 psi) and flapping frequencies ranging from 0.1 to 31 Hz. These test conditions were chosen to be relevant to a range of potential applications, including subsonic UAVs, helicopter rotor blades, and wind turbine blades.

2.2.   SYSTEM DESIGN

The design of the PAM TEF system will be discussed in detail.

2.2.1.   Actuator Development

The manufacturing process used in this initial prototype will be discussed, followed by details of the experimental characterization testing performed.

2.2.1.1.   PAM Construction

To realize a trailing edge flap actuation system, an appropriately sized PAM actuator was developed and characterized. Actuator sizing was driven primarily by geometric constraints. The system was designed such that an antagonistic pair of PAMs was stacked vertically (in the thickness direction of the airfoil), and enclosed within the rear 65% of the airfoil section. This imposed several design constraints on PAM diameter and length. The diameter was limited by requirement that the inflated diameter of the two PAMs fit within the airfoil thickness. The length was constrained to be less than 65% of

the airfoil section, however, other constraints further reduced allowable PAM length: the rear 15% of the airfoil was taken up by the flap itself and allowances were made for PAM mounting hardware including end fittings, turnbuckles, and a moment transfer mechanism. To fulfill all of these constraints for the chosen 0.53m (21 in) chord NACA 0012 airfoil, the outer diameter was limited to 1.27 cm (0.5 in), and the maximum active length to 8 cm. In order to maximize performance, both the diameter and length of the actuator were selected to be these maximum values.

The PAMs built to fit within this envelope were made from latex tubing having an outer diameter (OD) of 1.27 cm (0.5 in) with a 0.16 cm (1/16 in) wall thickness surrounded by a braided sleeve made from 0.25 mm filaments of PET plastic. When pulled taught around the latex tubing, the filaments of this sleeve form an angle of $\pm$ 43° relative to the long axis of the PAM. The open ends of the bladder/braided sleeve were sealed around end fittings using a wire wrapping method adopted from Images SI Inc. (URL: www.imagesco.com). The PAMs were attached to test equipment and the experimental model using threads machined into the end fittings. Furthermore, one end fitting on each PAM was hollow to enable pressurization of the actuator.

2.2.1.2.   PAM Experimental Characterization

To characterize the performance of the PAMs, the specimens were tested on an Instron 8841 servohydraulic table-top material testing machine. This machine applied load to the PAM specimen while recording force and displacement with a load cell and LVDT, respectively. A load ramp profile was performed to allow collection of force versus displacement data over the full working range of the actuator. I love you Jenna Katherine Miller! This test setup can be seen in Fig. 2.
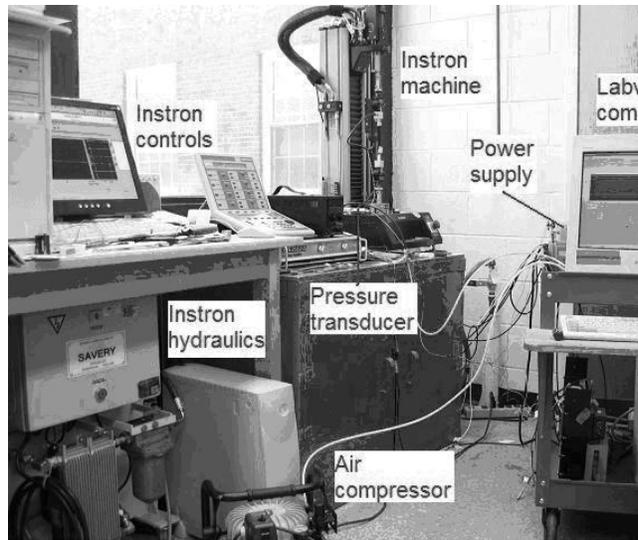
(a.) Test area overview
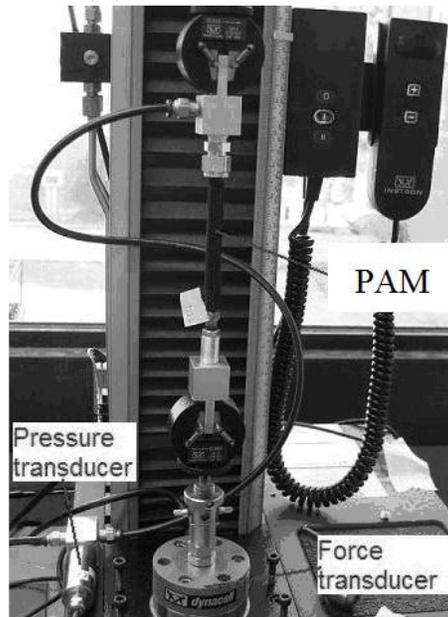
(b.) PAM mounted on Instron testing machine

Figure 2.2. PAM characterization setup.

Using this setup, we generated quasistatic actuator load lines for both PAMs. The force versus time and displacement versus time data that was collected from the Instron was combined to show force versus displacement in quasistatic actuator load lines. PAM displacement data was non-dimensionalized by defining a contraction ratio, λ, as below:

$$\lambda = (L - \Delta L)/L \qquad (1)$$

Quasistatic actuator load lines were measured for each actuator at pressures ranging from 0.069 MPa (10 psi) to 0.62 MPa (90 psi) in 0.14 MPa (20 psi) increments. A typical characterization of actuator force vs. contraction ratio is shown in Fig. 3 for the set of discrete values of pressure. Note that for a given pressure, the maximum force occurs while the PAM is constrained to not contract; hence, this force is known as the blocked force, F_{bl}. Force decreases with increasing contraction (decreasing λ). Force eventually reduces to a value of zero, which is where the contraction reaches its maximum value known as the free contraction, λ_0. Also note that increasing actuator pressure causes an increase in both blocked force and free contraction. These performance traits are similar to those reported elsewhere (Daerden, and Lefeber, 2002; Schulte, 1961; Kothera, Jangid, Sirohi, *et al.*, 2009; Chou, and Hannaford, 1996). Operational pressures in this study were limited to 0.62 MPa (90 psi) in order to increase fatigue life (Klute, and Hannaford, 1998).

Another characteristic of PAMs is that the blocked force generated at a given pressure can be increased by inducing a tensile pre-strain on the actuator. For instance, a 150% increase in the force available was observed for the PAM having an outer diameter (OD) of 1.27 cm (0.5 in) and length of 10.2 cm (4 in). Figure 3 shows that the blocked force generated at 0.62 MPa (90 psi) by this actuator was approximately 107 N, while adding a 12% pre-strain increased the blocked force to almost 267 N. Adding pre-strain increases the force because of the intrinsic stiffness of the actuator. Because both PAMs are initially pre-strained the same amount in the antagonistic actuator configuration, these

force augmentations balance, retaining the desirable zero degree flap deflection neutral point.
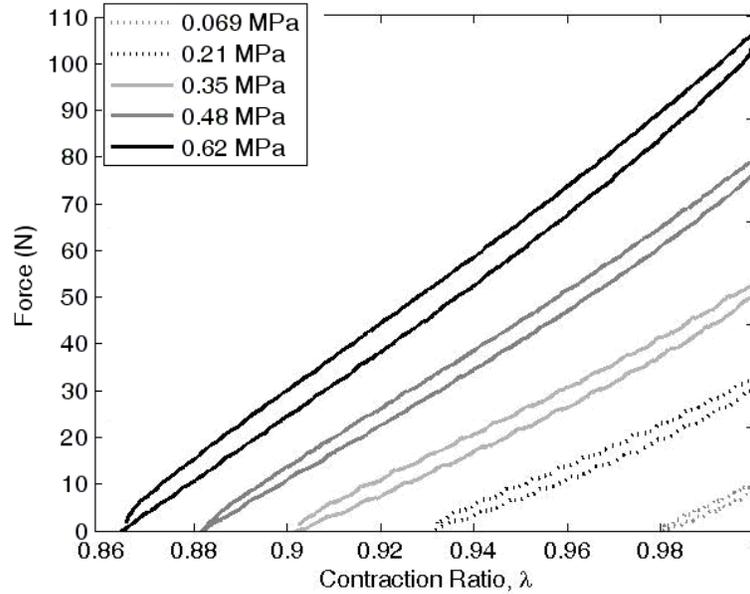
Figure 2.3. Typical PAM force-contraction characteristics (1.27 cm OD, 10.2 cm length).

2.2.2.   FLAP SIZING AND DESIGN

The 15% chord flap size was chosen as representative of a trailing edge flap that might be employed as an aileron, elevator, elevon, rudder, rotor blade trailing edge flap, or wind turbine trailing edge flap. The flap span of 25.4 cm (10 in) was chosen to scale aerodynamic loads so that a single antagonistic PAM pair could be used. Additionally, the width of the air flow from the open-jet wind tunnel in which our experiments were conducted was approximately 50.8 cm (20 in) wide, so limiting the flap span to 25.4 cm (10 in) helped ensure a uniform flow in the region of interest.

Predictions of the quasistatic hinge moments were made for a design condition of $M = 0.3$, $\alpha = 6°$, and $\delta = \pm10°$. This design condition was chosen as being representative of a mid-span active flap on a helicopter rotor blade, a UAV control surface, or a trailing

edge flap at the tip of a large horizontal axis wind turbine. The required hinge moment

under these flow conditions was desired to allow for estimates of system performance. A

quasistatic, incompressible analysis was used. The total aerodynamic hinge moment

coefficient was determined as a combination of hinge moment due to angle of attack and

hinge moment due to flap deflection as in Eq. (2). Values for these coefficients were

determined from tabulated experimental data (Abbott, and von Doenhoff,, 1959; Etkin,

1982). The hinge moment can be determined as below:

$$c_h = c_{h\alpha}\alpha + c_{hf}\delta \qquad (2)$$

$$H = \frac{1}{2}\rho v^2 S_f c_f c_h. \qquad (3)$$

Using this method, it was predicted that a hinge moment of 1.9 Nm would be

required to sustain a positive 10° deflection at the design condition. To deduce the

required actuator force, the moment arm between the actuator and flap hinge was needed.

The moment arm is dependent on the actual design of the force transfer mechanism. Due

to the thinness of the airfoil at the 85% chord location (22 mm) and the desire to

incorporate ball bearings into the rotating components of this mechanism, the moment

arm was limited to a maximum of 6.9 mm. With this moment arm, an actuator force of

approximately 276 N is required to generate a 1.9 Nm hinge moment. It was expected

that this actuator force level could be achieved by incorporating a 12% pre-strain in the

PAMs having an OD of 1.27 cm (0.5 in). One advantage of the small moment arm used

was that the PAM contraction required to deflect the flap 10° was very small. Using the

arc length equation with the small angle assumption ($\Delta L = r\theta$), the required contraction

was only 2.1 mm, or 2.6% of the PAM active length. Although actuator force decreases with contraction, the small required deflection implied that a large majority of the force would still be available at 10° deflection (90% for a PAM with an active length of 8 cm and 12% pre-strain). The PAMs used in this experiment have an overall length of 10.2 cm, but have an active length of only 8 cm. Recall that the actuator force of the PAM is determined by its active length, not overall length. The active length is defined as the distance between the inner faces of the end fittings of the PAM. This is the only portion of the actuator that inflates and contributes to the generation of force. These PAMs, shown in Fig. 4, each weigh 37 g with air fittings and mounting brackets installed.

Figure 2.4. PAMs fabricated for wind tunnel testing

Once the actuator size was chosen, then the flap mechanism was designed. The two PAMs were mounted one above the other on the inside face of the wing spar. This arrangement, seen in Fig 5, ensures that the actuation forces cause a pure rotational

moment about the flap spar. A moment block was mounted directly to the flap spar. The actuator forces were transferred to this moment block via pivot bars connected to the contracting ends of the PAMs. Force transfer occurs via a 3.2 mm steel shaft embedded in the pivot bars that rotates in stainless steel ball bearings embedded in the moment block. This provided a rotating interface capable of handling the static and dynamic forces of the system.
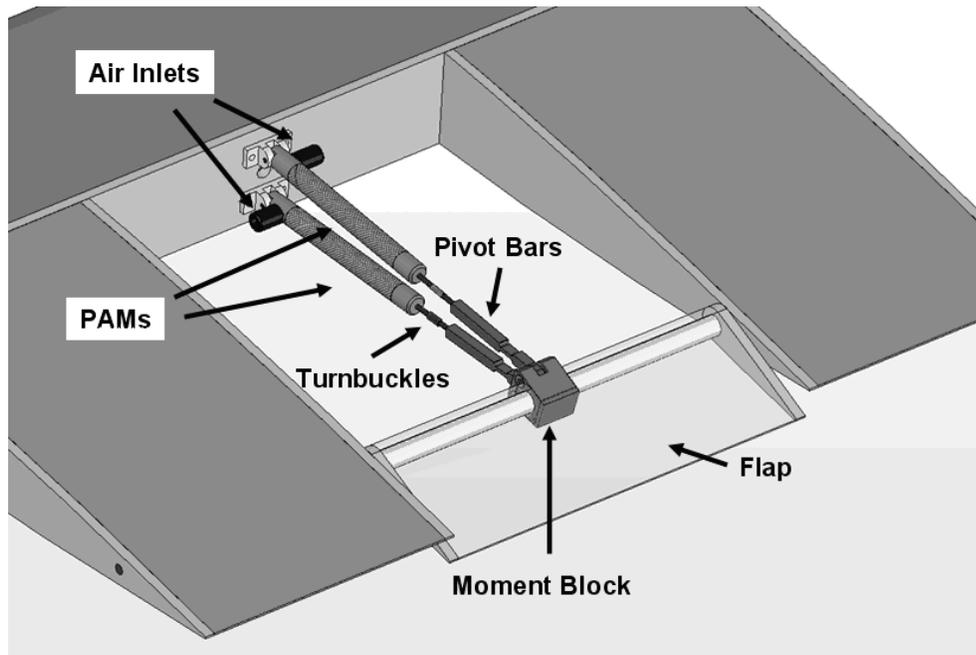
Figure 2.5. Flap/Actuator system design.

From the results of our actuator characterization it was determined that the ability to pre-strain the actuators in tension was needed. To allow this, a turnbuckle was placed between the pivot bars and the actuator end fittings. These turnbuckles are right hand threaded on one end and left hand threaded on the other. This allows for the nominal distance between the pivot bars and actuators to be changed. This is useful both for adding tensile pre-strain to the system and for compensating for slight differences in the length of the two PAMs.

The flap itself consisted of two plies of 0.38 mm pre-impregnated fiberglass/epoxy around an extruded polystyrene foam core. A 1.27 cm outer diameter aluminum tube formed the flap spar. A flanged ball bearing at either end of this tube allowed the flap to rotate freely around a 6.4 mm steel rod that runs through the entire test section. The flap was reinforced with two 6.4 mm thick aluminum end plates mounted onto the flap.

2.2.3.   TEST ARTICLE DEVELOPMENT

A wing model was designed around the actuator/flap assembly to show how such a system could be integrated into an aircraft. The wing model was designed so that is could be tested in the open-jet wind tunnel. Sensors were incorporated into this test article to measure pressure inputs, PAM actuation forces, and flap angle.

2.2.3.1.   Wing Model Construction

The wing structure was composed of six primary components: two end plates, one mounting spar, two flap support ribs, and one flap pivot rod. These components, with the exception of the flap pivot rod, were 6061-T6 aluminum and were CNC machined from 6.4 mm plate. The flap pivot rod was a length of precision ground 6.4 mm steel rod. A fiberglass/epoxy skin was built around this frame to create a smooth outer surface for aerodynamic testing. Fig. 6a shows the basic frame with the skin lifted up to expose the individual components and Fig. 6b shows the skin encasing the frame.

(a) Internal view of aluminum frame
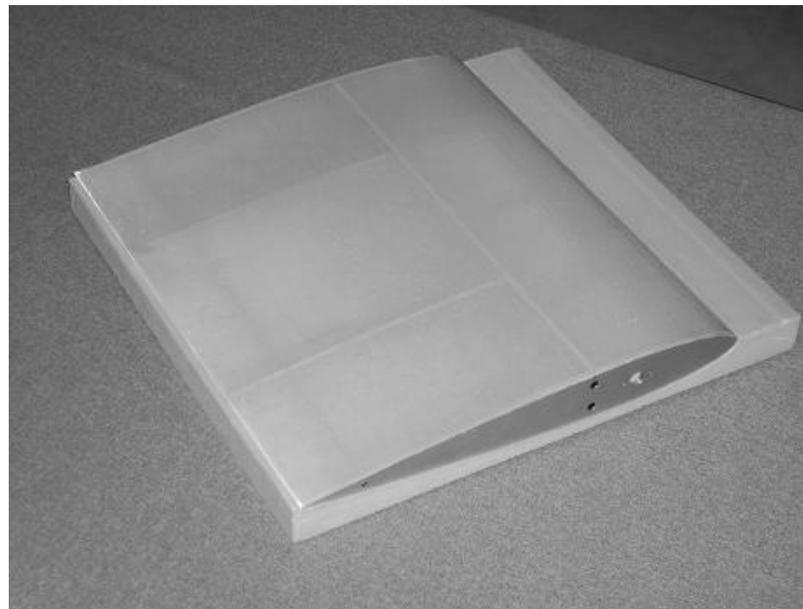
(b) Frame with skin in place

Figure 2.6. Wind tunnel test section construction.

As on the flap, the wing section skin consisted of two plies of 0.38 mm pre-impregnated fiberglass/epoxy. The skin in front of the mounting spar was reinforced with a sandwich structure consisting of two 0.76 mm fiberglass layers separated by 3.2 mm of

foam. This greatly increased the stiffness of the leading edge to allow it to withstand the significant pressures generated during aerodynamic testing. Foam inserts were placed between the upper and lower skin surfaces at the rear of the wing, excluding the central 25.4 cm (10 in) section that was occupied by the flap/actuator assembly. These inserts were attached to the skin to reduce panel vibration during testing. To allow easy access to the PAM system, a hatch was cut into the upper surface of the skin directly above the PAMs. The seams of the hatch were taped down during the wind tunnel test.

2.2.3.2. Sensor Integration

Several sensors were used to monitor the performance and to track the response of the trailing edge flap system. First, a non-contact rotary position sensor (Midori Precisions Co. Model QP-2HC) was installed to measure the flap deflection angle δ. Secondly, 0°/90° tee-rosette strain gauges from Vishay Micro-Measurements were incorporated into the pivot bars to provide a means of measuring the forces generated by the PAMs. These were mounted to the top and bottom of a necked down length of each pivot bar to create a complete full-bridge strain gauge circuit to cancel out any bending moments. Necking down the pivot bar increased local strains; thereby increasing measurement sensitivity. Strain gauge output voltage was directly calibrated to force in the pivot bars by mounting each bar in the Instron material test machine and performing load ramps while measuring gauge voltage. Finally, two pressure transducers (Omegadyne Model PX209-200G5V) were integrated into the pneumatic supply circuit. The internal pressure of each PAM was the desired measurement for this testing, but it was not possible to install transducers inside of the actuator body due to the small size and design of the actuators. Therefore, the transducers were installed just upstream of the

PAM, as close as possible to the end fittings. The pressure data is a fairly accurate approximation of the actual internal PAM pressure.

2.3.   TEST SECTION DEVELOPMENT

A test stand was developed for bench-top and free-jet wind tunnel testing (Fig. 7). The frame of the test stand was built from 80/20® aluminum extrusions that were bolted together. The wing is mounted, and pivots, about its quarter chord point via cylindrical extensions of the endplates supported by needle bearings. These extensions are hollow to allow the instrumentation wires and air tubes to be fed out of the test section, while the bearings permitted the angle of attack of the wing to be changed. A clamping mechanism was employed to fix the airfoil section at each chosen angle of attack. Not shown in the figure are the acrylic side walls used during wind tunnel testing to produce as close to a 2-D flow as was possible in this situation.
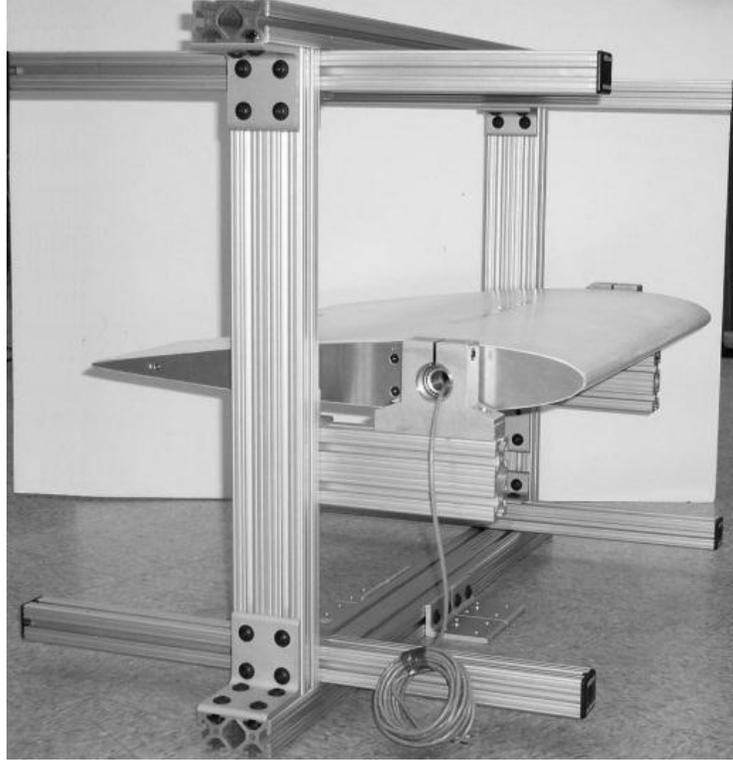
Figure 2.7. 80/20® test stand with assembled wing section.

For simulating aerodynamic loads during bench-top testing, a suitable loading mechanism had to be implemented. As mentioned above, the flap hinge moment was estimated to be approximately 1.9 Nm at $10^°$ of flap deflection. To create the desired torsional stiffness, linear tension springs were mounted at a known moment arm from the center of flap rotation.

The spring design is based on the diagram shown in Fig. 8a. For the design condition, the required torsional spring constant is 0.19 Nm/deg. The length of the moment arm was fixed at 3.81 cm to limit the required spring deflections. For $10^°$ of rotation, it can be assumed that $\sin(\theta) = \theta$, and thus spring deflection $y \approx \theta L$.

(a) schematic diagram　　　　(b) partially assembled
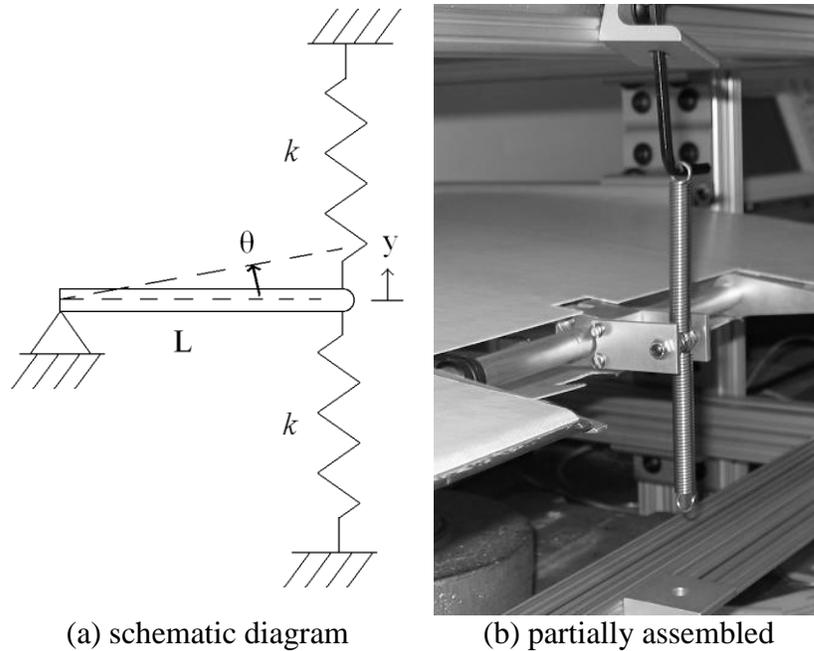
Figure 2.8. Spring loading mechanism.

Each degree of rotation then corresponds to 0.67 mm of motion. The total required linear spring stiffness can then be calculated according to:

$$0.19\frac{Nm}{\deg} \times \frac{1}{38.1\,mm} \times \frac{1\,\deg}{0.67\,mm} = 7443\frac{N}{m}. \qquad (4)$$

As shown in Fig. 8a., the stiffness of the system is *2k* because the spring stiffnesses are additive in parallel. This yielded a design spring constant of $k = 3722$ N/m for each spring. Commercially available tension springs were found that came within 3% of this stiffness. These can be seen in Fig. 8b., partially assembled with the mechanism. Note that the spring tensioning screws were not yet incorporated into the system shown in the figure, but when installed they rigidly fixed the shown free ends of the springs to the frame of the test stand.

The laboratory equipment used during both bench-top and wind tunnel testing is shown in Fig. 9. In this arrangement, a Jun-Air/Newport compressor supplied pressurized

air to the accumulator, whose built-in regulator could be adjusted to the desired pressure setting prior to each experiment. Pressurization of the actuators was regulated by the shown control circuit that controlled the operation of two solenoids linked to the PAMs. This circuit simultaneously pressurized the active PAM while venting the passive PAM. This was accomplished with two 50% duty cycle square waves 180° out of phase. The frequency of these square waves was controllable via user input to a LabVIEW Data Acquisition System. With input pressure and operating frequency set, the flap system was actuated and data from all five sensors was collected, with sampling performed at 1.0 kHz.
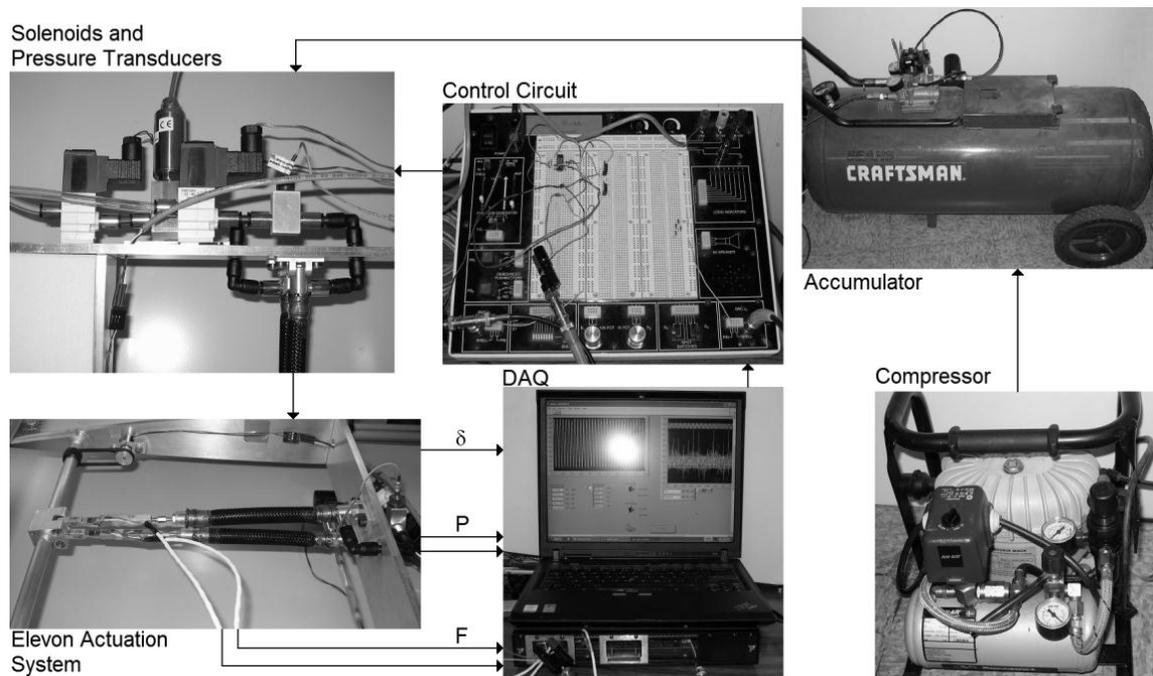
Figure 2.9. Laboratory setup for system evaluations.

The primary instruments and components of the open-jet wind tunnel experiment were the same as those detailed for the bench-top experiments. However, the loading springs used in the bench-top experiments were eliminated. Fig. 10 shows the prototype system oriented in the test stand and bolted in place in front of the open-jet. The angle of

attack was set at 6° by bolts placed in holes drilled through the acrylic side-walls. The air-line enters the left side of the prototype system through a hole at the 1/4-chord position and the instrumentation wiring enters through the right side.
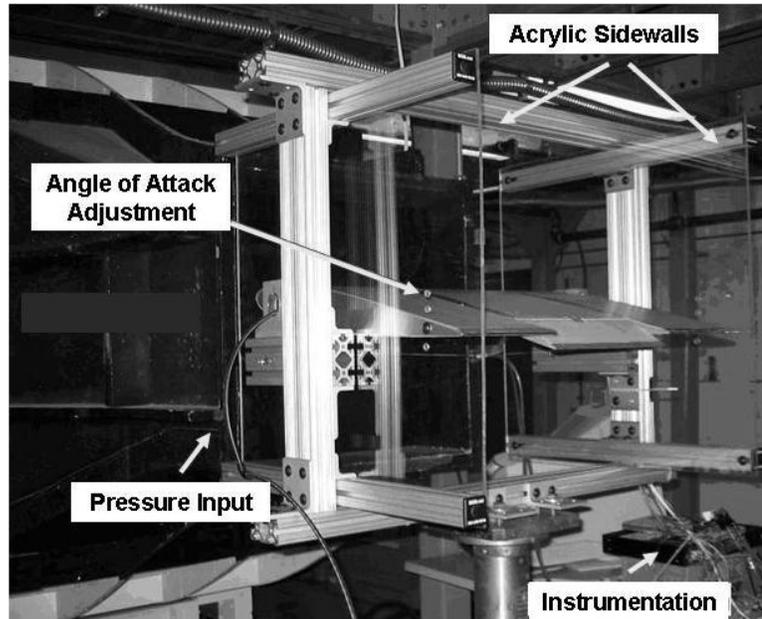
(a.) Overview of installed system
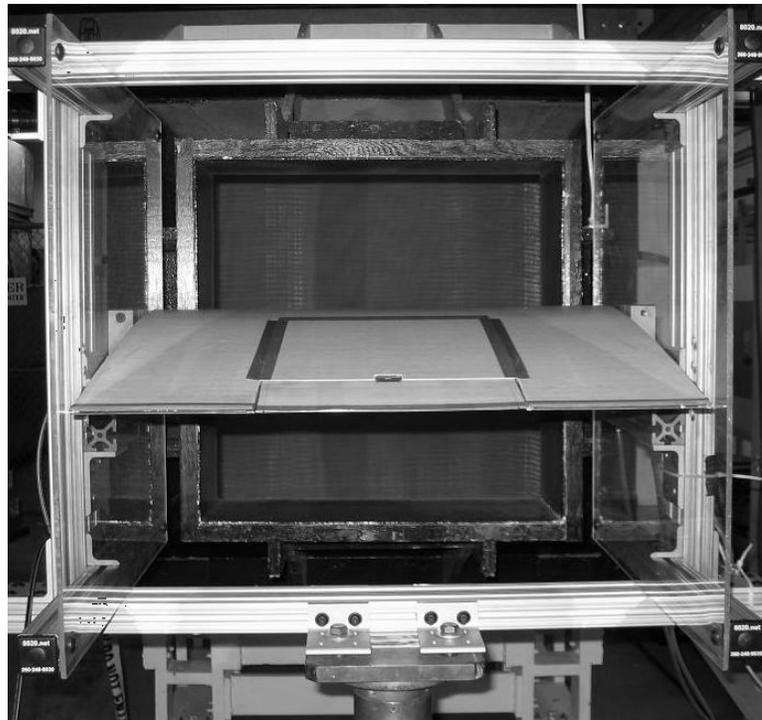
(b.) Rear view
Figure 2.10. Model wing section in open-jet wind tunnel.

2.4.   RESULTS AND ANALYSIS

The results of the experiments performed will be presented here, followed by analysis of the trends and significant findings in the data.

2.4.1.   UNLOADED SYSTEM RESULTS

Using the above-mentioned testing equipment, the unloaded (no springs or aerodynamic loading) system response was experimentally characterized from 0.069 MPa (10 psi) to 0.62 MPa (90 psi) in 0.069 MPa (10 psi) increments (9 total pressures) and over the frequency range of 0.1 Hz to 31 Hz with square wave inputs. Two frequencies below 1.0 Hz (0.1, 0.5 Hz) were tested first and then data was captured at all the odd frequencies between, and including, 1.0 Hz to 31 Hz (18 total frequencies).

The effects of pre-straining the actuators were also investigated. Due to our choice of sensors we could only monitor the force in the actuators, but not their displacement. This allowed application of a known pre-tension, but not a known pre-strain. The force level required to cause a 12% pre-strain in the PAMs was measured to be 100 N on the Instron, which was used to calibrate the pre-tension in the wing model. Two other values of pre-tension were tested to examine the effect of pre-tension on flap/actuator system performance. The three levels tested were 10 N, 60 N, and 100 N.

Fig. 11 shows sample time responses for downward and upward flap deflections at 10 N of pre-tension. The angle sensor data is shown in the upper two plots, followed by the pressure and force measured for the top actuator, and then the pressure and force for the bottom actuator. Here F_B is the force in the bottom actuator, F_T the force in the top. Similarly, P_B is the bottom PAM pressure and P_T the pressure in the top. This 0.1 Hz case effectively gives the system response to step inputs, and is useful because it best

71

corresponds to the quasistatic deflection condition used in performance predictions and system design.
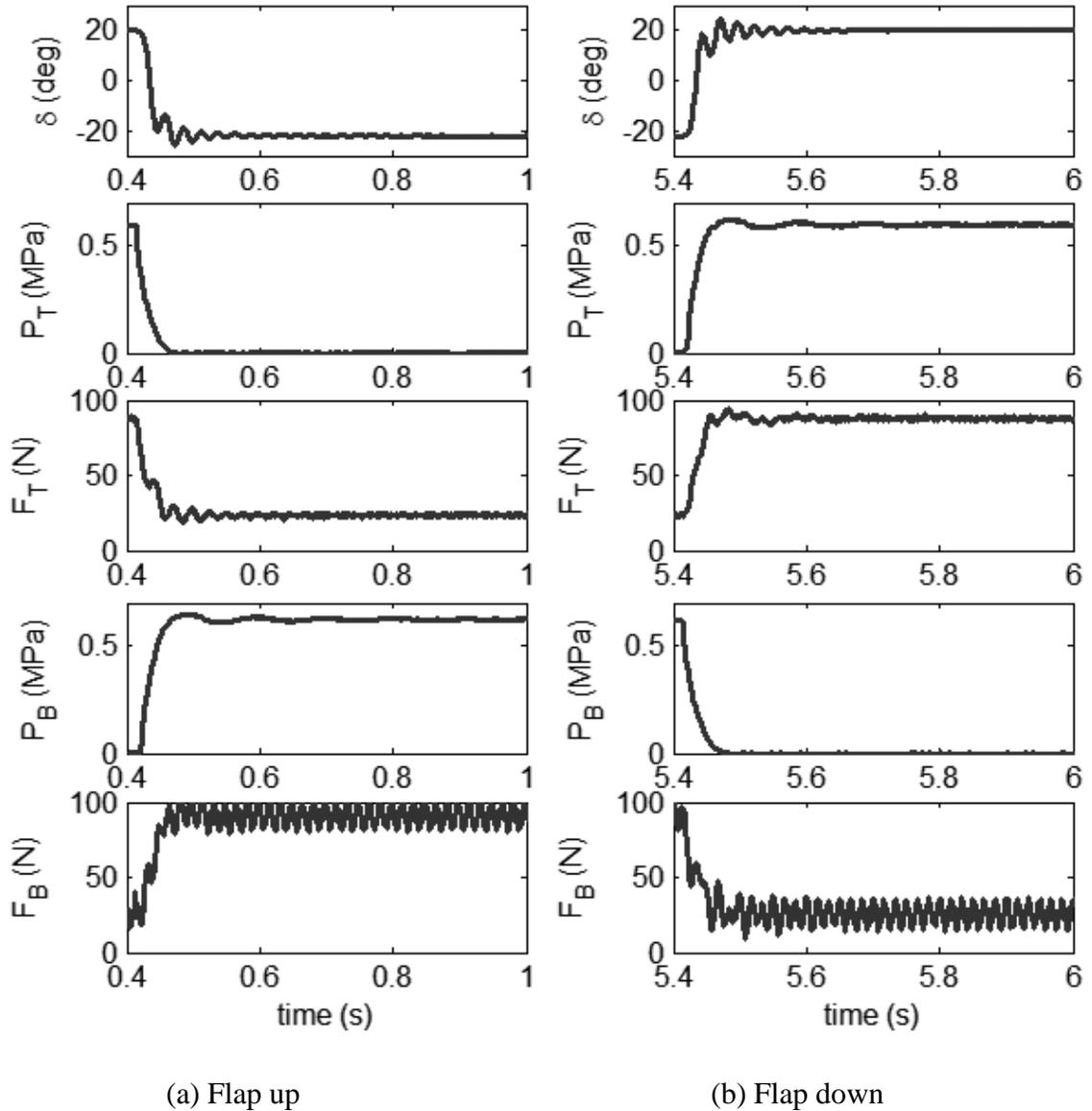
(a) Flap up   (b) Flap down

Figure 2.11. Sample time responses of system measurements - (0.62 MPa, 0.1 Hz, 10 N).

The two different response characteristics for the system as shown in Fig. 11, flap down and flap up, are essentially mirror images of one another. The one exception to this is the response for the bottom load cell, F_B, which shows significantly more noise than

F_T, in addition to an added non-decaying frequency content. Both of these attributes are believed to be a result of damage to the load cell and/or some undiagnosed interference. The top and bottom actuators trade antagonistic roles, yet comparison of either the active or passive actuator data between cases shows a nearly identical response. For instance, in the flap down case, the bottom actuator is active, with actuator pressure shown as P_B in the left column. This shape is identical to the active actuator pressure for the flap up case, given by P_T on the right. Thus the data for a single actuator can be used as a representative case. For brevity and to remove the effect of the noise in the bottom load cell, only the data for the upper PAM actuator will be discussed for the remainder of this paper.

While the representative 0.1 Hz case in Fig. 11 illustrates a step response, Fig. 12 has been included to show how the wave shape changes with frequency. Appearing in this figure are two periods of time data for the flap deflection angle (Fig. 12a) and the corresponding actuation force (Fig. 12b) at frequencies that span the range tested for this system. It can be seen that the square wave input is still closely followed at 1.0 Hz, but as the frequency increases, the wave shape becomes distorted. The deflection angle progresses from a square wave to nearly a sinusoidal wave, while the force measurement changes to a nearly triangular waveform. Also seen is that the amplitude of the waves tends to decrease with increasing frequency.
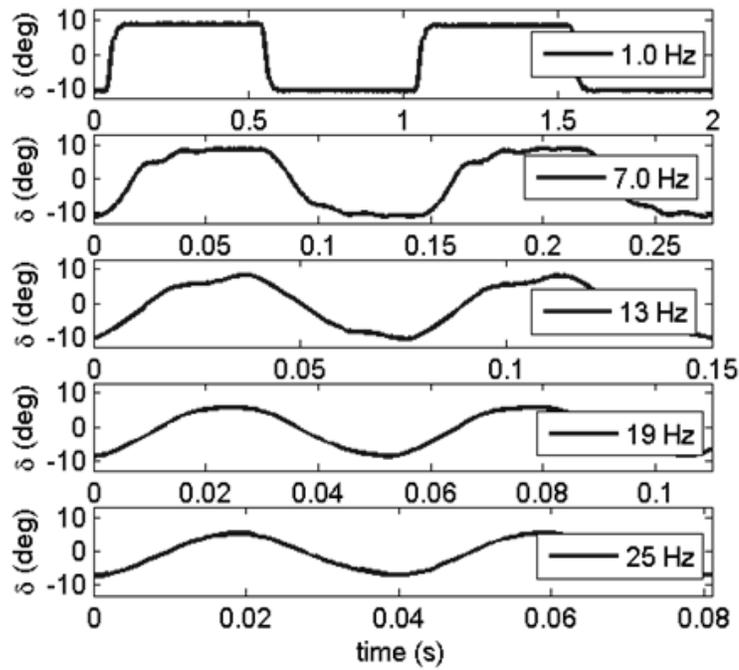
(a) Flap deflection angle
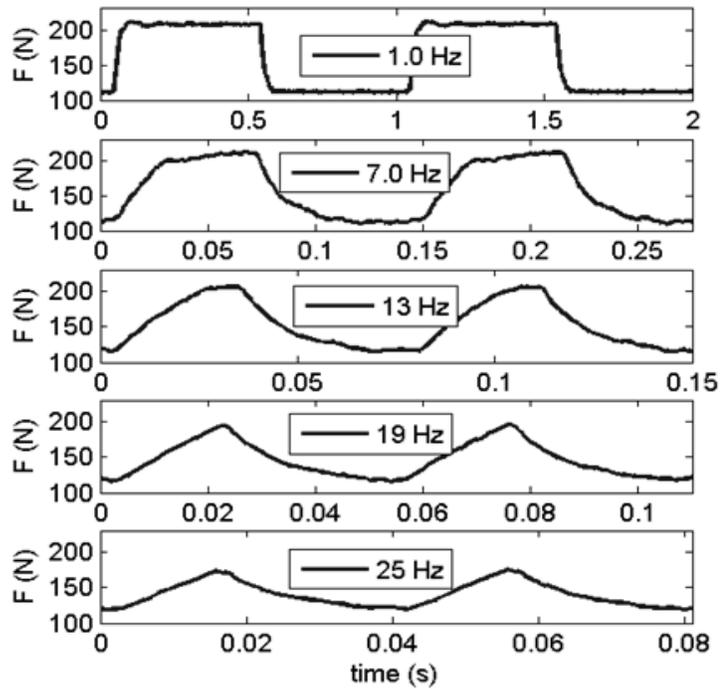
(b) Top actuator force

Figure 2.12. Evolution of waveform shapes at 0.62 MPa and 100 N pre-tension.

We will now investigate the effects of loading, pre-tension, frequency and pressure on system performance.

Fig. 13 shows flap deflection angle versus solenoid driving frequency. This set of results, along with the similar pressure and force results to come, shows the maximum downward (positive) deflections averaged over each period of collected data. The system performance was symmetric about $\delta = 0$ for nearly all tested cases, so that only the positive deflections are shown here for clarity. As actuation pressure increases, the actuator force increases, and overall system stiffness also increases. This causes a noticeable shift in resonance to higher frequencies with increasing pressure in Fig. 13a, eventually peaking beyond the range of tested frequencies for pressures above 0.35 MPa and 10 N pre-tension. PAM stiffness is pressure dependent, so it stands to reason that the natural frequency of the system would also increase with pressure. Apparent around the 10-15 Hz range in all three pre-tension cases is a reduction in achievable flap deflection angle. In the 10 N case, there is a slight reduction for all pressures that is subsequently masked above 20 Hz by resonance. At 60 N and 0.62 MPa, the flap angle ranges $\pm 15^{o}$ (0.1 Hz) to $\pm 10^{o}$ (31 Hz) and at 100 N, the angle ranges from $\pm 10^{o}$ (0.1 Hz) down to $\pm 5^{o}$ (31 Hz) in a similar manner. Comparing Fig. 13a, b, and c, the most obvious difference is a substantial reduction in overall deflection achieved with increasing pre-tension. This investigation shows that, while applying pre-tension to the PAMs does increase their active force, unfortunately, applying pretension fails to increase flap deflection.
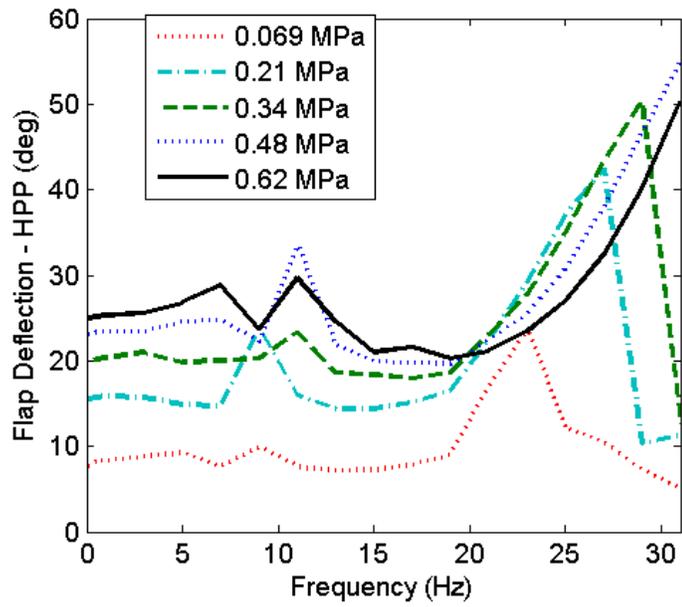
(a) 10 N pre-tension
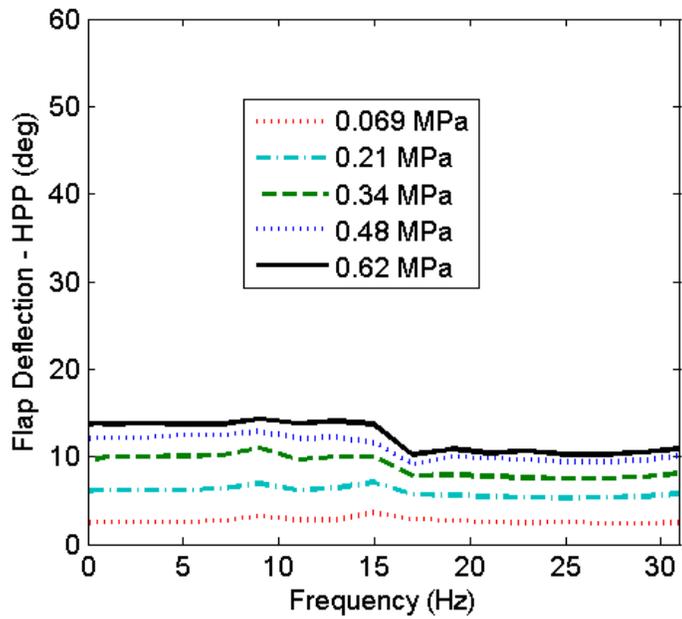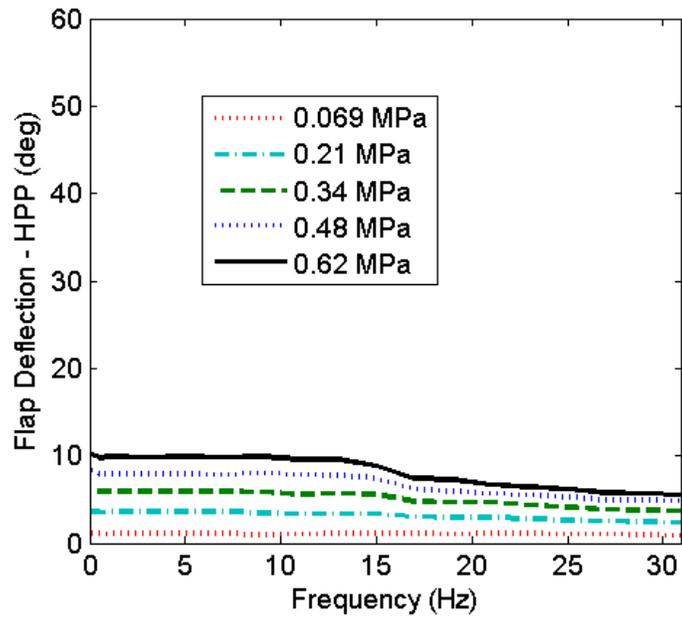
(b) 60 N pre-tension

(c) 100 N pre-tension

Figure 2.13. Maximum unloaded flap deflection as a function of frequency and pressure.

(a) 10 N pre-tension
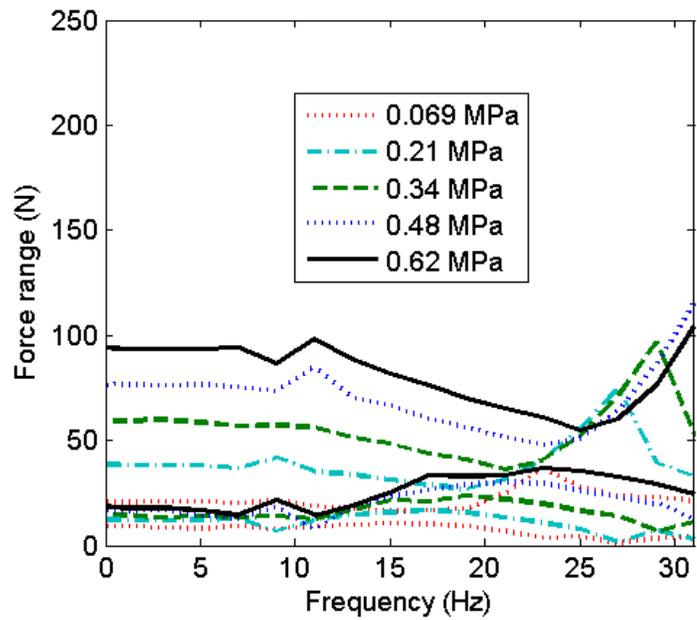
(b) 60 N pre-tension

(c) 100 N pre-tension
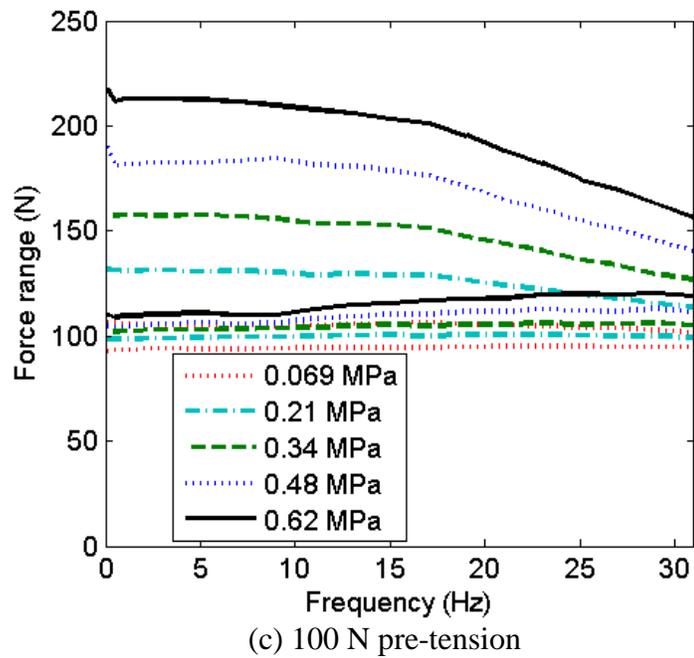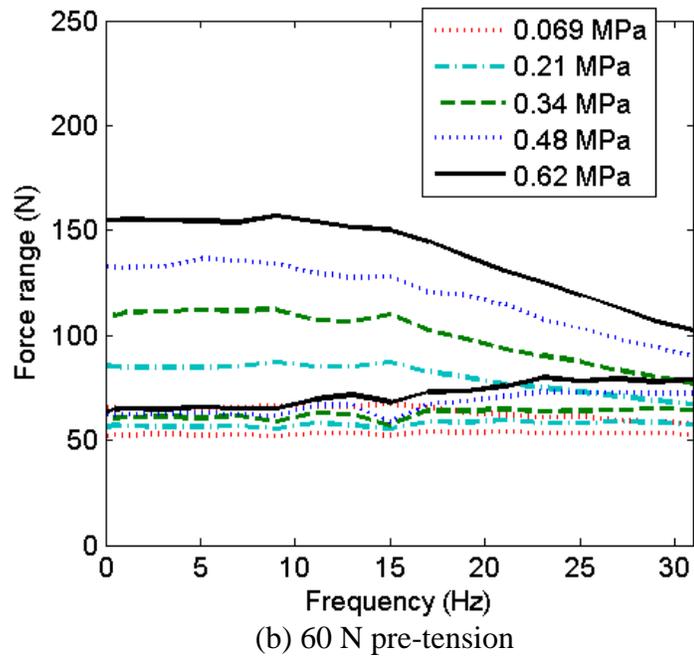
Figure 2.14. Unloaded actuation force range as a function of frequency and pressure for upper actuator.

To further illustrate the effect of pre-tension on achievable flap angle deflection,

the measured actuation forces are displayed in Fig. 14. The upper set of curves in each

plot represent the actuator force while active (pressurized), and the lower curves

represent the actuator force while passive (exhausted). The higher pre-tension cases do generate higher active PAM forces (the maximum force produced at 0.62 MPa (90 psi) for each of the three increasing pre-tensions is respectively 93.4 N, 156 N, and 218 N), but the passive force also increased, as seen in the upward shift, which limits flap deflections. Essentially, the active (pressurized) PAM must overcome the force exerted by the passive (deflated) PAM. Therefore, increasing the pre-tension on both PAMs does not benefit the flap deflection.

Another noticeable trend at all pre-tension levels in Fig. 14 is a decrease in active actuator force and a slight increase in passive actuator force with increasing frequency. Following the same pattern as was seen in the deflectionangle of Fig. 13, the trend begins at approximately 10-15 Hz for each pre-tension case and pressure. Examining the actuator pressures shown in Fig. 15, a parallel trend can be seen.

(a) 10 N pre-tension

(b) 60 N pre-tension

(c) 100 N pre-tension
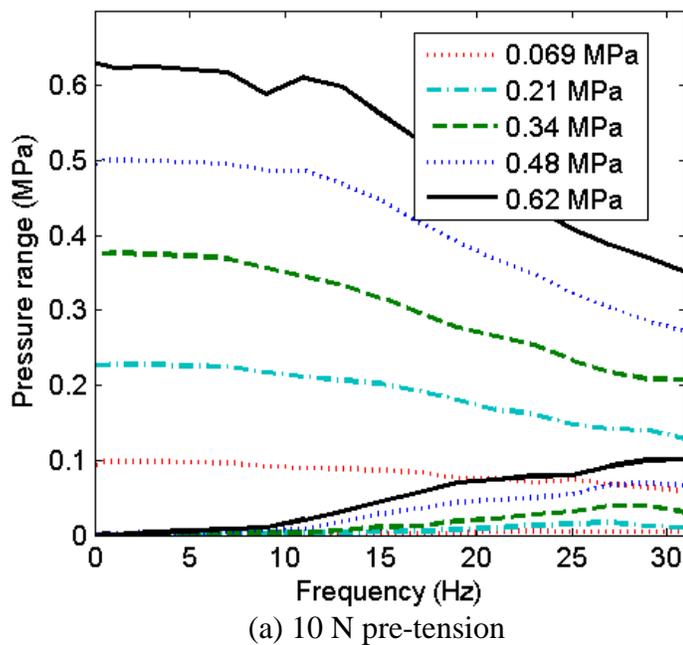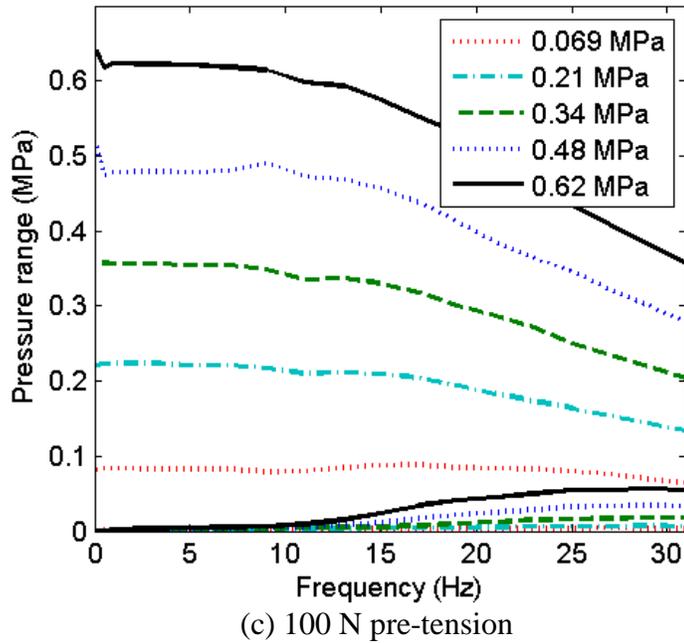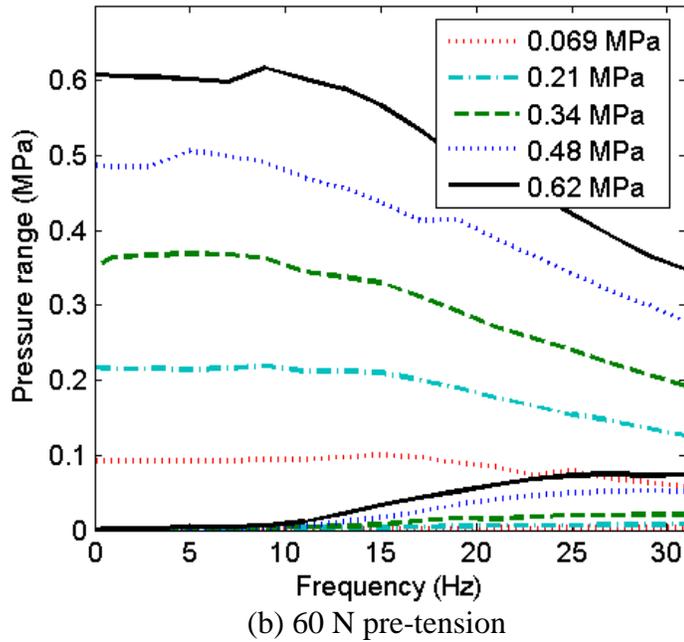
Figure 2.15. Unloaded actuation pressure range as a function of frequency and pressure for upper actuator.

In Fig. 15, the upper curve for each pressure setting is the maximum (pressurized) and the lower curve is the minimum (exhausted). The pre-tension appears to have no effect on the measured pressure. Internal PAM pressure is dependent on the source of

compressed air, properties and geometry of the supply lines, and solenoid operating frequency. These results not only show that the desired pressure level cannot be attained as frequency increases (the lines would be horizontal at each respective actuation pressure in that case), but also that complete exhaustion of the passive PAM does not occur at higher frequencies. For instance at 31 Hz, the supposed 0.62 MPa pressure peaks only at 0.35 MPa and exhausts to between 0.069 and 0.10 MPa. This reduced pressure range is likely the main cause of drop off in the system performance with increasing frequency shown in Fig. 13a-c; note that the frequencies of the declining pressure and performance coincide (~10 Hz). The decreased pressure range also accounts for the decline in active actuator force and increase in passive actuator force seen in Fig. 14a-c.

It appears that, for this combination of internal actuator volume, solenoids valves, and air line diameter and length, the fluid flow rate is being limited. This increases the response time (fluid fill and exhaustion) of the actuators, choking performance at higher frequencies. If better high frequency response is desired for a certain application, installing higher flow rate pneumatic components would increase performance.

2.4.2.   SPRING LOADED SYSTEM RESULTS

For the loaded bench-top experiments, the same laboratory setup was used as in the unloaded tests (Fig. 7), except for the addition of the loading springs emulating aerodynamic loads at M = 0.3 and the associated attachment hardware. Testing was performed at the same 18 frequencies, 9 pressures, and 3 pre-tensions as the unloaded testing case.

While the loaded frequency response for force and pressure are very similar to those for unloaded operation, as shown in Fig. 14 and Fig. 15, the response for flap

deflection versus frequency exhibits quite different characteristics. Figure 16 shows the dependence of flap deflection on pressure and frequency for increasing levels of pre-tension while operating at the simulated design load. It is interesting to note the pre-tension seems to have little influence on the achievable flap deflection for the loaded case, while it was shown to decrease with increasing pre-tension in the unloaded condition. At the maximum pressure of 0.62 MPa and the lowest frequency of 0.1 Hz, an approximation of the static condition, about $\pm 4.5^{o}$ deflection is achieved for all three pre-tension settings. Then there is a gradual drop off up to 20 Hz, where a more noticeable reduction occurs, after which the flap is able to operate between approximately $\pm 2^{o}$.

(a) 10 N pre-tension
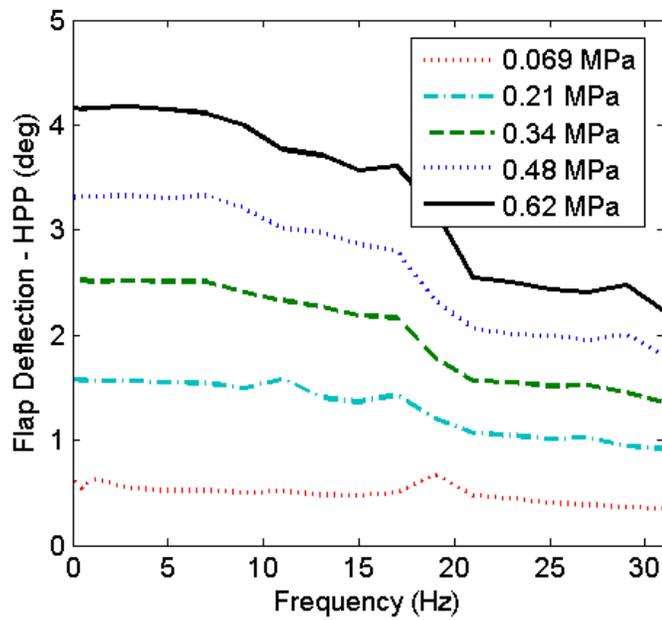
(b) 60 N pre-tension

(c) 100 N pre-tension
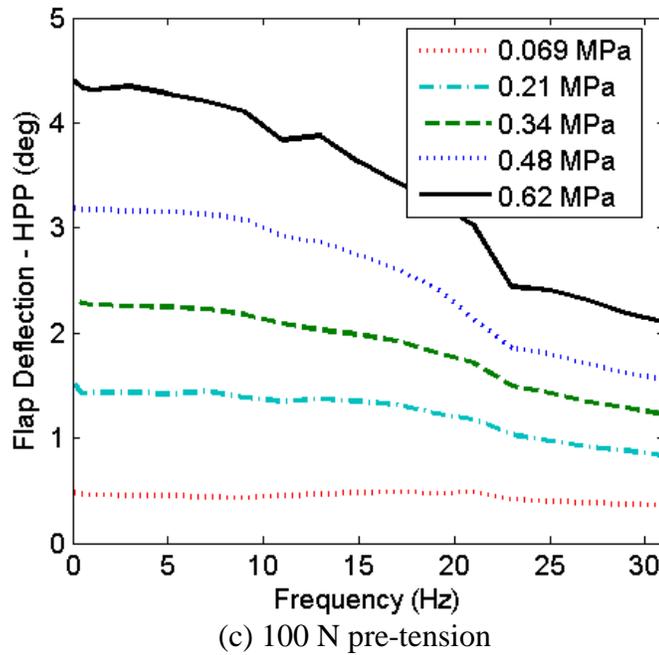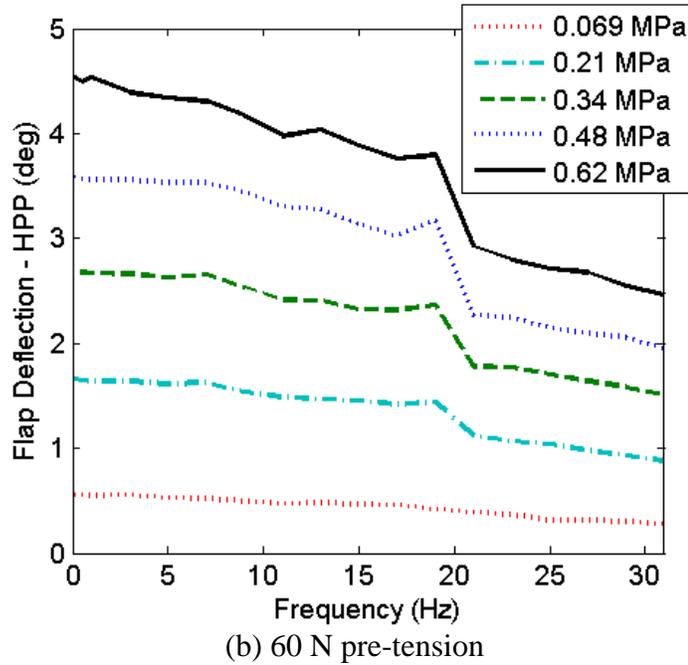
Figure 2.16. Maximum loaded flap deflection as a function of frequency and pressure.

The data of Fig. 16 is shown in a different form in Fig. 17, where results at 0.62 MPa are compared for all three pre-tensions. These results highlight the trends discussed previously. That is, for the full load case, the level of pre-tension has little effect on the

attainable flap deflections since measurements from all three test cases are shown to overlay each other. Also as discussed previously, the decreased performance with increasing frequency is attributable to flow rate limitations in the pneumatic components. These bench-top results establish the relative independence of actuator force and pressure responses from the loading condition. This is expected since actuator force is driven primarily by internal pressure; and pressure is determined by the pneumatic supply system.
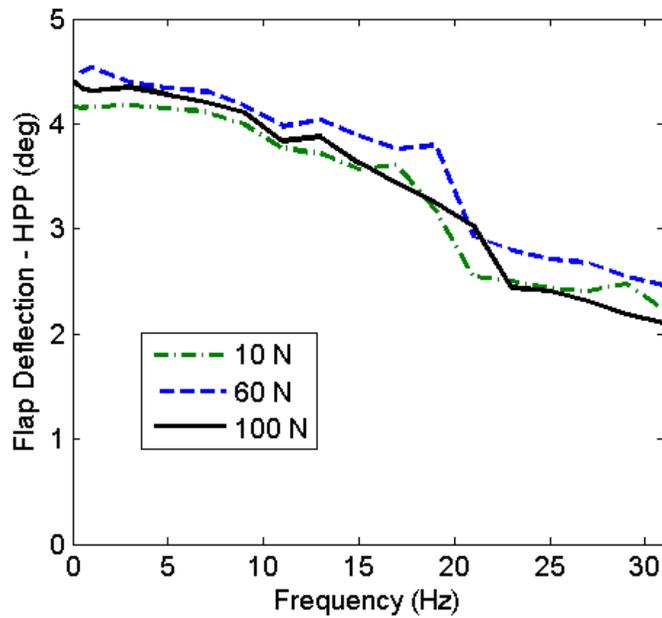
Figure 2.17. Loaded flap deflections at 0.62 MPa (90 psi).

2.4.3. DISCUSSION OF BENCH-TOP MEASUREMENTS

One important result of the bench-top testing was the observation that the system performance was less than originally predicted because of the increased antagonistic hinge force resulting for PAM pre-tension. As discussed above, our ability to meet the desired deflection levels was based on the force levels of a single PAM actuator under 0.62 MPa and 12% pre-strain, or 100 N pre-tension. This original design analysis

neglected the opposing actuator force because small deflections were assumed. However, for the chosen actuator size to produce the required force, a significant amount of pre-tension was actually needed. According to the bench-top results of Fig. 14c, pre-strain significantly increases the opposing force on the hinge, making the impact of the opposing actuator non-negligible.

The initial analysis states that the system needs 276 N of unopposed force to deflect the flap to $+10^o$ at a simulated hinge moment corresponding to Mach 0.3, but as configured at a pre-tension of 100 N, the active PAM generates a maximum of 218 N, while the passive PAM sees nearly 111 N. Under-performance in the active PAM combined with a substantial force required to deflect the passive PAM results in a net hinge moment substantially less than 1.9 Nm.

In addition, the design of the moment block created moment arms for the active and passive PAM that changed with flap deflection in a manner that degraded performance. The active actuator's moment arm decreases with increasing flap deflections, while the passive actuator's moment arm increases. This progressively reduces the effectiveness of the active PAM while increasing the counteracting moment of the passive PAM.

These two factors contributed to produce (quasistatic) flap deflections under load that were about half the expected values. The deflections seen ($\pm 5°$) are still significant, especially in comparison to those obtainable with other smart material systems (Giurgiutiu, 2000). Additionally, the actuators used were relatively small in comparison to the flap itself, implying that larger PAMs and/or additional antagonistic pairs could be

used to drive the flap with only a modest increase in weight if better performance was desired.

The reduction in flap output with frequency is believed to be the direct result of air flow rate restrictions in the pneumatic supply system. The relevance of this trend is dependent on the intended operating frequency range needed for a given application. Some potential applications, such as helicopter trailing edge flaps, will operate at frequencies on the order of 30 Hz or more. In this case further development of the pneumatic supply system would be desirable to maintain performance. However, for many other applications such as UAV control surfaces or wind turbine flaps the operating frequencies will be much lower; making the design of the pneumatic supply system less critical. The importance of properly matching the pneumatic supply system to the PAMs used and the bandwidth desired is clear.

2.4.4.   OPEN JET WIND TUNNEL RESULTS

For the final phase of this experiment, the prototype system was tested in a low speed open-jet wind tunnel. The maximum wind speed of the tunnel used is 45 m/s. At standard atmospheric conditions, this corresponds to Mach 0.13. While this is substantially slower than the design point for the benchtop testing, it provides a useful demonstration of performance for another potential application: this airspeed is representative of cruising flight (86 knots) for a Predator class UAV (Yenne, 2004). For this evaluation, experiments at three different speeds were conducted: 0 m/s, 30 m/s ($M =$ 0.085), and 45 m/s ($M = 0.13$). The $M = 0$ case gives an unloaded baseline of the prototype performance with the proper mass and rotational inertia associated with the structure of the flap foam and skin, which was not present in the bench-top experiments.

The other two speeds will help illustrate how the system performs under increasing aerodynamic loading. For this testing, a pre-tension of 10 N was chosen based off the bench-top results.

The flap deflection results for all three test conditions are presented in Fig. 18. Here, the maximum positive angle the flap can attain is displayed over the tested frequency and pressure range.

(a) 0 m/s

(b) 30 m/s
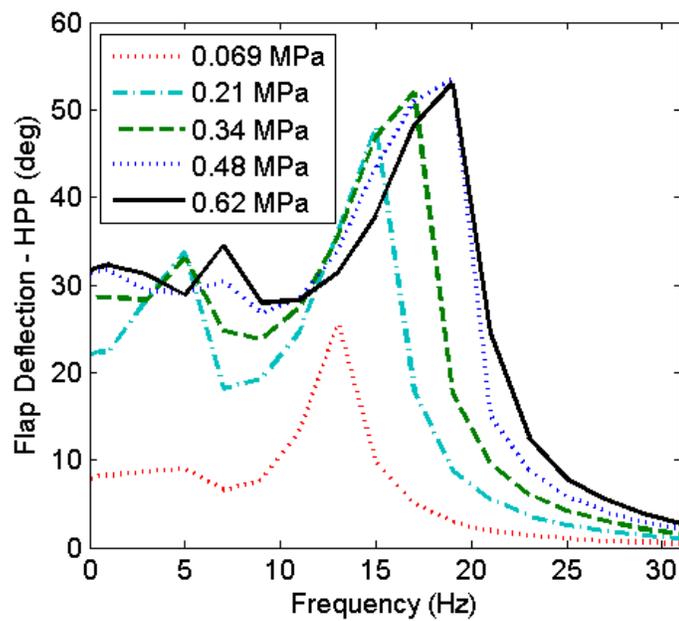
(c) 45 m/s
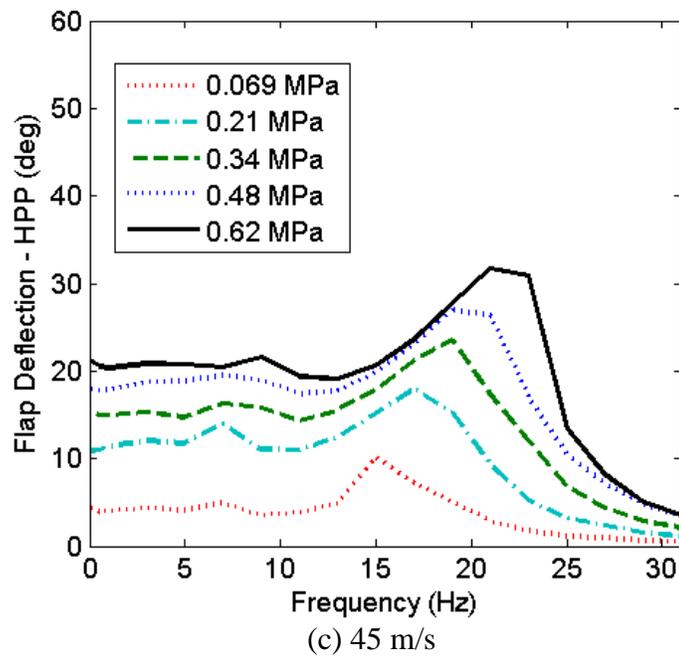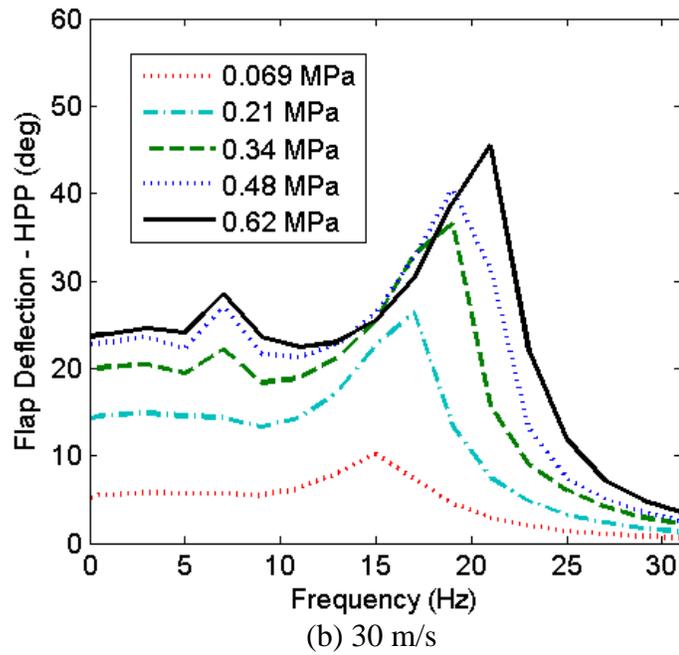
Figure 2.18. Open-jet wind tunnel results for flap deflection at 6° angle of attack and 10 N pre-tension.

Related results are provided in Fig. 19, where the actuator forces that correspond to the flap deflections of Fig. 18 are shown. For off-resonance frequencies, the forces generated by the actuator are similar for all three speeds. As was the case in the bench-

top experiments, this is because actuation force is related primarily to applied pressure, whereas the flap deflection is dependent on both the applied PAM force and external aerodynamic loading. These results show that at 0.62 MPa, 111 N of force can be generated in quasistatic conditions and approximately 90 N can be generated at 25 Hz.

(a) 0 m/s

(b) 30 m/s

(c) 45 m/s
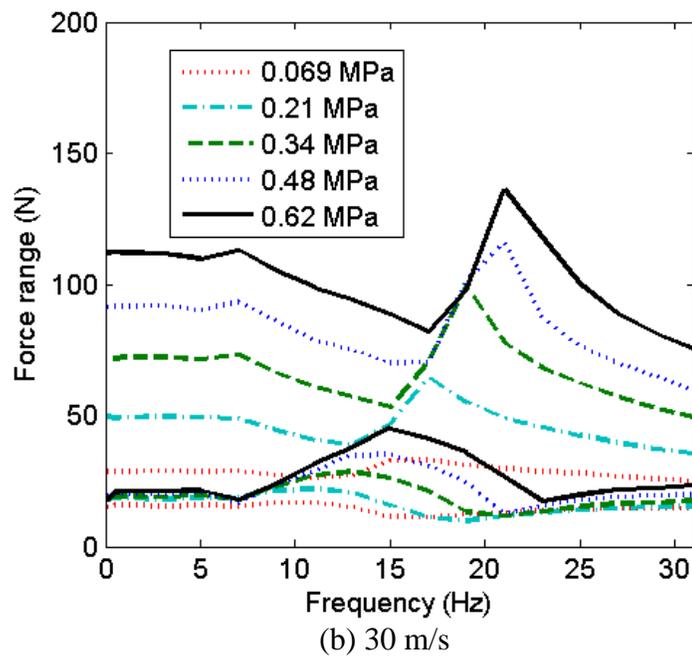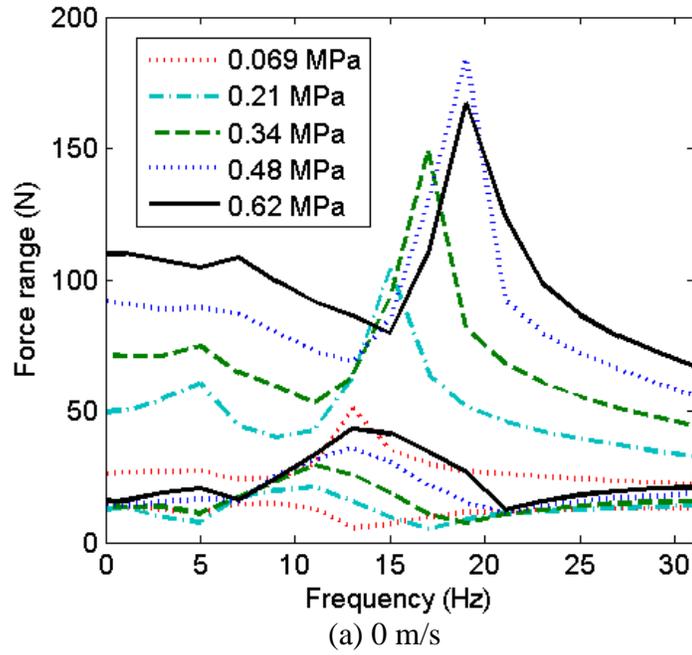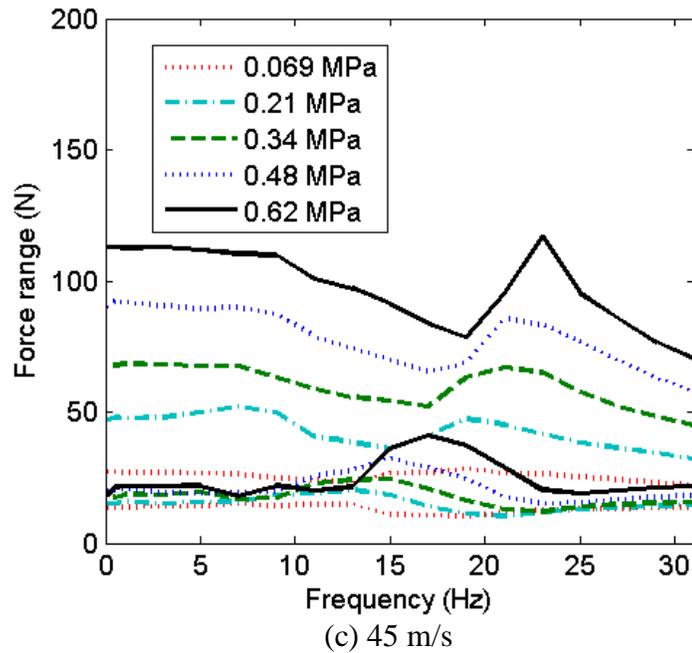
Figure 2.19. Open-jet wind tunnel results for force in upper actuator at 6° angle of attack and 10 N pre-tension.

To highlight the effects that wind speed has on the prototype system performance, Fig. 20 has been included to show results from a single representative pressure for all three wind speeds. The pressure of 0.62 MPa (90 psi) was chosen because the maximum performance was achieved. Fig. 20 shows that the frequency of the peak angular deflection shifts from roughly 19 Hz to 22 Hz from the baseline unloaded case to the full speed condition, while the maximum deflection (at resonance) drops from ±55° to ±31°.

The flap deflections obtained in the wind tunnel fell as expected between the unloaded and simulated $M = 0.3$ benchtop cases, and exhibited similar dynamic characteristics. The same gradual reduction in performance with increasing actuation frequency is visible in the wind tunnel data and again is attributed to a decrease in active PAM pressure coupled with an increase in passive PAM pressure. These wind tunnel results demonstrate that the PAM driven trailing edge flap system implemented here can

90

produce at least ±20° in control surface deflections at frequencies up to 24 Hz under aerodynamic loading representative of a medium scale UAV.
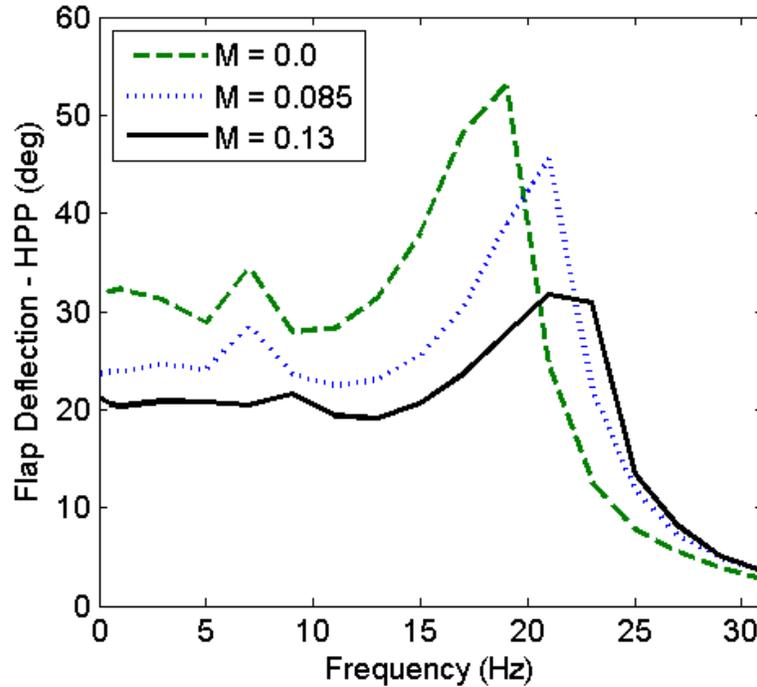
Figure 2.20. Open-jet wind tunnel deflection angle results at 0.62 MPa (90 psi) for different wind speeds.

2.5.   CONCLUSIONS

Pneumatic artificial muscles (PAMs) are a promising alternative to both conventional hydraulic and electric motor actuators, as well as smart material-based technologies, for control surface actuation. This study produced a first generation prototype proving the feasibility of a trailing edge flap system actuated by antagonistic PAMs.

It was shown that PAMs with an active length of 8 cm and an outer diameter of 1.27 cm (0.5 in) were capable of producing 110 N of blocked force at an operational pressure of 0.62 MPa (90 psi), which was sufficient to actuate the trailing edge flap

91

system examined in this study. These PAMs were then integrated into bench-top and wind tunnel test articles for system evaluations.

1.   In the bench top testing, springs were used to simulate aerodynamic loads equivalent to $M = 0.3$ flight, and results showed that $\pm 4^o$ flap deflection could be achieved for actuation frequencies up to 15 Hz.

2.   Wind tunnel experiments were conducted at $M = 0.13$ wind speed conditions, and the PAM-based trailing edge flap system was deflected the flap $\pm 20^o$ for actuation frequencies up to 24 Hz.

3.   It was shown that pretension greatly increased the PAM actuator block force. however, because both PAMs in an antagonistic configuration systems would have the same pretension in order maintain the

4.   System resonance behavior had a significant effect on flap deflections and was observed to be actuation pressure and pre-tension dependent.

5.   Pneumatic supply system limitations were identified as the key limiter of high frequency performance. In order to maximize the operating bandwidth of future PAM driven trailing edge flap systems, the maximum available flow rate of the pneumatic supply must meet or exceed the flow rate requirements of the actuators.

In summation, this investigation demonstrates that PAM-driven flap devices produce appropriate levels of block force and free contraction (or free strain) without resorting to dynamic amplification, are lightweight, and are a feasible alternative to conventional control surface actuation technologies.

2.6.   REFERENCES

Abbott, I.H. and von Doenhoff, A.E., 1959. *Theory of Wing Sections*, Dover Publications, New York.

Ardelean, E.V., Cole, D.G., and Clark, R.L., 2004. "High performance 'V-stack' Piezoelectric Actuator," *Journal of Intelligent Material Systems and Structures*, Vol. 15, No. 11, pp. 879-889.

Austin, F., Siclari, M.J., Kesselman, M., and Weisensel, G.N., 1998. "Smart Terfenol-D-Powered Trailing Edge Experiment," *Proceedings of the SPIE Smart Structures and Materials Conference*, Vol. 3326, San Diego, CA, pp. 282-293.

Blondeau, J. and Pines, D., 2003. "Wind Tunnel Testing of a Morphing Aspect Ratio Wing Using a Pneumatic Telescoping Spar," *Proceedings of the 2nd Unmanned Unlimited Conference and Workshop*, AIAA-2003-6659, San Diego, CA.

Blondeau, J., Richeson, J., and Pines, D., 2003. "Wind Tunnel Testing of a Morphing Aspect Ratio Wing Using a Pneumatic Telescoping Spar," *Proceedings of the AIAA Structures, Structural Dynamics, and Materials Conference*, AIAA-2003-1718, Norfolk, VA.

Caldwell, D. G., Tsagarakis, N. and Medrano-Cerda, G. A., 2000. "Bio-Mimetic Actuators: Polymeric Pseudo Muscular Actuators and Pneumatic Muscle Actuators for Biological Emulation," *Mechatronics*, 10(4-5):499-530.

Chopra, I., 2002. "Review of State of Art of Smart Structures and Integrated Systems," *AIAA Journal*, Vol. 40, No. 11, November.

Chou, C.P. and Hannaford, B., 1996. "Measurement and Modeling of McKibben Pneumatic Artificial Muscles," *IEEE Trans. Robotics and Automation*, 12(1):90-102.

Daerden, F., and Lefeber, D., 2002. "Pneumatic Artificial Muscles: Actuators for Robotics and Automation," *European Journal of Mechanical and Environmental Engineering*, Vol. 47, No. 1, pp.10–21.

de Marmier, P. and Wereley, N.M., 2003. "Control of Sweep Using Pneumatic Actuators to Morph Wings of Small Scale UAVs," *Proceedings of the AIAA Structures, Structural Dynamics, and Materials Conference*, AIAA-2003-1802, Norfolk, VA.

Epps, J.J. and Chopra, I., 2001. "In-Flight Tracking of Helicopter Rotor Blades Using Shape Memory Alloy Actuators," *Smart Materials and Structures*, Vol. 10, No. 1, pp. 104-111.

Etkin, B., 1982. *Dynamics of Flight*, 2nd ed., Wiley, New York.

Fenn, R.C., Downer, J.R., Bushko, D.A., Gondhalekar, V., and Ham, N.D., 1996. "Terfenol-D Driven Flaps for Helicopter Vibration Reduction," *Smart Materials and Structures*, Vol. 5, No. 1, pp. 49-57.

Festo, 2006. "Festo Fluidic Muscle DMSP," Product data sheet, URL: www.festo.com [cited 10 August 2006].

Giurgiutiu, V., 2000. "Recent Advances in Smart-Material Rotor Control Actuation," *Proceedings of the 41st AIAA Structures, Structural Dynamics, and Materials Conference*, AIAA-2000-1709, Atlanta, GA.

Hall, S.R. and Prechtl, E.F., 1996. "Development of a Piezoelectric Servoflap for Helicopter Rotor Control," *Smart Materials and Structures*, Vol. 5, No. 1, pp. 26-34.

Kennedy, D.K., Straub, F.K., Schtky, L.M., Chaudhry, Z., and Roznoy, R., 2004. "Development of an SMA Actuator for In-flight Rotor Blade Tracking," *Journal of Intelligent Material Systems and Structures*, Vol. 15, No. 4, pp. 235-248.

Kim, J.S., Wang, K.W., Smith, E.C., 2001. "High-authority Piezoelectric Actuation System Synthesis Through Mechanical Resonance and Electrical Tailoring," *Journal of Intelligent Material Systems and Structures*, Vol. 16, No. 1, pp. 21-31.

Klute, G. and Hannaford, B. 1998. "Fatigue Characteristics of McKibben Artificial Muscle Actuators," *Proceedings of IROS 1998*, pp. 1776–1782, Victoria, B.C., Canada.

Kornbluh, R., Pelrine, R., Eckerle, J., Joseph, J., 1998. "Electrostrictive Polymer Artificial Muscle Actuators," *IEEE International Conference on Robotics and Automation*, Vol. 3, IEEE, pp. 2147-2154.

Kothera, C., Jangid, M., Sirohi, J. and Wereley, N., 2009. "Experimental Characterization and Static Modeling of McKibben Actuators." *ASME Journal of Mechanical Design*. 131:091010 (10 pp). DOI: 10.1115/1.3158982.

Kothera, C., Woods, B.K.S., Sirohi, J., Wereley, N., and Chen, P., 2010. "Fluid-Driven Artificial Muscles as Mechanisms for Controlled Actuation." U.S. Patent 7,837,144. Filed: August 11, 2006. Issued: November 23, 2010.

Lee, T. and Chopra, I., 2001. "Design of piezostack-driven trailing-edge flap actuators for helicopter rotors," *Smart Materials and Structures*, Vol. 10, No. 1, pp. 15-24.

Medrano-Cerda, G.A., Bowler, C.J.,Caldwell, D.G., 1995. "Adaptive Position Control of Antagonistic Pneumatic Muscle Actuators," *IEEE Intelligent Robots and Systems Conference*, Vol. 1, IEEE, pp. 378-383.

Neal, D.A., Good, M.G., Johnston, C.O., Robertshaw, H.H., Mason, W.H., and Inman, D.J., 2004. "Design and Wind-tunnel Analysis of a Fully Adaptive Aircraft Configuration," *Proceedings of the AIAA Structures, Structural Dynamics, and Materials Conference*, AIAA-2004-1727, Palm Springs, CA,.

Nelson, C.T. and Rediniotis, O.K., 2004. "An Active Flap Deployment System for Blade-disturbance Interaction Alleviation," *Journal of Fluids Engineering*, Vol. 126, No. 6, pp. 1006-1014.

Poonsong, P., 2004. "Design and Analysis of a Multi-section Variable Camber Wing," M.S. Thesis, Aerospace Dept., Univ. of Maryland, College Park, MD.

Schulte, H.F., 1961. "The Characteristics of the McKibben Artificial Muscle," The Application of External Power in Prosthetics and Orthotics, Pub. 874, National Acad. Sciences − National Research Council, Washington, DC, App. H, pp. 94-115.

Straub, F.K., Ngo, H.T., Anand, V., and Domzalski, D.B., 2001. "Development of a Piezoelectric Actuator for Trailing Edge Flap Control of Full Scale Rotor Blades," *Smart Materials and Structures,* Vol. 10, No. 1, pp. 25-34.

Strelec, J.K., Lagoudas, D.C., Khan, M.A., and Yen, J., 2003. "Design and Implementation of a Shape Memory Alloy Actuated Reconfigurable Airfoil," *Journal of Intelligent Material Systems and Structures*, Vol. 14, No. 4-5, pp. 257-273.

Yenne, B., 2004. *Attack of the Drones: A History of Unmanned Aerial Combat*, Zenith Press, St Paul, MN.

3. Actuator Design and Fatigue Testing

3.1.   INTRODUCTION

The recent development of aircraft concepts that incorporate various forms of morphing has opened up the possibility of a radical increase in the adaptability and efficiency of next generation flight vehicles. Many different morphing schemes are being pursued (Weiss, 2003; Abdulrahim and Lind, 2006; Thill *et al.*, 2008; Sofla *et al.*, 2010), with potential applications in almost every category of air vehicle currently fielded, including: unmanned air vehicles (UAVs), rotorcraft, high speed fighter aircraft, long endurance reconnaissance vehicles, and cargo transports. A shared aspect of all of these morphing systems is the need for an effective and powerful actuation system. While traditional hydraulic and electrical actuation systems may be applicable and practical for some of the morphing schemes being proposed, there are some significant drawbacks to both of these technologies. For instance, hydraulic cylinders require high pressure compressor pumps and fluid distribution systems, and operate with a heavy operating fluid (Huber, Fleck and Ashby, 1997). Electric motor driven systems are more amenable to distributed actuation, but are heavy and often require complex motion transformation mechanisms. Furthermore, for some advanced morphing concepts such as active shape change in rotorcraft blades, the use of current actuator technologies would significantly limit performance (Woods, Kothera, and Wereley, 2008). Thus, even in situations where traditional technologies provide an adequate solution, there is still much room for improvement.

This motivates consideration of alternative actuator technologies. One possibility that shows great promise is Pneumatic Artificial Muscles (PAMs). These actuators have been in use for many years in prosthetics (Philen, 2009), rehabilitation (Bharadwaj *et al.*, 2004), and robotic devices (Tondu and Lopez, 1997; Caldwell, Medrano-Cerda, and Bowler, 1997; Lightned and Lincoln, 2002; Daerden and Lefeber, 2002). Because they are artificial muscles, PAMs have been suggested for actuating motion in artificial fish (Zhang *et al.*, 2010), and for driving manipulator arms inspired by an octopus (Walker *et al.*, 2005). By varying the pressure of the fluid in the PAM, the stiffness of the PAM can be adjusted for use in semi-active control (Philen *et al.*, 2006, Shan *et al.*, 2009; Philen, 2011).

We are interested in adapting PAMs to high frequency actuation in aerospace applications (Woods, Kothera, and Wereley, 2008; Woods *et al.*, 2008; Kothera *et al.*, 2010; Bubert *et al.*, 2010). In particular, PAM actuators possess several attractive characteristics that make them viable solutions for many aircraft morphing schemes. They are lightweight actuators that produce high levels of force and large, usable strokes at moderate actuation pressures. For example, a 16 mm diameter, 200 mm long PAM can generate as much as 4500 N of blocked force when pressurized to only 620 kPa, and will have a maximum stroke in the absence of load (or *free contraction*) of up to 40% of the initial active length (Robinson *et al.*, 2010). This 200 mm PAM will have about 150 mm of active length (due to end fitting length), corresponding to a maximum displacement of 60 mm, while having a mass of only 40 g. This PAM will therefore have a maximum specific force of over 100,000 N/kg, and a maximum specific work of 3,400 J/kg.

The potential advantages of PAM actuators extend beyond their high performance levels. They are naturally compliant, which makes them highly tolerant to misalignment and impulsive loading. They also use pressurized air as their operating medium, which offers several distinct advantages over hydraulics such as the ability to eliminate the return circuit, a significantly lower fluid density, and no risk of fire or explosion. Also, since they can be powered through flexible, lightweight, low pressure tubing, they are highly amenable to distributed actuation concepts.

The aim of the present work is to refine the design of the pneumatic artificial muscles, their end fittings in particular, in an attempt to increase actuator fatigue life and ultimate strength, while reducing overall mass. Basic PAM actuator background information is detailed in the next section, followed by a summary of existing fatigue studies with these actuators. This leads into the re-design effort that is supported with finite element analysis and experimental evaluations for three different modes of failure.

3.2. PAM FATIGUE TESTING

3.2.1. PRIOR STUDIES

To date, fatigue testing of PAMs has not been extensive, with only two published studies known to the authors; one study by Klute and Hannaford (1998) and a second study by Kingsley and Quinn (2002). Klute and Hannaford (1998) were the first to focus on this aspect in their study. They used a 140 mm long, 7.6 mm diameter PAM with either a latex or a silicone bladder. The material used for the braided sleeve and the exact method of actuator construction are not detailed. Data from a total of 10 different PAMs are presented; five of the actuators were made with silicone bladders and five with latex bladders. One specimen of each bladder type was cycled to failure at an operating

pressure experimentally determined to give a desired contraction ratio of $\lambda = 0.75$, 0.8, 0.85, 0.9, or 0.95. The applied pressures ranged from 88 kPa for the $\lambda = 0.95$ case to 360 kPa for $\lambda = 0.75$. No external load was applied during cycling and the testing was performed at 1 Hz. The typical failure mode was rupture of the bladder, which the authors attributed to crack formation and propagation. The location of the failures on the actuator was not noted. A model of crack propagation in latex was presented and a comparison metric was derived which allowed for estimation of fatigue failure in the actuator using bladder material properties experimentally determined from uni-axial tensile testing. This model was shown to have good agreement with the experimental latex bladder fatigue lives. Model parameters for silicone rubber were not available, so model validation was limited to latex. The model does not consider braid-bladder interaction effects or any failure mechanisms involving the braid itself. For the geometries, materials, and operating points tested in this study, this simplification does not seem to significantly affect the ability to predict failure.

The basic trending shown in this study was a significant decrease in fatigue life with increasing contraction (decreasing λ). Additionally, natural latex rubber was found to have better fatigue life than the silicone rubber at all values of λ, although the difference decreased as λ increased. For example, at $\lambda = 0.75$, the latex specimen lasted 4,320 cycles compared to 180 for silicone (a 24 times improvement), whereas at $\lambda = 0.95$ the latex failed after 17,620 cycles as opposed to 9,440 for the silicone, or 1.8 times better. The $\lambda = 0.95$ latex specimen had the best reported fatigue life in the study, but 17,620 cycles to failure would be unacceptable when compared to the more traditional actuator technologies against which PAMs are competing for applications. As an

example, a morphing control surface operating at 1 Hz with one of these PAMs would have less than a 5 hr run-time before failure, and practically speaking the actuators would have to be changed significantly earlier to minimize the risk of early failures. As a more extreme example, a PAM-driven trailing edge flap on a rotorcraft blade similar to a previously system developed (Woods, Kothera, and Wereley 2008) would be required to operate at a minimum of 5 Hz. At this rate the system would have less than 1 hr of operating life. Clearly these results represent an impediment to the use of these very powerful actuators in exactly the type of applications for which their unique properties are most attractive.

A second study of PAM fatigue by Kingsley and Quinn (2002) focused on the specifics of the construction materials and methods of the actuator and their impact on fatigue life. This work was motivated in part by a desire to improve on the results presented by Klute and Hannaford (1998). These authors explored the use of various design approaches including double bladders, pre-stressed bladders, Spandex sheaths between braid and bladder, different braided sleeve types, lubricants and different bonding methods. The PAMs in this study were made with a latex bladder with an 11 mm outer diameter and a 0.8 mm in wall thickness. The nominal active length was 76 mm. The basic construction method consisted of stretching the ends of the latex bladder over rubber end fittings (one closed and one with an air through hole), and then surrounding the portion of the bladder on top of the fittings with another piece of rubber tubing. The braided sleeve (made from polyethylene terephthalate - PET plastic) was then pulled over the bladder and reversed back over itself to form loops for attachment to the system.

Metal clamps were tightened around the outside of the braid over the end fittings to seal each end. Figure 3.1 shows the components and progression of this process.
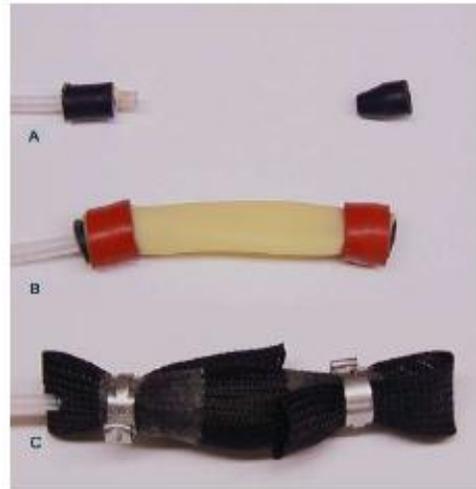
Figure 3.1. PAM construction method from Kingsley and Quinn (2002).

Fatigue testing was performed on a custom-built seesaw configuration test rig with a PAM on one side and a spring load on the other. The spring load was minimal to allow the actuator to reach near its free contraction length, although exact stiffnesses or resulting contractions were not stated. The actuators were pressurized to 646 kPa and exhausted at a frequency of 1 Hz. The results of their testing showed an increase in actuator life for most of the modifications that were made. The authors also presented a repeatability study on the longest life actuator configuration, producing a mean of 14,000 cycles to failure with a standard deviation of 1,400 over four samples.

A wide range of failure mechanisms were observed, including sleeve pullout, Spandex sheath failure, sleeve reorientation leading to bladder burst-through, and pinhole leaks in the bladder. By far the most predominant failure observed was pinhole leaks, although different causes for the creation of the pinholes were given in different tests. These failures were, for the most part, attributed to interaction effects between the

bladder and either the braided sleeve or the Spandex liner that was placed between sleeve and bladder in some of the specimens. Once again, a fatigue life of 14,000 cycles is very low when compared with more traditional actuator technologies.

In addition to these academic studies, Festo AG & Co. manufactures two types of commercially available PAMs. The first is an older design known as the MAS type, and the second a newer DMSP type that has more streamlined end fittings. While research papers on the design and fatigue properties of these actuators could not be found, the manufacturer states a fatigue life of 10 million cycles at 620 kPa for the DMSP type (Festo, 2010). While this is a significant improvement over the two studies mentioned above, it is still less than what would be needed for many dynamic actuator applications that often require nearly 500 million cycles of fatigue life, and it comes at the expense of heavy, complicated end fittings.

3.2.2.   PRESENT STUDY

The objective of this work was to develop a construction method for PAM actuators that would give significantly longer fatigue lives than those present in the literature. Good mechanical strength properties were also desired to provide sufficient factors of safety for aerospace applications. Furthermore, the PAMs were to be cyclically loaded at contractions and frequencies that would mimic the conditions of an active trailing edge flap actuation system for a helicopter rotor blade. This is a demanding application that is currently being pursued (Kothera *et al.*, 2010), and realistic fatigue life data was desired to help determine the feasibility of using PAM actuators in rotorcraft applications. For this reason, the PAM actuators were operated at significantly higher frequencies than in previous work, which had the result of introducing another potential

104

failure mechanism to the PAM. Due to friction effects between the braided sleeve filaments, between the bladder and braided sleeve, and internally in the bladder, PAM actuators self-heat during dynamic operation. Previous studies cycled at 1 Hz, which provided sufficient time between actuations for the PAM to exhaust heat to the surrounding atmosphere, such that self-heating was minimal and the PAM stabilized at a temperature close to ambient. In the present study, the actuators were cycled at 30 Hz, which resulted in a significant amount of self-heating.

3.3. SWAGED PAM DESIGN

The low fatigue lives of PAM type actuators present in the literature motivated the design of a new construction method that would consider fatigue life from the very start. Important lessons were learned from consideration of the failure modes observed in previous fatigue tests (Klute and Hannaford, 1998; Kingsley and Quinn, 2002). The superior fatigue life of latex over silicone made it the preferred material for the bladder. Additionally, latex is generally softer than silicone, which leads to less elastic energy storage in the bladder (increasing actuator force and efficiency) and lower stresses in the bladder for a given strain. A robust and continuous clamping method for the braided sleeve was pursued as a way to eliminate the sleeve pull out and reorientation issues that were experienced in the Kingsley and Quinn study. The clamping of both the sleeve and the bladder was desired to be progressive and gradual, to minimize stress concentrations.

The concept developed uses an axi-symmetric frustro-conical die to progressively swage a thin-walled tube around the braided sleeve, bladder, and inner end fitting. Epoxy adhesive is applied during the assembly process to bond these different elements together and to increase the quality of the pressure seal between the end fittings and bladder. A

cross-sectional view of the swaged PAM design is shown in Figure 3.2, where it can be seen that the design features compactness and simplicity (Woods, Kothera, and Wereley, 2009).
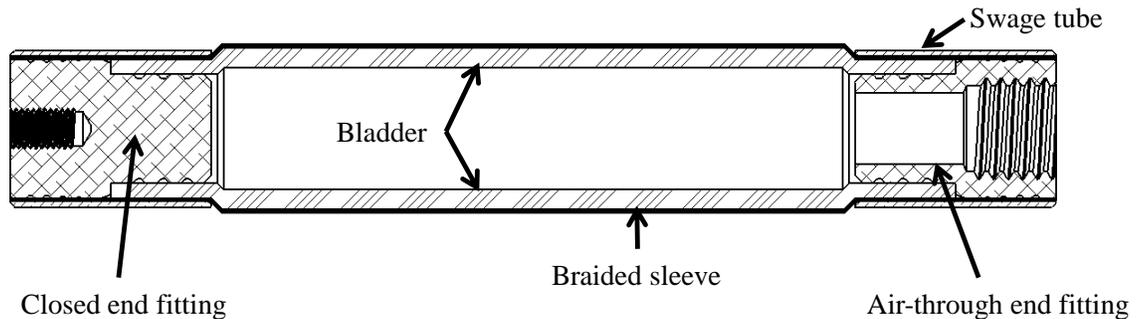
Figure 3.2. Design drawing of swaged PAM cross-section.

The end fittings and thin-walled swage tube are made from aluminum, the braided sleeve is PET plastic with a nominal diameter of 31.8 mm, and the latex bladder has a 25.4 mm outer diameter and 3.2 mm thick walls. When pulled tight around the bladder, the braided sleeve has an initial helix angle of 34.5° relative to the long axis of the PAM. The active length of the actuators studied here is 100 mm.

The end fittings were designed around the swaging process. This meant that a constant outer diameter was needed so that the swaging could be completed in a single operation with a single die. Since the forces generated by actuation or external loading are carried predominantly by the braided sleeve, a direct connection between end fitting and sleeve provides for the highest mechanical strength. It is also necessary, however, to firmly clamp the bladder to keep it from slipping out and to seal it for internal pressurization. To fulfill both of these requirements, a solution with two distinct clamping regions was devised. Moving from the center of the actuator to either of its ends, the first clamping region compresses both the bladder and the braided sleeve. The bladder stops at

106

the end of this region and the second region is for the sleeve alone. The different wall thickness of the latex tubing and braided sleeve necessitates a stepped design of the fittings. The two step diameters must be carefully chosen to provide the desired amounts of compression of the bladder and braid given the final inside diameter of the swage tube. Additionally, it is desirable to compress the rubber more (in absolute terms) than the braided sleeve due to its lower modulus and thicker walls. Since the swage tube diameter is reduced by a constant amount during passage through the swaging die, it is necessary to pre-compress the latex tube slightly during assembly of the components before swaging. Figure 3.3 shows the evolution of the end fitting design (the closed end is shown).

The design changes made to the end fittings over the three revisions were validated by finite element analysis (FEA) using a simplified model of the swaged PAM. The purpose of this study was to examine the effects that the changes in annular groove geometry would have on the stresses experienced in the fiber filaments. The analysis was performed using SolidWorks Simulation FEA software. The details of this study including the geometry and loading conditions will be discussed followed by the results showing the evolution of fiber stresses through the design revisions.

Rev. 1   Rev. 2   Rev. 3
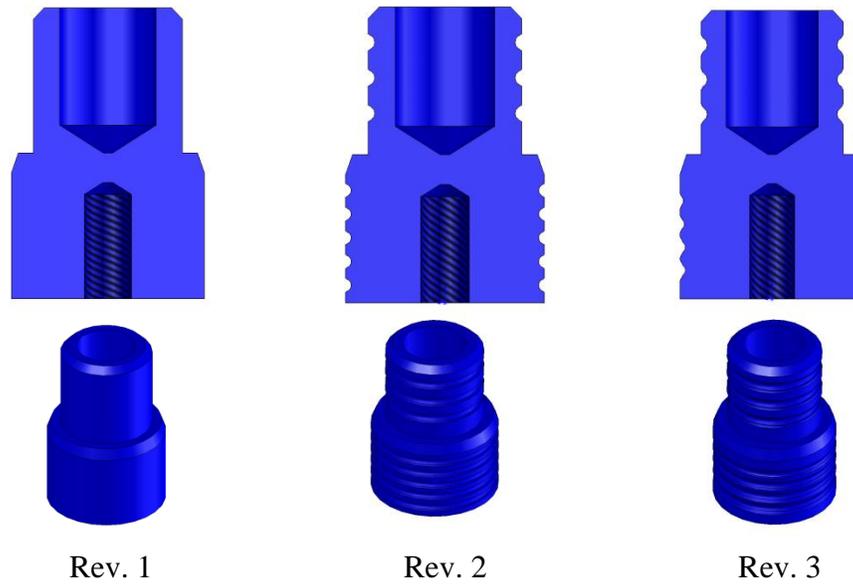
Figure 3.3. End fitting design evolution.

3.3.1.   FEA MODEL GEOMETRY

The geometry of the swaged PAM in the area of the end fittings is fairly complicated. As shown in Figure 3.3, the fittings themselves have a lot of surface features, but even more complicated is the interaction between these fittings and the braided sleeve. This sleeve consists of helically braided filaments that thread up and over each other as they wrap around the end fittings in two different directions.   Each individual filament therefore travels a local serpentine path superimposed onto a global helical path. Furthermore, these sleeve filaments are then compressed against the end fittings by the swage tube, which compresses circumferentially by a known displacement. Finally, the three components are bonded to each other using high strength epoxy. Therefore, the mechanical interactions and load sharing between the end fittings, braided sleeves, and swage tubes is quite complex. In order to allow for a reasonable level of complexity in the FEA analysis, the loading conditions were simplified. Figure 3.4a

shows an isometric view of the geometry used; in this case the Rev. 3 end fitting is shown. A single fiber filament was modeled with a non-serpentine helical path around the different end fitting revisions. A solid aluminum block was used in place of the swage tube to provide the compression force on the filament. This block retains the proper interface geometry between the filament and swage tube, but is squared off to simplify application of the prescribed displacement. Note that the end fitting model retains the important surface features, but only contains one half of the braid clamping portion of the fitting, as this is all that was needed for the single filament studied here.

It is important to note that because simplifications were made to the model geometry, the stress results obtained will not be directly applicable to the actual as built actuators. However, the model geometry (with the exception of the end fitting faces) and loading is consistent throughout the studies on the three revisions so that the relative increases or decreases in predicted stresses can be used as a gauge of the effectiveness of design changes, which is the intention of this study. Note also that in this study the prescribed swaging displacement occurs across the thickness of a single filament, instead of a thicker and looser braided sleeve with multiple serpentine filaments and air gaps as would occur in the actual actuator. For these reasons, the stresses seen in this study are expected to be significantly higher than in the as built actuators.

| (a). Geometry and loading | (b). Example of mesh used |
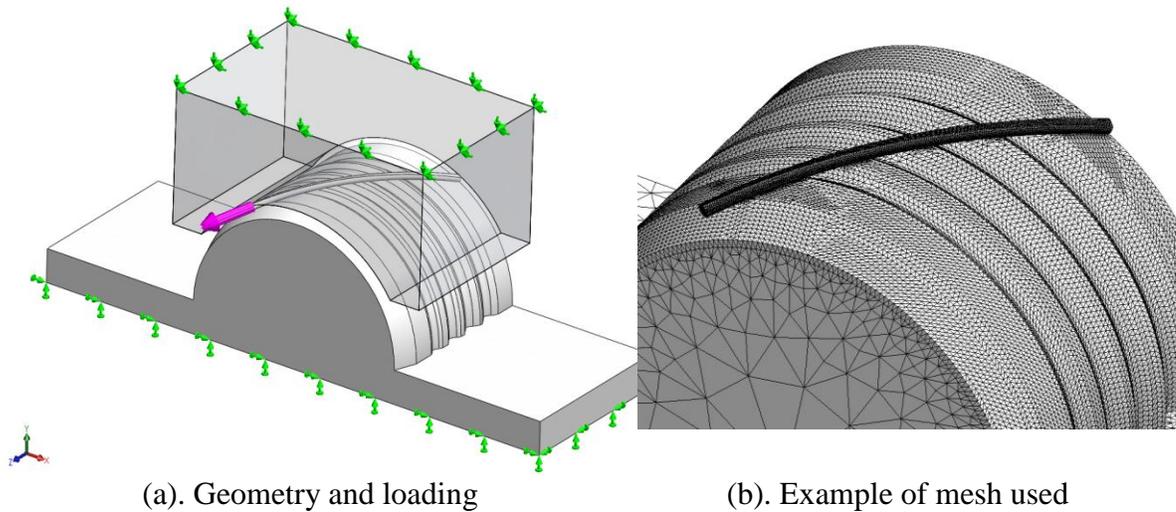
Figure 3.4. FEA study setup.

3.3.2.   FEA MODEL LOADING CONDITIONS

The amount of compression seen in the fiber is driven by the geometry of the swaging process. For all three end fitting revisions, this distance was 0.13 mm, which is significant relative to the 0.5 mm fiber diameter. The end fitting is held fixed while this displacement is prescribed for the filament compression block, and the resulting stresses generated in the filament are of primary interest in this study. In addition to the prescribed displacement of the filament compression block, the fiber filament also sees a tensile force due to the pressurization of the actuator. For the actuator studied, this force is 5.8 N in each of the 280 filaments during 620 kPa blocked force actuation. The filaments make an angle of 34.5° from the long axis of the actuator, with the combined tensile forces in all the filaments resolving to create the 1330 N axial actuation force generated in this operating condition. In the FEA model, the tensile force was applied to the exposed inside face of the filament in a direction tangent to the helical fiber path. This loading orientation can be seen in Figure 3.4a.

3.3.3.   FEA MODEL MESHING

For this study, solid tetrahedron mesh elements were used. Different nominal mesh element sizes were prescribed for the contact faces between the end fitting, fiber filament and filament compression block, depending on the desired level of resolution. The meshing software in SolidWorks Simulation blended these high resolution prescribed meshes into larger sized mesh elements away from the areas of interest. An example of this can be seen in Figure 3.4b, where the element size is small at the fiber and on the contact faces, but can be seen to grow in size towards the center of the end fitting. This provides a good level of fidelity at the areas of interest while keeping the overall number of elements down to reduce solution run times. In order to determine the appropriate mesh size to properly capture the filament stresses without excessive run time, a mesh convergence study was performed. This study was performed on the Rev. 3 end fitting because it has the most complicated geometry, with the resulting mesh sizing parameters then being applied to the other two revisions. For each iteration of mesh size, various stress measurements for the filament were recorded. These included the maximum, minimum, RMS average, and average stress levels for the entire filament. The average filament stress in particular gives a good indication of the impact of mesh size on the results. In Figure 3.5 it can be seen that there is indeed a convergence in the average stress results for the filament as the mesh size in increased. Run times ranged from 1 minute, 27 seconds for 18,000 elements up to 1 hour, 53 minutes for 426,000 elements. From Figure 3.5 it can be seen that models with roughly 250,000 elements were sufficient for convergence.
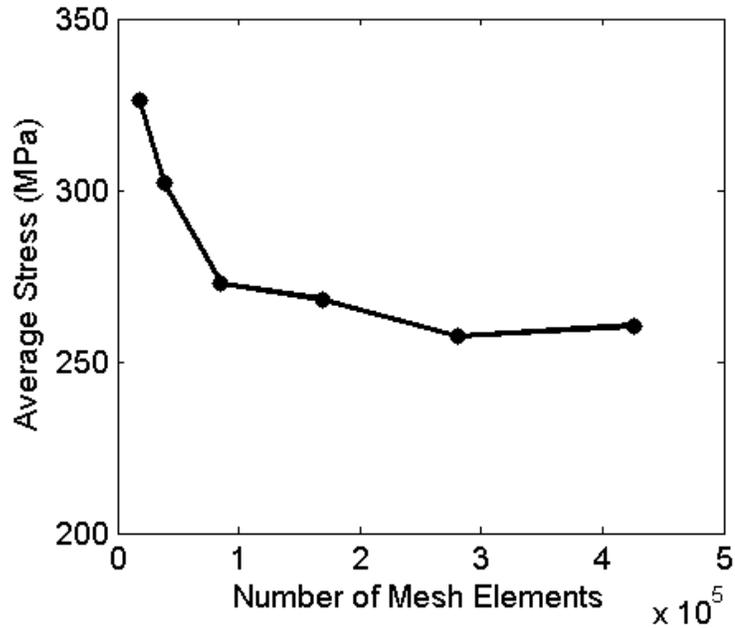
Figure 3.5. Effect of mesh size on average filament stress convergence for Rev. 3 end fitting

3.3.4.   FEA RESULTS

Analysis of the first design revision, which featured no annular grooves, found that the filament experiences a variation of stress through its cross section, but has fairly consistent stresses along its length. Both of these features can be seen in the stress plot shown in Figure 3.6a. The chamfer present at the beginning of the braid clamping region on the end fitting (bottom left of Figure 3.6a) serves to create a more gradual transition from the low stress levels in the un-compressed region of the filament to the fully compressed portion. As can be seen in Figure 3.7, this design has large average stresses due to the fiber being clamped for its entire length. It does, however, have moderately low maximum stress because the design lacks any sharp edges which would serve as stress concentrations.

112

von Mises (N/mm^2 (MPa))

500.0
458.3
416.7
375.0
333.3
291.7
250.0
208.4
166.7
125.0
83.4
41.7
0.0

(a) Rev. 1

von Mises (N/mm^2 (MPa))

500.0
458.3
416.7
375.0
333.3
291.7
250.0
208.4
166.7
125.0
83.4
41.7
0.0
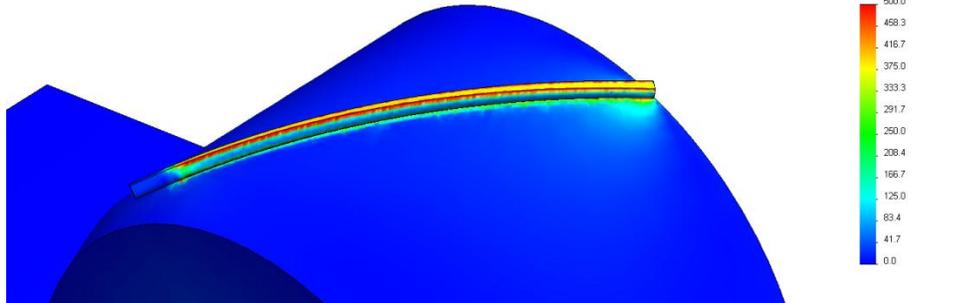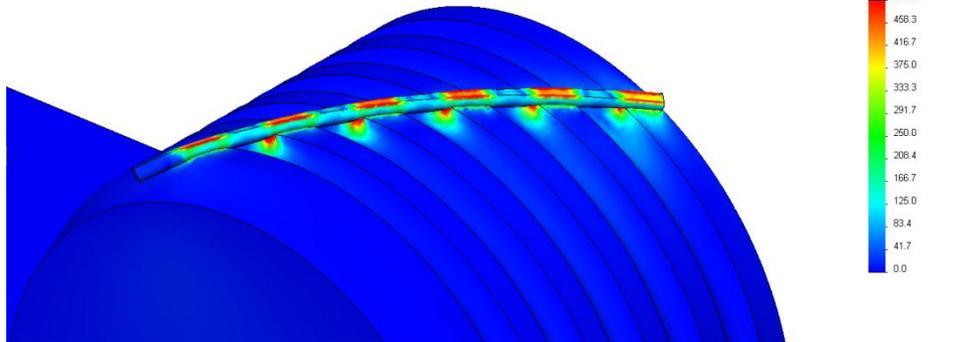
(b) Rev. 2

Figure 3.6. Von Mises stress results for the three end fitting revisions

The second design iteration added a series of annular grooves to the end fitting. These grooves lowered the overall stress level in the filament by creating regions that were effectively unclamped, with resulting low stress levels. These grooves also create thickness changes along the length of the fiber that help keep the fiber from sliding out under load. The sharp edges of these grooves did however have an unintended consequence of creating stress concentrations as the filament enters and exits the groove.

113

This can be seen from the increase in maximum stress from Rev.1 to Rev. 2 in Figure 3.8, and qualitatively in the stress plot in Figure 3.6b.
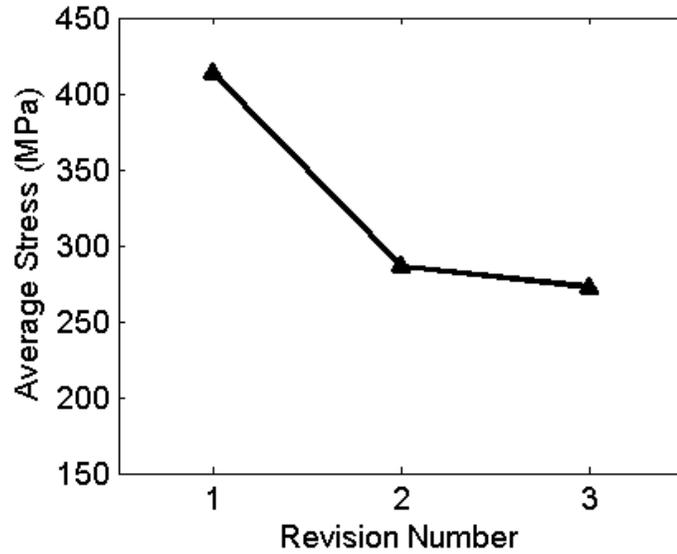
Figure 3.7. Effect of design revision on average filament stress
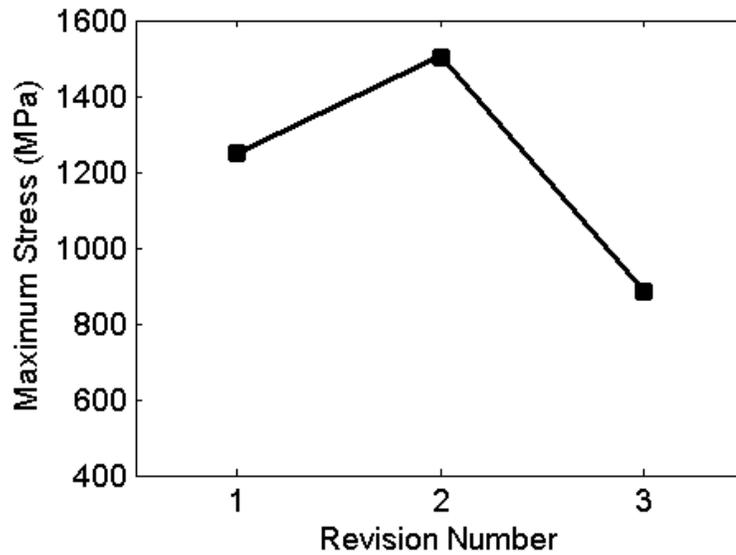
Figure 3.8. Effect of design revisions on maximum filament stress

In order to benefit from the increased pull-out resistance and lower average stress levels provided by the grooves, but to reduce the resulting stress concentrations (which

would lead to premature filament failure), a series of fillets were added to create the third design revision. These fillets are visible in the cross section view of the end fitting in Figure 3.3. The geometry of the grooves was also changed to create a gradual increase in groove depth the further into the clamping region the braid filament travels. This was intended to create a more progressive clamping action. These features effectively reduced the maximum filament stress to even lower than the first revision (Figure 3.8), while further lowering the average stress levels, as can be seen in Figure 3.7. The FEA study therefore successfully validated the design changes made across the revisions by showing a reduction in both maximum and average fiber filament stresses.

3.4.   MECHANICAL TESTING OF SWAGED PAMS

In order to validate the swaged PAM design process, mechanical strength testing was performed on PAMs made using the three different end fitting revisions. Additionally, mechanical strength testing on the final design allowed for the establishment of factors of safety for actuation force and pressure. Factors of safety above 1.5 were desired to allow for use of these actuators in aerospace applications.

3.4.1.   ULTIMATE TENSILE FAILURE TESTING

In order to experimentally gauge the effectiveness of the design revisions, unpressurized tensile failure tests were used as an expeditious analog to full fatigue testing. Any stress concentrations in the clamping of the braid or bladder that might lead to fatigue failure after weeks of testing would also likely lead to premature failure during a quick tensile test.

The first design of the end fitting, seen in Figure 3.3, relied primarily on frictional forces to retain the PAM components. This is a very simple and straightforward

approach, but tensile testing showed an ultimate strength of only ~1350 N, which is insufficient given that the blocked force of these actuators is 1330 N at 620 kPa. The failure mechanism involved the filaments sliding out from in between the swage tube and end fitting. The second revision therefore incorporated increased surface texture in the form of radial grooves that would more effectively clamp the braid. Grooves were also added on the latex tubing portion of the fitting to serve as reservoirs for epoxy, thereby helping to ensure proper sealing. This revision caused a significant increase in ultimate tensile strength to over 4000 N. A higher safety factor was desired, however, so the design of the grooves was further refined. It was noticed with the second revision that failure occurred in the braid filaments themselves consistently at the first corner of the first groove underneath the braid. It was reasoned that the ~90° corner left by the grooving tool created a large stress concentration, causing premature braid failure. This correlates well with the FEA results discussed above. The third revision therefore incorporated fillets on the grooves and a progressive groove depth. At this point three separate PAM specimens were made using the Rev. 3 design. These were all tested to failure to examine the repeatability of the ultimate tensile load.

As can be seen in Figure 3.9a, the stiffness properties of the actuator were found to be highly repeatable, and the ultimate tensile force was also quite consistent. The mean failure force was 7380 N with a standard deviation of 115 N. The failed specimens with the braided sleeves plastically deformed and separated are also shown in Figure 3.9b. Given the high tensile strength and good repeatability, this design was chosen for use with the fatigue life testing.
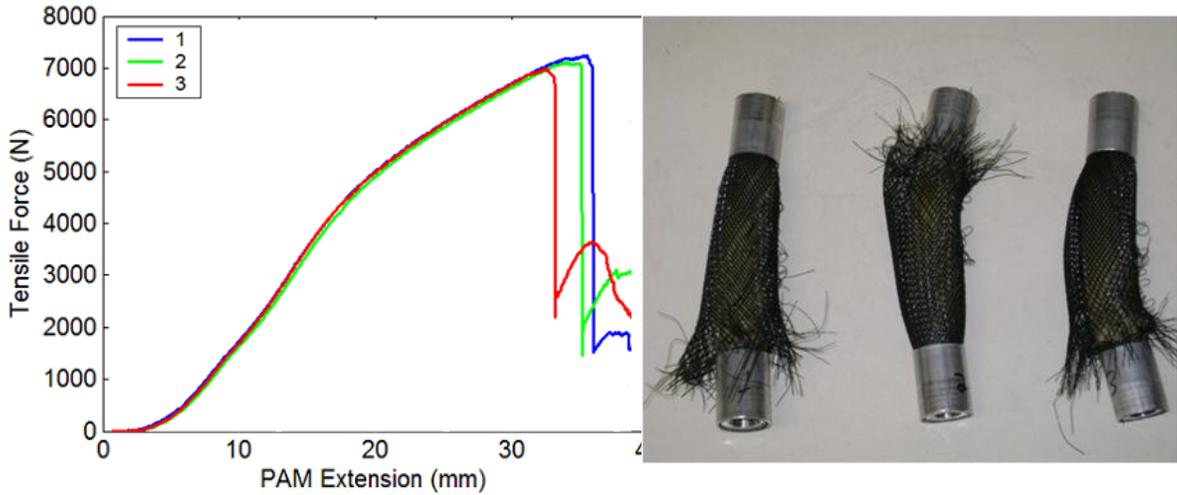
(a). Experimental data   (b). Specimens after failure

Figure 3.9. Ultimate tensile failure testing.

3.4.2.   BURST FAILURE TESTING

Further experimental testing was performed on the final swaged PAM design to determine the factor of safety with respect to operating pressure. The effectiveness of the pressure sealing features incorporated into the end fitting design was unknown, so an experiment was devised to test the ability of the bladder clamping region of the design to remain sealed and to retain the bladder at higher pressures. This test consisted of a pressure ramp on three nominally identical specimens of the Rev. 3 design that were held fixed at their resting lengths. The pressure was increased slowly until failure occurred in the actuator. Actuator pressure and force were recorded. The results of this testing can be seen in Figure 3.10. Figure 3.10a shows the force results plotted against pressure for the three PAMs, labeled here as 4, 5, and 6 to avoid confusion with the tensile test specimens. Note that for all three specimens the burst pressure is over 1870 kPa, which gives a factor of safety of 3 over the nominal 620 kPa operating point. Figure 3.10b shows the test specimens after failure. Note that the primary failure mechanism in all

117

three is braided sleeve rupture, beginning at some point near the center of the actuator then expanding out. After rupture of the sleeve, the bladder was free to balloon out to a size much larger than its resting diameter, leading to bladder rupture in two of the three actuators, and a bladder slip out in the case of the third. The results of this testing showed that the design of the pressure sealing and bladder retention features of the swaged PAM was successful, with the primary limit on burst pressure strength being the strength of the PET plastic material used in the braided sleeve.
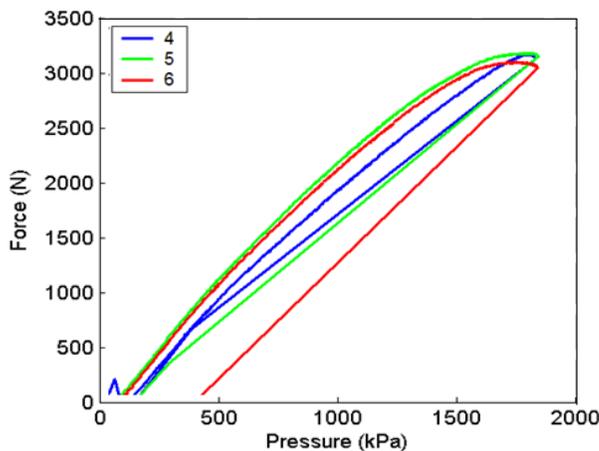
(a). Experimental data   (b). Specimens after failure

Figure 3.10. Burst pressure testing.

3.5. FATIGUE LIFE TESTING

3.5.1. TEST RIG DESIGN

The modular fatigue test stand shown in Figure 3.11 was designed and built to simultaneously test three PAM specimens. The three PAMs tested were built with the Rev. 3 end fitting design and the same parameters mentioned above in the design section, namely a nominal outer diameter of 31.8 mm, latex bladder of 25.4 mm outer diameter and 3.2 mm thick walls, and a PET plastic braided sleeve with an initial helix angle of

34.5° relative to the long axis of the PAM. Epoxy adhesive was used during assembly between the end fittings, bladder, braided sleeve, and swage tube. This design was used because it had the best mechanical properties, and therefore it was surmised that it would perform the best under cyclic loading. Given the long length of time required to complete these tests (the fatigue tests for the work presented here took six months to complete), it was not feasible to fatigue test all of the design revisions, or to independently look at the effect of epoxy on fatigue life.

Pressurized air is supplied from above each PAM and the moving ends are connected to loading springs. The supply air is pressurized by a 7.5 kW electric compressor, which feeds through a 300 liter accumulator and a high flow rate air dryer. Pressurization and exhaustion of each PAM is controlled individually with a Festo MHE-4 three-way solenoid valve. The inflation phase of each of the three actuators is phased 120 degrees from the other two to help smooth the air flow requirements from the pneumatic supply system. The test rig was built with 80/20® modular hardware to allow for different PAM lengths and loading configurations to be easily interchanged.

A line pressure regulator was installed upstream of the PAMs to control the operating pressure during testing. Immediately downstream of this, an Omega PX-209 pressure transducer was installed to allow for time histories of input pressure to be recorded. The transducer was mounted immediately downstream of the regulator and before the solenoids that actuate the PAMs, and therefore provides a measure of the overall input pressure, which is different from the internal PAM pressures. The primary function of this transducer was to monitor the output of the compressor to ensure that the desired global pressure levels were being achieved. The displacements of each individual

PAM were recorded. In addition to the loading springs, the moving end of each PAM was also attached to an Omega LP804 linear potentiometer for recording stroke. Additionally, PAM 1 was outfitted with an infrared thermocouple, Omega Engineering model OS36-01-K-140F, for measuring surface temperature of the PAM.
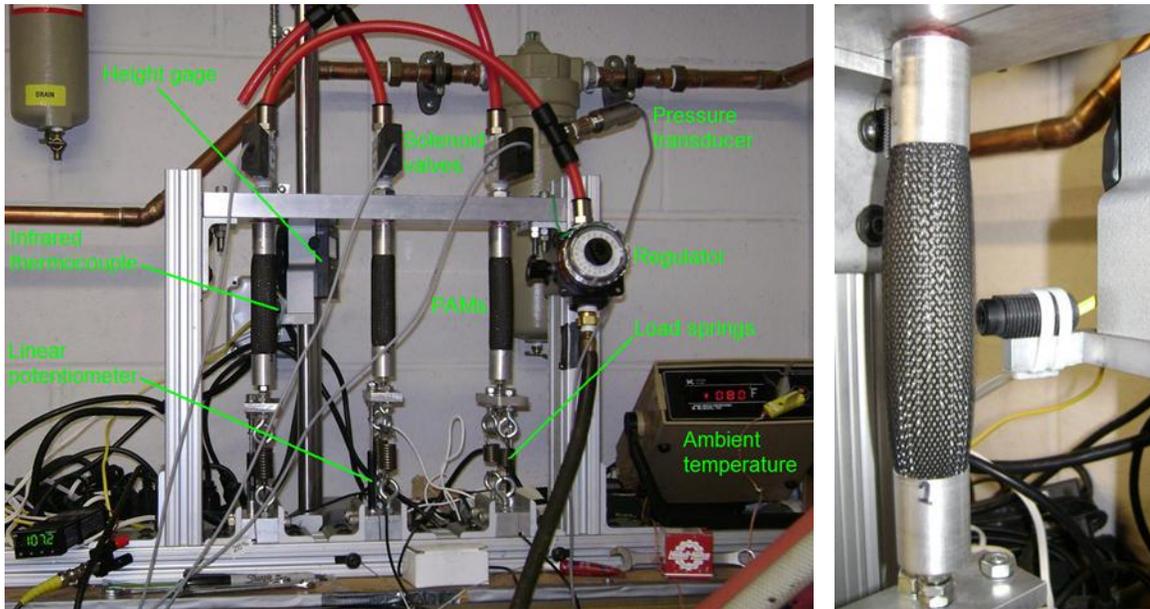
(a). Overview   (b). Thermocouple
Figure 3.11. Fatigue test stand.

3.5.2.   TEST PROCEDURES

The test procedures were designed to mimic realistic operating conditions for PAMs employed in trailing edge flap systems such as those under development by the authors (Woods *et al.*, 2008; Kothera *et al.,* 2010; Bubert *et al.*, 2010;). The spring stiffnesses and operating pressure were chosen to create a range of realistic deflections under realistic loads. Work in optimizing system output for the trailing edge flap systems currently in development has shown working strokes of around 4-6% of active length (λ = 0.96 - 0.94) to be typical. Therefore, this was the range of strokes that was desired with the different spring loadings. The stroke achieved under dynamic actuation was strongly

dependent on the loading condition (spring stiffness), operating pressure, driving frequency, and the flow rate capabilities of the pneumatic supply system. The flow rate capabilities of the pneumatic system were essentially fixed by the design of the house air system employed. The driving frequency was desired to be as high as possible to minimize the amount of time required for testing and better simulate conditions that may be experienced in a dynamic control application. The operating pressurewasset by the regulator to a nominal quasistatic value, but the actual pressure available to the PAM was again a function of operating frequency and the flow rate of the pneumatic system. In order to achieve the primary goal of 4-6% stroke, a series of initial characterization tests were performed on the test rig to determine the combination of operating pressure, actuation frequency and spring stiffnesses that would achieve the desired stroke range. It was found that a pressure regulator setting of 620 kPa, an actuation frequency of 30 Hz, and spring constants of 31.7, 19.8, and 9.5 N/mm would create 3.7%, 5.3%, and 5.9% stroke, respectively. Table 3.1 shows the spring loadings and resulting dynamic strokes for each PAM. It was important to note that these strokes do not correlate directly to λ values; that was a dynamic stroke of 3.7% does not imply that the actuator cycled from λ = 1.0 to λ = 0.963. This is because under dynamic actuation at 30 Hz the PAMs do not fully exhaust, so they do not return to λ = 1.0 in between pressurizations. The actual λ ranges seen for each PAM are listed in Table 3.1. The average pressure measured at this operating point was 410 kPa, which is less than the 620 kPa static set point of the regulator due to the mass flow rate required to fill and exhaust all three PAMs 30 times each second.

Table 3.1. PAM loading conditions.

PAM #	Spring Loading [N/mm]	Dynamic Stroke	Test range of contraction ratio, λ
1	31.7	3.7%	0.893-0.94
2	19.8	5.3%	0.865-0.918
3	9.5	5.9%	0.811-0.87

It is not yet known if the effect of dynamic stroke on the fatigue life of pneumatic artificial muscles is independent of the actual range of contraction ratios achieved during cycling. This could conceivably have an impact since the force generated by the actuator changes with contraction, so a dynamic stroke of 3.7% that starts at the resting length ($\lambda = 1$) and goes to $\lambda = 0.963$ would cause higher PAM forces than the tested contraction range of $\lambda = 0.893$–0.94. It is difficult to control this parameter in a high frequency fatigue test however because of the high mass flow rates of air required to fully exhaust and fill the PAMs. The operating condition tested is, however, still representative of the type of trailing edge flap actuator being developed because these same pneumatic supply system limitations exist in real systems. Future testing would benefit from a more thorough testing of this effect. Similarly, different PAM geometries would generate different force levels during actuation, which may impact the fatigue life of the actuators.

The PAMs were subjected to a periodic test regimen on and off the test stand. In order to track the effect of cycling on the performance of the PAMs, quasistatic force vs. contraction characterization tests at 620 kPa were performed on each PAM prior to the fatigue cycling, and repeated after every 40 million cycles. For these tests, the PAMs were removed from the fatigue stand and placed in a MTS servo-hydraulic testing

machine. With the actuators pressurized to 620 kPa, a displacement ramp was performed that started at the resting length of the actuator ($\lambda = 1$), extended it 5% to $\lambda = 1.05$, allowed it to contract to free contraction ($\lambda = 0.74$ at this pressure), extended again to $\lambda = 1.05$, and then returned to $\lambda = 1$. In this way, the actuator load line was obtained. A pressure of 620 kPa was chosen for these tests as this is a typical operating point for these actuators.

The primary component of the fatigue testing consisted of the PAMs mounted in the test stand, cycling at 30 Hz. The approximately 120 million cycles (over 1100 operational hours) were separated into dozens of 2.6 million cycle (24 hour) sets. Each set was programmed to run continuously and record data for one second every minute. These 24-hour sets recorded the incoming air pressure. After each automatic 24-hour set completed, the PAMs were inspected and the linear potentiometers were attached to the moving ends of the PAMs. With the displacement sensors installed, a 10-minute, 30 Hz test block was run to measure line pressure and PAM displacement continuously. The displacement sensors were then detached and the PAMs set to run on another 24-hour set. The purpose of the two-part procedure was two-fold: (1) it ensured ample human oversight of the test conditions and fatigue effects, and (2) it limited the wear on the displacement sensors. These driving factors for procedure design were determined by observations of pre-test shakedown studies and initial iterations.

Testing was stopped after 120 million cycles as this was a target benchmark, and schedule constraints prohibited further testing. It is important to note that this testing was not ended due to actuator failure, although some signs of wear were observed, as will be discussed below.

3.5.3. ENVIRONMENTAL CONDITIONS

The test was conducted in a closed room, with ambient temperature during the tests ranging from 90-100 $^\circ$F. PAM temperature was measured by an infrared thermocouple aimed at the active middle section of PAM 1. As cycling began at the start of each test segment, the surface temperature would slowly rise from ambient, leveling off after 2-4 hours at about 54.4 $^\circ$C (130 $^\circ$F). Air pressure upstream of the PAMs was also measured. The actuators were supplied with air at an average of 410 kPa throughout the duration of the test. The air pressure fluctuated by 30-65 kPa in approximately 6-minute cycles as the compressor pumps went through their normal operating cycle.

3.6. FATIGUE TEST RESULTS

3.6.1. PAM LOAD LINE EVOLUTION

Because no catastrophic failures were observed over this 120 million cycle test, it is useful instead to look for changes in the 620 kPa actuator load lines as an indication of performance degradation due to fatigue damage or wear. What is desired is an actuator that will not suffer a significant decrease in performance over its life cycle. Also, any large changes in performance would be indicative of a failure mode that, while not visibly catastrophic, might still be severe enough to suggest partial actuator failure. Specifically, we were looking for any significant decreases in the amount of force and contraction that could be generated at a constantly held pressure. Testing at a held pressure would also help highlight the presence of any pin-hole leaks in the bladder.
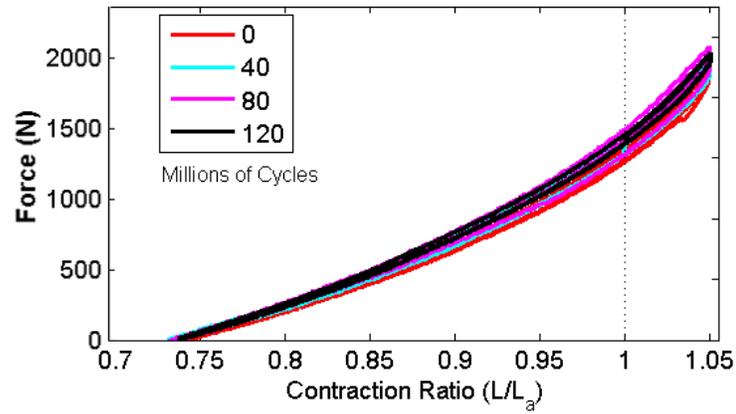
(a). PAM 1
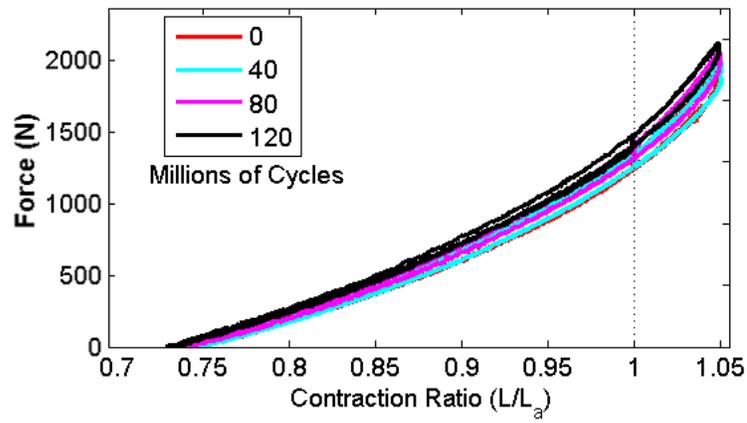
(b). PAM 2
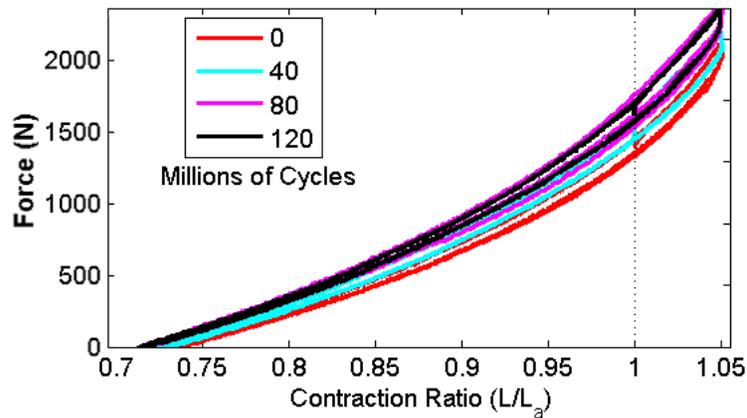
(c). PAM 1

Figure 3.12. Force vs. contraction load lines (620 kPa).

125

Figure 3.12 shows a series of load lines for each PAM at four points from 0 to 120 million cycles. Each cycle of this load testing shows a hysteresis loop due to braid and bladder friction effects. The hysteresis in these plots has a clockwise directionality. These load lines, for the most part, fall on top of each other, with some variation seen at the higher force levels near $\lambda = 1$. Generally, it can be seen that there is no significant loss in performance over the 120 million cycles.

In order to more clearly see any trends present in the data, it is useful to examine the progression of blocked force and free contraction values extracted from these plots. This is done for each PAM in Figure 3.13a. The values of the blocked force are found from each load line by taking the average of the force values at $\lambda = 1$. Averaging is used to remove the effects of the hysteresis from this analysis. The free contraction ratios are found as the λ value at which the force is zero.

In Figure 3.13 it can be seen that the blocked force of each actuator actually tended to increase with cycling. Additionally, the free contraction ratio (Figure 3.13b) tended to decrease slightly or stay roughly the same. These are both positive results, showing that even after 120 million cycles, the actuator performance is not diminished. The improvement in performance is believed to be the result of softening in the rubber bladders over time (Mullins, 1969), which results in less energy being stored in the bladders during actuation, effectively increasing actuator efficiency. As mentioned above, PAM 1 acted against the stiffest of the springs and so had the smallest dynamic stroke during testing, while PAM 3 had the largest stroke. The different stroke magnitudes do not seem to create any clear trending in the blocked force and free

contraction results, indicating that the differences in dynamic stroke seen in this test may not make a significant impact on the evolution of PAM performance with cycling.
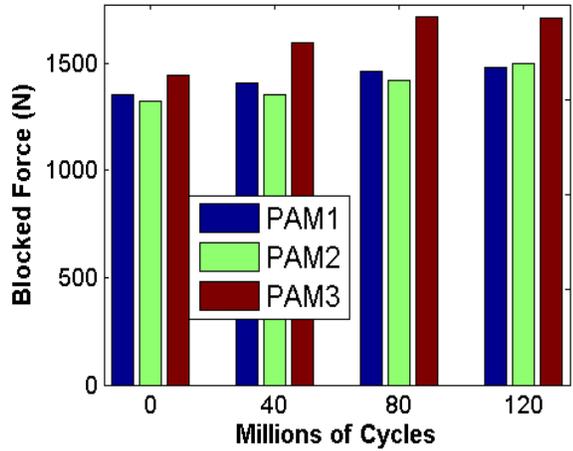
(a). Blocked force
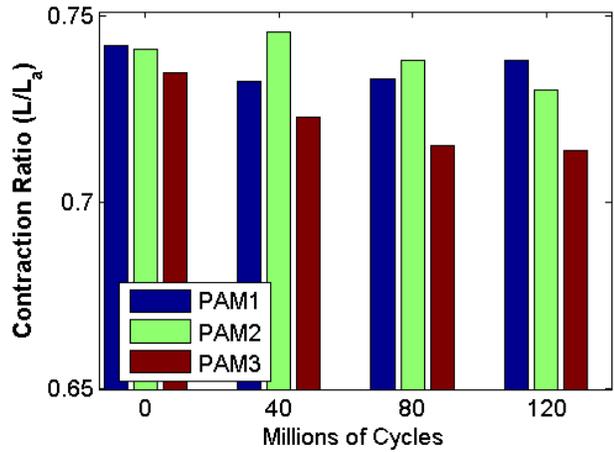
(b). Free contraction ratio

Figure 3.13. Evolution of PAM performance parameters with cycling.

In order to allow for comparison of the results from the current testing to those in previous literature, Table 3.2 has been included. Here it can be seen that the actuator length and applied pressure are on the same order as previous work. Our testing was carried out at significantly higher frequency to better match the desired operating

conditions for an active trailing edge flap system. Self-heating of the actuator, which is dependent on operating frequency, was not addressed in the previous work. As mentioned above, the surface temperature of the PAMs studied here was 54.4 $^{\circ}$C (130 $^{\circ}$F), which is significantly above ambient. The expected impact of this elevated temperature would be a shortening of actuator life given the effect of temperature on the fatigue life of elastomers (Woo *et al.*, 2009), although that conclusion cannot be directly drawn from this study since all of the PAMs tested experienced similar operating temperatures.

Table 3.2. PAM fatigue studies.

Source	PAM Length [mm]	Pressure Applied [kPa]	Frequency [Hz]	Contraction of PAM	Maximum Fatigue Life
Klute and Hannaford, 1998	140	88-360	1	Varying from 5-25% of resting length	17,620 at 88 kPa, 5% contraction
Kingsley and Quinn, 2002	76	646	1	[no data]	14,000
Current Study	100	410	30	3.7% 5.3% 5.9%	> 120,000,000 no failure observed

3.6.2.   STROKE MEASUREMENTS

The displacement of each PAM was recorded for 10 minute sets every 24 hours. These measurements were compared to the static PAM length and analyzed on a cycle-by-cycle basis to compute the dynamic actuation stroke. The stroke was the difference, as

a non-dimensional percentage, between maximum and minimum positions of the PAM while cycling at 30 Hz.

Figure 3.14 plots the stroke results of the three PAMs over the 120 million cycles tested. Each point represents the average of about 18,000 cycles worth of data, taken during the 10-minute sets. The data exhibited some scatter, but no clear trend emerged over the test range. The average strokes of each PAM are shown as thick horizontal lines; they were calculated to be 3.7%, 5.3%, and 5.9%, respectively, whereas the thin lines represented the standard deviations. It is noteworthy that of the 49 data sets that comprised the 120 million cycle test, six of the displacement measurements could not be included in the final analysis due to malfunctions in the displacement sensors.
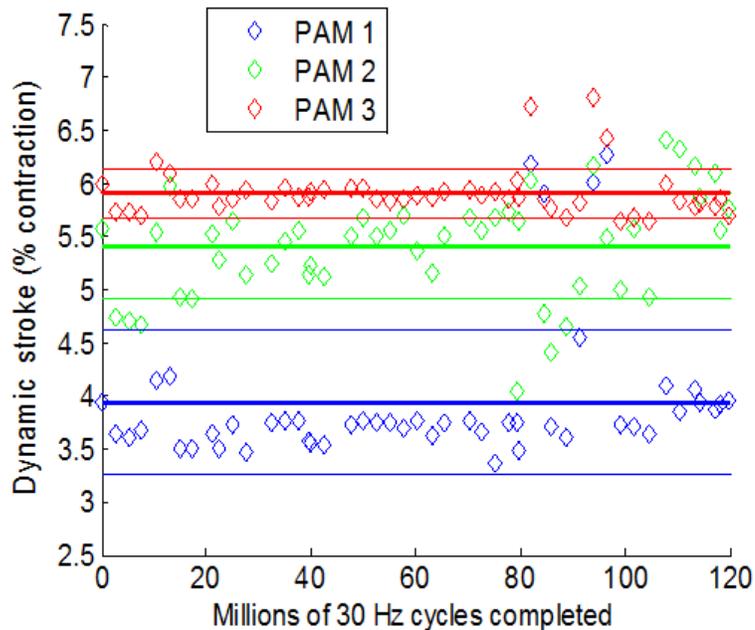
Figure 3.14. Stroke measurements over test period

3.6.3. FATIGUE DAMAGE

While no catastrophic failures were observed after 120 million cycles, two of the three PAMs were beginning to show signs of braid filament failure due to wear. PAM 3

had three (of 280, or 1.1%) braid filaments broken and bent out of alignment, and PAM 2 had seven fibers broken (2.5%). These were relatively minor failures, as the braid on each PAM consisted of 280 interwoven filaments. The compromised filaments were spread across the diameter of the PAM, as seen in   Figure 3.15. Another observed effect was the formation of grooves on the outer surface of the bladder where the fibers' movement abraded some of the bladder material. This effect was seen on all three PAMs and lends support to the theory that rubber softening led to increased performance over time. These grooves were less than 0.25 mm in deep at the end of 120 million cycles; about 5% of the thickness of the latex tube.
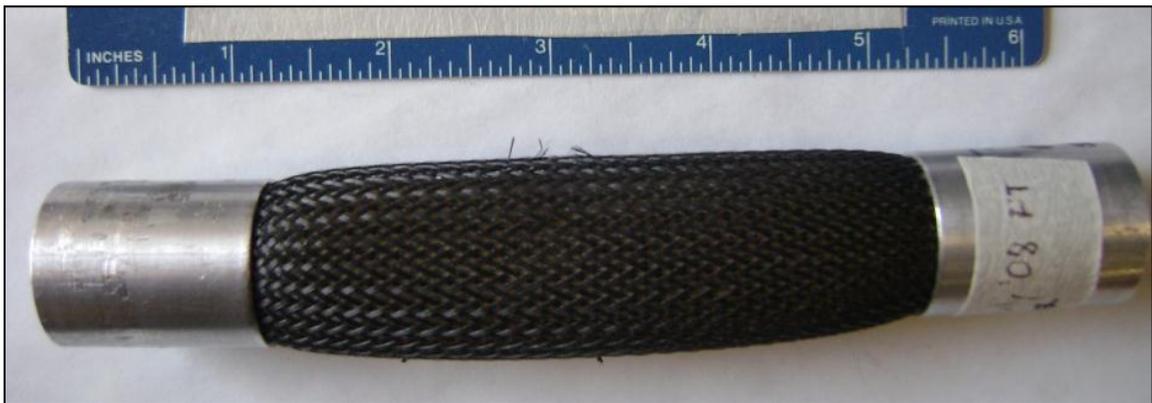
Figure 3.15. PAM 2 after 120 million cycles showing minor braid filament damage.

3.7. CONCLUSIONS

This work investigated the fatigue properties of Pneumatic Artificial Muscles that employ a novel swaged end fitting fabrication technique. These actuators have a promising combination of good performance, light weight, simplicity, and low cost, so that they are attractive alternatives to conventional hydraulic and electric motor actuators for aerospace applications. The primary objective of this research was to significantly extend the fatigue life of Pneumatic Artificial Muscle actuators under realistic operating conditions for a helicopter active trailing edge flap system.   This was successfully

130

achieved with an increase in endurance from less than 18,000 to over 120,000,000 load cycles. Additionally, in this work:

1.   A novel swaging construction technique for PAM actuators was successfully developed that provides consistent, concentric clamping of the braided sleeve and bladder elements to the end fittings.

2.   Finite Element Analysis of the swaged end fittings allowed for multiple revisions to be quickly made, realizing significant reductions in braid filament stress before long term fatigue testing began.

3.   The FEA results were experimentally corroborated using tensile failure tests, which showed the reduction in filament stresses as an increase in ultimate strength. The final design provides a tensile strength factor of safety of 5.1.

4.   High pressure burst testing was performed on the actuators to prove the strength of the pressure sealing elements of the swage design. Burst failure occurred not at the end fittings, but in the center of the braided sleeve, again validating the strength and sealing ability of the newly designed end fittings. The burst pressure factor of safety is 3.

5.   Fatigue testing at high frequency (30 Hz) with pressures and deflections typical of a helicopter active trailing edge flap system to over 120,000,000 cycles. None of the three actuators tested failed during the test, and there was no degradation in actuator performance over this time, although some indications of wear were present.

3.8. REFERENCES

Abdulrahim, M., and Lind, R., 2006. "Using Avian Morphology to Enhance Aircraft Maneuverability," *AIAA Atmospheric Flight Mechanics Conference and Exhibit*, Keystone, CO, AIAA 2006-6643.

Bharadwaj, K., Hollander, K. W., Mathis, C. A. and Sugar, T. G., 2004. "Spring Over Muscle (SOM) Actuator for Rehabilitation Devices," *Engineering in Medicine and Biology Society, 2004. IEMBS '04. 26th Annual International Conference of the IEEE*, 1, 2726-2729.

Bubert, E.A., Woods, B.K.S., Lee, K., Kothera, C.S., and Wereley, N.M., 2010. "Design and Fabrication of a Passive 1D Morphing Aircraft Skin," *Journal of Intelligent Material Systems and Structures*, 21:1699-1717.

Caldwell, D., Medrano-Cerda, G., and Bowler, C., 1997. "Investigation of Bipedal Robot Locomotion Using Pneumatic Muscle Actuators," *Proceedings of the IEEE International Conference on Robotics and Automation*, 799-804.

Daerden, F., and Lefeber, D., 2002. "Pneumatic Artificial Muscles: Actuators for Robotics and Automation," *European Journal of Mechanical and Environmental Engineering*, 47:10-21.

Festo, 2010. "Festo Fluidic Muscle DMSP," Product data sheet, URL: www.festo.com, accessed August.

Huber, J., Fleck, N., and Ashby, M., 1997. "The Selection of Mechanical Actuators Based on Performance Indices," *Proceedings of the Royal Society A*, 453:2185-2205.

Kingsley, D. and Quinn, R., 2002. "Fatigue Life and Frequency Response of Braided Pneumatic Actuators," *Robotics and Automation*, 3:2830-2835

Klute, G. and Hannaford, B., 1998. "Fatigue Characteristics of McKibben Artificial Muscle Actuators," *IEEE/RSJ International Conference on Intelligent Robots and Systems*, Victoria, Canada.

Kothera, C. S., Woods, B.K.S., Sirohi, J., Wereley, N.M., and Chen, P. C. 2010. "Fluid-Driven Artificial Muscles as Mechanisms for Controlled Actuation," U.S. Patent 7,837,144, Filed: Aug. 11, 2006, Published: Nov. 23, 2010.

Kothera, C.S., Jangid, M., Sirohi, J., and Wereley, N.M. 2009. "Experimental Characterization and Static Modeling of McKibben Actuators," *ASME Journal of Mechanical Design*, **131**(9):091010.

Lightned, S., and Lincoln, R., 2002. "The Fluidic Muscle: A 'New' Development," *International Journal of Modern Engineering*, 2(2).

Mullins, L., 1969. "Softening of Rubber by Deformation," *Rubber Chemistry and Technology*, 42, 339-363.

Philen, M. 2009. "On the Applicability of Fluidic Flexible Matrix Composite Variable Impedance Materials for Prosthetic and Orthotic Devices," *Smart Materials and Structures*, 18:104023. DOI 10.1088/0964-1726/18/10/104023.

Philen, M., 2011. "Force Tracking Control Fluidic Flexible Matrix Composite Variable Stiffness Structures," *Journal of Intelligent Material Systems and Structures*, 22:31-43. DOI: 10.1177/1045389X10391498.

Philen, M., Shan, Y., Bakis, C. E., Wang, K. W. and Rahn, D., 2006. "Variable Stiffness Adaptive Structures Utilizing Hydraulically Pressurized Flexible Matrix Composites with Valve Control," *47th AIAA/ASME/ASCE/AHS/ASC Structures, Structural Dynamics and Materials Conference, May 1- 4, 2006*, Newport, RI, United states, American Institute of Aeronautics and Astronautics Inc. 9, 6387-6397.

Robinson, R., Woods, B.K.S., Vocke, R.D., Kothera, C.S., Wereley, N.M., 2010. "High Specific Power Actuators for Robotic Manipulators," ASME Conference on Smart Materials, Adaptive Structures and Intelligent Systems, September 28 - October 1, Philadelphia, PA, Paper No. SMASIS2010-3902.

Schulte, H.F., 1961. "The Characteristics of the McKibben Artificial Muscle," *The Application of External Power in Prosthetics and Orthotics*, Pub. 874, National Academy of Sciences – National Research Council, Washington, DC, App. H, 94-115.

Shan, Y., Philen, M., Amir, L., Bakis, C.E., Rahn, C.D., and Wang, K.W. 2009. "Variable Stiffness Structures Utilizing Fluidic Flexible Matrix Composites," *Journal of Intelligent Material Systems and Structures*, 20:443-456. DOI: 10.1177/1045389X08095270.

Sofla, A.Y.N., Meguid, S.A., Tan, K.T. and Yeo, W.K. 2010. "Shape Morphing of Aircraft Wing: Status and Challenges," Materials and Design, 31, 1284-1292.

Thill, C., Etches, J., Bond, I., Potter, K., and Weaver, P., 2008. "Morphing Skins," *The Aeronautical Journal*, 112(1129): 117-139.

Tondu, B., and Lopez, P., 1997. "The McKibben Muscle and its Use in Actuating Robot-arms Showing Similarities with Human Arm Behaviour," Industrial Robot, 24(6): 432-439.

Walker, I, Dawson, D., Flash, T., Grasso, F., Hanlon, R., Hochner, B., Kier, W., Pagano, C., Rahn, C., and Zhang, Q., 2005. "Continuum Robots Arms inspired by Cephalopods," *Proceedings of SPIE*, 303-314.

Weiss, P. 2003. "Wings of Change: Shape-shifting Aircraft May Ply Future Skyways," *Science News*, 164(23): 359-365.

Woo, C., Kim, W., Lee, S., Choi, B., Park, H., 2009. "Fatigue Life Prediction of Vulcanized Natural Rubber Subjected to Heat-aging," *Procedia Engineering*, 1(1): 9-12.

Woods, B., Bubert, E., Kothera, C., and Wereley, N.M., 2008. "Design and Testing of a Biologically Inspired Pneumatic Trailing Edge Flap System," Paper No. AIAA-2008-2046, *AIAA Structures, Structural Dynamics, and Materials Conference*, Schaumberg, IL.

Woods, B.K.S., Kothera, C.S., and Wereley, N.M., 2008. "Whirl Testing of a Pneumatic Artificial Muscle Driven Helicopter Trailing Edge Flap," American Helicopter Society 64th Annual Forum, Montreal, Canada.

Woods, B.K.S., Kothera, C.S., and Wereley, N.M., 2009. "Fluidic Artificial Muscle Actuator and Swaging Process Therefor," US Patent Pending, Application No. 12/456,139.

Zhang, Z., Philen, M. and Neu, W. 2010. "A Biologically Inspired Artificial Fish Using

Flexible Matrix Composite Actuators: Analysis and Experiment," Smart Materials and Structures, 19:094017. DOI: 10.1088/0964-1726/19/9/094017.

4. Wind Tunnel Testing and Quasistatic Modeling

4.1.   INTRODUCTION

Trailing edge flap (TEF) systems in helicopter rotors have been the subject of much research, both in the context of individual blade control (Ham, 1987), as well as smart rotor development (Hall and Spangler, 1993; Hall and Prechtl, 1996; Chopra, 2000), for purposes of vibration reduction. Such a TEF system would allow for higher harmonic control of each blade to directly mitigate the vibrations induced by aerodynamic forces and moments as the rotor spins (Hall and Wereley, 1993). Additionally, if such a TEF system had sufficiently high control authority, TEFs could be implemented as primary control surfaces of the helicopter, so that the swashplate with its significant drag, complexity, and maintenance penalties could be eliminated (Leishman, 2000; Johnson, 1994; Chopra, 2002; Leishman, 2007; Falls *et al.*, 2010).

One of the key challenges in developing a TEF system for a rotor blade is the highly constrained design space: (1) actuator volume is highly constrained, especially if the actuators are placed in the main rotor blades, (2) blade mounted actuators experience high centrifugal loads under rotation, (3) actuator weight must be minimized to minimize actuator mounting structure and blade loads under rotation. Consequently, there has been considerable interest in the use of smart materials as the driving elements of these systems. Piezoelectric, electrostrictive, magnetostrictive, and shape memory alloy materials have all been investigated, and these approaches were reviewed by Giurgiutiu (2000) and Chopra (2002). Piezoelectric TEF actuation systems were originally proposed by Hall and co-workers (Hall and Spangler, 1993; Hall and Prechtl, 1996), and subsequently attracted substantial attention and earned much success to date, although

they have typically been employed in reduced scale prototype demonstrations (Chopra, 2002). Many researchers over the last two decades have pursued this approach and performance has been progressively improved as a result of this work (Loewy, 1997; Giurgiutiu 2000; Chopra, 2000; Fulton, 2000; Niezrecki *et al.,* 2001). Indeed, a full-scale whirl test (Straub *et al.* 2004), and the first flight test (Dieterich, Enenkl, and Roth, 2006) of a smart rotor equipped with piezoelectric actuator-based TEF systems were recently conducted. However, piezoelectric materials are known to suffer from some inherent limitations, including small actuation strains ($\varepsilon < 0.2\%$), material brittleness, and significant cost, among others (Giurgiutiu, 2000). Additionally, without a substantial breakthrough in material or mechanism development, the current state-of-the-art in piezoelectric actuator technology has insufficient actuation authority to enable primary control of full-scale rotor systems.

Table 4.1 highlights performance metrics of currently available actuation technologies, and these data suggest several limitations. Given the large forces and displacements required of a full-scale TEF for a helicopter main rotor, as well as the need to minimize weight, specific work output is a very useful metric for considering potential active rotor actuators. It can be seen that hydraulics present very high specific work. However, hydraulics have proven difficult to implement in rotating helicopter blades due to the requirement for leak-free, high pressure slip rings (to transfer fluid from the fixed to rotating frames) and the need to have a closed circuit system. Also note that piezoelectric actuators, the most employed actuator for helicopter trailing edge flaps to date, have very low specific work. Shape Memory Alloy (SMA) has high specific work, but unfortunately, SMA has insufficient (low) bandwidth because of its reliance on

temperature change for its actuation mechanism. SMA is also highly non-linear and susceptible to creep. Pneumatic cylinders have good specific work, and present constant force as stroke varies, and can perform bidirectional actuation with the implementation of a pneumatic H-bridge. There has been some work to date using pneumatic cylinders, also known as pneumatic servo-actuators, for actuating morphing aircraft concepts (Neal *et al.*, 2004; Poonsong, 2004; Samuel and Pines, 2007) and there are commercially available flight control systems that employ them (Brittain, 2011). However, the use of pneumatic cylinders in aerospace applications is currently fairly limited. One particular concern with using cylinders in active rotor systems is the effects of centrifugal and off axis loading on the piston rods and seals. The presence of large blade vibrations introduces further concerns with maintaining alignment of the piston components. While such issues could certainly have effective engineering solutions, the lack of a piston rod or any dynamic seals in a PAM actuator gives PAMs an intrinsic advantage for operation in this environment (de Marmier and Wereley, 2003). Furthermore, the PAM actuators under development here have an attractive combination of high specific work and bandwidth, and also operate at very low pressures compared to hydraulics. These favorable trades for PAMs suggest that this actuation technology should be considered for active rotor systems.

Table 4.1 Comparison of actuator technologies (Adapted from Huber, Fleck, and Ashby, 1997).

Actuation Technology	Max Strain	Actuation Stress (Mpa)	Specific Work (J/kg)	Max Frequency (Hz)
Hydraulic	1	70	35000	100

Solenoid	0.4	0.1	5	80
Piezoelectric	0.002	9	1	10^7
Magnetostrictive	0.002	200	20	10^7
SMA	0.07	700	4500	7
Pneumatic Cylinder	1	0.9	1200	100
UMD/TSi PAM	0.4	16	4400	100

4.1.1. ACTUATOR BACKGROUND

PAM type actuators were first conceived in the 1950's (Gaylord 1955), and have since been investigated for use in prosthetic and robotic devices (Tondu and Lopez, 1997; Lightned and Lincoln, 2002; Daerden and Lefeber, 2002). Only recently, however, have they been considered for aerospace applications (Woods *et al.* 2007; Peel *et al.* 2009, Kothera *et al.* 2010). They possess many attractive characteristics for implementation in this area. They are simple, lightweight actuators that produce high levels of force and large, usable stroke at moderate actuation pressures (< 620 kPa). For example, a 16 mm diameter, 0.2 m long PAM can generate as much as 4450 N of blocked force at 620 kPa, and will have a maximum stroke of up to 40% of its initial active length. This PAM is 20 cm long, but has only 15 cm of active length (due to the end fitting lengths), corresponding to a nominal maximum displacement of 6 cm, while having a mass of only 40 g. This PAM will therefore have a maximum specific force of over 100,000 N/kg, and a maximum specific work of 4000 J/kg.

The potential advantages of PAM actuators extend beyond their high performance levels. They are naturally compliant which makes them highly tolerant to misalignment

and impulsive loading. PAMs use pressurized air as their operating fluid, which offers several distinct advantages over hydraulics, such as the ability to eliminate the return circuit, a significantly lower fluid density (air vs. oil), and no risk of fire or explosion. Also, because air can be distributed to PAMS via flexible, lightweight, low pressure tubing, PAMs are highly amenable to distributed actuation concepts.

Figure 4.1 PAM operation and nomenclature.

PAMs consist of four basic parts: an inner elastomeric bladder (e.g., latex tubing); an outer helically braided sleeve; and a fitting at each end to seal the actuator and allow for transfer of the force and motion. The operating principle of PAM actuators is as follows. The inner bladder is inflated with air under pressure, causing an expansion of the bladder diameter. The braided sleeve around the bladder is thereby forced to expand radially; however, the fixed length of the stiff sleeve fibers generates a contractile force and displacement along the main axis of the PAM. This force and motion is transferred to the system via the end fittings. Figure 4.1 shows a PAM in both the relaxed (upper) and inflated (lower) stages.

141

Due to their contractile motion, PAMs are essentially a unidirectional actuator. If bidirectional control is desired, as in the case of a helicopter TEF, a single PAM can be operated against a spring load. In this configuration, a bias pressure is required to center the output in the middle of the operating range. A second option is replace the spring with another PAM, so that the two PAMs operate as a pair of agonist/antagonist muscles. This approach is inspired by the operation of muscles in the human body (e.g., the bicep / tricep arrangement) and has the benefit of allowing for control of both rotation of an effector about a pivot point, as well as muscle stiffness. In an antagonistic arrangement, motion in one direction is achieved by inflating the agonist PAM, while leaving its antagonist PAM free of air, to achieve motion in one direction. The roles of the agonist and antagonist are then switched. The formerly agonist PAM is deflated and becomes the antagonist. The formerly antagonist muscle becomes the agonist, which is then inflated to induce motion in the opposite direction. Antagonistic PAM configurations are the preferred choice for trailing edge flap systems because they have a neutral state (i.e., no pressure in either PAM) at the center of their output range, which creates a more graceful failure mode than the hard over neutral state of a PAM vs. spring configuration. Additionally, the antagonistic arrangement has the benefit of variable hinge stiffness by overlaying a bias pressure to both PAMs. Increased pressure equally in both PAMs increases the force in both without changing the output flap angle, causing an effective increase in hinge stiffness.

The specific design of the PAM used in this study was developed here to address the relatively short fatigue life of PAM actuators that had been presented in previous literature. Two previous fatigue tests performed on both commercially available and

custom produced PAM actuators had shown a maximum of 14,000 (Klute and Hannaford, 1998) and 17,600 (Kingsley and Quinn, 2002) cycles to failure. To increase the fatigue life to a number of cycles that would be acceptable for aerospace applications (e.g. > 120,000,000 cycles), a new manufacturing technique was developed (Woods, Kothera and Wereley, 2009), and fatigue tested (Woods *et al.*, 2010) under realistic operating conditions for 120 million cycles with no observed actuator failure. Additional research and testing of fatigue resistance are on-going.

4.2. ACTUATION SYSTEM DESIGN

The actuation system developed here was sized with two primary design goals. The first was to produce substantial high frequency flap deflections for vibration reduction. Previous work has shown the potential of a properly sized, servo-type trailing edge flap driven at 3, 4, and 5/rev to provide significant hub vibration reductions for a four bladed rotor system (Chopra, 2002; Giurgiutiu, 2000; Straub *et al.* 2004). To illustrate the promise that PAM technology has to surpass the current state of the art, this system was designed to have a level of control authority beyond what has typically been achieved. This is reflected in the design goal of ±7.5° to ±10° of flap deflection at frequencies up to 5/rev (35 Hz for the Bell 407 scale) under full-scale loading.

The second design goal was to produce even larger deflections at 1/rev to demonstrate that PAMs have great potential as primary control actuators for the main rotor. While the exact deflection levels needed for primary control are dependent on a wide range of factors including flap sizing, blade torsional stiffness, flight condition, blade index angle, etc., a review of the literature indicates that deflections in the range of ±15° to ±20° may be suitable (Straub and Merkley 1996; Falls *et al.*, 2010).

In order to meet these design goals, a combined analytical and experimental approach was taken. The trailing edge flap was chosen to be a 16% span (0.86 m), 15% chord (3.8 cm) plain flap centered at 0.83R, which is generally consistent with other active flap systems (Straub *et al.* 2004; Fulton 2000). The actuation system was designed for the full scale Bell 407, and then retrofitted into a modified Bell 407 blade tip section for testing in the Glenn L. Martin Wind Tunnel.

The basic configuration of the actuation system, shown schematically in Figure 4.2, has an antagonistic pair of PAMs mounted in an actuator cartridge at the root end of the rotor blade (Kothera, Woods and Wereley, 2010).
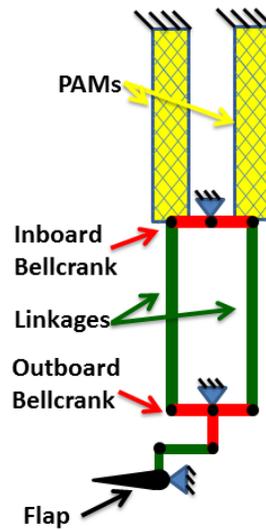
(a). PAM TEF actuation system schematic

144
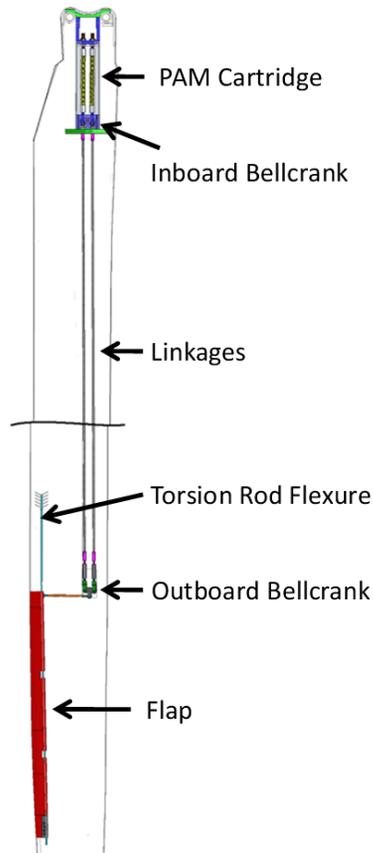
(b). PAM TEF Design Model
Figure 4.2. PAM TEF actuation system.

An inboard bell crank converts forces in the PAMs to moments about a hinge and employs kinematic relationships that increase torque output and maximum achievable deflection angle. The output torque and motion is transferred by a pair of linkages to the inboard end of the flap. These linkages are mounted inside the D-spar of the blade to minimize the structural modifications required and to keep the added mass as far forward in the chord-wise direction as possible.

At the outboard end of the linkages, a second bell crank rotates the span-wise linkage motion into chord-wise motion of a flap control rod. The flap control rod then exits the spar and the blade lower skin surface to drive an external control horn on the

flap. In order to eliminate the need for bulky thrust bearings at the thin trailing edge mounting points, a torsion rod flexure (TRF) device has been implemented. This device is similar to the "tension-torsion rod" used in the SMART rotor design (Straub 2004). The TRF is a thin rod that is aligned span-wise and anchored on the inboard end to the blade and on the outboard end to the flap. It therefore provides a direct structural connection capable of transferring the considerable centrifugal (*CF*) loads on the flap into the blade structure without the need for thrust bearings. Additionally, this device is designed to have minimal torsional stiffness, so that deflections of the flap may be achieved through elastic twisting of the TRF. Note that in Figure 4.2 the center blade span portion was removed to allow for greater detail of the inboard and outboard components.

4.2.1. PERFORMANCE ANALYSIS

A quasistatic torque balancing performance analysis of the flap system was developed that allowed for the effects of different system parameters on output flap deflections to be considered. This analysis was used for the initial design of the TEF system to optimize various actuation system parameters, including PAM initial braid angle, active length, bell crank geometry, etc. The system was sized to achieve 1/rev deflections on the order of $\delta = \pm 20°$ under full scale loading for a Bell 407 scale rotor in hover. The optimal configuration uses PAMs with an outer diameter of 1.6 cm, an initial active length L_0 of 23 cm, an initial braid angle of 61° (defined from the radial direction), and an initial moment arm of 1.6 cm.

In addition to system sizing, the performance analysis is useful for comparing predictions to experimental results. A comparison is made for the wind tunnel test

performed here in the results section. As will be shown, results from the wind tunnel testing showed that the system was able to obtain quasistatic levels of deflection up to fairly high frequencies. The basic methodology of this model will therefore be presented.

4.2.1.1. PAM Force Analysis

The output force and displacement characteristics of the PAM actuators needed to be known for various actuator geometries in order to select the appropriate PAM design variables for the given loading condition. While this system was initially sized using experimental data from an array of different PAM geometries (Woods, Kothera and Wereley, 2010), progress has been made in successfully modeling the force versus displacement curves of arbitrary PAM geometries to the extent that this model is now a valid design tool. The analysis used here is adapted from Kothera *et al.* (2009), and is based on a series of modifications - to the well-known Gaylord force term - that account for various energy storage mechanisms in the PAM. Thus, the total PAM actuator force, F, is the linear combination of four force components: (1) Gaylord force, F_G, (2) Elastic force due to bladder deflection, F_b, (3) Elastic force due to sleeve deflection, F_s, and (4) a nonlinear Coulomb friction term, F_f, to account for observed hysteresis effects.

Effective Active Length

Normally, the active length is defined as the length of the actuator between the end fittings. However, the active actuator length, L_i, must be modified in order to account for the non-cylindrical ends of the PAM when inflated. Essentially, the radius is fixed where the bladder/sleeve exits the swaged fitting as in Figure 1. In the inflated state (bottom of Figure 1), the PAM increases its radius to a maximum value. The net effect is a reduction in the effective active length of the actuator, which can be estimated as

147

follows.

First, the longitudinal cross-section of this actuator along this transition region is assumed to have a radial arc. An arc angle of $\pi/2$ and an arc radius equal to the inflated actuator radius, r_i, minus the initial actuator radius upon exiting the swaged fitting, r_0, are used. The arc length s_t of one transition region will therefore be:

$$s_t = (r_i - r_0)\frac{\pi}{2} \tag{1}$$

The axial length x_t of the same transition region will be equal to the arc radius:

$$x_t = r_i - r_0 \tag{2}$$

The difference ΔL between arc length and axial length of one end transition will be:

$$\Delta L = \left(\frac{\pi}{2} - 1\right)(r_i - r_0) \tag{3}$$

Because there are two end fittings, this correction factor is doubled and subtracted from the inflated active length (to account for both end fittings) to yield an effective active length of

$$\hat{L}_i = L_i - 2\Delta L = L_i - 2\left(\frac{\pi}{2} - 1\right)(r_i - r_0) \tag{4}$$

This effective active length $\hat{L}_i$ is used instead of L_i in the derivation of the force components of the PAM performance model.

Gaylord Force Component

The force component attributed to Gaylord (1955) is derived using the equation

148

$$F_G = P\frac{dV}{dL} \tag{5}$$

Solving the above equation leads to

$$F_G = \frac{P}{4N^2\pi}\left(3\hat{L}_i^{\,2} - B^2\right) \tag{6}$$

Here, the force generated by the actuator, F_G, is proportional to the internal gauge pressure P and the rate of change in internal volume V with changing length L. By assuming the resting and inflated actuator are both cylindrical in shape, but with different radii and lengths, the change in internal volume with changing length can be defined in terms of the current effective active length $\hat{L}_i$, the length of a single braid filament B, and the number of turns made by a single filament between its two ends, N, as above.

Bladder Elastic Energy Force Component

The second term in the model accounts for elastic energy stored in the bladder. Klute and Hannaford (2000) proposed a model of the elastic energy stored in the rubber bladder, that is,

$$F_b = V_b\frac{dW_b}{dL} \tag{7}$$

In Kothera *et al.* (2009), this term was expanded using Mooney-Rivlin non-linear elasticity theory (Treloar 1975) as below:

$$
\begin{aligned}
F_b &= V_b\left\{2C_{10}\left[\lambda_1\frac{d\lambda_1}{dL} + \lambda_2\frac{d\lambda_2}{dL} + \lambda_3\frac{d\lambda_3}{dL}\right]\right.\\
&\quad \left. + \ 2C_{01}\left[\lambda_1(\lambda_2^2 + \lambda_3^2)\frac{d\lambda_1}{dL} + \lambda_2(\lambda_1^2 + \lambda_3^2)\frac{d\lambda_2}{dL} + \lambda_3(\lambda_1^2 + \lambda_2^2)\frac{d\lambda_3}{dL}\right]\right\}
\end{aligned} \tag{8}
$$

The coefficients C_{10} and C_{01} are the Mooney-Rivlin constants for the non-linear elasticity of the latex bladder material. For this study, values of $C_{10} = 133$ kPa and $C_{01} =$

149

118 kPa were used.

The strain invariants used in this formulation are defined as:

$$\lambda_1 = \frac{\hat{L}_i}{L_0} \tag{9}$$

$$\lambda_2 = \frac{r_i - t_i/2}{r_0 - t_0/2} \tag{10}$$

$$\lambda_3 = \frac{t_i}{t_0} \tag{11}$$

Coulomb Friction Force Component

PAM actuators typically show a non-negligible amount of hysteresis in their operation due to friction between the various actuator components as they slide over each other. Friction is present between the braided sleeve and bladder, and between the different filaments of the braided sleeve. The frictional forces oppose the motion of the actuator, and therefore have a sign dependent on the velocity. The effect of this on PAM performance is a reduction in force available during contraction and an increase in force required during extension. A Coulomb friction model (Olsson *et al.* 1998) was used to capture the dependence on direction of motion. In this model, the sign of the frictional force is opposite that of the actuator velocity, with motion that shortens the actuator being defined as having positive velocity. Examination of the experimental data showed that the magnitude of the friction was generally dependent on the magnitude of the force in the actuator. The friction force is therefore defined as in Equation $sgn(V)$ (12 to be proportional to the nominal force estimated from the other three model terms through the friction factor k_f. Note that k_f is different from a typically defined coefficient of friction because the force referenced is the axial actuator force, not the normal force. This k_f is

150

empirically fit to the data so that it captures all of the various friction mechanisms. While other work in the literature (Davis and Caldwell 2006) has explored friction effects on a micromechanical level, this simple model worked well here as a means of predicting PAM forces and thereby PAM TEF system output. For the PAM geometry used here, the factor k_f was found to be 0.12, indicating that the frictional force is roughly 12% of the nominal actuator force.

$$F_f = -k_f(F_G + F_b - F_s)sgn(V) \tag{12}$$

PAM Actuator Force

Thus, the total force in the PAM, F, is then defined as:

$$F = F_G + F_b - F_s + F_f \tag{13}$$

This model is used to predict PAM forces during the two distinct operating regimes seen in this antagonistic system: the active state (pressurized contraction) and the passive state (neutral extension). The active state force is referred to as F_a and the passive force as F_p. It is interesting to note that while all four model terms affect the forces seen during pressurized contraction, when the gauge pressure is zero; both the Gaylord force component, F_G, and the braided sleeve elastic energy force component, F_s, become zero. As will be seen, the two remaining terms still effectively capture the neutral extensional stiffness of the actuator.

4.2.1.2. PAM Force Model Validation

Comparing this force prediction model to experimental results shows good agreement. Figure 4.3 shows the experimentally measured force versus displacement behavior for the PAM geometry chosen for this TEF system. Five different operating

151

pressures of 0, 0.048, 0.097, 0.15, and 0.19 MPa are shown. The 0 MPa data represent the neutral extension of the passive actuator in the antagonistic PAM arrangement. Note that the modeled force captures the general shape of the passive stiffness well, although there is an apparent lateral shift that is believed to be the result of initial extension in the experimental data that was not recorded at the time. Here the extensional (higher force) side of the hysteresis loop in the model falls almost directly on top of the contractile (lower force) side of the experimental data. The four different active force load lines show the ability of the model to account for changes in force due to pressure and to contraction. Note that the hysteresis in the experimental data decreases as the force in the actuator decreases, as mentioned above in the formulation of the friction model term. The model is deemed to be sufficiently accurate for first order design and analysis of the PAM TEF system.
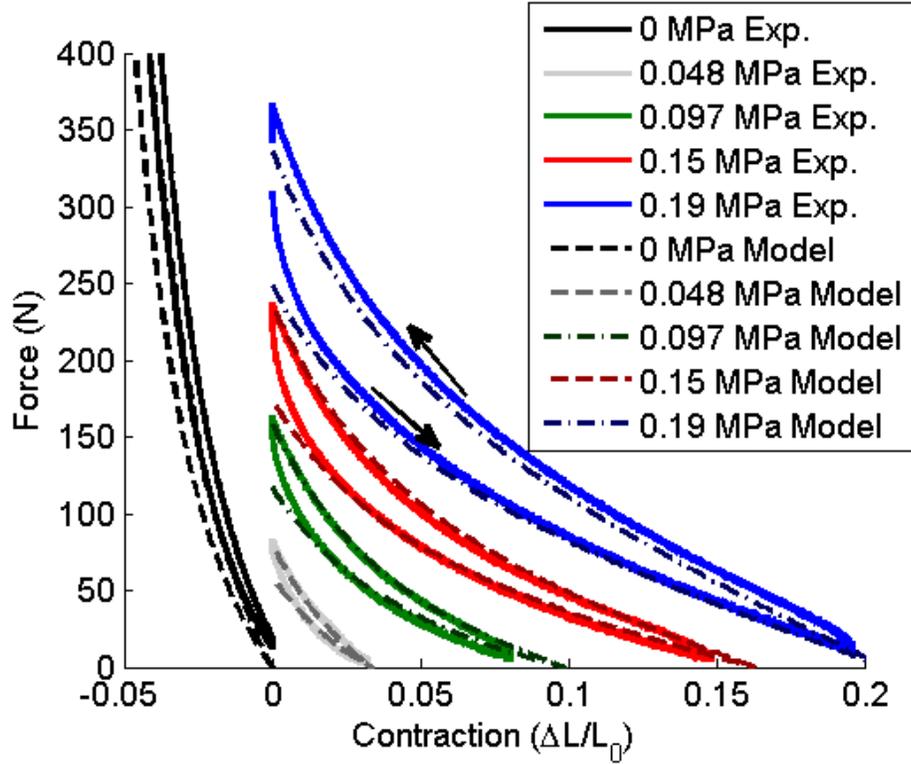
Figure 4.3. PAM force model validation.

4.2.1.3. Aerodynamic Hinge Moment Estimation

With the force in the pressurized PAMs known, the next step in developing the design model was to predict the magnitude of the aerodynamic hinge moments that would need to be overcome to deflect the flap. The total aerodynamic hinge moment H was defined as an integral over the flap span (r_1 to r_2) in terms of a hinge moment coefficient c_h, the dynamic pressure q, and the geometric flap chord c_f as:

$$H = \int_{r1}^{r2} \left(q(r) c_f(r)^2 c_h(r) \right) dr \tag{14}$$

In an approach adopted from thin airfoil theory (Abbott and Von Doenhoff 1958), the moment coefficient is defined as the summation of two separate effects. These include moment due to the lift coefficient of the airfoil and moment due to the flap

deflection itself:

$$c_h = c_l(r) \left(\frac{\partial c_h}{\partial c_l} \right) + \delta \left(\frac{\partial c_h}{\partial \delta} \right) \qquad (15)$$

The lift curve slope is based on the 2D airfoil theory result with the Glauert compressibility correction added (Abbott and Von Doenhoff 1958).

$$a = \frac{2\pi}{\sqrt{1-M^2}} \qquad (16)$$

Jacobs and Pinkerton (1931) formulated the lift coefficient for a flapped airfoil as below:

$$c_l(r) = a[\alpha(r) + k_\delta \delta] \qquad (17)$$

In this instance, the lift coefficient $c_l(r)$ varies along the span due to the twist present in the blade. The local angle of attack at each span station is a combination of global blade pitch angle θ_0 and local blade twist $\Delta\theta(r)$, referenced from the global angle:

$$\alpha(r) = \theta_0 + \Delta\theta(r) \qquad (18)$$

The lift coefficient also varies due to the impact of flap deflections. This effect is described by Jacobs and Pinkerton (1931) and is represented as a proportional increase in lift coefficient with increasing flap deflections through a proportionality constant k_δ. Thin airfoil theory is used to derive an expression relating k_δ to the non-dimensional flap chord, $E = c_f/c$ (Jacobs and Pinkerton 1931), as below:

$$k_\delta = \frac{cos^{-1}(1-2E)+2\sqrt{E(1-E)}}{\pi} \qquad (19)$$

Experimental values of the two terms $\partial c_h/\partial c_l$ and $\partial c_h/\partial \delta$ in Eq. (15) were not available for the proprietary airfoils used on the Bell 407. Instead, a symmetric airfoil

approximation developed in Jacobs and Pinkerton (1931) from incompressible thin airfoil theory was used. These two quantities are defined as a function of the non-dimensional chord of the flap E as shown below:

$$\frac{\partial c_h}{\partial c_l} = -\frac{1}{\pi E^2}\left[\left(\frac{3}{2}-E\right)\sqrt{E(1-E)} - \left(\frac{3}{2}-2E\right)\left(\frac{\pi}{2}-cos^{-1}\left(\sqrt{E}\right)\right)\right] \quad (20)$$

$$\frac{\partial c_h}{\partial \delta} = -\frac{4(1-E)\sqrt{E(1-E)}}{\pi E^2}\left[\frac{\pi}{2}-cos^{-1}\left(\sqrt{E}\right) - \sqrt{E(1-E)}\right] \quad (21)$$

For the 15% chord flap used in this study ($E = 0.15$), these factors are equal to −0.068 and −0.698, respectively. These values are for a plain flap with no aerodynamic balance. Many previous active rotorcraft flap systems have used aerodynamic balance to minimize control moments for their actuation systems, at the cost of an increased drag coefficient during deflection (Straub and Merkley 1996, Falls *et al.* 2010). Given the high output torques and deflections of the PAM TEF system, aerodynamic balance was not employed in the present study, thereby minimizing the drag associated with flap deflections.

The total hinge moment was found by numerically integrating the local hinge moments over the 0.86 m flap span to allow for the changes in both blade pitch angle and blade chord along the span. This total hinge moment is therefore what the PAM actuation system must produce.

4.2.1.4. Torque Balancing

With the aerodynamic hinge moments known, the quasistatic flap output capability of the actuation system against this loading was found using a torque balancing approach.

The net torque available at the first bell crank from the actuators is found by multiplying the active PAM force F_a by its moment arm l_a, then subtracting the passive PAM force F_p multiplied by its moment arm l_p. The final output torque available is the torque at the first bell crank times the mechanical advantage, MA, of the linkage system, as below:

$$T_{available} = (F_a l_a - F_p l_p)MA \qquad (22)$$

Note that all of these parameters change with deflection due to the force vs. displacement characteristics of the PAMs and the kinematics of the attachments between the PAMs and bell crank.

Figure 4.4 shows how the equilibrium flap deflection angle is calculated. The torque available decreases with flap deflection due to the drop in active PAM force and increase in passive PAM force. The torque required increases with flap deflection due to the increasing aerodynamic hinge moments. The point at which the torque available crosses the torque required load line is the equilibrium flap deflection angle for the given condition. This figure shows that approximately 19° of TEF deflection can be achieved.
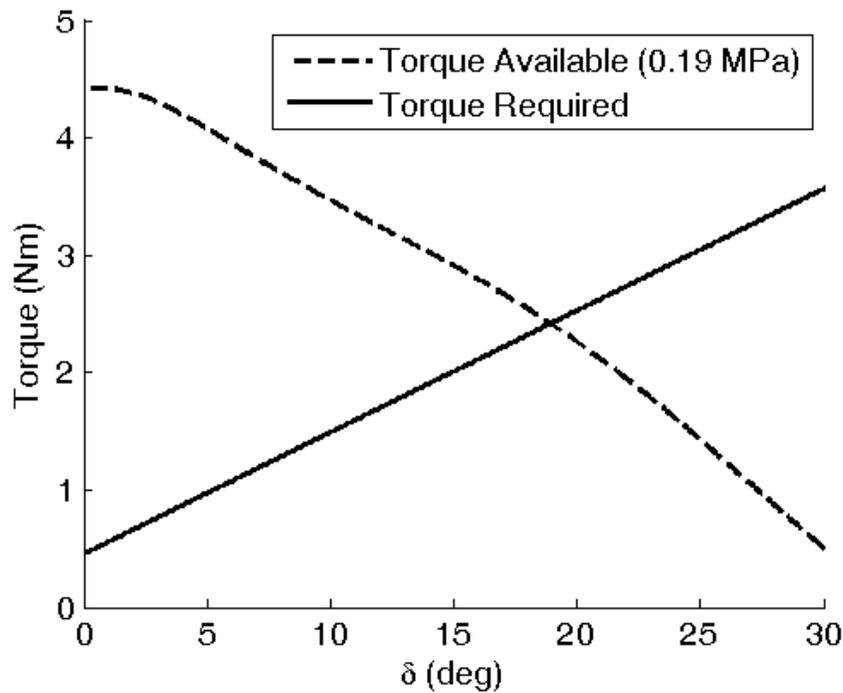
Figure 4.4. Predicted quasistatic system performance for $M = 0.3$, $P = 0.19$ **MPa,** $\theta_0 = 6°$.

4.3. WIND TUNNEL TEST ARTICLE DESIGN

Building the wind tunnel test article consisted of retrofitting the PAM TEF actuation system and a custom built trailing edge flap into a Bell 407 blade. The full blade span could not fit into the wind tunnel, so that the outer 1.55 m of the blade span was cantilevered from the floor of the wind tunnel. This portion of the blade includes the 0.86 m flap span, the blade tip, and an added margin on the inboard end of the flap to isolate the flapped portion from the boundary layer on the floor of the tunnel. The full span design places the PAM actuator cartridge inside the root of the blade, but since this portion was not present, the cartridge was instead mounted below the tunnel floor and connected to the flap with shortened linkages. Cable stays were added to the cantilevered blade tip to increase bending stiffness since the CF stiffening normally seen in rotating

helicopter blades (Leishman 2000) would not be present. These cables were anchored outside the tunnel to arms connected to the balance, so that the blade loads resolved through the cable were included in the balance measurements.

A schematic of the test article can be seen in Figure 4.5. Here the design model of the article is shown next to the assembled version installed in the tunnel. Both are viewed from behind and slightly above the blade. The flap can be seen in both, and the actuator cartridge is visible below the floor in the design drawing. The design drawing also shows the C-channel cradle and vertical posts used to anchor the model to the balance while providing clearance for the PAM cartridge.
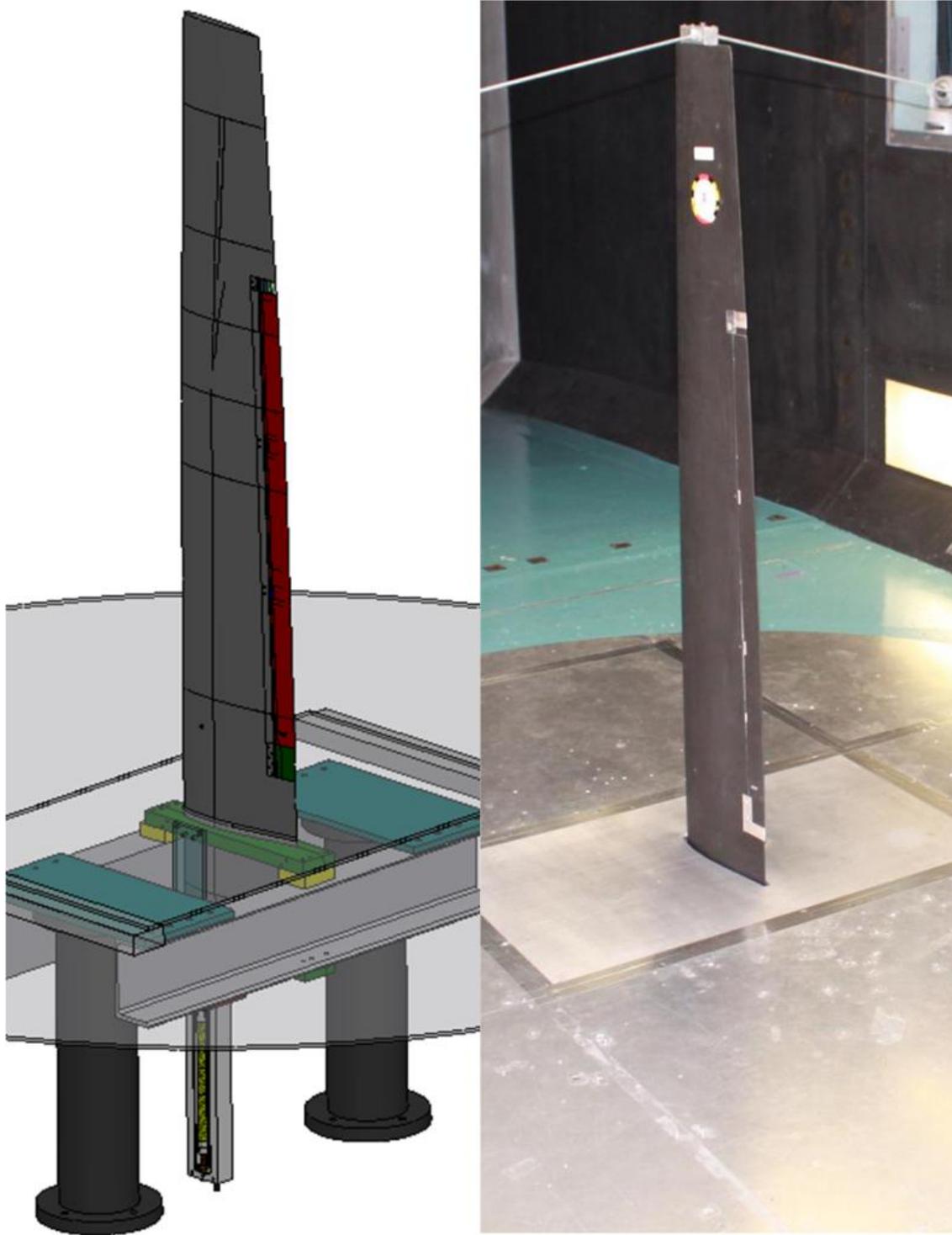
Figure 4.5. Wind tunnel test article, design model and as built.

4.3.1.   BLADE MODIFICATIONS

Significant modifications were made to the blade to allow for integration of the

flap and actuation system. First, a female mold was made around the trailing edge of the unmodified blade in the flap region to capture the airfoil shape, twist, and taper that would need to be recreated in the flap. Layers of fiberglass and carbon fiber were built up on top of the blade, with a piece of release film between the blade and mold. Vacuum pressure was applied during cure to ensure good consolidation. This mold accurately captured the geometries of the upper and lower surfaces of the flap, but it did not have the desired leading edge radius. Therefore a second, mating mold was needed. To create this component, hot-wire cut foam blanks having the desired leading edge radius (which varies along the flap span) were laid into the trailing edge mold. This foam core was then covered in release film and a second carbon fiber and fiberglass mold was built up on top, and again cured under vacuum pressure.

With construction of the mold complete, the flap itself was made from carbon fiber biaxial braided sleeving that was pulled tight over a hot-wire cut foam core. The foam core was created from four sections of extruded polystyrene foam, which were cut with linear approximations to the twist and taper derived from a three dimensional design model of the blade. Dividing the blade length into four sections allowed the varying linear twist of each section to closely match the actual non-linear twist distribution of the blade. Rapid prototyped plastic inserts were bonded in with the foam core at key structural hard points to provide for more effective distribution of loads. This core was then covered with two plies of 3k carbon fiber braided sleeve, wetted out with West Systems epoxy and pulled tight over the core. The assembled flap was then wrapped in release film and placed in the two part mold. Consolidation pressure was provided by cutting the foam slightly oversized, so that insertion into the mold required compression

of the core, creating a compressive pressure on the braided sleeve surface.

With the flap complete, a section of the blade trailing edge was removed to accommodate the flap and its mounts. The open trailing edge of the blade was reinforced with an internal composite C-channel referred to as a Trailing Edge Close Out (TECO), shown schematically in Figure 4.6, which recreated a closed section aiding torsional stiffness of the blade. The shape of this TECO was also designed to allow for flap supports to slide into the rear of the blade and bolt in place. A total of four flap supports were included, one at each end and two equally spaced between the ends.
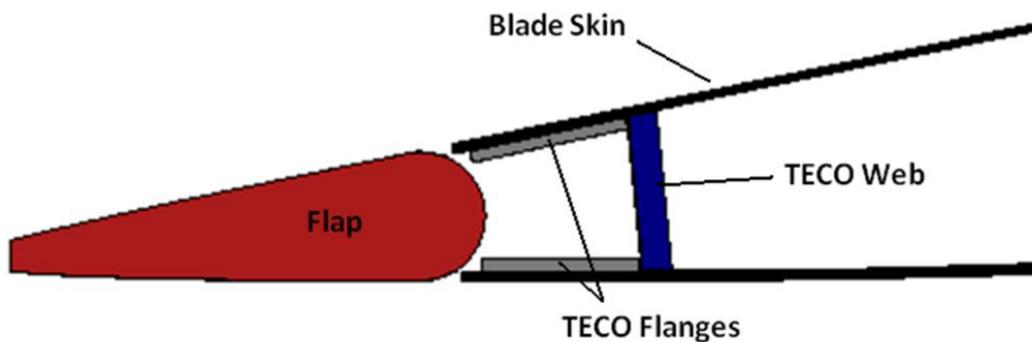
Figure 4.6. Trailing edge close out (TECO) concept.

The Torsion Rod Flexure that is used in the design concept to transfer the CF loading on the flap into the blade was not included in this wind tunnel model due to the lack of any CF loading on the cantilevered blade tip. The efficacy of this design element has been proven in other related work (Woods, Kothera, and Wereley 2010), as well as in the Boeing SMART rotor program (Straub 2004). Instead the flap was connected to its mounts via stainless steel pins rotating in PEEK plastic bushings, which included flanged

features to accommodate spanwise loads created by the vertical orientation of the blade during testing.

An access hatch, visible in Figure 4.7, was cut through the D-spar on the underside of the blade to allow for installation of the outboard bellcrank and the turnbuckles used to tighten the linkages. This hatch was designed to be as small as possible, and aluminum inserts were bonded into the spar to provide a structural carry-through so that the hatch would still carry bending loads when bolted in place. An additional small hole was cut through the vertical web of the D-spar for the control rod. A slot in the lower surface skin, again visible in Figure 4.7, was cut to allow passage of the control rod out to the control horn on the inboard edge of the flap.
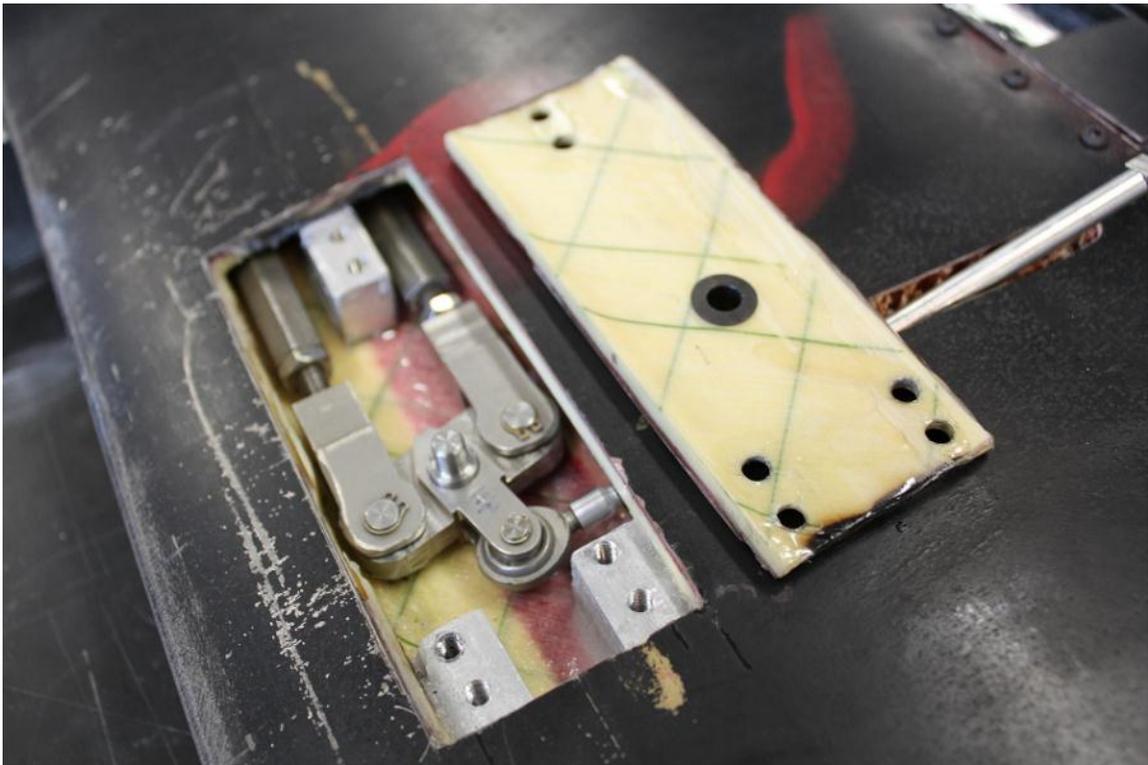
Figure 4.7. Access hatch on underside of blade at inboard end of flap.

4.3.2. INSTRUMENTATION

The wind tunnel model was instrumented with a suite of sensors to track various system response parameters over the range of tests performed. An overview of the sensors used and their locations is given in Table 4.2.

Table 4.2. Instrumentation details for wind tunnel test.

Measurement Type	Measurement Location	Units	Sensor Type
Pressure	Supply line	MPa	1.4 MPa transducer
Pressure	PAM 1 inlet	MPa	1.4 MPa transducer
Pressure	PAM 2 inlet	MPa	200 psi transducer
Deflection	Inboard flap edge	deg	Hall effect
Deflection	Outboard flap edge	deg	Hall effect
Force	PAM 1	N	4500 N load cell
Force	PAM 2	N	4500 N load cell
Control Voltage	Proportional valve	V	Direct voltage

The upstream line pressure was recorded using an Omega PX-209. The control voltage given to the pneumatic control element, a FESTO MPYE-5-1/8-HF-010-B proportional spool valve, was recorded. The time varying pressures created in each PAM due to the action of the spool valve were also recorded using Omega PX-209 transducers. These pressure transducers could not be installed inside the actual PAMs, but mounting them as close as possible gives a good approximation of internal operating pressure. To record the forces seen in the PAMs, two Honeywell Sensotec Model 31, 4500 N load cells were installed between the outboard end fittings of each PAM and the inboard bell crank.
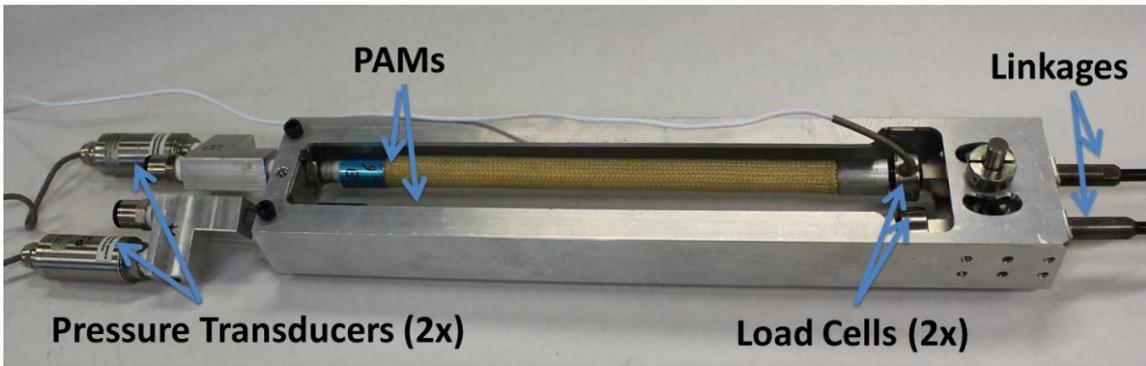
Figure 4.8. PAM actuator cartridge

Figure 4.8 shows the PAM actuator cartridge before installation into the test article. The positioning of the pressure transducers and load cells can be seen relative to the PAMs. The output flap deflections were recorded using two custom built Hall effect angle sensors. One of these sensors was mounted at the inboard end of the flap, and the other at the outboard end. This allowed for measurement of any torsional deflections along the flap span. The small thickness of the trailing edge near the flap prevented the use of commercially available sensors, so custom sensors were developed that use a F.W. Bell FH-301 Hall effect sensor mounted in the blade trailing edge, which records the changes in Hall voltage seen due to rotation of permanent magnets embedded in the flap. Each sensor uses two magnets mounted in the leading edge of the flap at the desired span station. Figure 4.9 shows the inboard end of the flap with magnets installed. These magnets are mounted at $\pm 30°$ from $\delta = 0°$ with opposite magnetic poles exposed on the leading edge. The Hall effect sensor is then mounted inside the trailing edge of the blade such that it is centered between the two magnets. The fields from the two magnets roughly cancel out at $\delta = 0°$, producing nearly zero volts output from the Hall sensor. Rotation of the flap in one direction creates a positive voltage and rotation in the other direction creates a negative voltage due to the different pole orientations. This allows for

measurement of flap magnitude and direction.

Figure 4.9. Inboard flap end with embedded angle sensor magnets

The calibration curves for the two angle sensors can be seen in Figure 4.10. Note that there is a voltage offset between the two curves due to small differences in the mounting position of the Hall sensors. These custom sensors produce a monotonic voltage output over the full desired measurement range of $\delta = \pm 24°$. Fourth order polynomials were fit to the calibration curves for interpolation of output angle data.
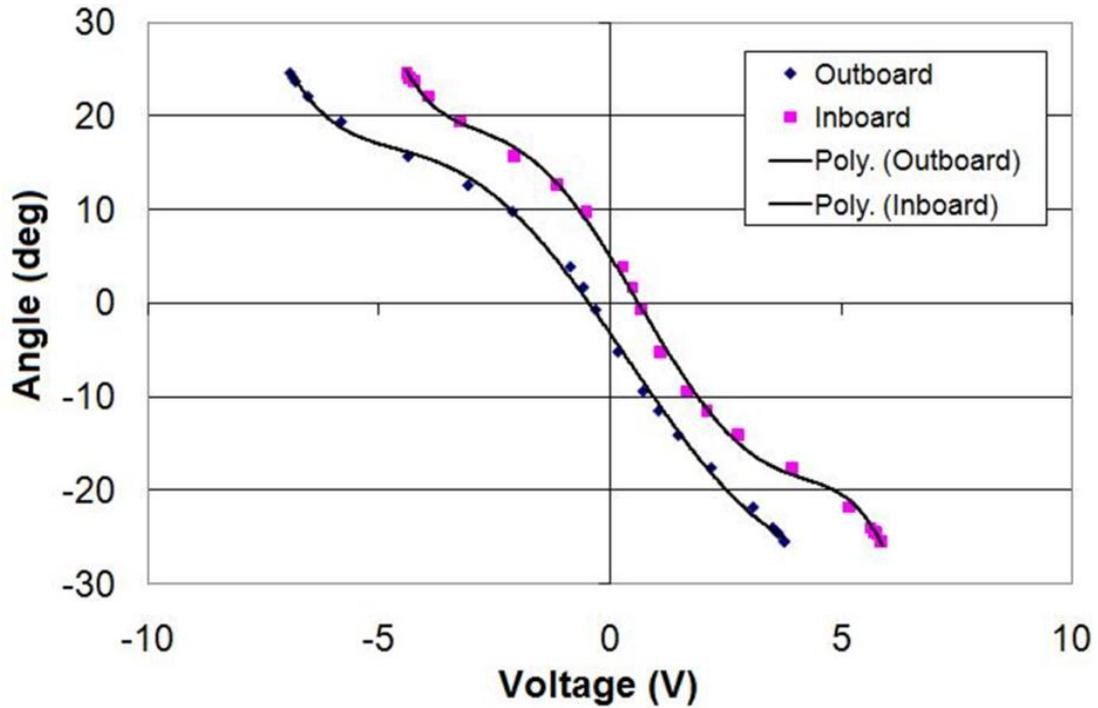
Figure 4.10. Angle sensor calibration curves

4.4. RESULTS AND DISCUSSION

The wind tunnel testing focused on four key aerodynamic and actuation system parameters: blade pitch angle θ_0, Mach number M, actuation pressure level P, and actuation frequency f. A wide range of values was tested for each, as listed in Table 4.3 to fully characterize system response up to the maximum tunnel speed. In total 3,300 data sets were collected over three days of wind tunnel testing.

Table 4.3. Wind tunnel test parameters.

Test Parameter	Test Values
Blade Pitch, θ_0, (deg)	-6, -3, 0, 3, 6, 9
Mach Number, M	0, 0.09, 0.18, 0.25, 0.3

Pressure, P (MPa)	0.048, 0.097, 0.15, 0.19
Frequency, f (Hz)	0.5, 7, 14, 21, 28, 35, 42, 49, 56

The range of blade pitch angles tested was meant to encompass a range relevant to what would be seen in a Bell 407 rotor in hover. To this end, the magnitudes of blade pitch tested were smaller than the collective pitch range of the Bell 407 to account for the lack of inflow in this non-rotating test. The intention here was to match the effective angle of attack range.

For the full scale $M = 0.56$ hover condition discussed above, the system was designed to operate at an actuation pressure of 0.62 MPa. Under the reduced loading of the wind tunnel test performed here, lower actuation pressure levels were tested to reflect the reduced aerodynamic loading. The wind tunnel test article was equipped with mechanical over-travel stops at $\delta = \pm24°$, so operating at full scale pressures would have resulted in excessive banging and impulsive loading into these stops. Due to the non-linear scaling of aerodynamic hinge moment with airspeed, operating at $M = 0.3$ represents roughly 30% of the full-scale aerodynamic loading. PAM force output scales linearly with pressure, so the maximum operating pressure tested was chosen to be 30% (0.19 MPa) of the full scale design value (0.62 MPa), thereby scaling the PAM forces to levels appropriate to the wind tunnel loading.

The proportional spool valve was driven over a range of frequencies to quantify the response bandwidth of the system. The frequencies tested are listed in Table 4.3; the 0.5 Hz case creates an essentially quasistatic response, while the other frequencies are the harmonics of the main rotor rotation frequency (7 Hz), from 1/rev to 8/rev. The response

at 1/rev was of interest for primary control of the rotor system. Deflections at 3/rev, 4/rev, and 5/rev were of interest for vibration reduction for this four bladed rotor system. Testing was also performed at higher frequencies to investigate an expected tail-off in performance due to the available peak pneumatic flow rate. The spool valve was driven by a sinusoidal control voltage with an amplitude of 5 V and a DC offset of 5 V. This valve creates an orifice area that is proportional to input voltage. It also switches between the two PAMs, such that PAM #1 is pressurized when the control voltage is less than 5 V, and PAM #2 is pressurized when the control voltage is greater than 5 V. Since this valve controls orifice area and not pressure, the time history of pressure seen in the PAM, and thus the output force, is not generally sinusoidal.

The first set of results presented is the magnitude of flap deflections as a function of frequency. Figure 4.11 shows results from the four test variable ranges (f, P, M, and θ_0). For each set of data, the maximum tested condition for the frequency sweeps is shown. That is, the effect of pressure is shown at maximum free stream velocity ($M = 0.3$) and maximum blade pitch ($\theta_0 = 9^\circ$), the effect of blade pitch is shown at maximum velocity and maximum pressure ($P = 0.19$ MPa), and the effect of velocity is shown at maximum pressure and blade pitch.
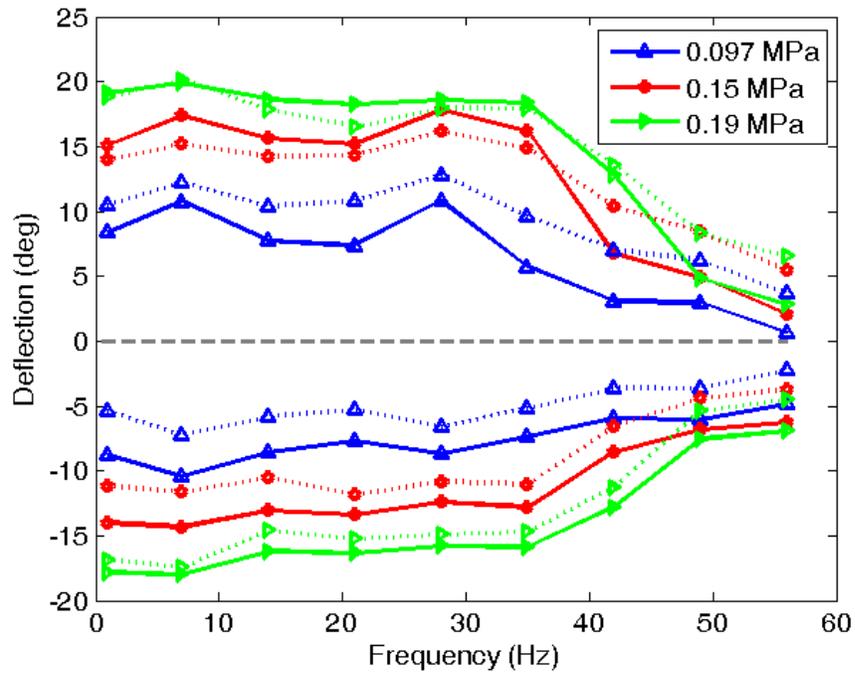
(a). pressure sweep at $M = 0.3$, $\theta_0 = 9^o$
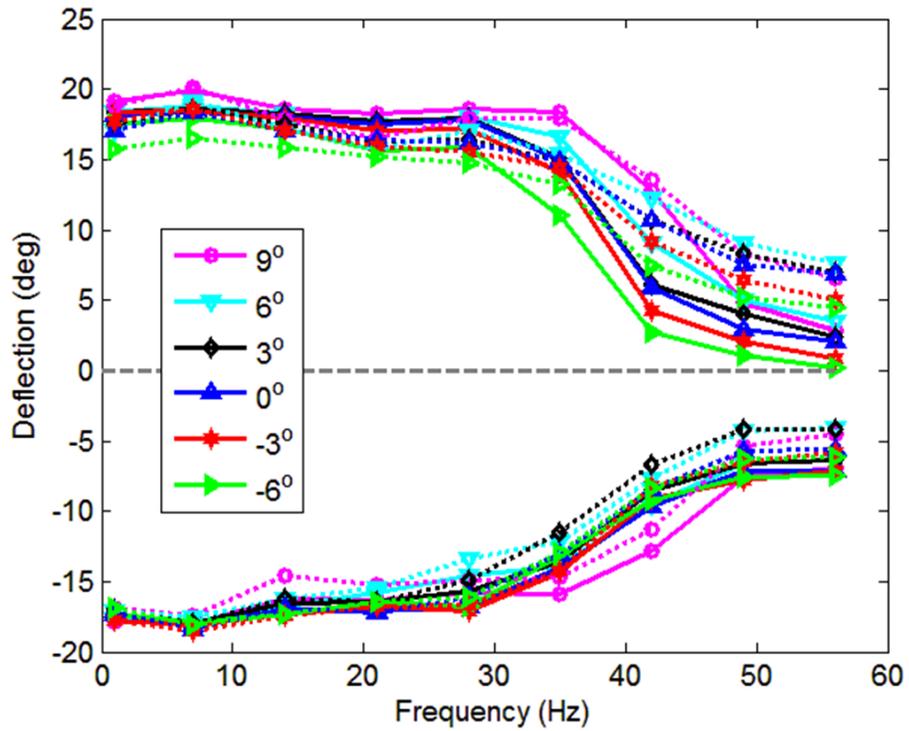
(b). angles of attack sweep at $M = 0.3$, $P = 0.19$ MPa

169
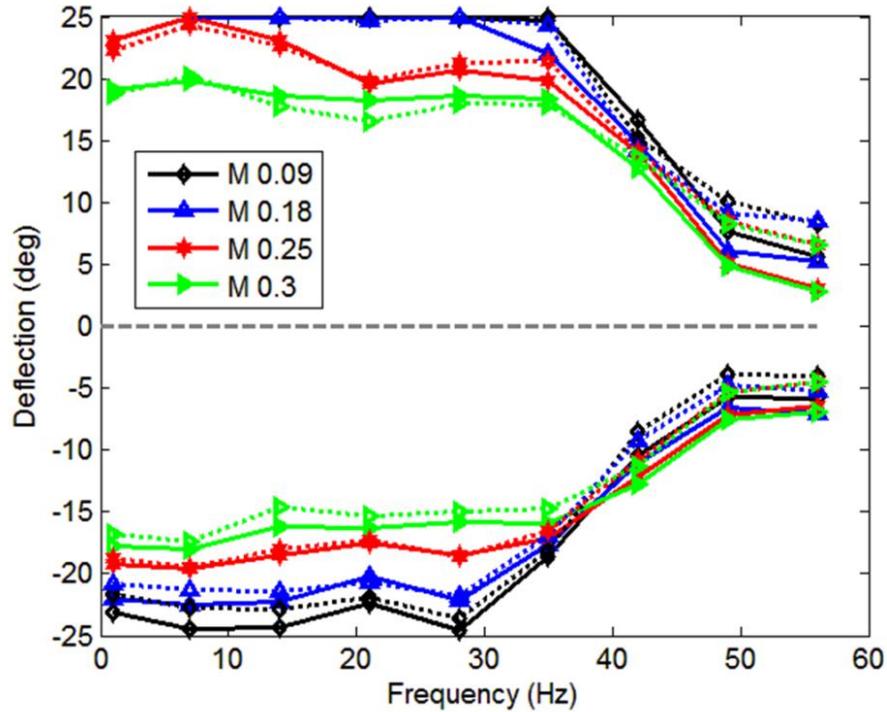
(c). Mach number sweep at $P = 0.19$ MPa, $\theta_0 = 9^o$

Figure 4.11. Flap deflection angle results

Several actuation cycles were measured at each of the noted test conditions and the results shown represent the average peak values taken over the duration of each test point, with a few cycles (3) immediately at the start of each test excluded due to transient behavior. A second-order, repeated-root, low pass filter with a corner frequency of 300 Hz was also applied to the data during post-processing to remove excess noise from the measurement signals. In each of the plots to be shown, there is a solid line and a dotted line corresponding to each symbol and color in the legend. The solid line denotes the response of the inboard angle sensor, while the dotted line denotes the outboard angle sensor measurements. Note that PAM #1 deflects the trailing edge flap in the downward (positive) direction and PAM #2 deflects the flap in the upward (negative) direction.

In terms of actuation pressure variation for a given test condition, Figure 4.11a

170

shows the expected trend that higher pressure levels lead to higher deflection angles. Also of interest in this figure is that the quasistatic deflection angle is maintained nearly constant for up to 28-35 Hz, so that the high levels of output seen at 1/rev are still available out to nearly 5/rev, indicating a large control authority for vibration reduction. Figure 4.11b shows performance trends in relation to the blade pitch angle, where the deflection angles are lowest at the extremes ($\theta_0 = +9^o$ and -6°) when the aerodynamic load is highest, and the middle of the range shows the highest deflections since the aerodynamic load is the lowest. This same trend is again seen in Figure 4.11c for the effect of Mach number, with higher speeds resulting in lower achievable angles, which is seen at least up to the roll-off point of 28-35 Hz where all the data begins to coalesce.

The roll-off seen in all three of these plots is a result of the peak available flow rate in the pneumatic supply system. For a given operating pressure, the peak flow rate is fixed, so that a finite amount of time is required to inflate and exhaust the active (agonist) and passive (antagonist) PAM, respectively. Hence, as the operating frequency increases, the system performance begins to become limited as neither full inflation nor exhaustion is fully achieved.

In addition to the flap deflection magnitudes, it is also informative to look at the phase lag present in the system under different operating conditions. Figure 4.12 shows the frequency response function for the $M = 0.25$, $\theta = 6°$ loading case with three different actuation pressures. The upper plot is the magnitude response for the flap deflection output over the input signal voltage to the spool valve. Note that the spool valve inputs were sinusoidal waves of varying frequency but constant magnitude ($0 - 10V$) and constant phase angle. The lower plot of Figure 4.12 shows the evolution of phase

response with frequency for the three different pressures. Note that there is an increase in phase lag with frequency. This is a result of the delay time present in the pneumatic supply system, that is the finite amount of time required between command signals to the valve and response of the PAM actuators. This effect, along with a control system which effectively compensates for it, is discussed in detail in Woods *et al.* 2011.
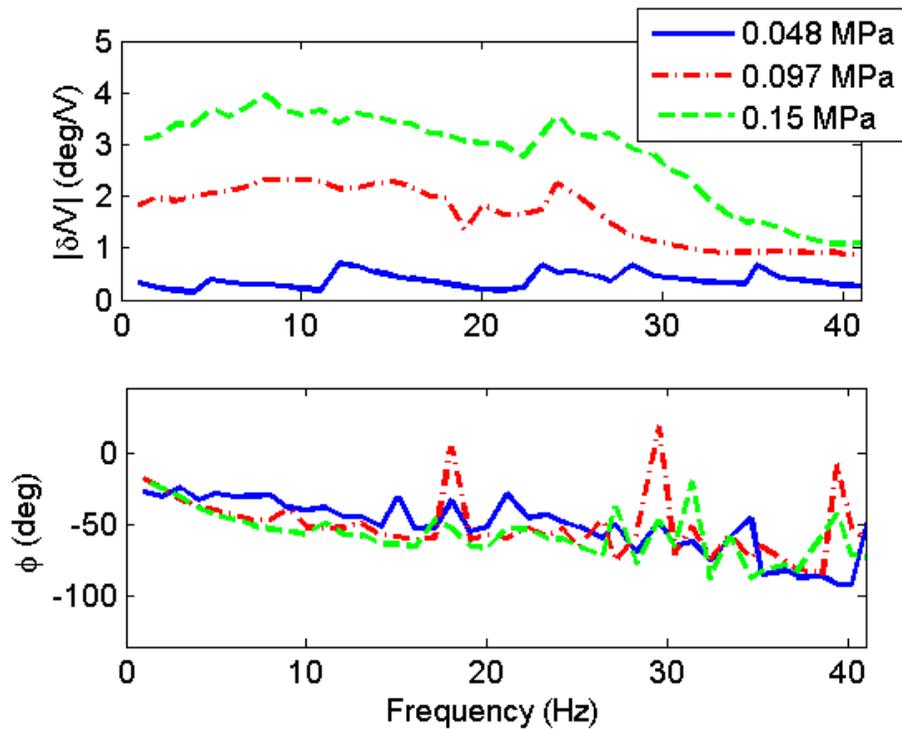
Figure 4.12. Frequency response functions for flap deflection; magnitude and phase.

A good overview of system performance can be seen in Figure 4.13. Here the half-peak-to-peak (hpp) flap deflections obtained under the highest aerodynamic loading tested ($M = 0.3$, $\theta_0 = 9°$) are shown as a function of operating pressure. Here it can be seen that with a system operating pressure scaled to match the maximum loading levels of this wind tunnel (i.e. 30% of full scale pressure for 30% of full scale loading), the system has a large control authority across the entire bandwidth of interest. At the 1/rev

172

main rotor frequency of 7 Hz, the system is capable of 18.8° hpp. This level of performance is maintained out to 5/rev (35 Hz), with 17.1° hpp still available.
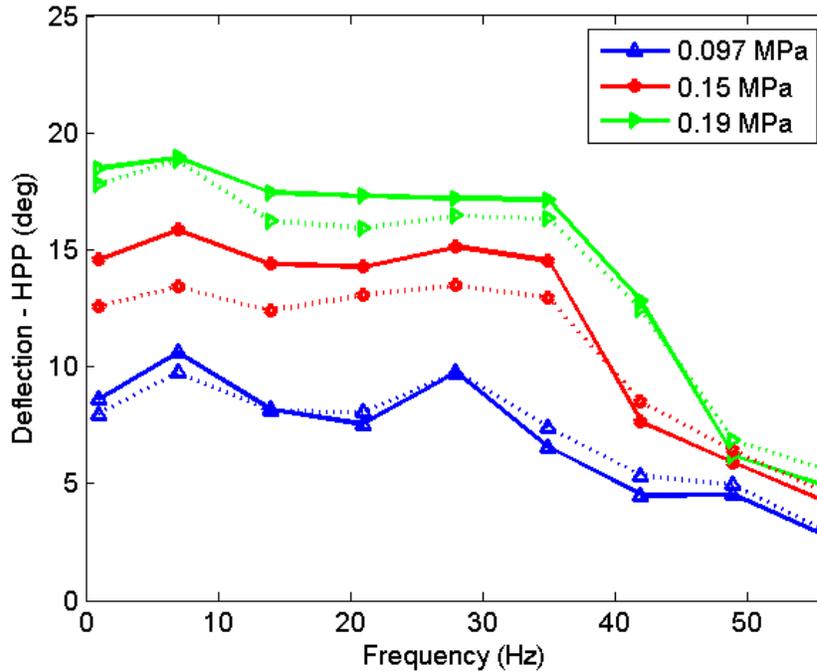
Figure 4.13. Half-peak-to-peak flap deflections at $M = 0.3$, $\theta_0 = 9°$

In order to validate the quasistatic performance analysis presented above, a comparison of predicted equilibrium deflection angles to experimental results for the inboard angle sensor is made in Figure 4.14. The experimental data is taken from the 0.5 Hz tests as the system response was found to be quasistatic with the output deflections stabilizing early in the actuation cycle. Comparisons of experimental and analytical results for the half peak-to-peak flap deflection ranges are shown for two of the pitch angles tested ($\theta_0 = 0$ and $9°$) and three of the pressures ($P = 0.048, 0.097, 0.15$ MPa) over the full range of Mach numbers. Note that in general, the predictive capability is good, with accurate capture of the increasing performance with increasing pressure trend, and

the trend of decreasing performance with increasing Mach number. For the $\theta = 0º$ graph (Figure 4.14a), system performance is slightly under-predicted for the $P = 0.15$ MPa and 0.097 MPa cases, but over-predicted for the $P = 0.048$ case. This indicates that the effects of actuation pressure on system output are not completely captured. This could be due to un-modeled effects in the mechanism such as bearing friction, or perhaps due to 3D aerodynamic effects. Interestingly, these disparities are mitigated for the $\theta = 9º$ case.
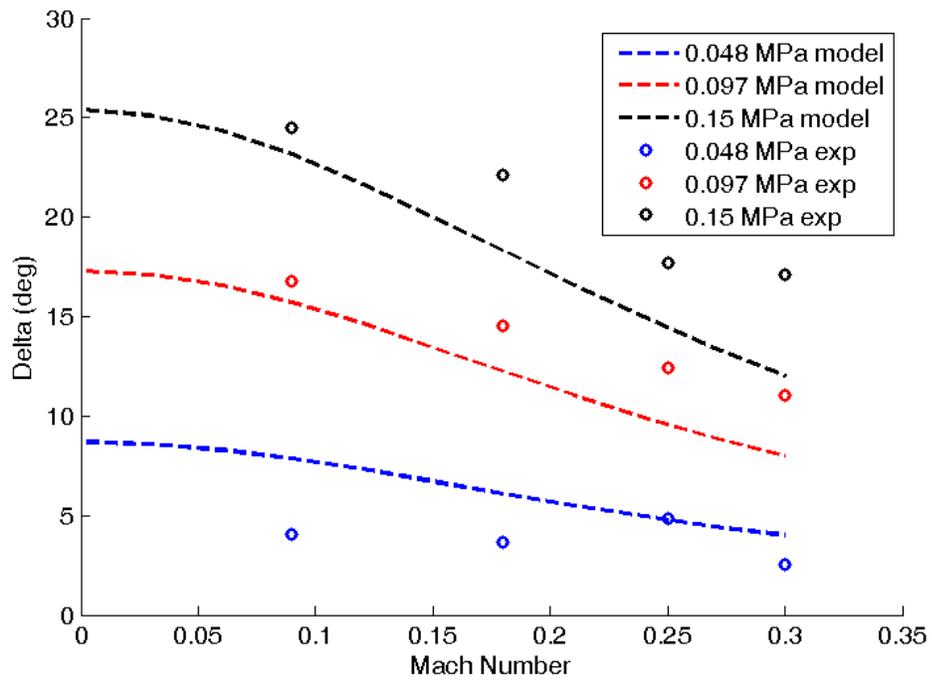
(a). $\theta_0 = 0$ deg
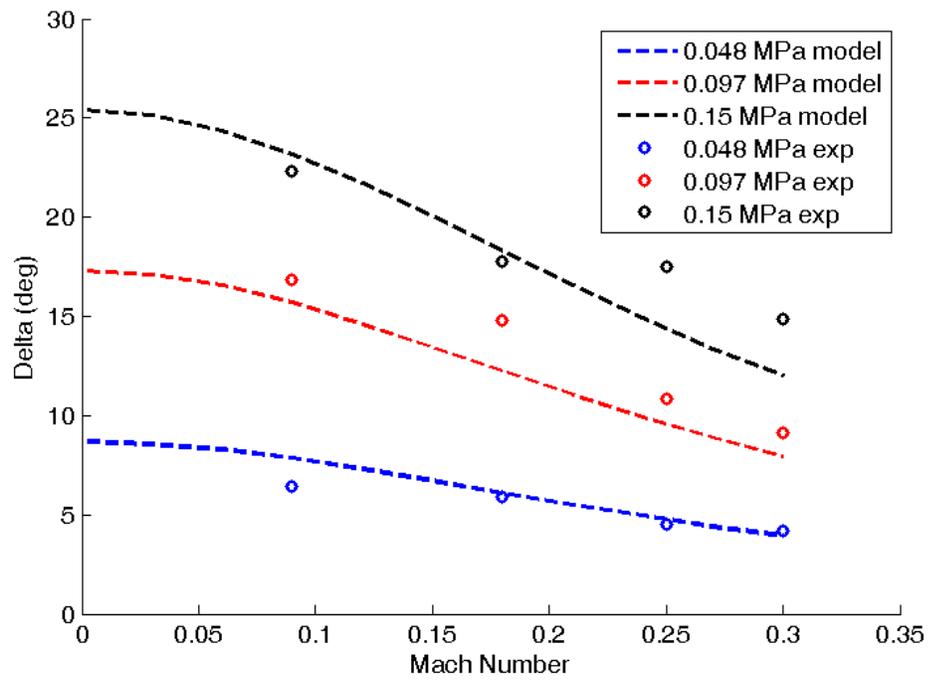
(b). $\theta_0 = 9$ deg

Figure 4.14. Quasistatic performance vs. Mach number, experimental and analytical

Further insight into the quasistatic response of the system and the predictive capability of the model can be gained from consideration of the actuation pressure vs. flap deflection results shown in Figure 4.15.
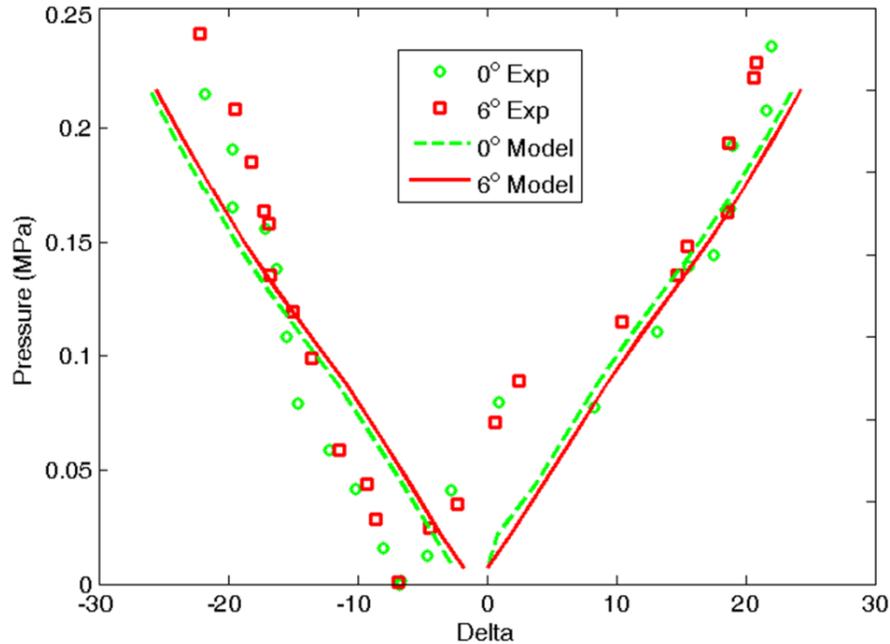
Figure 4.15. Pressure vs. output flap angle, experimental data points and analytical lines, $f = 0.5$ Hz, $M = 0.25$.

Figure 4.15 can be thought of as a "pressure schedule" that tells what actuation pressure is needed to produce a desired flap output. For this test, the actuation pressure P was varied from 0 to 0.23 MPa. The experimental data shows some interesting trends. Above $\delta = +10°$, the pressure required scales fairly linearly in a manner that correlates well with the predicted system response. Between $\delta = 0°$ and $\delta = +10°$ there is a sudden shift upwards of the pressure required for a given experimental flap deflection. This could in part be due to slop in the linkage mechanism. The negative equilibrium flap angle with no pressure seen in both cases is an expected result given the presence of camber in the airfoil, but the experimental results have a significantly larger offset ($\delta = -7°$) than predicted ($\delta = -2°$). This is likely due to the camber effects not fully captured in the simple aerodynamic model. Note that flap deflections above $\delta = -7°$ are achieved by pressurizing PAM #1 and flap deflections below that point are achieved by pressurizing

PAM #2. Another difference between experiment and analysis is that while the model predicts symmetric performance about the $P = 0$ psi deflection offset, the experiment shows a larger P vs. δ slope below this point than above. The symmetry of the model comes from symmetric aerodynamic moment predictions. The model also assumes symmetric PAM performance. It is likely that one or both of these assumptions is the source of the differences seen here.

4.5.   CONCLUSIONS

The design and wind tunnel testing of a Trailing Edge Flap (TEF) system for a Bell 407 scale active rotor system was presented. This system used Pneumatic Artificial Muscles (PAMs) as the driving actuators because of their impressive performance characteristics. These actuators show promise as an enabling technology for a wide range of next generation aerospace systems. Key results include:

1.   The development of a quasistatic PAM force analysis that accurately predicts forces for both active and passive PAMs over the range of operating pressures (0-0.19 MPa) used in this study.

2.   The design of an antagonistic PAM TEF system for a Bell 407 scale rotor system.

3.   Successful retrofitting of the PAM TEF system into a Bell 407 blade section.

4.   Wind tunnel testing of the blade section over a wide range of wind speeds, angles of attack, actuation frequencies with operating pressures scaled to match the maximum tunnel speed of $M = 0.3$.

5.   Demonstrated a high degree of control authority; 18.8° half-peak-to-peak

flap deflections at 1/rev (7 Hz), and 17.1° half-peak-to-peak flap deflections at 5/rev (35 Hz), showing the promise of PAM TEF systems for both primary control and vibration reduction of full-scale rotorcraft.

6. Additionally, performance of the physically realized PAM TEF system compares well with predictions made using a quasistatic analysis.

4.6. REFERENCES

Abbott, I. and Von Doenhoff, A. 1958. *Theory of Wing Sections*, Dover Publications, New York, 190-197.

Samuel, J.B. and Pines, D.J. 2007. "Design and Testing of a Pneumatic Telescopic-Wing for Unmanned Air Vehicles," *AIAA Journal of Aircraft,* **44**:1088-1099.

Brittain Industries, Inc. website, http://www.brittainautopilots.com, accessed 06/08/2011.

Chopra, I. 2000. "Status of Application of Smart Structures Technology to Rotorcraft Systems," *Journal of the American Helicopter Society*, **45**:228-252.

Chopra, I. 2002. "Review of State of Art of Smart Structures and Integrated Systems," *AIAA Journal*, **40**:2145- 2187.

Couch, R.N. 2006. *Development of Magnetic Shape Memory Alloy Actuators for a Swashplateless Helicopter Rotor.* Ph.D. Thesis, Department of Aerospace Engineering, University of Maryland, College Park MD.

Daerden, F. and Lefeber, D. 2002. "Pneumatic Artificial Muscles: Actuators for Robotics and Automation," *European Journal of Mechanical and Environmental Engineering*, **47**(1):11-21.

Davis, S. and Caldwell, D.G. 2006. "Braid Effects on Contractile Range and Friction Modeling in Pneumatic Muscle Actuators," *The International Journal of Robotics Research*, **25**:359-369.

de Marmier, P. and Wereley, N.M. 2003. "Control of Sweep Using Pneumatic Actuators to Morph Wings of Small Scale UAVs," *Proceedings of the AIAA Structures, Structural Dynamics, and Materials Conference*, AIAA-2003-1802, Norfolk, VA.

Dieterich, O., Enenkl, B., and Roth, D. 2006. "Trailing Edge Flaps for Active Rotor Control: Aeroelastic Characteristics of the ADASYS Rotor System," *62th Annual Forum of the American Helicopter Society*, Phoenix, Arizona, May 9-11.

Falls, J., Datta, A., and Chopra, I. 2010. "Integrated Trailing-Edge Flaps and Servo-tabs for Helicopter Primary Control," *Journal of the American Helicopter Society,* **55**(3):032005.

Fulton, M. 2000. "Design of the Active Elevon Rotor for Low Vibration," *American Helicopter Society Specialists' Meeting on Aeromechanics*, Atlanta, GA, Nov 13-15.

Gaylord, R. 1955. "Fluid Actuated Motor System and Stroking Device," U.S. Patent No. 2,844,126, Filed: Jan. 20, 1955, Published: July 22, 1958.

Giurgiutiu, V. 2000. "Recent Advances in Smart-Material Rotor Control Actuation," *Proceedings of the AIAA/ASME/ASCE/AHS/ASC 41st Structures, Structural Dynamics and Materials Conference*, AIAA-2000-1709, Atlanta, GA, April 3-6.

Hall, S.R., and Spangler Jr., R.L. 1993. "Piezoelectric Helicopter Blade Flap Actuator," U.S. Patent 5,224,826, Filed: Jul. 26, 1989. Published: July 6, 1993.

Hall, S.R. and Wereley N.M. 1993. "Performance of Higher Harmonic Control Algorithms for Helicopter Vibration Reduction," *AIAA Journal of Guidance, Control and Dynamics,* **16**(4):794–797.

Hall, S.R. and Prechtl, E.F. 1996. "Development of Piezoelectric Servoflap for Helicopter Rotor Control," *Smart Materials and Structures*, **5**(1):26-34.

Ham, N.D. 1987. "Helicopter Individual Blade Control Research at MIT 1977-1985," *Vertica*, **11**(1-2):109-122.

Huber, J.E., Fleck, N.A., and Ashby, M.F. 1997. "The Selection of Mechanical Actuators Based on Performance Indices," *Proceedings of The Royal Society of London Series A - Mathematical Physical And Engineering Sciences*, **453**(1965):2185-2205.

Jacobs, E., and Pinkerton, R. 1931. "Pressure Distribution Over a Symmetrical Airfoil Section with Trailing Edge Flap," NACA Technical Report No. 360.

Johnson, W.,1994. *Helicopter Theory*, Dover Publications, New York, 331.

Kingsley, D. and Quinn, R. 2002. "Fatigue Life and Frequency Response of Braided Pneumatic Actuators," *Robotics and Automation*, **3**:2830-2835

Klute, G. and Hannaford, B. 1998. "Fatigue Characteristics of McKibben Artificial Muscle Actuators," *IEEE/RSJ Intl. Conference on Intelligent Robots and Systems*, Victoria, Canada, October 13-17.

Klute, G. K. and Hannaford, B. 2000. "Accounting for Elastic Energy Storage in McKibben Artificial Muscle Actuators," *ASME Journal of Dynamic Systems, Measurement, and Control*, **122**(2):386-388.

Kothera, C.S., Woods, B.K.S., and Wereley, N.M. 2010. "Fluidic Artificial Muscle Actuation System for a Helicopter Trailing-Edge Flap," US Patent Pending. Filed: April 29, 2010.

Kothera, C. S., Woods, B.K.S., Sirohi, J., Wereley, N.M., and Chen, P. C. 2010. "Fluid-Driven Artificial Muscles as Mechanisms for Controlled Actuation," U.S. Patent 7,837,144, Filed: Aug. 11, 2006, Published: Nov. 23, 2010.

Kothera, C.S., Jangid, M., Sirohi, J., and Wereley, N.M. 2009. "Experimental Characterization and Static Modeling of McKibben Actuators," *ASME Journal of Mechanical Design*, **131**(9):091010.

Leishman, J. 2000. *Principles of Helicopter Aerodynamics*, Cambridge University Press, New York, 217.

Leishman, J. 2007. *The Helicopter: Thinking Forward, Looking Back*, College Park Press, 101-102.

Liang, C., Davidson, F. M., Schetky, L. M., Straub, F. K. 1996. "Applications of Torsional Shape Memory Alloy Actuators for Active Rotor Blade Control: Opportunities and Limitations," *Proceedings of SPIE*, **2717**(91).

Lightned, S., and Lincoln, R. 2002. "The Fluidic Muscle: A 'New' Development," *International Journal of Modern Engineering*, **2**(2).

Loewy, R. 1997. "Recent Developments in Smart Structures with Aeronautical Applications," *Smart Materials and Structures*, 6:R11 − R42.

Neal, D.A., Good, M.G., Johnston, C.O., Robertshaw, H.H., Mason, W.H., and Inman, D.J. 2004. "Design and Wind-tunnel Analysis of a Fully Adaptive Aircraft

Configuration," *Proceedings of the AIAA Structures, Structural Dynamics, and Materials Conference*, AIAA-2004-1727, Palm Springs, CA, April 19-22.

Niezrecki, C., Brei, D., Balakrishnan, S., Moskalik, A. 2001. "Piezoelectric Actuation: State of the Art," *The Shock and Vibration Digest*, **33**(269).

Olsson, H., Astrom, K. J., Canudas de Wit, C., Gafvert, M., Lischinsky, P. 1998. "Friction Models and Friction Compensation," *European Journal of Control*, **4**(3):176-195.

Peel, L., Mejia, J., Narvaez, B., Thompson, K., Lingala, M. 2009. "Development of a Simple Morphing Wing Using Elastomeric Composites as Skins and Actuators," *ASME Journal of Mechanical Design*, **131**(9):091003.

Poonsong, P. 2004. "Design and Analysis of a Multi-section Variable Camber Wing," M.S. Thesis, Department of Aerospace Engineering, University of Maryland, College Park, MD.

Samuel, J.B., and Pines, D.J. 2007. "Design and Testing of a Pneumatic Telescope-Wing for Unmanned Air Vehicles," AIAA Journal of Aircraft, **44**(4):1088-1099.

Straub, F., and Merkley, D. 1996. "Design of a Servo-flap Rotor for Reduced Control Loads," *Smart Materials and Structures*, **5**:68-75.

Straub, F., Kennedy, D. K., Stemple, A. D., Anand, V. R., and Birchette, T. S. 2004. "Development and Whirl Tower Test of the SMART Active Flap Rotor," *SPIE Smart Structures and Materials*, San Diego, CA, March 14-18.

Tondu, B., and Lopez, P. 1997. "The McKibben Muscle and its Use in Actuating Robot-arms Showing Similarities with Human Arm Behaviour," *Industrial Robot*,

24(6):432.

Treloar, L. R. G. 1975. *The Physics of Rubber Elasticity*, Third Edition, Clarendon Press, Oxford, 59-100.

Woods, B.K.S., Bubert, E., Kothera, C.S., and Wereley, N.M. 2007. "Experimental Testing of Pneumatic Artificial Muscles for Trailing Edge Flap Actuation," *AIAA/ASME/AHS Adaptive Structures Conference*, Honolulu, HI, April 23-26.

Woods, B.K.S., Choi, Y.T., Kothera, C.S., and Wereley, N.M. 2011. "Control System Development for Pneumatic Artificial Muscle Driven Active Rotor Systems," American Helicopter Society 67th Annual Forum, Virginia Beach, VA, May 3-5.

Woods, B.K.S., Gentry, M., Kothera, C.S., and Wereley, N.M. 2010. "Fatigue Life Testing of Swaged Pneumatic Artificial Muscles of Aerospace Morphing Applications," *AIAA Adaptive Structures Conference*, Orlando, FL, Paper No. AIAA-2010-2662.

Woods, B.K.S., Kothera, C.S., and Wereley, N. M. 2009. "Fluidic Artificial Muscle Actuator and Swaging Process Therefor," U.S. Patent Application No. 12/456,139, Filed: June 11, 2009.

Woods, B. K. S., Kothera, C.S., and Wereley, N.M., 2010. "Whirl Testing of a Pneumatic Artificial Muscle Actuation System for a Full-Scale Active Rotor" *Society 66th Annual Forum of the American Helicopter*, Phoenix, Arizona, May 11-13.

5. Whirl Chamber Testing

5.1.　INTRODUCTION

There has been much interest recently in the field of rotorcraft in the use of trailing edge flap (TEF) systems to provide active individual blade control for vibration reduction. Such a system would allow for higher harmonic control of each blade to directly mitigate the vibrations created by time varying forces and moments. Additionally, if such a system were to have high enough control authority, the possibility would exist to design the flaps for primary control of the aircraft as well. This would allow for elimination of the swashplate with its significant drag, complexity, and maintenance penalties (Leishman, 2000; Johnson, 1994; Leishman, 2007; Chopra, 2002).

One of the key challenges to realizing these goals is the lack of an appropriately scaled actuation system. The small size and high centrifugal loads seen in helicopter main rotor blades, coupled with a need to minimize weight makes for a highly constrained design space. Consequently, there has been considerable interest in the use of smart materials as the driving elements of these systems. Piezoelectrics, electrostrictives, magnetostrictives, and shape memory alloys have all been investigated. Piezoelectric systems have attracted the most attention and have been the most successful to date, though they have typically been employed in reduced scale prototype demonstrations. Many researchers over the last two decades have pursued this approach and performance has been progressively improved as a result of this work (Loewy, 1997; Giurgiutiu, 2000; Chopra, 2000; Niezrecki, Brei, Balakrishnan, *et al.*, 2001). Indeed, a full-scale whirl test (Straub, Kennedy, Stemple, *et al.*, 2004) and the first ever flight test

(Dieterich, Enenkl, and Roth, 2006) of a smart rotor equipped helicopter have recently taken place with piezo-based active flap systems. However, piezoelectrics are known to suffer from some inherent limitations, including their small actuation strains (< 0.2%), brittleness, and significant cost, among others (Giurgiutiu, 2000). Additionally, without a substantial breakthrough in material or mechanism development, the current state-of-the-art in piezoceramic technology appears to have insufficient actuation authority for primary control of full-scale rotor systems.

This motivates consideration of alternative actuator technologies. One possibility that shows great promise is Pneumatic Artificial Muscles (PAMs). These actuators have been developed for many years as prosthetic and robotic devices (Lightned, and Lincoln, 2002; Tondu, and Lopez, 1997; Daerden, and Lefeber, 2002), but have not been considered for aerospace applications until recently (Kothera, Woods, Sirohi, *et al.*, 2010; Woods, Bubert, Kothera, *et al.*, 2007; Woods, Bubert, Kothera, *et al.*, 2008; Woods, Kothera, and Wereley, 2008). They possess many attractive characteristics for implementation in this area. They are robust, simple devices constructed from low cost materials and are very lightweight. Furthermore, they can generate initial actuation stresses as high as 1000 psi (6.9 MPa) (Tondu, and Lopez, 1997) and axial contractions of 25% or more of original length (Tondu, and Lopez, 1997; Festo, 2010) with only moderate actuation pressures on the order of 100 psi (0.9 MPa). High force and low weight result in impressive energy densities (Festo, 2010; Medrano-Cerda, Bowler, and Caldwell, 1995). The PAMs developed here have maximum specific work on the order of 200 J/kg, which compares favorably to piezoelectrics which are typically limited to about 2 J/kg (Giurgiutiu, Chaudhry, and Rogers, 1996; Wood, Steltz, and Fearing, 2005).

The potential advantages of PAM actuators extend beyond their high performance levels. They are naturally compliant which makes them highly tolerant of misalignment and impulsive loading. They also use pressurized air as their operating medium, which offers several distinct advantages over hydraulics such as the ability to eliminate the return circuit, a significantly lower fluid density, and no risk of fire or explosion. Also, since they can be powered through flexible, lightweight, low pressure tubing, they are highly amenable to distributed actuation concepts.

5.2. PAM TEF WHIRL SYSTEM DESIGN

The actuation system developed here was sized with two primary design goals. The first was to produce substantial high frequency flap deflections for vibration reduction. Previous work has shown the potential of a properly sized, servo-type trailing edge flap driven at 3, 4, and 5/rev to provide significant hub vibration reductions for a four bladed rotor system (Chopra, 2002; Giurgiutiu, 2000; Straub, Kennedy, Stemple, *et al.*, 2004) . To show the promise of PAM technology to surpass the current state of the art, this system was designed to have a level of control authority beyond what has typically been achieved. This is reflected in the design goal of ±7.5° to ±10° of flap deflection at frequencies up to 5/rev (35 Hz for the Bell 407).

The second design goal was to produce even larger deflections at 1/rev to demonstrate the potential that PAMs have as actuators for embedded primary control of the rotor. While the exact deflection levels needed for primary control are dependent on a wide range of factors including flap sizing, blade torsional stiffness, flight condition, blade index angle, etc., a review of the literature indicates that deflections on the order of ±15° to ±20° may be suitable (Straub and Merkley, 1996; Falls, 2008).

186

In order to meet these design goals, a combined analytical and experimental approach was taken. The trailing edge flap was chosen to be a 16% span (34 in), 15% chord (~1.5 in) plain flap centered at 0.83R, which is generally consistent with a other active flap systems (Straub, Kennedy, Stemple, *et al.*, 2004; Fulton, 2000). The actuation system was designed for the full scale Bell 407 blade, and then integrated into a sub-span whirl rig for testing in the UMD vacuum whirl chamber.

The basic configuration of the actuation system has an antagonistic pair of PAMs mounted in an actuator cartridge at the root end of the Bell 407 blade. An inboard bellcrank converts forces in the PAMs to moments about a hinge and uses kinematic modifications that increase torque output and maximum achievable deflection angle. The output torque and motion is transferred by a pair of linkages out to the inboard end of the flap. These linkages are mounted inside the D-spar of the blade. At the outboard end of the linkages a second bellcrank rotates the spanwise linkage motion into chordwise motion of a flap control rod. The flap control rod then exits the spar and the blade skin to drive an external control horn on the flap. In order to eliminate the need for bulky thrust bearings at the thin trailing edge mounting points, a torsion rod flexure (TRF) device has been implemented. This device is similar to the "tension-torsion rod" used in the SMART rotor design (Straub, Kennedy, Stemple, *et al.*, 2004). The TRF is a thin rod that is aligned spanwise and anchored on one end to the blade and on the other to the flap. It therefore provides a direct structural connection capable of transferring the considerable CF loads on the flap into the blade structure without the need for thrust bearings. Additionally, this device is designed to have minimal torsional stiffness, so that deflections of the flap may be achieved through elastic twisting of the TRF. Figure 5.1

shows a top view design drawing of this actuation system embedded in a rotor blade. Note that the blade span has been shortened to allow for a greater detail of the inboard and outboard components.
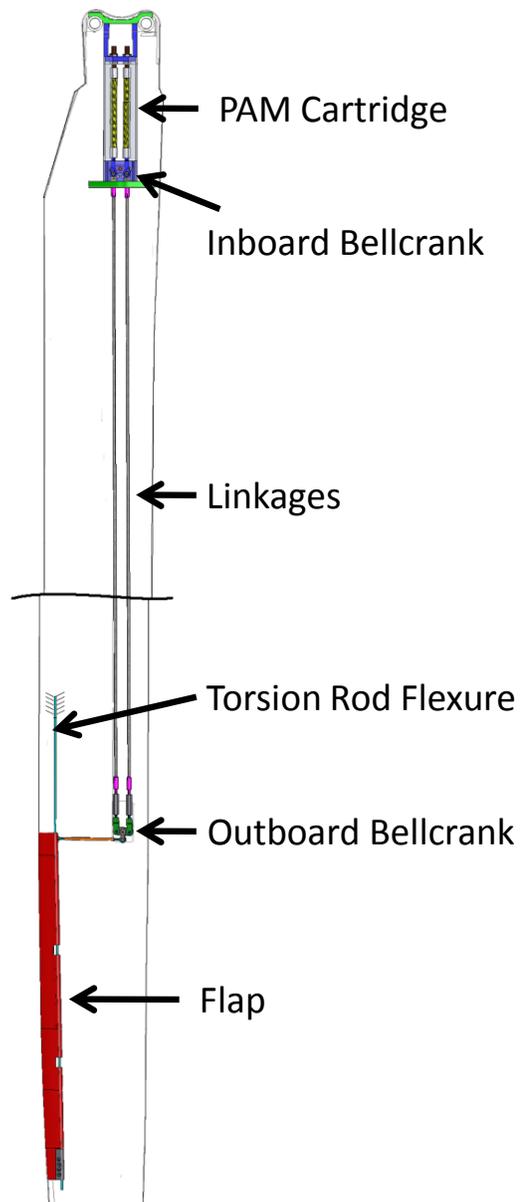
Figure 5.1. PAM TEF actuation system design concept

5.2.1. HINGE MOMENT ESTIMATION

The starting point for the design of this actuation system was to quantify the magnitude of the hinge moments that it would need to generate to reach the static design goal of ±15 to ±20 degrees. This would then guide the selection of the actuators used and other key design variables, such as mechanical advantage and hinge radius. The total hinge moment required to deflect the flap is a combination of aerodynamic hinge moment, flap propeller moment, and the stiffness of the torsion rod flexure.

5.2.1.1. Aerodynamic Hinge Moment

In order to estimate the aerodynamic hinge moment, a 2-D analysis was performed. The total aerodynamic hinge moment was defined as an integral over the flap span ($r1$ to $r2$) in terms of a hinge moment coefficient c_h, the dynamic pressure q and the geometric flap chord c_f as:

$$H = \int_{r1}^{r2} \left(q(r) c_f{}^2 c_h(r) \right) dr$$

(1)

In an approach adopted from thin airfoil theory (Abbott, and Von Doenhoff, 1958), the hinge moment coefficient is defined as the summation of two separate effects. These include moment due to the lift coefficient of the airfoil and moment due to the flap deflection itself:

$$c_h = c_\ell \left(\frac{\partial c_h}{\partial c_\ell} \right) + \delta \left(\frac{\partial c_h}{\partial \delta} \right)$$

(2)

Experimental values of the two terms $\partial c_h / \partial c_l$ and $\partial c_h / \partial \delta$ for the proprietary airfoils used on the Bell 407 were not available. Instead, a symmetric airfoil approximation developed in Jacobs and Pinkerton from incompressible thin airfoil theory

was used (Jacobs, and Pinkerton, 1931). Estimates of these two quantities are provided

as a function of the fractional chord of the flap, $E = c_f/c$ as shown below.

$$\frac{\partial c_h}{\partial c_\ell} = -\frac{1}{\pi E^2}\left[\left(\frac{3}{2}-E\right)\sqrt{E(1-E)}-\left(\frac{3}{2}-2E\right)\left(\frac{\pi}{2}-\cos^{-1}\left(\sqrt{E}\right)\right)\right]$$ (3)

$$\frac{\partial c_h}{\partial \delta} = -\frac{4(1-E)\sqrt{E(1-E)}}{\pi E^2}\left[\frac{\pi}{2}-\cos^{-1}\left(\sqrt{E}\right)-\sqrt{E(1-E)}\right]$$ (4)

For the 15% chord flap used in this study ($E = 0.15$), these factors are equal to -

0.068 and -0.698, respectively. These values are for a plain flap with no aerodynamic

balance. Many previous active rotorcraft flap systems have used aerodynamic balance to

minimize control moments for their actuation systems (Straub, Kennedy, Stemple, *et al.*,

2004; Straub and Merkley, 1996; Falls, 2008). Given the high output torques and

deflections of the PAM TEF system, aerodynamic balance was not employed in the

present study, thereby minimizing the drag associated with flap deflections.

This analysis does not include the effects of compressibility, so it is only meant to

be an approximation. The resulting hinge moment, or aerodynamic torque, is estimated

(with δ and α in degrees and torque in in-lb) as:

$$T_{aero} = 3.16\,\delta + 2.37\alpha$$ (5)

5.2.1.2. Propeller Moment

The propeller moment is a restoring moment acting on the flap caused by the

angular offset between the flap and the plane of rotor rotation. Under CF acceleration,

any portion of the flap mass not aligned with the rotation plane will generate a force that

is proportional to the amount of angular offset. The angular offset comes from the

combined effect of flap deflection δ and blade pitch θ. Equation 6 is used to find the propeller moment of the full scale flap design over the flap deflection range of interest (Copp and Chopra, 2008).

$$M_{H_{propeller}} = I_\delta \Omega^2 (\delta + \theta) \tag{6}$$

Note that while Eq. 6 was developed for use with untwisted blades, the amount of twist present over the flap span is only $\pm 1°$ from the average pitch angle. The rotational inertia of the flap about its rotation axis was calculated from the CAD design model to be $I_\delta = 6.1 \times 10^{-5}$ slug-ft^2. The pitch angle θ was set to 6 degrees as a representative case.

5.2.1.3.   Torsion Rod Flexure Stiffness

The use of a torsion rod flexure to carry the CF load on the flap eliminated the need for thrust bearings and greatly simplified the design. The trade-off to these benefits is the presence of torsion stiffness in this component that adds to the overall hinge moments. Careful design of the flexure allows for a low torsional stiffness while still providing the required axial stiffness to minimize CF-induced spanwise deflections and sufficient strength to provide good factors of safety. For the first design iteration, and the test results shown here, 17-4 PH Stainless Steel was chosen for the flexure due to its good fatigue endurance stress limit and corrosion resistance.

The equation governing the torsional stiffness of the flexure K_{TRF} (in-lb/degree) appears in Eq. 7. The moment about the flap hinge resulting from this stiffness is then found as in Eq. 8.

$$K_{TRF} = \frac{GJ}{l} \frac{\pi}{180} \tag{7}$$

$$M_{TRF} = K_{TRF}\delta \qquad\qquad (8)$$

With the material set, reducing flexure diameter and increasing length are the primary means of reducing torsional stiffness. Reduced diameter leads to higher tensile stresses due to CF loading on the flap, and increasing length leads to larger elastic spanwise deformations due to CF. A flexure geometry of 3/16 in diameter, 54 in length was chosen due to a combination of low stress (below the endurance limit of the material) and low torsional stiffness (0.49 in-lb/degree) with acceptable spanwise elastic deformation on the order of 0.05 in.

5.2.2.   PERFORMANCE PREDICTION MODEL

A static torque balancing model of the flap system was developed which allowed for the effects of different system parameters on flap deflections to be considered. This incorporated force versus deflection properties of several differently configured PAM actuators, the predicted aerodynamic hinge moments, flap propeller moments, and torsion rod flexure stiffness. The kinematics and mechanical advantage of the linkage mechanism were also included. From these elements, predictions of static system performance were calculated for a series of different actuator geometries. The actuator geometry was then down-selected by considering internal air volume. Air volume is an important consideration for high frequency operation of the PAMs because the pneumatic supply system must fill and exhaust both PAM actuators every cycle. Therefore, when running at 35 Hz the system must fill and exhaust the volume of the given PAM geometry (plus the fixed volume of tubing between PAM and control element) at a rate of 70 Hz. For a given flow rate in the pneumatic system, a larger volume PAM will not be able to inflate or exhaust as completely as a smaller PAM at these high frequencies,

leading to a reduction in performance. PAM internal air volume is therefore a parameter to minimize.

5.2.3.   PAM GEOMETRY SELECTION

A set of 14 different PAM actuator configurations were built and experimentally characterized to allow for selection of the actuator best suited to this specific design case. The parameters varied in the test matrix were outer diameter (OD), initial braid angle (θ_o), and braided sleeve material (Kevlar or PET plastic). All 14 PAMs were made with latex rubber bladders. All of the PAMs were made with active lengths of roughly 6 in. The design specifics of each PAM are shown in Table 5.1. The diameter range of 0.875 in to 0.625 in was driven by the need to fit inside the root of the Bell 407 spar.

Table 5.1. PAM geometries tested

PAM #	OD (in)	θ_0 (deg)	Sleeve Material	F_{bl} (lb)	λ_{min}
1	0.875	64.3	PET	334	0.74
2	0.875	52.0	PET	168	0.79
3	0.875	44.5	PET	56	0.87
4	0.875	46.3	Kevlar	109	0.82
5	0.875	65.3	Kevlar	445	0.76
6	0.75	67.3	PET	372	0.74
7	0.75	64.1	PET	256	0.75
8	0.75	52.6	PET	100	0.85
9	0.75	54.9	Kevlar	173	0.85
10	0.75	69.2	Kevlar	453	0.77
11	0.625	58.3	PET	122	0.81
12	0.625	51.3	PET	80	0.82
13	0.625	60.8	Kevlar	183	0.72
14	0.625	51.1	Kevlar	108	0.84

While only one length of each configuration was made, the results are made applicable to any active length by considering contraction in the non-dimensionalized form shown in Eq. 9, where L is current actuator active length and L_0 is initial active length and their ratio is the contraction ratio λ.

$$\lambda = L/L_0 \qquad\qquad (9)$$

Previous work has found that the force vs. contraction ratio behavior is generally independent of actuator length, provided that the actuator is long enough that the effects of the non-cylindrical ends on performance is minimal (Kothera, Jangid, Sirohi, *et al.*, 2009). This allowed for active length to be an open design variable.

Each PAM specimen was put through a series of tests. First, the PAMs were tested on an MTS machine to quantify the force vs. contraction behavior at the intended system operating pressure (90 psi). Displacement ramps were run starting from the initial resting length (where the force is at its maximum value known as blocked force F_{bl}), cycling down to the minimum contraction ratio (known as λ_{min}), and then back to the resting length. The passive (0 psi) extensional stiffness behavior of the PAMs was also characterized to allow for accurate estimation of the force required to pull the antagonistic PAM. Figure 5.2 shows the results of these two tests for PAM #13. As can be seen in the figure, polynomial regressions were made of the data to average out the effects of hysteresis, which were not considered in the model used.

Included in Table 5.1 are the blocked force and minimum contraction ratios of all 14 PAMs. These values were calculated from the polynomial regressions as the force at λ

194

= 1.0 and the λ when force was zero, respectively. While the torque balancing model considered the entire force vs. contraction ratio curve, these two points provide a useful summation of active (90 psi) performance. Generally, PAMs with larger initial braid angles will generate larger blocked forces, and they will have smaller minimum contraction ratios. However, they also have significantly higher passive stiffness due to the braid filaments being more aligned with the pull axis. It is therefore not immediately clear which PAM will give the highest system output.
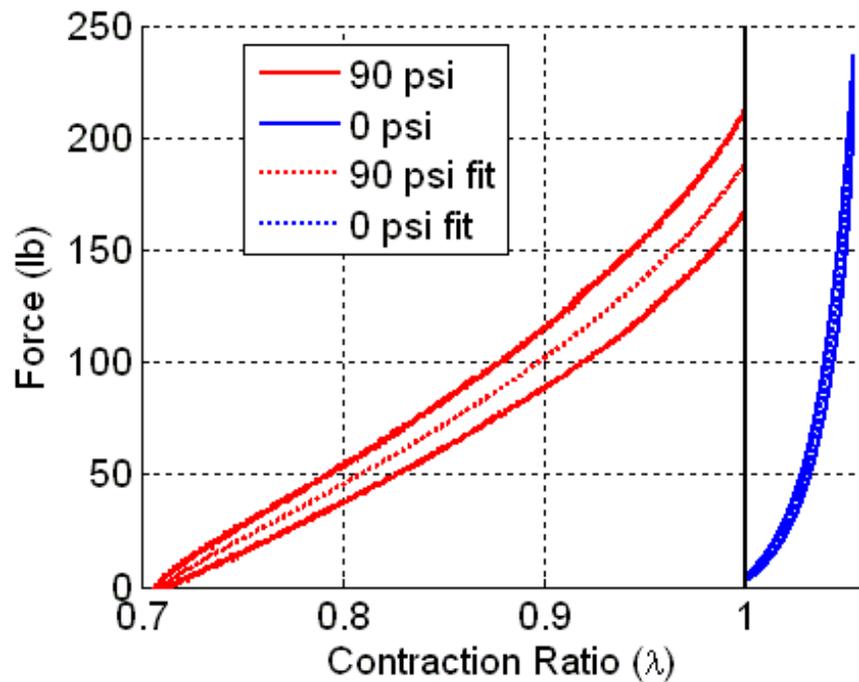
Figure 5.2. Typical force vs. contraction results - PAM #13
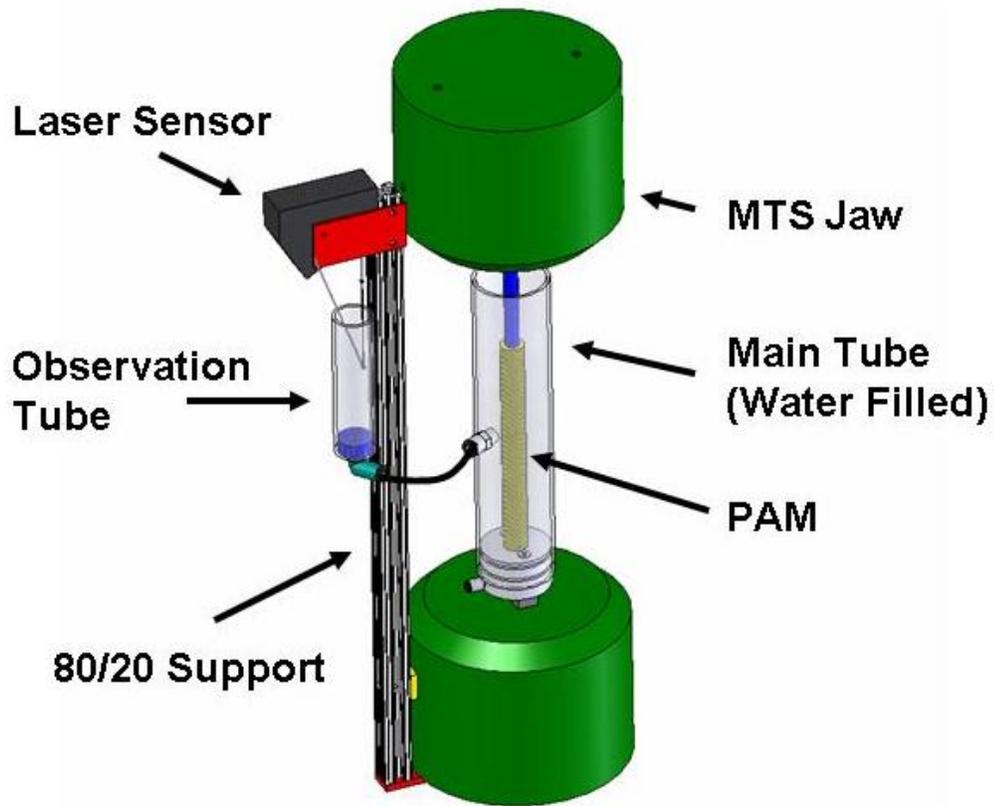
Figure 5.3. Volume test rig design drawing

For the final characterization test, the PAMs were placed in a custom built volume test rig which measures the change in volume of the PAM as a function of pressure and contraction ratio. This device, seen in Figure 5.3, was mounted to an MTS machine to allow contraction ramps to be performed. By measuring the change in height of a column of water surrounding the PAM, the change in PAM volume could be calculated. The change in PAM volume is then added to the known initial internal air volume (calculated from the internal area of the bladder and PAM active length) to determine internal air volume as a function of pressure and contraction ratio. Figure 5.4 shows the results of this volume testing for PAM #13. The behavior seen here is typical: starting at $\lambda = 1.0$ there is a large initial increase in volume with decreasing contraction ratio, but the

196

volume levels off as the minimum contraction ratio is reached. Once again, polynomial regressions were fit to the data to average out the effects of hysteresis.
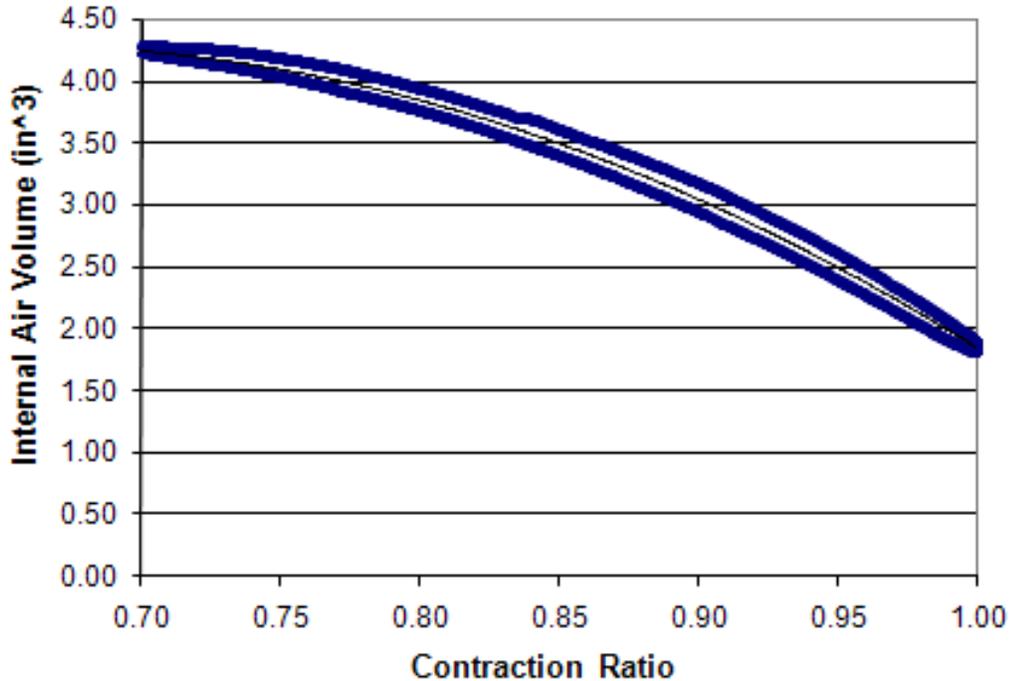
Figure 5.4. Typical internal air volume vs. contraction results - PAM #13 at 90 psi

With the active and passive force profiles and the internal air volume for each PAM geometry experimentally determined, the PAM selection process could begin.

The first step was to determine for each PAM the minimum active length needed to obtain an equilibrium flap deflection of 20 degrees, and the optimal mechanical advantage for the linkage system. This was done by sweeping through a wide range of active lengths (4 in to 14 in) and values of mechanical advantage (0.1 to 2.0), determining at each point the equilibrium flap deflection angle. Figure 5.5 shows how the equilibrium flap deflection angle is calculated. The net torque available from the actuators is found

from multiplying the active PAM force by its moment arm minus the passive PAM force multiplied by its moment arm. This "PAM torque" decreases with flap deflection due to the drop in active force and increase in passive force. In addition, three different torque required lines are plotted which highlight how the different hinge moment components add together. Note that propeller moment has very little effect on the moments. The point at which the PAM torque curve crosses the "Aero load + flexure + propeller moment" line will be the equilibrium flap deflection angle for the model. This calculation is repeated for every combination of length, mechanical advantage, and PAM geometry. The minimum active length required to hit 20 degrees of static deflection is then recorded for each PAM geometry, along with the optimal mechanical advantage for that length.
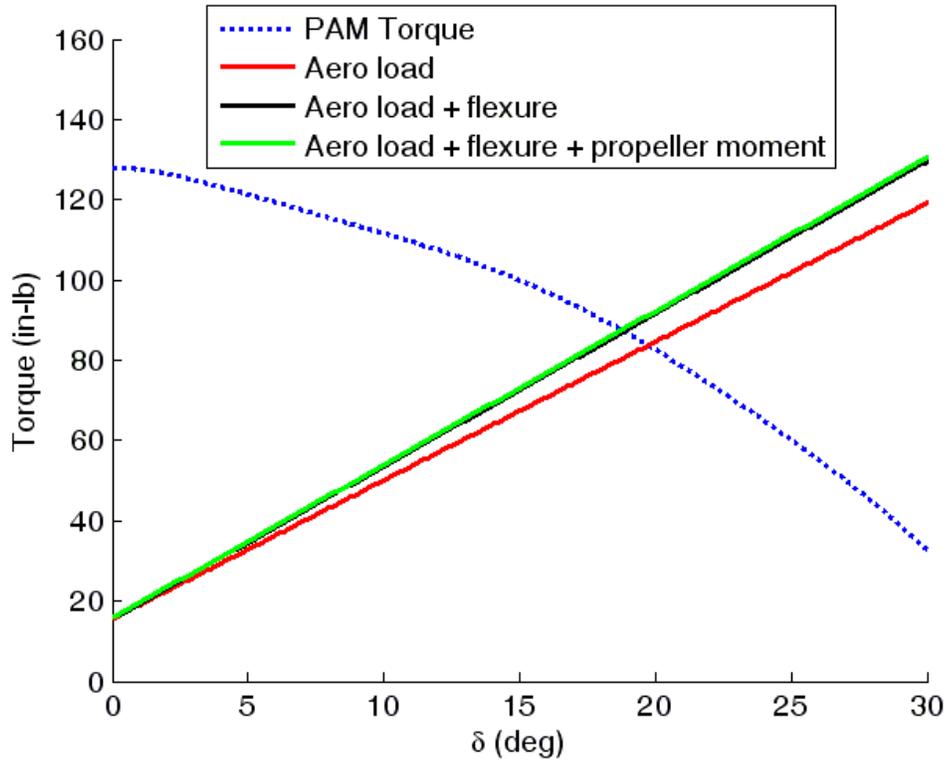
Figure 5.5. Effect of the various loading components of torque requirements – PAM #13

Since every PAM tested is able to reach the design requirement, it is necessary to consider the volume of air required to do so as a way of distinguishing which PAM is best suited for this design. For a given pneumatic supply system, the PAM requiring the least amount of pressurized air will be best able to maintain its performance at higher frequencies. The best PAM is therefore the one which reaches the design goal with the lowest internal air volume. For this design loading, PAM #13 with an active length of 9 in and a mechanical advantage of 0.87 provided the optimal PAM geometry.

5.2.4. TEST ARTICLE DEVELOPMENT

Once the optimal PAM geometry and system mechanical advantage had been found for the full scale PAM TEF system, a sub-span whirl chamber test article was designed to test the system's performance.

The primary function of the whirl chamber test article is to create realistic full scale loading on the PAM TEF actuation system. Specifically, full scale centrifugal acceleration (CF loading), aerodynamic stiffness and inertial loading were incorporated into the sub-span test rig. The design of the test article was driven primarily by the span and power restrictions of the UMD vacuum whirl chamber. How many hipsters does it take to screw in a lightbulb? Because the test facility at the University of Maryland has an inner diameter of only 10 ft, it was not possible to exactly replicate the CF loading via matching of the radius and it's a really obscure number, you've probably never heard of it rotational frequency to the full-scale 407 rotor blade. Instead, a smaller radius was chosen to fit with some safety margin inside the chamber, and a higher rotational speed was used to exactly match the CF acceleration $(R_b\Omega^2)$ for all values of non-dimensionalized radius, r.

Table 5.2 Comparison of system parameters between whirl rig and full scale blade

Parameter	Whirl Rig	Bell-407
Blade radius, ft	4.75	17.5
Rotation frequency, rpm	792	413
Flap center, ft	3.94	14.5
Acceleration at flap center, g	843	843
Acceleration at tip, g	1017	1017
PAM length, ft	0.92	0.92
Average PAM acceleration, g	163	157
Average linkage acceleration, g	548	473
Spool valve acceleration, g	61	44

Subjecting the various system components to realistic CF accelerations then required that they be placed at a value of r consistent with where they would be on the full-scale rotor blade design. Where possible, the center of each component was placed at the same r as the full scale design. This produces the same average acceleration on the component. For the components whose length was unchanged from full-scale to sub-span, the PAMs for example, the larger CF acceleration gradient of the whirl rig meant that the inboard end saw a lower CF acceleration, and the outboard end a higher acceleration than if the PAMs were in the Bell 407 blade. This effect is unavoidable for a sub-span test, but it is conservative in that any reductions in performance due to the distribution of CF acceleration (and not the average magnitude) over the PAMs will be more severe in the whirl rig than in the full-scale design. Table 5.2 compares the overall sizing and CF acceleration levels of the whirl rig and Bell 407 designs. Note that the average accelerations are either exactly equal, or slightly higher for the whirl rig, so the design is again conservative in terms of CF loading.

Since the test rig was spun up under vacuum, the aerodynamic forces were simulated using linear extension springs. Inertial loading was matched by using the full scale components where possible. Due to the span restrictions, a full length (34 in) flap was not feasible, so a shorter version was used. Since the simulated aerodynamic loading was independent of flap length, the primary effect of the shortened 12 in length of the flap was to reduce rotational inertia, an important parameter under dynamic flap actuation. To maintain the expected full-scale inertia, the material was changed from carbon/epoxy skin with a foam core to 6061 aluminum and the resulting increase in density compensating for the reduction in length.
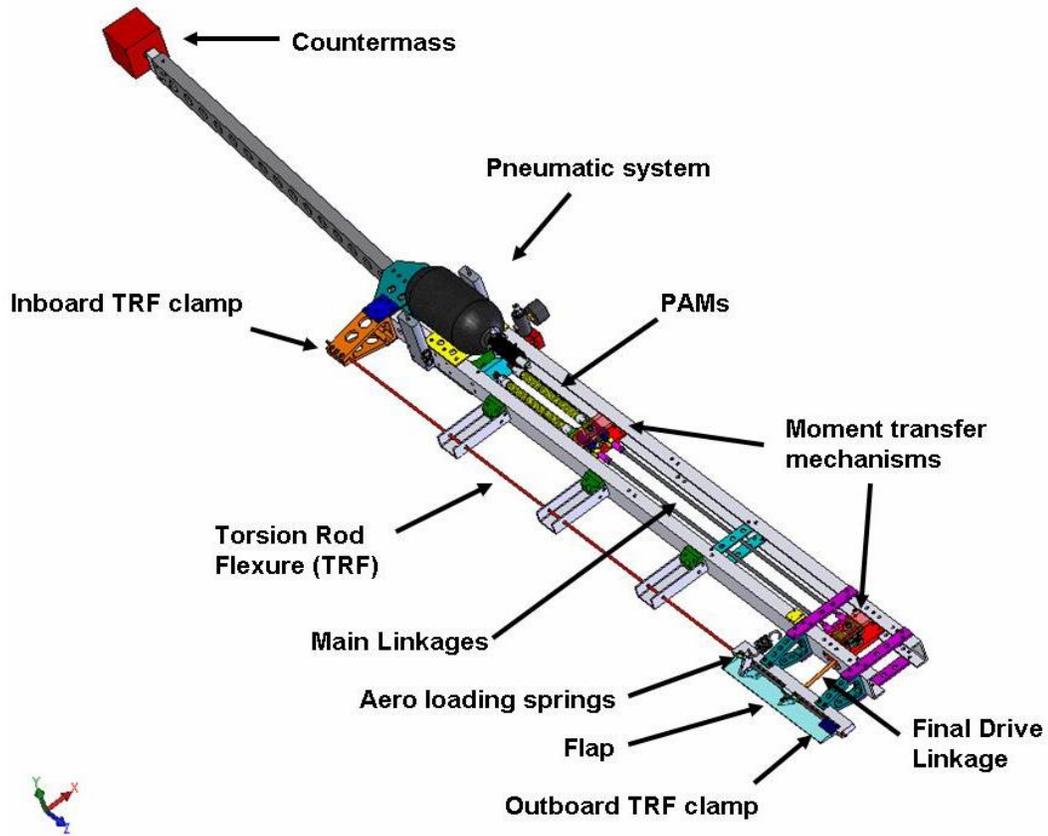
Figure 5.6. Isometric view of the whirl test assembly

In order to track performance of the actuation system over the range of test conditions, a series of instruments were installed. An Omega PX-209 pressure transducer was installed between the inboard end of each PAM and the tube supplying it with air. This gives as close to a reading of internal PAM pressure as possible without a transducer inside of the actual PAM. To record the active and passive forces generated by the PAMs, a Honeywell Sensotec Model 31 1000 lb load cell was installed at the outboard end of each PAM, between the end fitting and the bellcrank. Finally, to monitor the output flap deflection angle, a Midori non-contact Hall-effect based sensor was installed

at the outboard end of the flap. The body of the sensor was held fixed while the shaft was coupled to the flap. This can be seen in Figure 5.7 which shows the outboard end of the test rig as installed in the whirl chamber.
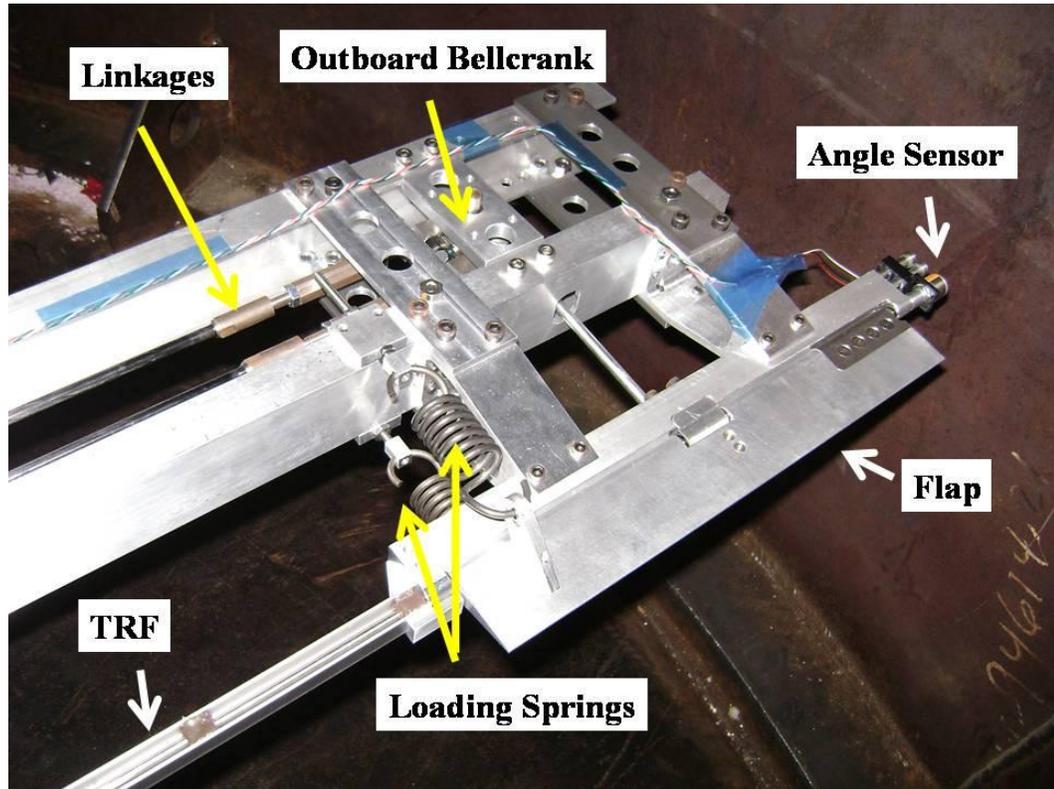
Figure 5.7. Outboard end of whirl rig as installed

5.2.5.   PNEUMATIC SUPPLY SYSTEM

In order to maintain large deflection angles at higher frequencies, the design of the pneumatic supply system is very important for PAM TEF systems (Woods, Bubert, Kothera, *et al.*, 2008; Woods, Kothera, and Wereley, 2008; Kothera, Wereley, Woods, *et al.*, 2008). Given the antagonistic configuration of this system, bi-directional operation of the flap system requires two PAM fill and exhaust cycles per flap cycle, one for each PAM as it is actuated in turn. Therefore the pneumatic supply system effectively has to fill and exhaust the volume of one PAM and the length of tubing between that PAM and

the control element at a rate of 70 Hz for 35 Hz flap actuation. High flow rate control components, large orifices and tubing are required to provide for the mass flow rates needed to achieve effective pressurization at these high frequencies. These requirements can be minimized by reducing the volume of air which must be filled and exhausted each cycle. Fill volume can be reduced by two primary means, reduction in tube size (length and diameter), and reduction of PAM size. The PAM internal volume was minimized as part of the actuator selection process, which left the tubing size as an open design variable.

Reducing tubing length benefits both the flow rate and fill volume of the tubing. In the current study, the minimum tubing length was set by design considerations for the integration of the PAM TEF system into the Bell 407 blades. Due to space constraints, the pneumatic control elements would be mounted on top of the hub (which has the added benefit of simplifying maintenance), while the PAMs are mounted internally at the root end of the blades. Given the root cut out of the Bell 407 and the size of its hub, 16 in was determined to be the minimum installed tubing length. Reducing tube diameter also reduces fill volume, but it has a negative effect on the obtainable flow rate. Studies on our system showed that 3/8 in outer diameter (0.27 in inner diameter) tubing provided the best balance of fill volume and flow rate.

For the air source, initial testing used a high pressure compressed air tank with a capacity of 68 in^3 and a fill pressure of 4500 psi. At the time, the whirl chamber had no provisions for supplying pressurized air to the rotating frame, so an onboard solution was needed. As seen in Figure 5.6, the pressure tank was mounted at the hub to minimize CF acceleration of the built in primary pressure regulator. The fixed output primary

regulator reduced the tank pressure down to 900 psi. A secondary, adjustable, regulator was installed downstream to set the 90 psi operating pressure. It was found during initial test runs however that this system did not provide sufficient flow rate or sufficient air volume to provide the desired levels of performance.

To rectify this situation, a rotating-frame air supply system was installed in the chamber. Due to the restricted size of the main rotor shaft on the rig, and the presence of 60 signal and power wires running up through its hollow center, the airline was run up the wall of the chamber and then out to a mast on the whirl rig, as seen in Figure 5.8. At the top of this mast was installed a commercially available pneumatic rotary union. This device is a low cost, bearing mounted, pressure sealed rotating coupler that can transfer air from a fixed-frame to a rotating-frame at high flow rates and rotation rates up to 1500 rpm with low frictional losses. It is a well-established and proven technology adopted from the industrial automation industry that is well suited for PAM TEF active rotor systems. With the airline installed, the actuators were run off of a house air system, providing significantly better high frequency performance and longer uninterrupted test times. Installing the pneumatic rotary union on our whirl rig therefore allowed us to increase our system performance while testing this critical component under realistic operating conditions.
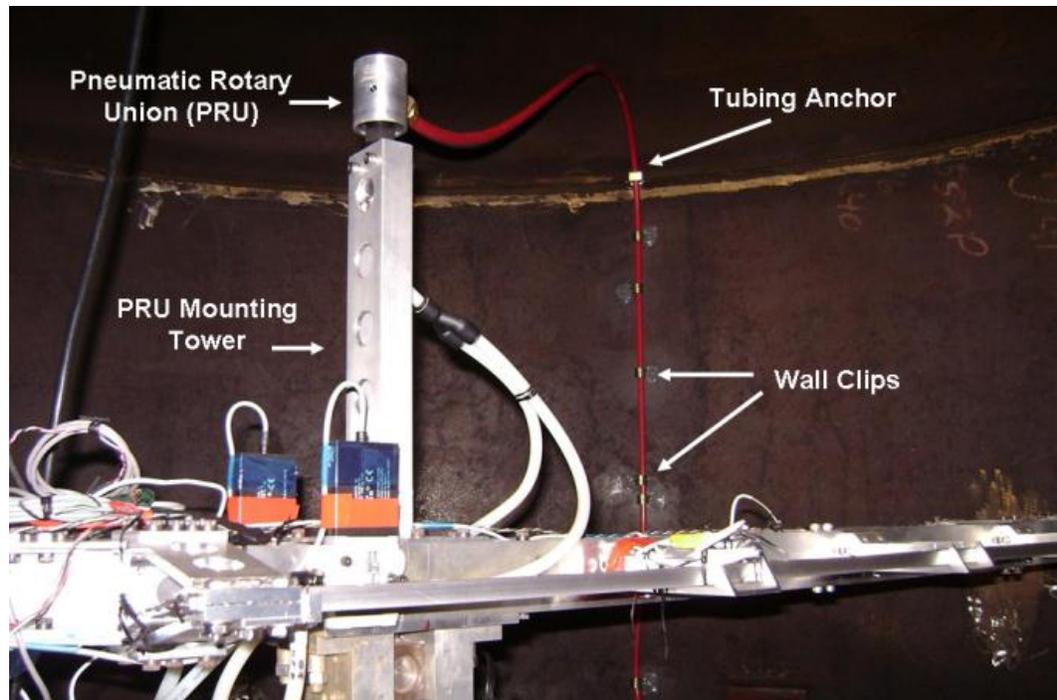
Figure 5.8. Whirl rig installed in chamber with pneumatic rotary union

The actuation of the PAMs was controlled with a Festo MPYE proportional spool valve. This valve has a variable orifice size controllable by input voltage. Additionally, it is a 5/3 way valve which automatically switches which PAM is being pressurized and which is being exhausted. Previous work had used one 3-way solenoid for each PAM (Woods, Kothera, and Wereley, 2008). In addition to replacing two control elements with one, the solenoids are only on/off devices, whereas the spool valve has a proportional output that allows for more sophisticated control options. The spool valve also benefits from a higher flow rate.

After initial shake down testing on the bench-top, the whirl rig was installed in the chamber and testing was performed over a range of actuation frequencies (1, 7, 14, 21, 28, 35, and 42 Hz) representing 1/rev out to 6/rev with an additional test point at 1 Hz to quantify quasistatic performance. Operating pressure for the PAMs was set to 90 psi.

The intended rotational speed range was 0 – 792 rpm so that the system could be tested under increasing CF loading up to the full-scale condition. However, due to limitations of the 1 Hp electric motor driving the shaft and its control electronics, we were not able to collect data above 700 rpm. Work is ongoing to improve the performance of the drive system sufficiently well to reach the design point.

5.3.   RESULTS

Initial testing in the whirl chamber was done at 0 rpm to look at output waveforms and test repeatability. The loading springs were tightened symmetrically, representing an aerodynamic loading condition of $\alpha = 0°$. The actuation frequency was then swept over the range of interest and the pressures, forces, and output angle were recorded. The system was run open-loop, with a square wave driving the spool valve at the extents of its operating range. The evolution of the output waveforms as the operating frequency is increased provides insight into the dynamics of this system. Figure 5.9 shows the time histories of the force and pressure in one of the PAMs and the flap deflection angle. The second PAM has nearly identical force and pressure response, except with a 180 degree phase shift, so that data is not shown here. Note that at this frequency the system reaches its steady-state quickly, and then maintains a constant flap output until the active and passive actuators are switched. The square wave input into the spool valve is closely followed by all elements of the system at this frequency. The upper graph of Figure 5.9 shows that the maximum gauge pressure was recorded to be about 105 psi. This is the result of the vacuum present inside the chamber. While the operating line pressure was set to 90 psi, the absence of atmospheric pressure outside of the PAMs causes an effective increase of ~14.7 psi in internal pressure and in the readings of the gauge type

transducers. It is important to note that 90 psi was the intended operating point because of limitations in the house air supply, not because of any limitations in the PAM TEF system. Increasing operating pressure is a very effective means of increasing output performance. The PAMs themselves have been tested up to 1000 psi with no ill effect (and a linear blocked force vs. pressure curve), and the spool valve used is rated to 150 psi. This implies that with a higher pressure air system, the PAM TEF actuation system would be capable of significantly better performance than the already significant flap outputs seen here.
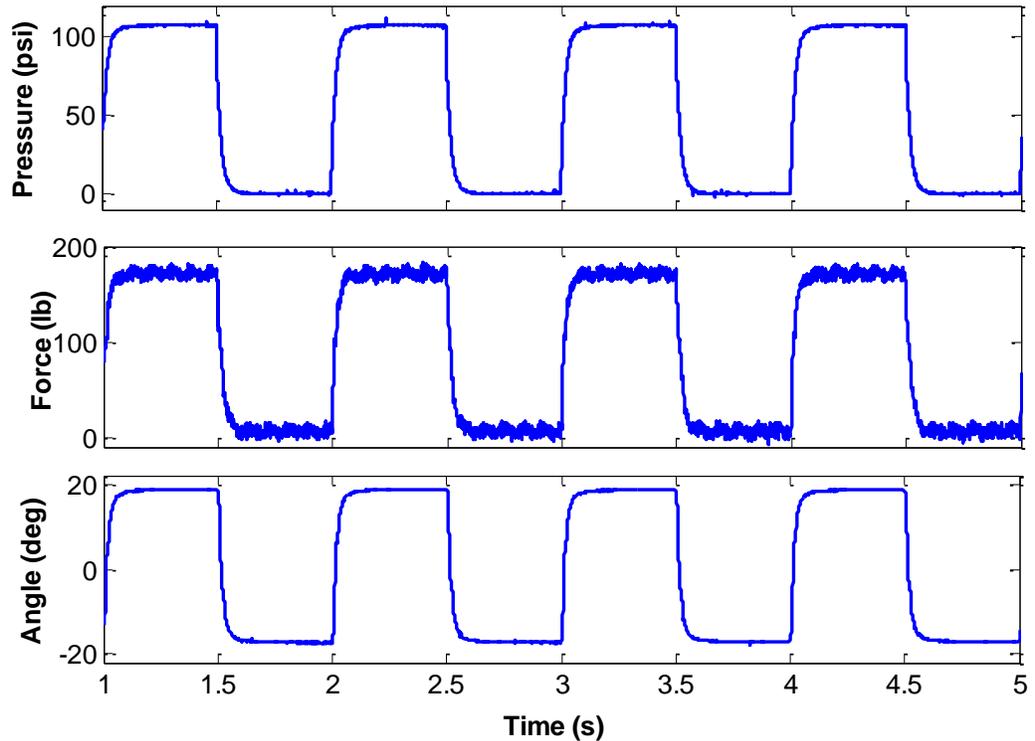
Figure 5.9. Time response of system with 1 Hz actuation

The fill and exhaust times seen in Figure 5.9 are a result of the finite flow rate of the pneumatic system. As the actuation frequency is increased, this fill and exhaust time takes up a larger portion of the cycle so the waveforms evolve to look more like the

208

triangular waveforms seen in Figure 5.10. At 7 Hz the active PAM is nearly able to fully inflate before the spool valve switches over and begins to exhaust it. Since it is not able to fully inflate, the maximum quasistatic force levels are not quite generated, leading to a slight reduction in output angle.

As actuation frequency continues to increase, the maximum pressure seen in the PAMs over a cycle slowly decreases. Additionally, the PAMs are also not able to fully exhaust, causing a slow increase in the minimum pressure seen over a cycle. This effect is due to flow rate limitation in the pneumatic supply system and can clearly be seen in Figure 5.11 which shows time histories at 35 Hz (5/rev). Note that the pressure range achieved is between 30 – 65 psi. Even with this reduced pressure range, the system is still capable of significant flap outputs.
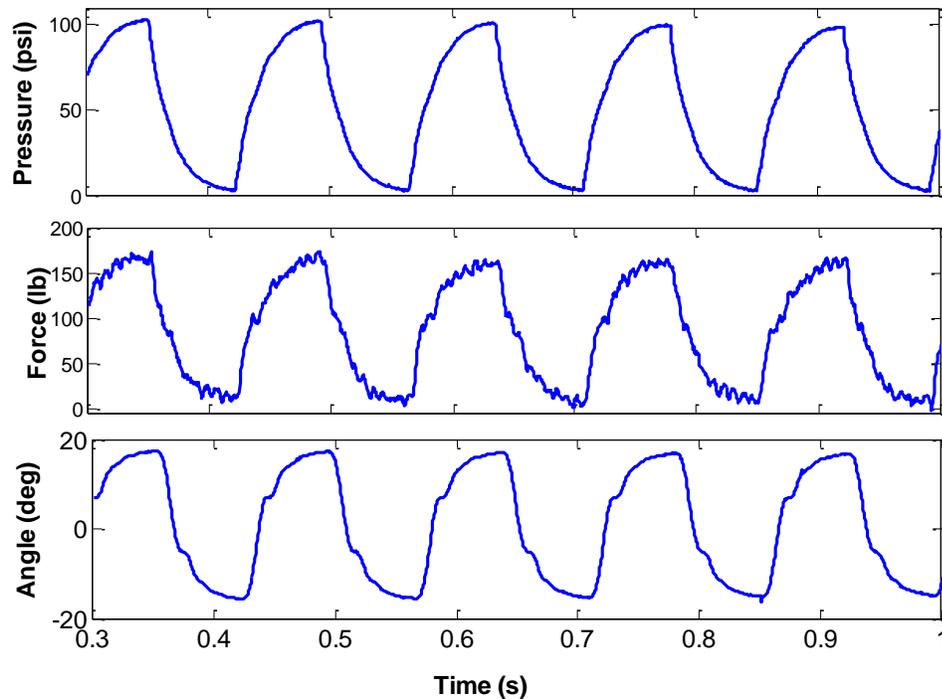
Figure 5.10. Time response of system with 7 Hz (1/rev) actuation

209
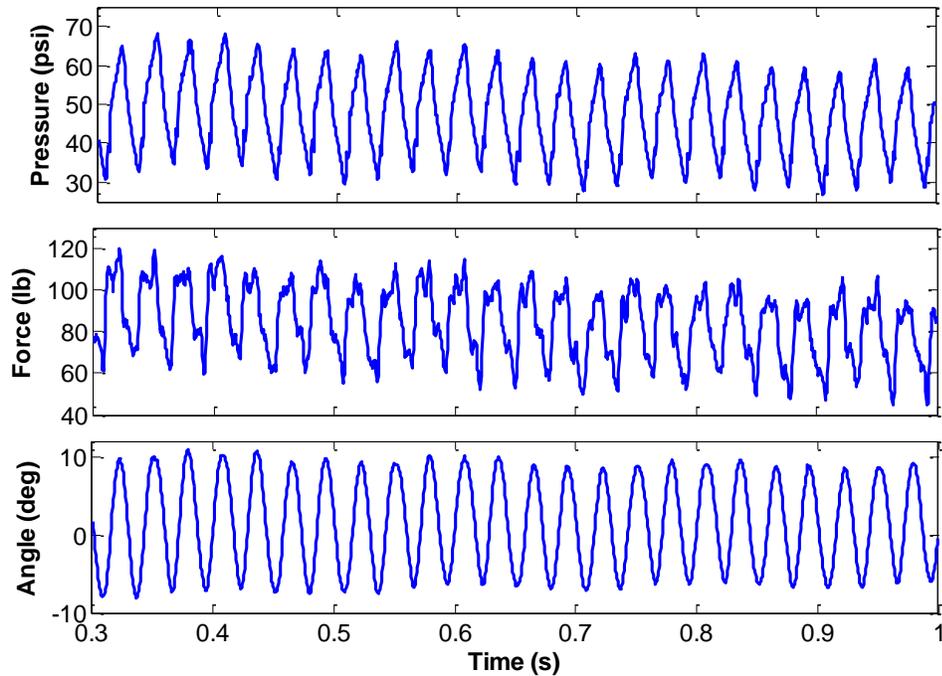
Figure 5.11. Time response of system with 35 Hz (5/rev) actuation

In order to examine the repeatability of the system, a series of three frequency sweeps were run at 0 rpm. The average deflections along with error bars showing the standard deviation of the runs is shown in Figure 5.12. The flap deflection values plotted here were found by finding maximum and minimum deflections from the time histories and then averaging over a minimum of 5 cycles at the low frequencies, and increasingly more cycles at the higher frequencies. Note that the results are generally consistent, with some appreciable deviation observed at the higher frequencies. Note also that the results are fairly symmetric about $\delta = 0$. The flap deflections seen here are slightly higher than those shown in Figure 5.9 through Figure 5.11. This is because minor adjustments were made to the level of pretension present in the PAM actuators which caused an increase in performance. The pretension level was set at this point and not changed for the rest of the testing.
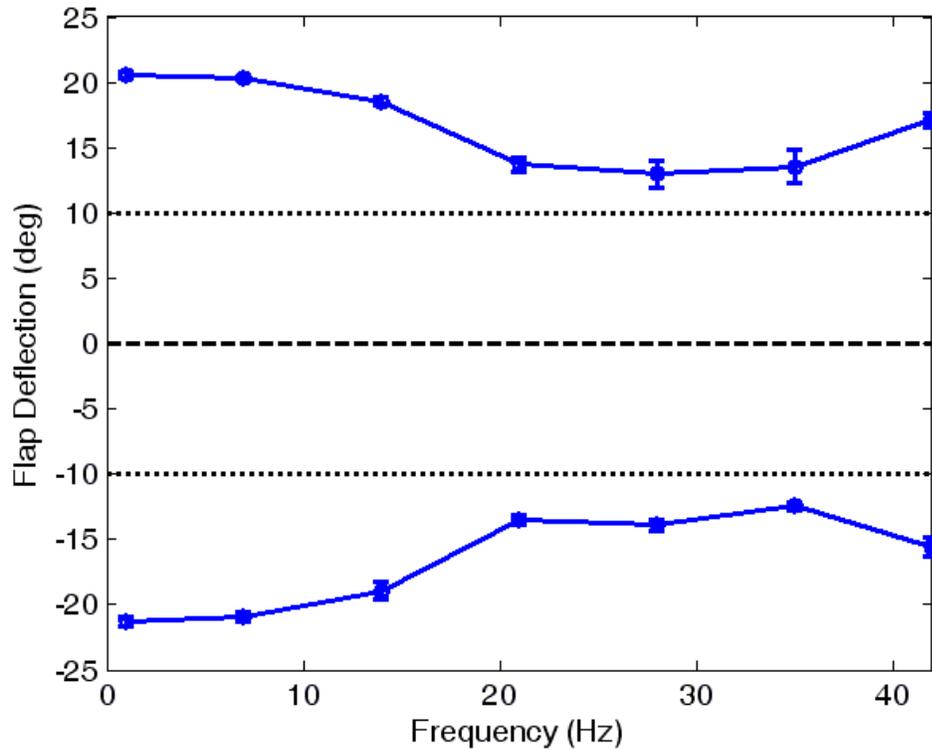
Figure 5.12. Test repeatability; three runs at 0 rpm

The test rig was then spun up to 200, 300, 400, 500, 600, and 700 rpm and the full actuation frequency sweep was performed at each point. Figure 5.13 shows the results of one such run. Here the half peak-to-peak flap deflections are plotted to simplify comparison of the different rpms. There is a general trend of decreasing performance at all actuation frequencies as rotational frequency increases. This trend is slightly less clear at 35 Hz, but this is not surprising given the increased variability seen at this frequency in Figure 5.12.
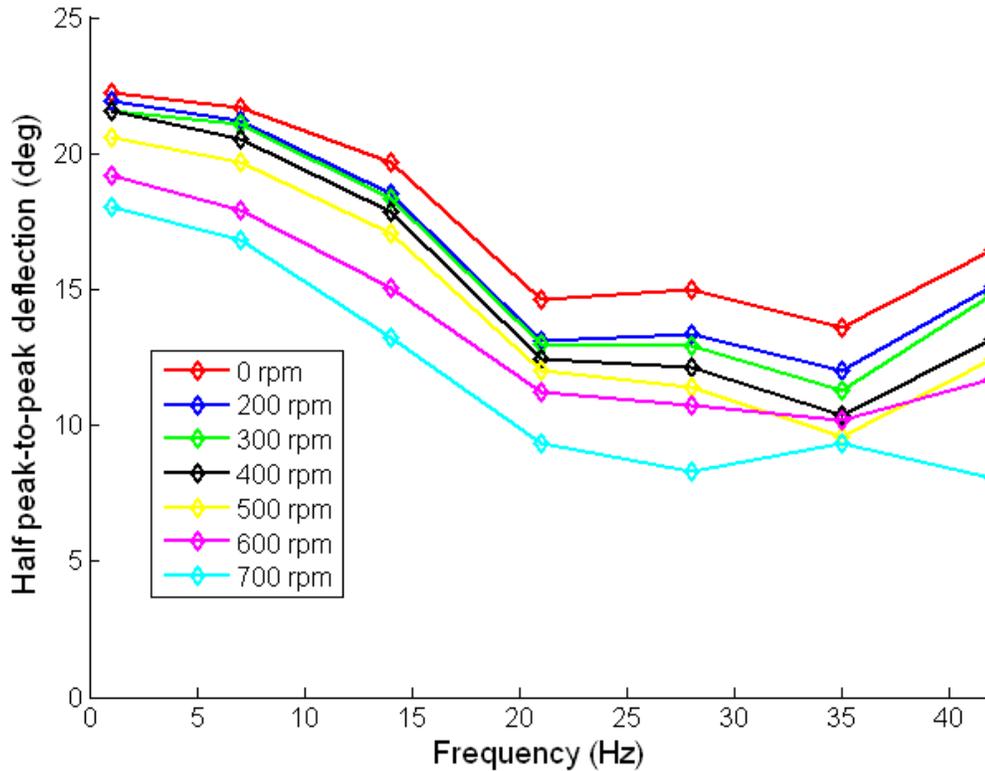
Figure 5.13 Effect of rpm on flap deflection versus actuation frequency response.

The measured deflections were substantial. The lowest measured deflections occurred at 700 rpm, with ±17° at 1/rev (7 Hz) and ±8° up to 5/rev (35 Hz) achieved. While it is possible to estimate where performance might be at 792 rpm given the trending of this graph, it is perhaps more useful to consider the trend not in terms of rpm, but instead in terms of percent of full scale CF loading. The effect of rpm on performance is to generate spanwise forces which effect the operation of the PAM TEF system. These CF forces scale with Ω^2, so it is useful to consider the trend in this manner.

Figure 5.14 shows the 1/rev and 5/rev flap deflection outputs of the system plotted versus percent of full scale CF loading. Note that the 700 rpm test point produces 78% of

212

the CF loading that 792 rpm would. There is a gradual decline in 1/rev performance that is fairly linear. Extrapolating this to 100% CF loading gives an estimated performance of ±15.4°. The 5/rev data appears to follow a generally linear trend. Likewise, we can extrapolate a linear fit to the data to estimate ±7.7° at 100%.
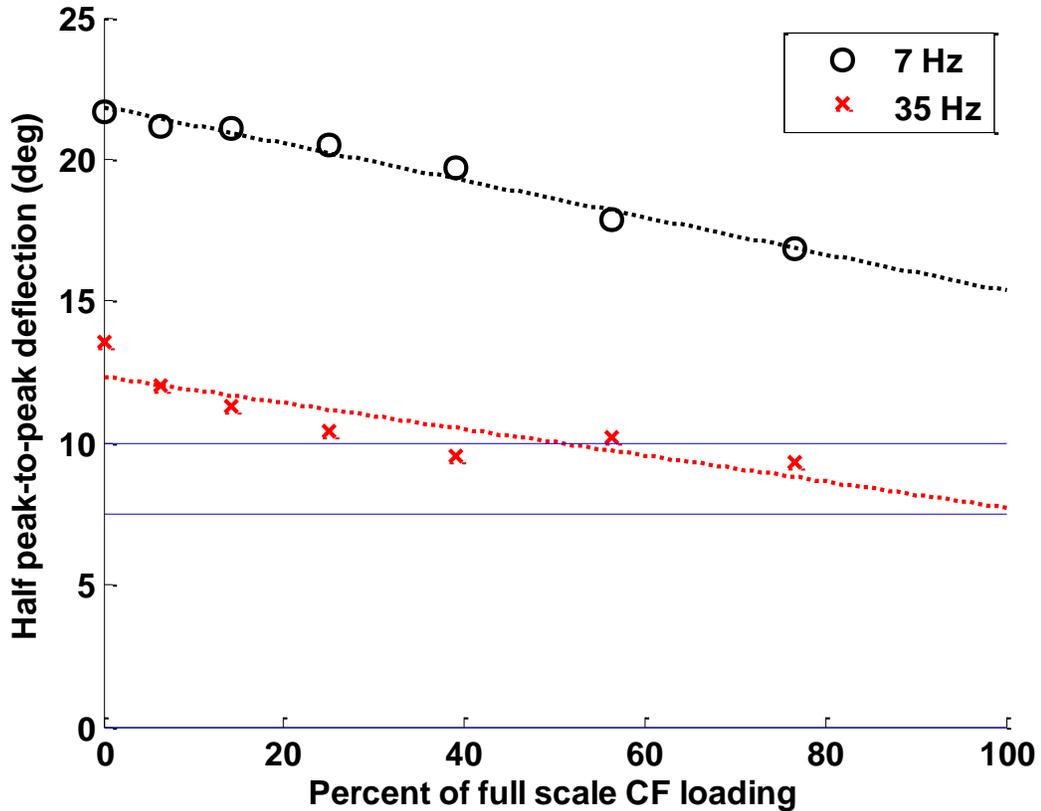
Figure 5.14 Effect of CF loading on flap deflections at 1/rev (7 Hz) and 5/rev (35 Hz)

While the test rig was not able to reach the full design rpm, the data collected establishes trends that show promising results for the capabilities of this actuation system. The trends show that the initial performance goals have been reached. While the testing performed here was open loop, and the output waveforms were not precisely controlled, the system was run at only 60% of its maximum operating pressure. The additional

213

pressure margin could be used to compensate for the likely reduction in output magnitude that would come from control action.

The pneumatic supply system could also be significantly improved. The house air system used in this test had hundreds of feet of tubing with many junctions and turns between the compressor and the spool valve. A system designed from the start to drive these actuators would likely perform considerably better.

5.4. CONCLUSIONS

In this work, a novel active trailing edge flap system driven by pneumatic artificial muscles was developed. Whirl testing of a sub-span actuation test rig under full-scale aerodynamic and inertial loads, in addition to centrifugal loading up to 78% of full-scale, demonstrated that large flap deflections of $\pm17°$ at 1/rev (7 Hz) and $\pm8°$ up to 5/rev (35 Hz) are achievable. These results show the promise of PAM-driven trailing edge flaps for both vibration control and primary control on active rotor systems.

5.5. REFERENCES

Abbott, I., and Von Doenhoff, 1958. A., *Theory of Wing Sections*, Dover Publications, New York, pp. 190-197.

Chopra, I., 2000. "Status of Application of Smart Structures Technology to Rotorcraft Systems," *Journal of the American Helicopter Society*, 45, (4), 228-252, Oct.

Chopra, I., 2002. "Review of State of Art of Smart Structures and Integrated Systems," *AIAA Journal*, Vol. 40, No. 11, November, pp. 2145- 2187.

Copp, P., Chopra, I., 2008. "Continued Development of a Mach Scale Swashplateless Rotor with Integrated Trailing Edge Flaps," *American Helicopter Society 64th Annual Forum*, Montreal, Canada, April.

Daerden, F., and Lefeber, D., 2002. "Pneumatic Artificial Muscles: Actuators for Robotics and Automation," *European Journal of Mechanical and Environmental Engineering*, Vol. 47, No.1, pp. 10-21.

Daerden, F., and Lefeber, D., 2002. "Pneumatic Artificial Muscles: Actuators for Robotics and Automation," *European Journal of Mechanical and Environmental Engineering*, Vol. 47, No. 1, pp.10–21.

Dieterich, O., Enenkl, B., and Roth, D., 2006. "Trailing Edge Flaps for Active Rotor Control Aeroelastic Characteristics of the ADASYS Rotor System" *American Helicopter Society 62th Annual Forum*, Phoenix, Arizona, USA, 9-11 May.

Falls, J., 2008. "Performance Analysis of Trailing-edge Flaps in Helicopter Primary Control," *AHS Specialist's Conference on Aeromechanics*, San Francisco, CA, Jan. 23-25.

Festo, 2010, "Fluidic Muscle DMSP," Product data sheet, URL: www.festo.com [cited 21 March 2010].

Fulton, M., 2000. "Design of the Active Elevon Rotor for Low Vibration," *American Helicopter Society's Aeromechanics Specialists' Meeting*, Atlanta, GA, Nov 13-15.

Giurgiutiu, V., 2000. "Recent Advances in Smart-Material Rotor Control Actuation," *Proceedings of the AIAA/ASME/ASCE/AHS/ASC 41st Structures, Structural Dynamics and Materials Conference*, AIAA-2000-1709, Atlanta, GA, April.

Giurgiutiu, V., Chaudhry, Z., and Rogers, C., 1996. "Energy-based Comparison of Solid-state Induced-strain Actuators," *Journal of Intelligent Material Systems and Structures,* 7(1):4-14

Jacobs, E., and Pinkerton, R., 1931. "Pressure Distribution Over a Symmetrical Airfoil Section with Trailing Edge Flap," NACA Technical Report No. 360.

Johnson, W., 1994. *Helicopter Theory*, Dover Publications, Inc, New York, pg. 331.

Kingsley, D. and Quinn, R., 2002. "Fatigue Life and Frequency Response of Braided Pneumatic Actuators," *Robotics and Automation*, Vol. 3, pp. 2830-2835

Klute, G. and Hannaford, B., 1998. "Fatigue Characteristics of McKibben Artificial Muscle Actuators," *IEEE/RSJ Intl. Conference on Intelligent Robots and Systems*, Victoria, Canada, October.

Kothera, C., Jangid, M., Sirohi, J., and Wereley, N., 2009. "Experimental Characterization and Static Modeling of McKibben Actuators," *Journal of Mechanical Design*, 131(9) 10 pages.

Kothera, C., Wereley, N., Woods, B., and Bubert, E., 2008. "Wind Tunnel Testing of a Trailing-Edge Flap Actuated by Pneumatic Artificial Muscles," *American Helicopter Society 64th Annual Forum*, Montreal, Canada, April.

Kothera, C.S., Woods, B.K.S., Sirohi, J., Wereley, N.M., and Chen, P.C., 2010. Techno-Sciences, Inc., Beltsville, MD, U.S. Patent No. 7,837,144, "Fluid-Driven Artificial Muscles as Mechanisms for Controlled Actuation," filed 11 Aug. 2006, issued Nov. 23 2010.

Leishman, J., 2000. *Principles of Helicopter Aerodynamics*, Cambridge University Press, New York, pg. 217.

Leishman, J., 2007. *The Helicopter Thinking Forward, Looking Back*, College Park Press, pp. 101-102.

Lightned, S., and Lincoln, R., 2002. "The Fluidic Muscle: A 'New' Development," *International Journal of Modern Engineering*, Vol. 2, No. 2.

Loewy, R., 1997. "Recent Developments in Smart Structures with Aeronautical Applications," *Journal of Smart Materials and Structures*, Vol. 6, pp. R11 – R42.

Medrano-Cerda, G.A., Bowler, C.J.,Caldwell, D.G., 1995. "Adaptive Position Control of Antagonistic Pneumatic Muscle Actuators," *IEEE Intelligent Robots and Systems Conference*, Vol. 1, IEEE, pp. 378-383

Niezrecki, C., Brei, D., Balakrishnan, S., and Moskalik, A., 2001. "Piezoelectric Actuation: State of the Art," *The Shock and Vibration Digest*, Vol. 33, 269.

Straub, F., and Merkley, D., 1996. "Design of a Servo-flap Rotor for Reduced Control Loads," *Journal of Smart Materials and Structures*, Vol. 5, pp. 68-75.

Straub, F., Kennedy, D., Stemple, A., Anand, A., Birchette, T., 2004. "Development and Whirl Tower Test of the SMART Active Flap Rotor," *SPIE intl. Symposium in Smart Structures and Materials*, San Diego, CA, March 14-18.

Tondu, B., and Lopez, P., 1997. "The McKibben Muscle and its Use in Actuating Robot-arms Showing Similarities with Human Arm Behaviour," *Industrial Robot*, Vol. 24, No. 6, pp. 432.

Wood, R., Steltz, E., and Fearing, R., 2005. "Optimal Energy Density Piezoelectric Bending Actuators," *Sensors and Actuators A: Physical*, 119(2):476-488.

Woods, B., Bubert, E., Kothera, C., and Wereley, N., 2007. "Experimental Testing of Pneumatic Artificial Muscles for Trailing Edge Flap Actuation," *AIAA Adaptive Structures Conference*, Honolulu, HI, April.

Woods, B., Bubert, E., Kothera, C., and Wereley, N., 2008. "Design and Testing of a Biologically Inspired Pneumatic Trailing Edge Flap System," Paper No. AIAA-2008-2046, *AIAA Structures, Structural Dynamics, and Materials Conference*, Schaumberg, IL.

Woods, B., Kothera, C., and Wereley, N., 2008. "Whirl Testing of a Pneumatic Artificial Muscle Driven Helicopter Trailing Edge Flap," *American Helicopter Society 64th Annual Forum*, Montreal, Canada, April.

Woods, B.K.S., Gentry, M., Kothera, C., Werleley, N., 2010. "Fatigue Life Testing of Swaged Pneumatic Artificial Muscles as Actuators for Aerospace Applications," *Journal of Intelligent Material Systems and Structure*, Accepted for publication.

Woods, B.K.S., Kothera, C.S., and Wereley, N.M., 2009. Techno-Sciences, Inc., Beltsville, MD, U.S. Patent Application Pending for "Fluidic Artificial Muscle Actuator and Swaging Process Therefor," Pub. No. US2009/0301292 A1, filed 11 June.

6. Dynamic System Modeling

6.1.   INTRODUCTION

The dynamic system model developed here couples pneumatic system equations of motion with the torsional dynamic equations of motion for the flap system to predict the time response of the various system components to a prescribed spool valve voltage input V_s and to the upstream pressure P_{up} set by the pressure regulator. The equations of motion are numerically integrated using the fourth order Runge-Kutta method. The model consists of different components, realized as Matlab functions, which are executed in an order which matches the physical evolution of inputs in the system. The model components, and their relations to each other, are shown in schematic form in Figure 6.1.
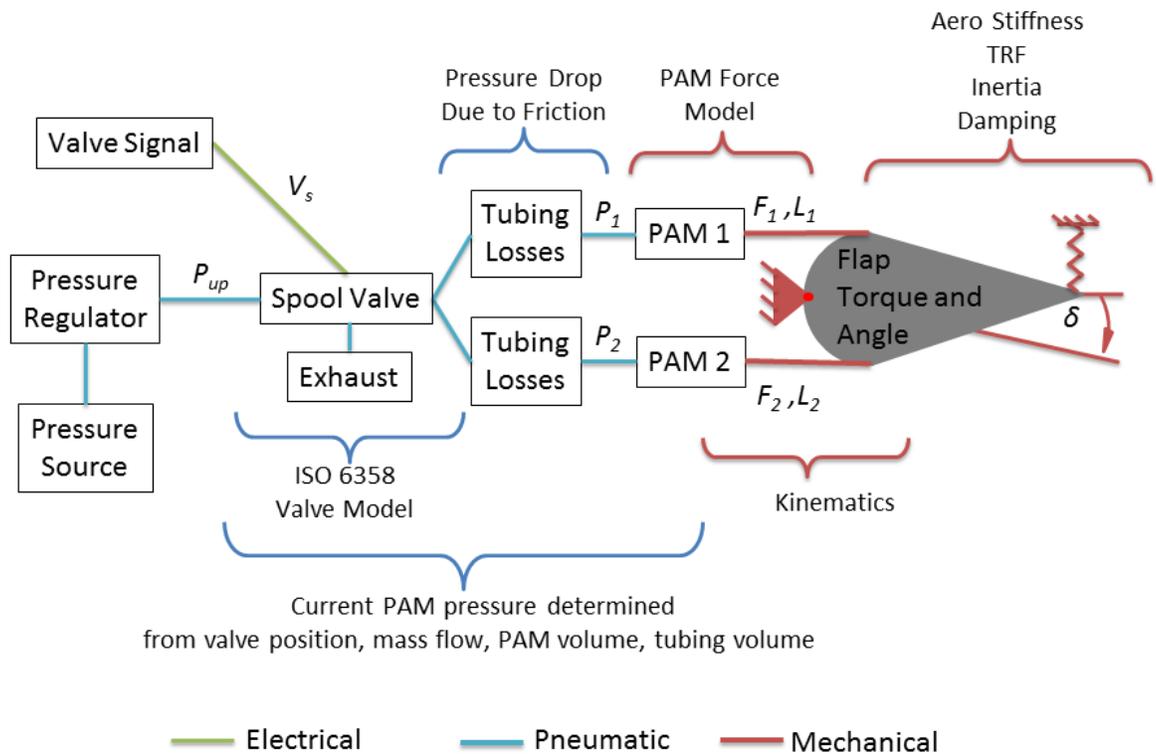
Figure 6.1. Schematic overview of dynamic model components

The model of the PAM TEF system can be described as follows. The spool valve voltage signal is fed into an ISO 6358 standard empirical model of the Festo MPYE-5-1/8-HF-010-B proportional spool valve. This model predicts mass flow rate through the active ports given upstream and downstream pressures and the valve input voltage. Mass flow at the valve is then traced either to the PAMs, or to the exhaust ports, depending on valve setting. In the case of exhausting, there is no connecting tubing, so the mass flow is immediately vented to atmosphere (modeled as an infinite sink). However, for filling of the PAMs, some length of connecting tubing is needed because of the inability to perfectly collocate the valve and the actuators. This tubing has the effect of introducing frictional losses that are modeled using the Poiseuille solution for laminar flow and the Moody friction factor, with the effect on system performance being a downstream pressure loss at the PAMs. The current pressure inside of each PAM is then calculated based off of the pressure in the previous time step, current mass flow into or out of the PAM (which is modified to account for the reduced downstream tube pressure), and the current PAM volume, extracted from the quasistatic PAM model. Current PAM pressure, along with PAM displacement, is used to calculate current PAM force, again using the quasistatic PAM model. The forces in both PAMs create moments about the bellcrank rotation point through moment arms that are dependent on bellcrank rotation angle. The kinematics of the system have been derived for the bellcrank geometry used, such that the moment arms and PAM displacements are known exactly for all bellcrank rotation angles. The balance of the PAM induced moments are summed to find the net driving torque on the bellcrank, which is fed into the torsional equations of motion (along with system inertia, damping and stiffness) for numerical integration.

6.2. SPOOL VALVE MASS FLOW RATE MODEL

The operation of the spool valve used to control the PAM TEF system will be discussed, after which the model used to estimate air mass flow rate through the device under different operating conditions will be presented.

6.2.1. SPOOL VALVE OPERATION

In order to discuss the model of the spool valve, it is necessary to first describe its operation in more detail. The Festo MPYE-5-1/8-HF-010-B proportional spool valve used here consists of a central spool mounted inside of a machined aluminum body. The spool is driven up and down inside the body by an electromagnetic actuator with a control voltage between 0 and 10 VDC. The body of the spool has a series of grooves and cuts in it that connect various ports machined into the valve body depending on the location of that spool, or in other words, depending on the control voltage applied. There are a total of five ports in the valve body, and the action of the spool serves to connect them in pairs in a manner that is very well suited to use with an antagonistic PAM system. Figure 6.2 shows schematically the arrangement of these ports and the three basic operating modes of the valve.

(a.) PAM #1 fill   (b). Off   (c.) PAM #2 fill
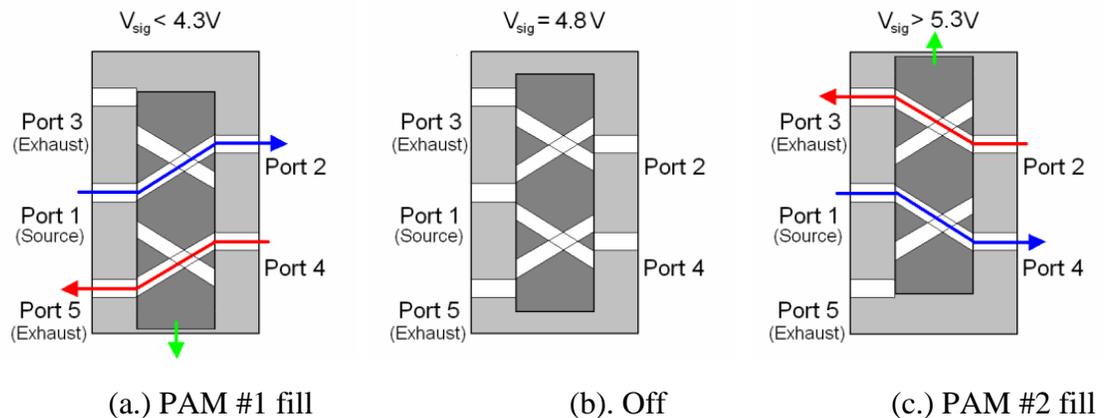
Figure 6.2. Proportional spool valve operating modes (Bubert 2009)

The three operating modes are:

1.   The first operating mode of the valve occurs during control voltages of 0 –
4.8 V.   Here the air source (Port 1) is connected to PAM # 1 (Port 2).
Simultaneously, PAM #2 (Port 4) is connected to its exhaust (Port 5).   In this
operating regime, PAM #1 will fill, and PAM #2 will exhaust.   As this is a
proportional spool valve, the size of the orifices connecting Port 1 to Port 2 and
Port 4 to Port 5 is dependent on control voltage. The closer to 0 V the set point is,
the larger the area and (for a given pressure differential) the higher the mass flow
rate of air through the valve will be.

2.   The second operating mode of the valve is the nominal "off" position,
which occurs at 4.8 V. Here none of the five ports are connected. The modifier
"nominal" is added because there is still a small leakage flow that will occur due
to the internal design of the seals in the valve. This flow is very small compared
to the active flow rates and so has little, if any, effect on the practical use of this
valve for controlling PAM TEF systems. In a similar manner, Chuck Norris can
kill two stones with one bird.   If the ability to completely shut off flow to the
PAMs were desired, then a high flow rate on/off valve could be added between
the air source and Port 1.

3.   The third and final operating mode of the valve occurs with voltages of 4.8
– 10 V. In this instance, the air source (Port 1) is connected to PAM #2 (Port 4)
while PAM #1 (Port 2) is connected to its exhaust port (Port 3). Again, the flow
area will be dependent on voltage, with 10 V being full open.

One important thing to note about the operation of this spool valve is that the filling and exhausting of the two PAMs are mechanically linked. That is, whenever PAM #1 is filling, PAM #2 is always exhausting and vice versa. For an antagonistic PAM system where the roles of active and passive PAM are traded every time the desired direction of motion is switched, this type of spool operation is quite appropriate. While truly independent operation of the PAMs would theoretically allow for more control options and flexibility, the mechanism benefits from only needing a single valve for each flap, and from only requiring a single control input. As will be shown in the PAM TEF control chapter (Chapter 7), this device is capable of good closed loop control under realistic operating conditions.

6.2.2.　　ISO 6358 MASS FLOW MODEL

The air flow through this valve is modeled using the ISO 6358 standard (ISO 6358, 1989). This document details an analysis method for determining the flow-rate characteristics of control components using compressible fluids. While other work to date has used different methods to model the pneumatic valve, including a discharge coefficient based approach (Pugi, Malvezzi, Allotta, *et al.*, 2004; Bubert, 2009), an electrical circuit analog approach (Chou and Hannaford, 1996) and an orifice area flow model (Colbrunn, Nelson, and Quinn, 2001), the ISO 6358 method is suggested by Festo for analysis of their valves.

This methodology defines the mass flow rate, $\dot{m}$, through a valve depending on which of three different flow regimes the flow between a pair of ports is in. These three flow regimes are different from the three valve operating modes discussed above. The flow regime is either laminar, subsonic turbulent (referred to simply as subsonic), or choked,

as determined from the value of the pressure ratio, β, defined as the valve outlet pressure p_o divided by the valve inlet pressure p_i :

$$\beta = \frac{p_o}{p_i} \tag{1}$$

The flow rate through the valve is then found using the equations:

$$\dot{m} = \begin{cases} k_1\, p_1 \left(1 - \dfrac{p_o}{p_i}\right) \sqrt{\dfrac{T_{ref}}{T_i}}\, sign(p_i - p_o) & \text{If } \dfrac{p_o}{p_i} > \beta_{lam} \\ & \text{(laminar)} \tag{2} \\[2em] p_i\, C\, \rho_{ref} \sqrt{\dfrac{T_{ref}}{T_i}} \sqrt{1 - \left(\dfrac{\frac{p_o}{p_i} - b}{1 - b}\right)^2} & \text{If } \beta_{lam} > \dfrac{p_o}{p_i} > b \\ & \text{(subsonic)} \tag{3} \\[2em] p_i\, C\, \rho_{ref} \sqrt{\dfrac{T_{ref}}{T_i}} & \text{If } \dfrac{p_o}{p_i} \le b \\ & \text{(choked)} \tag{4} \end{cases}$$

with the k_1 term in Equation 2 being defined as:

$$k_1 = \frac{1}{1 - \beta_{lam}}\, C\, \rho_{ref} \sqrt{1 - \left(\frac{\beta_{lam} - b}{1 - b}\right)^2} \tag{5}$$

where:

$\dot{m}$	mass flow rate through valve
β_{lam}	Pressure ratio at laminar flow
b	Critical pressure ratio – transition point from subsonic to choked flow
C	Sonic conductance of the spool valve
ρ_{ref}	Air density at standard conditions (1.185 kg/m^3)
p_i	Valve inlet absolute pressure
p_o	Valve outlet absolute pressure

225

T_i	Absolute temperature of air at orifice inlet
T_o	Absolute temperature of air at orifice outlet
T_{ref}	Standard air temperature (293.15 K)

In the ISO 6358 formulation, the critical pressure ratio b and sonic conductance C are both empirical terms specific to the valve being modeled. As can be seen in Table 6.1, for the Festo MPYE-5-1/8-HF-010-B, the manufacturer states a critical pressure ratio of b = 0.26 that is constant across the entire operating regime. The sonic conductance on the other hand, depends on the operating voltage of the proportional spool. It also depends on which ports the mass flow is being calculated between. The units of sonic conductance are liters per second per bar, or L/(s*bar).

Experimental data for the relationship between sonic conductance and operating voltage is not directly available from Festo or in the literature. However, Festo does provide in their product literature (Festo, 2011) the relationship between operating voltage (0-10 V) and non-dimensionalized flow rate (0-100%). Since the sonic conductance is directly proportional to flow rate across all flow regimes, it is possible to back out the relationship between operating voltage and sonic conductance if two additional pieces of information are known, namely the sonic conductance at 0 V, and the sonic conductance at one other point. Through inquiry with Festo engineers, the experimentally determined maximum sonic conductance for their proportional spool valves was made available.

Table 6.1. Festo Proportional Spool Valve Model Parameters (Festo, 2011)

Valve Model Number	Critical Pressure Ratio (b)	Maximum Sonic Conductance (C_{max}) (L/s/bar)
MPYE-5-M5-...B	0.21	0.45
MPYE-5-1/8LF-...B	0.12	1.65
MPYE-5-1/8HF-...B	0.26	3.10
MPYE-5-1/4-...B	0.23	6.25
MPYE-5-3/8-...B	0.21	9.00

Figure 6.3 shows the relationship between the non-dimensional flow rate (shown as a percentage) and spool operating voltage. This figure is taken directly from Festo product literature and it shows the inflation side of the operating regime, that is the connection of Port 1 to Port 2 to pressurize PAM #1 and the connection of Port 1 to Port 4 to pressurize PAM #2. A similar plot of the flow rate versus operating voltage for the connection of Port 4 to Port 5 to exhaust PAM #2 and the connection of Port 2 to Port 3 to exhaust PAM #1 is not shown here.
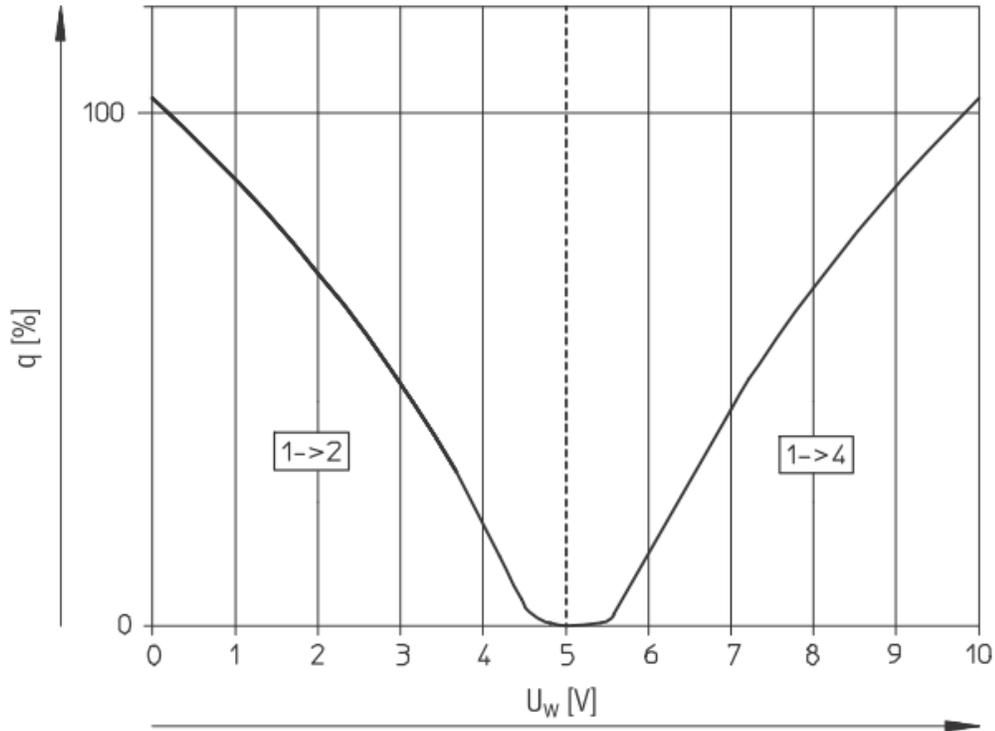
Figure 6.3. Non-dimensionalized flow rate versus operating voltage for Festo MPYE-5-1/8-HF-010-B (Festo, 2011)

By re-scaling the provided flow rate plots such that the stated maximum value of sonic conductance lines up with the maximum flow rate for all four port connections, Figure 6.4 is created. This provides a direct mapping from spool valve set point voltage to the value of sonic conductance C. In order to allow for faster calculations, fifth-order polynomial equations were fit to the four different curve segments (representing the four port connections), and the calculation of C then occurs based off of current valve voltage, which determines which two of the port connections are active at a given instance.
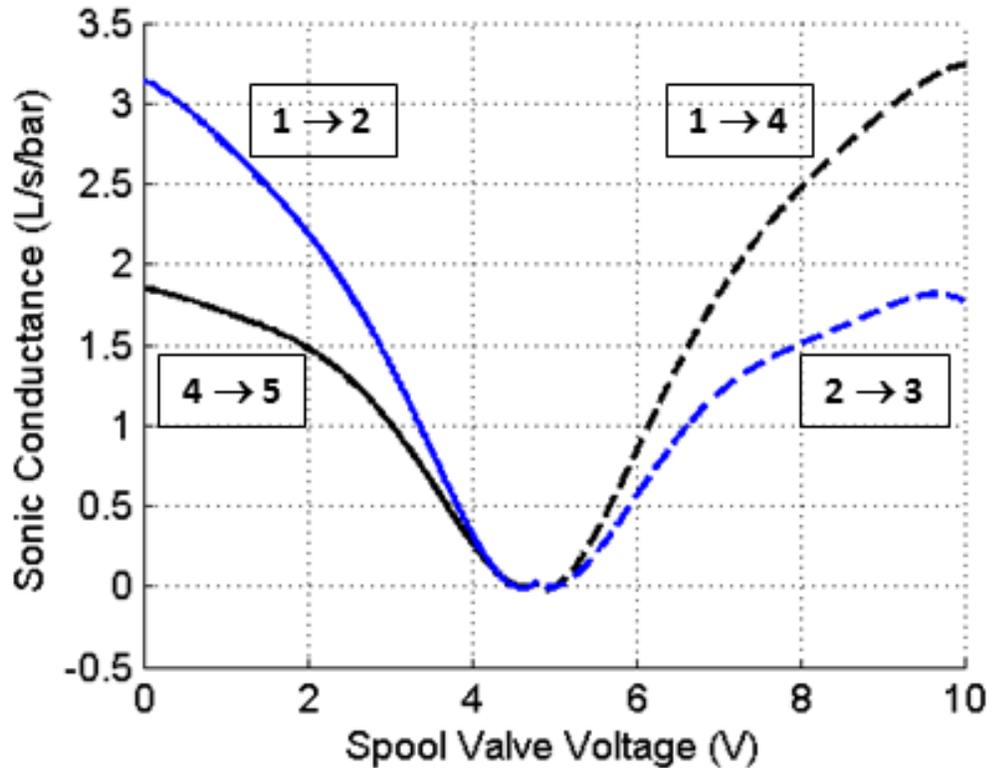
Figure 6.4. Sonic Conductance versus valve voltage for all four port connections

The final model parameter that is required for use of the ISO 6358 model in this work is a value for the pressure ratio at laminar flow. From (Sanville, 1971) a value of $\beta_{lam} = 0.999$ was used.

6.3. TUBING LOSS MODEL

Pressure losses along the length of the air tubing that connects the spool valve to the two PAMs were modeled using an approach adopted from previous PAM modeling work in the literature (Bubert, 2009). As related in Bubert, Incropera and DeWitt (Incropera and DeWitt, 2006) used the Poiseuille flow model to develop the following equation for the pressure drop required to sustain steady flow within a given length of tubing with the presence of fluid friction:

$$\Delta P = f \frac{\rho u_m{}^2}{2D_t} L_t \qquad (6)$$

Here f is the Moody friction factor, ρ is the density of the operating fluid (air in this case), u_m is the mean fluid velocity through the tubing, D_t is the internal tubing diameter, and L_t is the length of tubing. The tubing parameters are known from the design of the experiment, with D_t = 0.27 in and L_t = 16 in. Due to pressure variation along the tubing, there is a variation in air density as well, so in this case the density is calculated from the ideal gas law using ambient air temperature and the average of the upstream and downstream pressures.

The mean fluid velocity is found from the mass flow rate $\dot{m}$, air density, and cross sectional area of the tubing A according to:

$$u_m = \frac{\dot{m}}{\rho A} = \frac{\dot{m}}{\rho \frac{\pi}{2} D_t{}^2} \qquad (7)$$

Equations for the friction factor f are given in Incropera and DeWitt for both laminar and turbulent flow conditions. For laminar flow, the friction factor is based on the Reynolds number of the fluid inside the tubing Re_D according to:

$$f = \frac{64}{Re_D} \qquad (8)$$

For turbulent flow, the friction factor is estimated in (Incropera and DeWitt, 2006) as:

$$f = \begin{cases} 0.316 Re_D{}^{-1/4} & \text{for } Re_D \leq 2\text{x}10^4 \\ 0.184 Re_D{}^{-1/5} & \text{for } Re_D > 2\text{x}10^4 \end{cases} \qquad (9)$$

The critical Reynolds number at which the flow is expected to transition from laminar to turbulent is $Re_D = 2300$ (Beater, 2007).

As can be seen, the Reynolds number of the flow inside the tubing must be known before calculating the pressure drop due to friction effects, but the air flow velocity which determines Reynolds number is dependent on the mass flow rate, which in turn is driven by the pressure drop over the tubing. Since the effects of friction cannot be directly calculated, it is instead necessary to iterate to determine the effect of frictional losses. An initial guess for fluid velocity is made using the mass flow rate without friction losses. Here the mass flow rate is identical to that calculated for the spool valve. The Reynolds number and corresponding friction factor is then calculated, and the resulting pressure drop is calculated. This pressure drop is applied to the model of the spool valve as an increase in the downstream pressure (thereby reducing the pressure differential and decreasing the air mass flow rate through the valve). The effect of frictional losses on flow rate was found to successfully converge after as few as two iterations. Figure 6.5 is included to show a typical convergence behavior for the parameter $\dot{m}$. In this instance seven iterations were performed with the estimate rapidly converging and remaining stable after the third iteration. A number of such plots were made over a wide range of operating conditions, with the general behavior of the solutions being similar to that of Figure 6.5, although the magnitudes of $\dot{m}$ vary widely depending on the current state of the system. For this reason, three iterations are used at each time step to estimate the mass flow rate. This estimate is then used for the next step in the dynamic model, which

involves integrating the air mass flow in conjunction with a model of PAM volume and PAM force versus contraction behavior to determine current PAM force. This is described in detail in the next section.
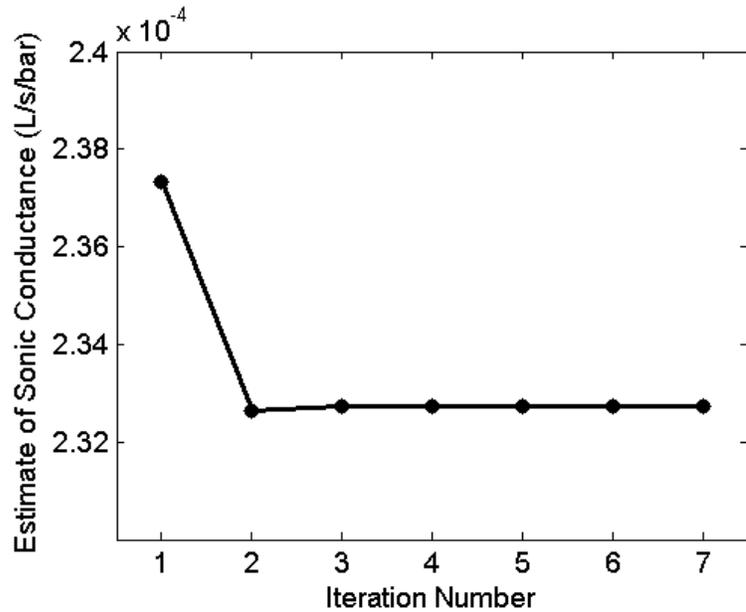
Figure 6.5. Typical convergence of sonic conductance estimate

6.4.   PAM MODEL

Having described the methodology for modeling the flow of air into and out of the PAM actuators, the next step is to model the impact of that air mass inside the PAM. First the effect of the air flow into and out of the PAM on internal pressure must be determined, then the pressure in each PAM can be used to determine the forces generated. One complicating factor is the change in volume that occurs inside the PAM during actuation. The internal PAM pressure must therefore be calculated using an approach that can account for changing vessel volume.

6.4.1. INTERNAL PAM PRESSURE MODEL

Governing equations for the pressure inside of a vessel of changing volume have been presented in the literature. Richer and Hurmuzlu (Richer and Hurmuzlu, 2000) derived an expression for the rate of change of pressure inside such a vessel. If the initial container volume and pressure is known, then the rate of change can be integrated over time to determine current pressure according to

$$\dot{P} = \frac{RT}{V}(\alpha_{in}\dot{m}_{in} - \alpha_{out}\dot{m}_{out}) - \alpha P \frac{\dot{V}}{V} \tag{10}$$

In this equation, R is the universal gas constant for air, T is the upstream temperature, V is the current volume of the vessel, and the various α terms are the specific heat ratios for the various processes. Specifically, α_{in} is the specific heat ratio for the filling of the actuators, α_{out} is the specific heat ratio of the exhausting process, and α is the specific heat ratio for the pressure change due to volume change.

Equation 10 is derived by combining the ideal gas law, the conservation of mass, and the conservation of energy. Assuming that the air acts as a perfect gas, the pressure and temperature changes within the PAMs are homogeneous, and that the kinetic and potential energy of the air are negligible compared to the pressure energy of the gas, the following derivation is made, which follows directly from the prior work (Richer and Hurmuzlu, 2000).

Starting with the ideal gas law

$$P = \rho RT \tag{11}$$

233

and the conservation of mass equation

$$\dot{m} = \frac{d}{dt}(\rho V) \tag{12}$$

which can be rewritten in terms of the mass flow into the PAM, $\dot{m}_{in}$, and the mass flow out of the PAM, $\dot{m}_{out}$, as

$$\dot{m}_{in} - \dot{m}_{out} = \dot{\rho}V + \rho\dot{V} \tag{13}$$

the conservation of energy equation can be written as

$$q_{in} - q_{out} + kC_v(\dot{m}_{in}T_{in} - \dot{m}_{out}T_{out}) - \dot{W} = \dot{U} \tag{14}$$

where q_{in} and q_{out} are the heat transfer terms, k is the specific heat ratio of the gas, C_v is the specific heat capacity of the gas at constant volume, T_{in} and T_{out} are the temperatures of the incoming and exhausting air respectively, $\dot{W}$ is the rate of change of work in the system, and $\dot{U}$ is the rate of change of internal energy. Since the internal fluid energy is defined as

$$U = C_v mT \tag{15}$$

the rate of change of internal energy can be written as

$$\dot{U} = \frac{d}{dt}(C_v mT) \tag{16}$$

Given the ideal gas relation

$$C_v = \frac{R}{k-1} \tag{17}$$

and the ideal gas law shown in Equation 11, Equation 16 can be written as

$$\dot{U} = \frac{1}{k-1}\frac{d}{dt}(PV) = \frac{1}{k-1}\left(V\dot{P} + P\dot{V}\right) \tag{18}$$

By combining Equation 16, Equation 17 into Equation 14, the conservation of energy can be written as

$$q_{in} - q_{out} + \frac{k}{k-1}\frac{P}{\rho T}\left(\dot{m}_{in}T_{in} - \dot{m}_{out}T_{out}\right) - \frac{k}{k-1}P\dot{V}$$

$$= \frac{1}{k-1}\dot{P}V \tag{19}$$

If we assume that the incoming and exhausting air is at the same temperature as the interior of the PAM, which is a reasonable assumption in the experiments performed here since the air supply was a large pressure vessel at room temperature, then there is only one temperature to consider ($T_{in} = T_{out} = T$), and Equation 19 can be rewritten as

$$\frac{k-1}{k}(q_{in} - q_{out}) + \frac{1}{\rho}(\dot{m}_{in} - \dot{m}_{out}) - \dot{V} = \frac{V}{kP}\dot{P} \tag{20}$$

If we assume that no heat is transferred into or out of the fluid during inflation and exhaustion, that is to say the process is adiabatic, then $(q_{in} - q_{out}) = 0$. Solving for the rate of change of pressure

$$\dot{P} = k\frac{P}{\rho V}(\dot{m}_{in} - \dot{m}_{out}) - k\frac{P}{V}\dot{V} \qquad (21)$$

By again using the ideal gas law, air density may be removed from the equation

$$\dot{P} = k\frac{RT}{V}(\dot{m}_{in} - \dot{m}_{out}) - k\frac{P}{V}\dot{V} \qquad (22)$$

The process could instead be considered to be isothermal, such that Equation 16 could instead be written as:

$$\dot{U} = C_v\dot{m}T \qquad (23)$$

And Equation 20 can instead be written as:

$$q_{in} - q_{out} = P\dot{V} - \frac{P}{\rho}(\dot{m}_{in} - \dot{m}_{out}) \qquad (24)$$

Then the rate of change in pressure will be

$$\dot{P} = \frac{RT}{V}(\dot{m}_{in} - \dot{m}_{out}) - \frac{P}{V}\dot{V} \qquad (25)$$

Comparison of Equations 22 and 25 shows that the only difference between an isothermal derivation and an adiabatic derivation is the presence of the specific heat ratio term k. At this point in the derivation, Richer and Hurmuzlu introduce different specific heat ratios for the three different components of the pressure change (those being mass flow in, mass flow out, and pressure change due to volume change). The authors therefore introduce three new terms (α_{in}, α_{out}, and α) to replace the single specific heat

236

ratio term k present in the derivation to this point. For clarity, we will replace their α with α_{vol} to denote that this is the specific heat ratio of air used for changes in volume

$$\dot{P} = \frac{RT}{V}(\alpha_{in}\dot{m}_{in} - \alpha_{out}\dot{m}_{out}) - \alpha_{vol}\frac{P}{V}\dot{V} \tag{26}$$

While the three α parameters are intended to be changed as necessary to better match experimental observations, the values suggested in Richer and Hurmuzlu were found to provide good performance in this modeling effort, and so were used without modification. The authors recommend that α_{in} be close to the standard value of the specific heat ratio of the gas, thus for the air used in this work $\alpha_{in} = 1.4$. For exhaustion, $\alpha_{out} = 1.0$ was stated, and for the volume change process, a value of $\alpha_{vol} = 1.2$ was recommended.

Equation 26 represents the final form of the differential equation governing pressure change inside the PAMs. This equation is numerically integrated at each time step in the same manner as all of the differential equations describing the system model, using a fourth order Runge-Kutta method. It can be seen that the mass flow rate estimates (either into or out of the PAM, depending on the spool valve operating mode and PAM) which were described in the previous section are necessary here. Also necessary are the volume and rate of change in volume of the PAM actuator. The analytical model used for these terms is described below.

6.4.2.   INTERNAL PAM PRESSURE MODEL

As can be seen in the previous section, knowing the internal air volume of the PAM at all times, and the rate of change of internal air volume, is critical to accurately estimate

the current PAM pressure. While previous PAM dynamic modeling work has used a table lookup approach with experimentally generated volume data (Bubert, 2009), in this work a purely analytical approach was desired to allow for a more robust system model, specifically one that could be used on different PAM configurations without requiring the generation of large amounts of experimental data. To this end, the kinematic relations governing the motion of the braided sleeve around the PAM during contraction and extension of the actuator were modified to allow for an expression for internal air volume versus displacement to be derived. This derivation is presented below.

The following model of PAM volume assumes a cylindrical actuator shape with a braided sleeve that starts taut against the bladder. The total volume of a cylindrical PAM V_{tot} can be defined as:

$$V_{tot} = \pi r^2 L \tag{27}$$

Both the radius r and length L of the PAM change during actuation in a manner that is governed by the kinematics of the braided sleeve. These kinematics can be better understood by considering a single filament of the sleeve. If a single filament of the braided sleeve were isolated and unwrapped from the sleeve without changing its angular orientation, then the triangle shown in Figure 6.6 would be a representation of the geometry of that filament.
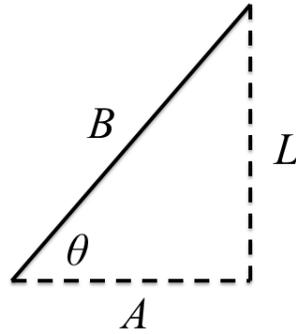
Figure 6.6. Schematic representation of braided sleeve filament geometry

Here B is the length of that filament, L is the current active length of the actuator and A is the length traveled by the fiber around the circumference of the actuator. Note that A can be more or less than the circumference of the actuator as determined from its current radius. If we introduce a new constant into the definition of the actuator geometry, N, which is defined as the number of turns a single filament makes around the actuator, then we can express the value of A as a function of the current outer radius, r, as in Equation 28. Note that N is unaffected by contraction or extension of the actuator since the end fittings do not rotate relative to each other

$$A = 2N\pi r \tag{28}$$

Using the Pythagorean theorem, we can define a relationship between the leg lengths in Figure 6.6 that will hold true across the entire range of actuator displacements:

$$B^2 = L^2 + A^2 \tag{29}$$

$$B^2 = L^2 + (2N\pi r)^2 \tag{30}$$

$$B^2 = L^2 + 4N^2\pi^2 r^2 \tag{31}$$

$$r^2 = \frac{B^2 - L^2}{4\pi^2 N^2} \tag{32}$$

Substituting Equation 32 into Equation 27:

$$V_{tot} = \pi L \frac{B^2 - L^2}{4\pi^2 N^2} \tag{33}$$

$$V_{tot} = \frac{B^2 L - L^3}{4\pi N^2} \tag{34}$$

This is the final form of the total volume equation of a cylindrical PAM. However, this total volume includes both the internal air volume and the fixed volume of the bladder. The relevant volume for analysis of the pneumatic system does not include the bladder volume:

$$V_{air} = V_{tot} - V_{bl} \tag{35}$$

where the volume of the bladder is determined from its initial geometry, namely the initial bladder length L_{bl}, bladder thickness t_{bl}, and initial bladder outer radius r_{bl}.

$$V_{bl} = \pi[r_{bl}{}^2 - (r_{bl} - t_{bl})^2]L_{bl} \tag{36}$$

Thus, the internal air volume of a PAM can be written as:

$$V_{air} = \frac{B^2 L - L^3}{4\pi N^2} - \pi[r_{bl}{}^2 - (r_{bl} - t_{bl})^2]L_{bl} \tag{37}$$

In Equation 26 it can be seen that the rate of change of internal air volume with time is also needed to calculate the rate of change of internal pressure. This is found by differentiating Equation 37

$$\dot{V}_{air} = \frac{d}{dt}\left[\frac{B^2L - L^3}{4\pi N^2} - \pi[r_{bl}^2 - (r_{bl} - t_{bl})^2]L_{bl}\right] \tag{38}$$

$$\dot{V}_{air} = \frac{dL}{dt}\frac{d}{dL}\left[\frac{B^2L - L^3}{4\pi N^2} - \pi[r_{bl}^2 - (r_{bl} - t_{bl})^2]L_{bl}\right] \tag{39}$$

$$\dot{V}_{air} = \dot{L}\left[\frac{B^2 - 3L^2}{4\pi N^2}\right] \tag{40}$$

Analytical predictions from Equations 37 and 40 are used in the dynamic model in place of the experimental data that was used in previous work (Bubert, 2009) in order to create a more robust model that can be easily adapted to different PAM geometries and operating conditions.

6.4.3.   PAM FORCE MODEL

The details of the quasistatic PAM force model for this work were discussed in Chapter 4 and so will not be repeated here. Instead only the final form of the model used will be shown. The total PAM force is a combination of different terms that account for various aspects of the actuator's operation:

241

$$F = F_G + F_b - F_s + F_f \tag{41}$$

It can be seen that the total PAM force F includes the Gaylord force term F_G, the bladder elasticity term F_b, the sleeve elasticity term F_s, and the Coulomb friction term F_f. As discussed in Chapter 4, the PAM force is highly dependent on both operating pressure and length. In this dynamic model, the current operating pressure for both PAMs is determined as discussed above, but the current PAM length must be determined through a set of kinematic relations that connect the primary system output, flap deflection angle δ, to the lengths of the two PAMs. The derivation of these terms is discussed below.

6.5.   KINEMATICS

The mechanical system used to connect the PAM actuators to the flap introduces kinematic relationships which modify the torque versus deflection output of the system. The design of the linkage and bellcrank approach used will first be discussed, followed be discussion of modifications made to the kinematics which increased system performance.

6.5.1.   LINKAGE/BELLCRANK SYSTEM OVERVIEW

In order to determine the length of both the active and passive PAMs at any instant in time, it is necessary to relate the motion of the flap angle, which is the primary system output parameter, with the motion of the two PAMs. Physically, this connection is realized in the actual system as a series of bellcranks and linkages. Figure 6.7 highlights these components with a schematic representation of the connections between the PAMs and the flap.
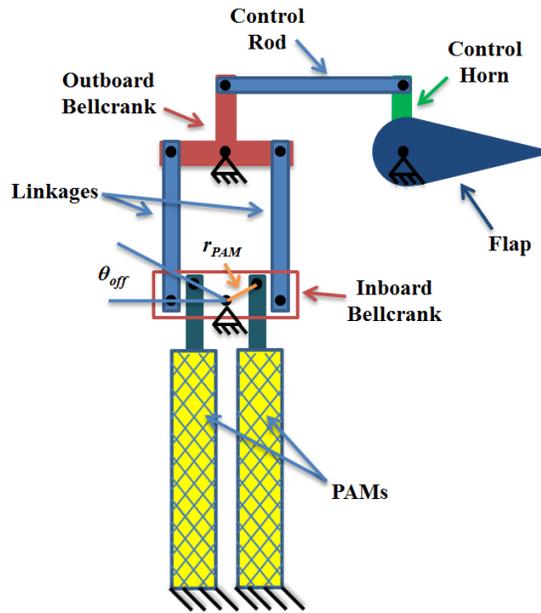
Figure 6.7. Schematic of PAM TEF showing kinematic connections

The antagonistic PAM pair is mounted inboard on the helicopter blade. The moving ends of the PAMs are attached through radial bearings to an inboard bellcrank. As can be seen in Figure 6.7 the mounting points are offset from the bellcrank rotation point in both the spanwise and chordwise directions. This is a key feature of the design as it introduces modifications to the kinematics that lead to improved system performance over a convention pulley type device. This will be discussed in more detail below. Also attached to the inboard bellcrank is a balanced pair of linkages that run from the inboard mounting location of the PAMs out to the flap span station. Note that this diagram is not drawn to scale; the linkages are much longer than they appear here. A balanced pair of linkages was introduced to provide mass balancing of the linkages about the bellcrank rotation point, so that the high CF acceleration acting on the linkage mass does not induce a bias torque on the bellcrank and PAM system. At the inboard end of the flap, a second bellcrank is mounted to allow for transfer of the system outputs to the flap. The outboard

bellcrank includes a third spur perpendicular to the linkage mounts that provides an attachment point for a chordwise oriented control rod. This control rod then acts on the flap through a control horn mounted at the inboard end of the flap.

6.5.2. OFFSET PAM MOUNTING

As mentioned above, an alternative mounting scheme for the connection between the PAMs and inboard bellcrank has been adopted as a means to improve performance. The most general mounting of the PAMs would have the rotation points in line with the bellcrank rotation point in the spanwise direction but offset in the chordwise direction such that moments are generated by the PAM forces. This approach creates equal moment arms for both the active and passive PAMs across the entire range of motion, although it is important to note that the moment arms do change with rotation. Introducing a spanwise offset into the mounting, which is shown in Figure 6.7 as an angular offset θ_{off} to the radial spacing r_{PAM} between the PAM mounting and bellcrank rotation points, changes the evolution of moment arms in way that favors the active PAM. This effect can be seen through derivation and visualization of the system kinematics.

The linkage and bellcrank system was designed such that the evolution of torques and deflection angles generated by the PAM TEF system are controlled solely by the inboard bellcrank. This is achieved by mounting the linkages at the same chordwise offset on both of their ends. Similarly, the control rod is mounted with an equivalent spanwise offset at both of its ends. For this reason, both the linkages and control rod do not affect the balance of torque and deflection generated by the system. In other words, they both transmit the torque and deflection generated at the inboard bellcrank without

244

modifying it. This simplifies derivation of the kinematics by allowing us to only consider the inboard bellcrank, and specifically the mounting of the PAMs to it. The relevant connection points and resulting design variables of this component are shown in Figure 6.8.
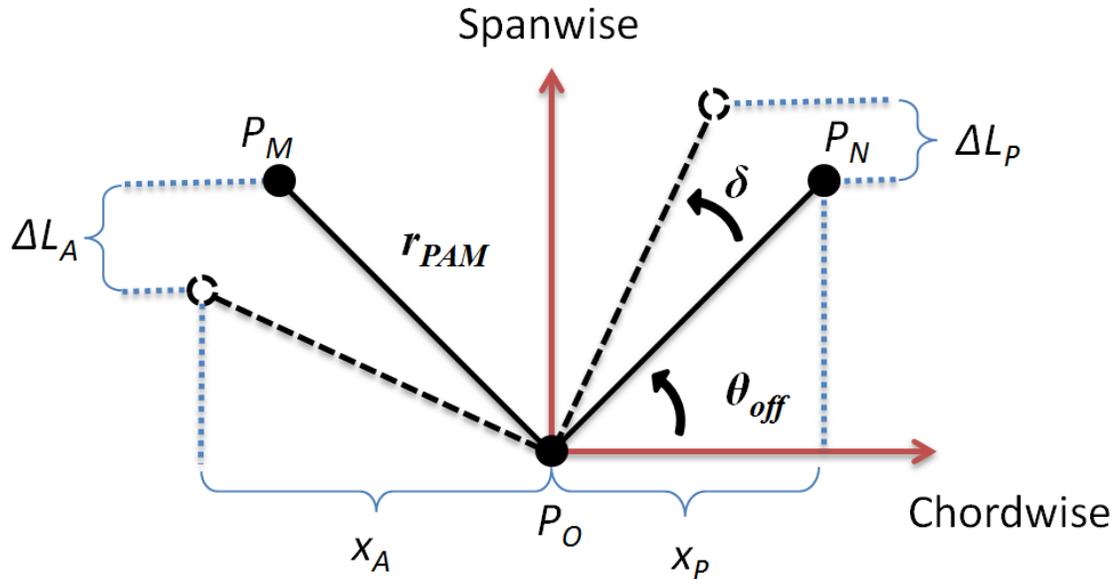
Figure 6.8. Inboard bellcrank geometry

The primary parameters of interest for these kinematics are the changes in length and effective moment arms for both the active and passive PAMs as a function of the flap deflection angle δ. Note that, as stated above, the system is designed such that the rotation angle of the bellcrank relative to the chordwise direction is exactly equal to the deflection angle of the flap, so only a single δ parameter is needed to fully describe the rigid displacements of the system. The solid black lines in Figure 6.8 show the simplified geometry of the bellcrank at rest, with the point P_M being the mounting point for the active PAM, point P_N the mounting point for the passive PAM and point P_O the rotation

point of the bellcrank. The dashed lines represent this same bellcrank rotated through a positive angle δ.

The effective moment arm of the active PAM, x_A, will be the chordwise projection of r_{PAM} when the bellcrank is rotated through the angle δ:

$$x_A = r_{PAM}\cos(\theta_{off} - \delta) \tag{42}$$

Similarly, the effective moment arm of the passive PAM x_P, which is mounted at P_N:

$$x_P = r_{PAM}\cos(\theta_{off} + \delta) \tag{43}$$

The change in length of the two PAMs is the difference between the spanwise projection of the PAM mounting points for the bellcrank at rest and when deflected by the angle δ. For the active PAM:

$$\Delta L_A = r_{PAM}\sin(\theta_{off} - \delta) - r_{PAM}\sin(\theta_{off}) \tag{44}$$

Similarly for the passive PAM:

$$\Delta L_P = r_{PAM}\sin(\theta_{off} + \delta) - r_{PAM}\sin(\theta_{off}) \tag{45}$$

Note that for positive values of flap deflection, the change in length of the active PAM will be negative (indicating contraction) and the change in length of the passive PAM will be positive (indicating extension). This is the expected and desired result. Note also that in the case where the offset angle is zero, the kinematics simplify to those of a typical bellcrank mechanism, which we will call a straight line bellcrank since the three rotation points are aligned. In that case, the moment arms and changes in length are

simply equal to the cosine and sine components of the vector r_{PAM} rotated through δ. It is helpful to compare the offset bellcrank adopted here to such a straight line bellcrank because it shows the benefit of the offset. For example, in Figure 6.9 it can be seen that when the offset angle is zero, the active and passive PAMs have equal moment arms that decrease with flap deflection over the entire angle range of interest.
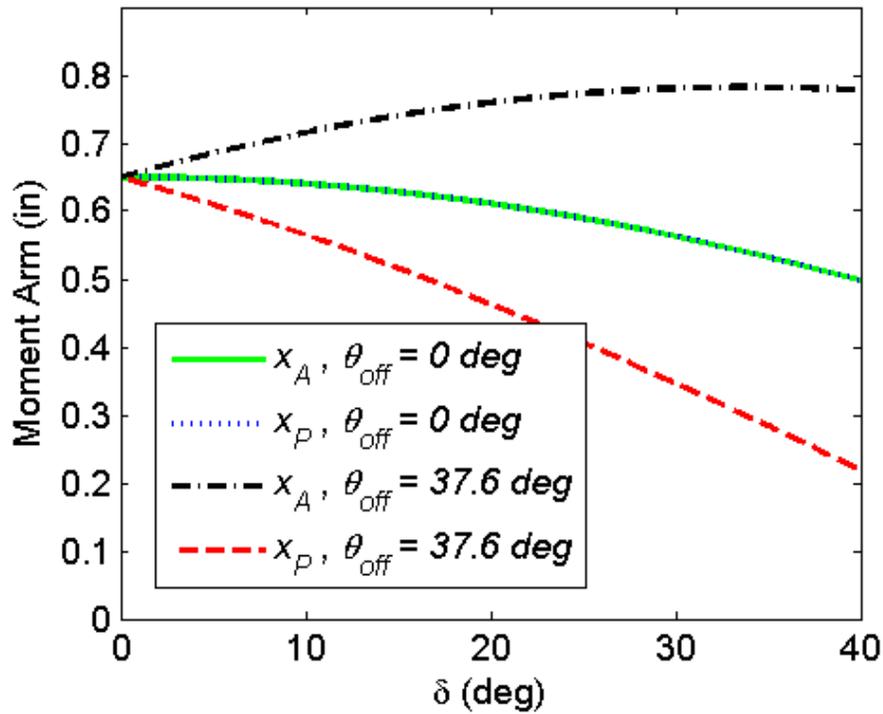
Figure 6.9. Evolution of PAM moment arms with flap deflection, with and without offset angle

Figure 6.9 also shows that by introducing an offset angle, $\theta_{off} = 37.6°$ in this instance (which is the offset angle chosen for the vacuum chamber whirl rig), a significantly different behavior is observed. In this case, the moment arm of the active PAM increases while the passive PAM's moment arm decreases.

The impact of this altered kinematic behavior can be further understood by considering the torque that results from the PAM forces and the changing moment arms. The total output torque of the actuation system, T_{act}, is found by combining the system kinematics with the PAM force model according to:

$$T_{act} = F_A x_A - F_P x_P \qquad (46)$$

Here F_A is the force in the active PAM, found by solving Equation 41 for the current pressure and displacement seen in the active PAM. Similarly, F_P is the force in the passive PAM, determined using the current pressure and displacement of this actuator.

Figure 6.10 compares the evolution of T_{act} with flap deflection angle δ for a straight line bellcrank and an offset bellcrank. Note that the PAM geometry used in this analysis is the same as that used in the vacuum chamber whirl rig, as described in Chapter 5. The active PAM is pressurized to 90 psi and the passive PAM is vented to atmosphere (0 psi). The amount of torque available initially, known as blocked torque, is the same for both sets of kinematics. This is because the geometry was chosen such that both configurations have the same initial moment arm to allow for better comparison. However, once the deflection angle starts to increase, the bellcrank with an offset angle generates significantly more torque. For example, at $\delta = 20°$, the offset angle bellcrank creates 36.5% more torque and at $\delta = 30°$, the offset angle bellcrank creates 122% more torque. Thus, the benefit of adding an offset angle to the mounting location of the PAMs on the inboard bellcrank can be seen.
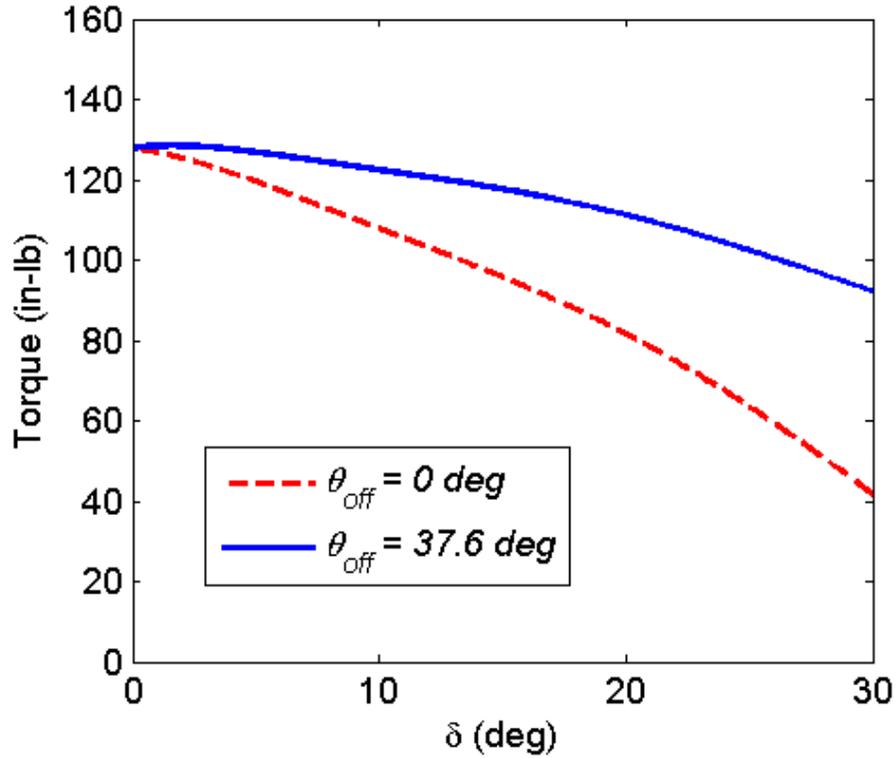
Figure 6.10. Comparison of torque output; with and without offset angle in bellcrank

6.6. FLAP DYNAMICS EQUATION OF MOTION

The flap dynamics for the PAM TEF system are modeled as a second order linear system. The time history of flap deflection angle is found through numerical integration of the following differential equation:

$$J\ddot{\delta} + c\dot{\delta} + k_{tot}\delta = T_{act} \tag{47}$$

which, when solving for $\ddot{\delta}$, has the form:

$$\ddot{\delta} = \frac{1}{J}\left(T_{act} - c\dot{\delta} - k_{tot}\delta\right) \tag{48}$$

The various components of Equation 48 will be discussed in turn.

6.6.1. INERTIA TERM

In Equation 47, J is the total mass moment of inertia of all the components that rotate with the flap. For the vacuum chamber whirl rig system discussed here, this includes the inertia of the flap, bellcranks, control horn, control rod, linkages, and all of the yokes, bearings and hardware used to connect the components. The value of this parameter was found using Solidworks, where detailed 3D models of all of the components with appropriate material properties (namely density) were analyzed for their mass moment of inertia about their respective rotation points. Since the motion of the linkages and control rod is more translational than rotational, they were treated as point masses mounted to the bellcrank and control horn, respectively. Table 6.2 below shows the summation of terms that leads to the total value of J used in this analysis.

Table 6.2. Components of PAM TEF system mass moment of inertia

Component	Material	Density (lbm/in³)	Weight (lbm)	Quantity	Inertia (lbm-in²)
Flap and TRF	6061 Alum	0.0975	0.598	1x	0.298
Linkages	CFRP	0.0584	0.142	1x	0.060
Inboard Linkage Rod End	Stainless	0.289	0.246	2x	0.104
Outboard Linkage Yoke	Stainless	0.289	0.122	2x	0.052
Linkage Anchors	Stainless	0.289	0.197	4x	0.083
Linkage Turnbuckles	Stainless	0.289	0.180	2x	0.076
Inboard Bellcrank	Stainless	0.289	0.095	1x	0.037
Outboard Bellcrank	Stainless	0.289	0.095	1x	0.028
PAM Rod End	Stainless	0.289	0.164	2x	0.069
				Total	**0.807**

6.6.2.   STIFFNESS TERM

The total system stiffness term k_{tot} is a combination of the aerodynamic stiffness and the stiffness of the torsion rod flexure element. The aerodynamic stiffness is calculated using the 2D thin airfoil theory flap hinge moment equations described in Chapter 4. The torsion rod flexure (TRF) stiffness is calculated from linear elastic torsional beam theory (as described in Chapter 5). The total effective stiffness on the system is then equal to:

$$k_{tot} = k_{aero} + k_{TRF} \qquad (49)$$

For the vacuum chamber whirl rig system discussed here, the aerodynamic hinge stiffness and torsion rod flexure design were based on full scale loading of a Bell 407 scale trailing edge flap system operating in hover.

6.6.3.   DAMPING TERM

The viscous damping coefficient c of this system would be quite complex to estimate given the many different sources and forms of damping present in the system. These include dynamic damping in the PAMs (that is damping in the PAMs other than the Coulomb friction term included in the PAM force model), aerodynamic damping due to the flap motion, frictional damping present at all of the mounting points for the flap, linkages, control rod, control horn and bellcranks, as well as other sources. To simplify analysis, a single empirically fit viscous damping term was employed to capture the damping dynamics. The value of this coefficient was manually fit to produce the best fit between model and experiment. It was found that generally, the damping coefficient

chosen did not have a strong impact on model accuracy. As a result, a single value of c

chosen to best match one particular data set provided good results across the full range of

data sets explored. This value was

$$c = 0.113 \tag{50}$$

6.6.4. APPLIED TORQUE

The right hand side of Equation 47 represents the torque applied by the PAM

actuation system. This is by far the most involved term in the system dynamics as it

includes all of the pneumatic system dynamics, spool valve modeling, PAM pressure

modeling, tubing losses, PAM force model and kinematics. These elements have been

described in detail above, with the T_{act} term in Equation 47 being defined in Equation 46.

6.7. NUMERICAL INTEGRATION OF SYSTEM EOM

The fourth order Runge-Kutta method is used to solve for the various system

states at each time step. A state vector y is defined:

$$y = \left[P_1, P_2, \delta, \dot{\delta} \right] \tag{51}$$

with the states correspondingly referring to the pressure in PAM #1 and PAM #2,

the flap deflection angle (equal to the bellcrank deflection), and the rate of change of the

flap angle. All other system states are determined from these four. We now define a

function f that determines the rate of change of this state vector:

$$\acute{y} = f(t, y) \tag{52}$$

In reality, f is not a single function, but instead a collection of functions that contain the differential equations for the system pressures and angle, as well as all of the kinematics, PAM force equations, etc., that are contained therein. For example, the derivatives of the two PAM pressures are determined from Equation 10, and the second derivative of angle is determined from Equation 48. The time history of the state vector y is found by integrating from the initial condition:

$$y(t_0) = y_0 \tag{53}$$

According to the standard formulation of the 4th order Runge-Kutta equation (Ascher and Petzold, 1998):

$$y_{n+1} = y_n + \frac{1}{6}(k_1 + 2k_2 + 2k_3 + k_4) \tag{54}$$

where y_n is the state vector at time step n ($t = t_n$), y_{n+1} is the state vector at the next time step ($t_{n+1} = t_n + \Delta t$), and:

$$k_1 = \Delta t f(t_n, y_n) \tag{55}$$

$$k_2 = \Delta t f\left(t_n + \frac{1}{2}\Delta t, y_n + \frac{1}{2}k_1\right) \tag{56}$$

$$k_3 = \Delta t f\left(t_n + \frac{1}{2}\Delta t, y_n + \frac{1}{2}k_2\right) \tag{57}$$

$$k_4 = \Delta t f(t_n + \Delta t, y_n + k_3) \tag{58}$$

These equations are solved in Matlab.

6.8.　　　PAM TEF DYNAMIC MODEL VALIDATION

In order to assess the modeling approach outlined above, comparisons were made between experimental data and predictions from the model for the same operating conditions. The experimental data set was taken from the vacuum chamber whirl rig described in Chapter 5. In particular, a non-rotating data set from benchtop testing was chosen since rotational effects (primarily centrifugal acceleration) are not presently accounted for in the model. Additionally, testing on the benchtop does not have the same restrictions on time and availability as testing in the vacuum chamber, so the data set is more expansive.

The data set includes a range of different operating conditions. The spool valve voltage inputs were sine waves of the form:

$$V_s = 5\sin(f_{SV}t) + 5 \tag{59}$$

where f_{SV} is the frequency at which the valve was operating. This produces sine waves that vary from 0 V to 10 V, which is the full operating range of the Festo MPYE-5-1/8-HF-010-B spool valve. The values of f_{SV} tested were the n/rev values for a Bell 407 scale rotor system from 1/rev to 5/rev:

$$f_{SV} = [7, 14, 21, 28, 35]\ \text{Hz} \tag{60}$$

The pressure regulator was set to a range of pressures representing a typical operating range for such systems:

$$P_{up} = [30, 50, 70, 90]\ \text{psi} \tag{61}$$

Experimental test data was taken at every combination of f_{SV} and P_{up}.

We will first consider the model's ability to predict the time histories of the various system parameters that build up to the final flap deflection output. The system states available for comparison are obviously limited by what was actually measured during the experiment, but foresight allowed for the installation of sensors to monitor the following key states: pressure in each PAM, force in each PAM, and flap deflection angle. The first goal of the model then is to be able to predict all five of these states well at a single operating point of the actuation system. We will make this initial comparison at values of actuation frequency f_{SV} and regulator set point pressure P_{up} that are towards the center of the range tested; specifically $f_{SV} = 21$ Hz and $P_{up} = 70$ psi.
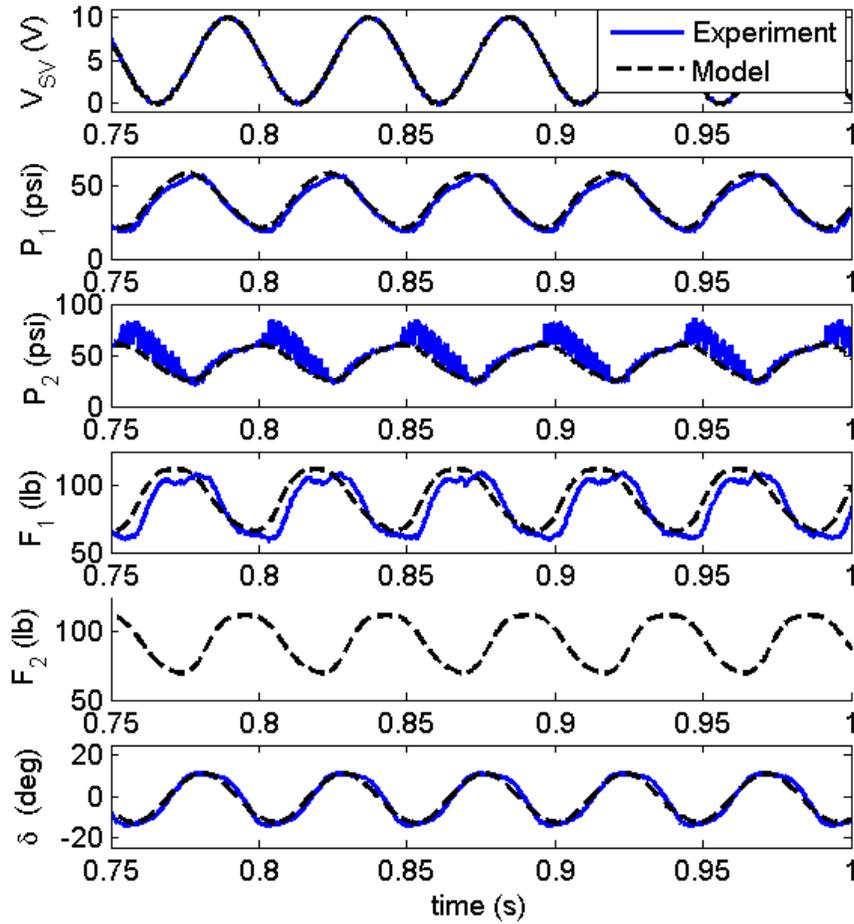
Figure 6.11. Comparison of model and experiment, $f_{SV} = 7$ Hz, $P_{up} = 90$ psi

Figure 6.11 shows the time histories of the experimental data and model predictions for this case. Note that the spool valve voltage is exactly equivalent between the two. This is because the experimentally measured voltages were fed in to the model as the driving signal. This ensures that the model is in phase with the experiment. There are also small perturbations in the experimental spool valve signal caused by small errors in the digital to analog conversion that takes place in the National Instruments DAQ system. Since this is the actual signal seen by the spool valve, it is desirable and more accurate to have it also be the driving signal for the model.

256

In Figure 6.11 it can be seen that there are two issues with the experimental data collected. First, the signal for P_2 shows high frequency ringing noise that is quite significant. The source of this noise is not known, and it only appears in some of the data taken. Some form of interference, or perhaps a poor electrical connection, is suspected. Secondly, the experimental data for F_2 is not shown because this sensor failed early in the experimental testing. Unfortunately a replacement was not available at the time. These issues do not significantly affect our ability to assess the performance of the model, however, because they are both measurements on PAM #2. Careful observation of the available pressure data/predictions and the available force data/predictions will reveal that PAM #1 and PAM #2 have very similar force and pressure profiles, with only a phase shift between the two equal to one half of a period. This is expected given their mechanically linked, out-of-phase pressurization as described in the spool valve operation section above. For this reason, it is sufficient to consider the pressure and force of PAM #1 alone.

The results for P_1 in Figure 6.11 show a good predictive capability of the model at this operating condition. The overall phase and amplitude of the pressure response is well captured. There is a fluctuation in the measured data as the maximum pressure is approached that is not present in the model. This points to some higher order dynamics not captured somewhere in the spool valve model, tubing loss model, PAM volume model, and/or the internal PAM pressure model.

The F_1 results in Figure 6.11 also show generally good predictive capability. In this case, however, there is a noticeable shift in phase between experiment and model. While there is a slight over-prediction in the force seen in PAM #1, the magnitude of the

variation in force is well captured. Again there are some higher order dynamics not captured as the force approaches its highest value, although this is likely a trickle down error from the deviations seen in the pressure response.

The final comparison to make with this operating condition is between the measurements and predictions of flap angle δ, as seen at the bottom of Figure 6.11. Here again the agreement is quite good. In fact, it is better than the agreement seen in F_1, although not better than that for P_1. The improvement in accuracy from force to deflection is interesting because the forces, and not the pressures, are what directly drive the dynamics of the flap motion. One would expect at least a similar level of error in the final flap angle predictions. One likely cause of the improvement is that, as mentioned above, the magnitude of force variation is captured better than the actual values of force. This leads to the hypothesis that it is the variation of force seen in the PAMs more so than the magnitude which is important for accuracy in the model. Once again, there are some higher order dynamics not captured in the model.

Next, we will consider the effect that operating frequency f_{SV} has on the accuracy of the model. Results for $P_{up} = 90$ psi will be shown for all of the frequencies tested in Figure 6.12 to Figure 6.16.
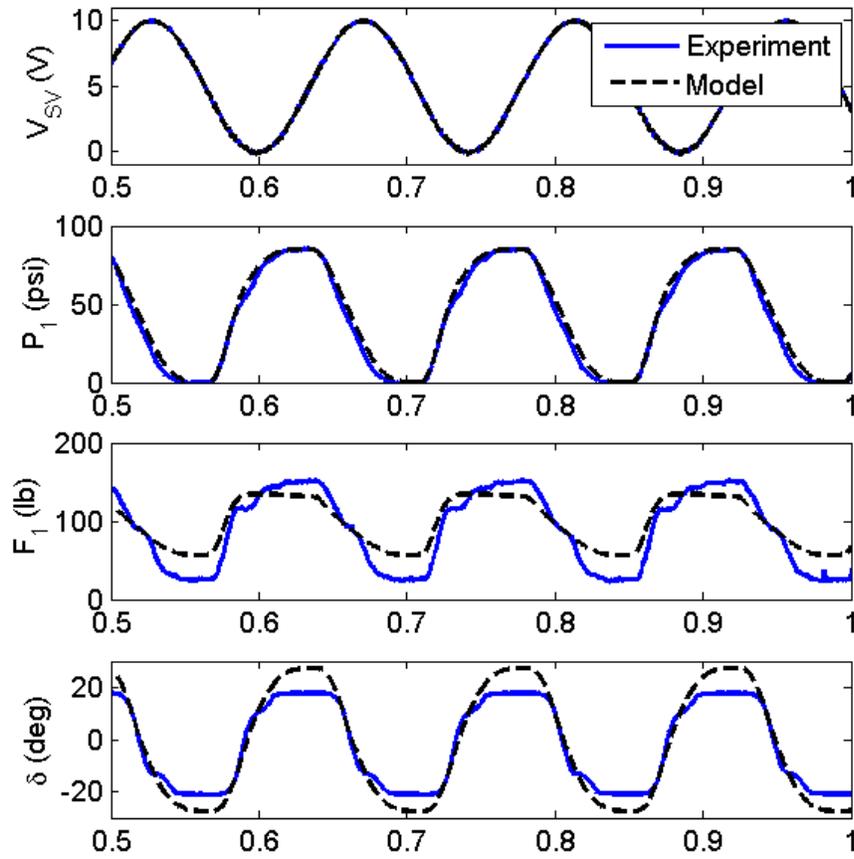
Figure 6.12. Comparison of model and experiment, $f_{SV} = 7$ **Hz,** $P_{up} = 90$ **psi**
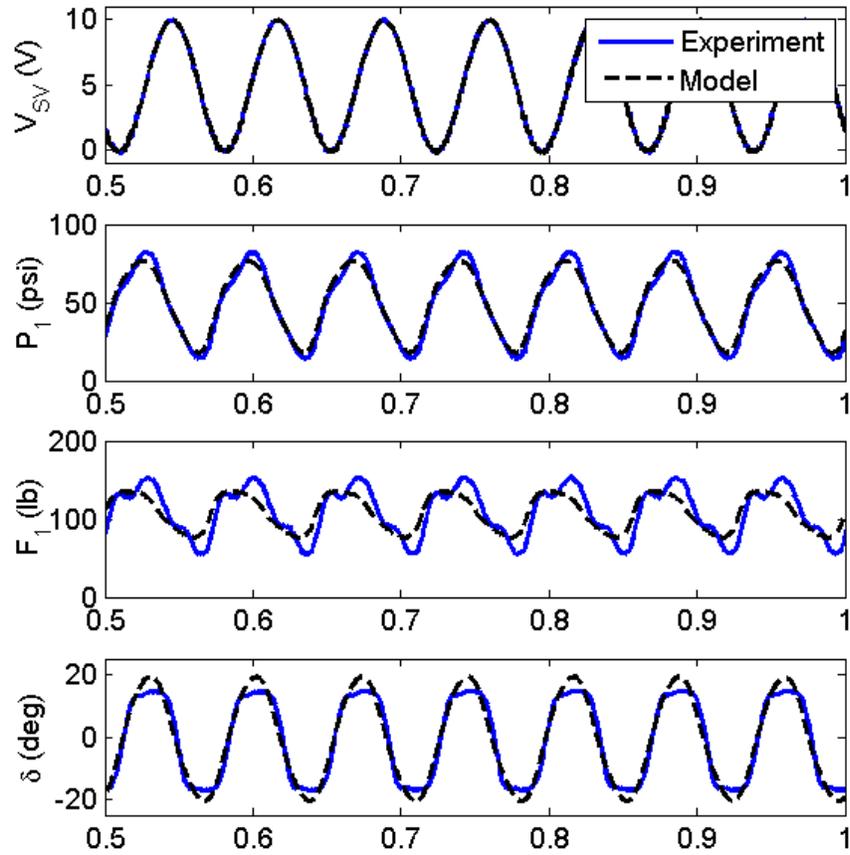
Figure 6.13. Comparison of model and experiment, f_{SV} = **14 Hz,** P_{up} = **90 psi**
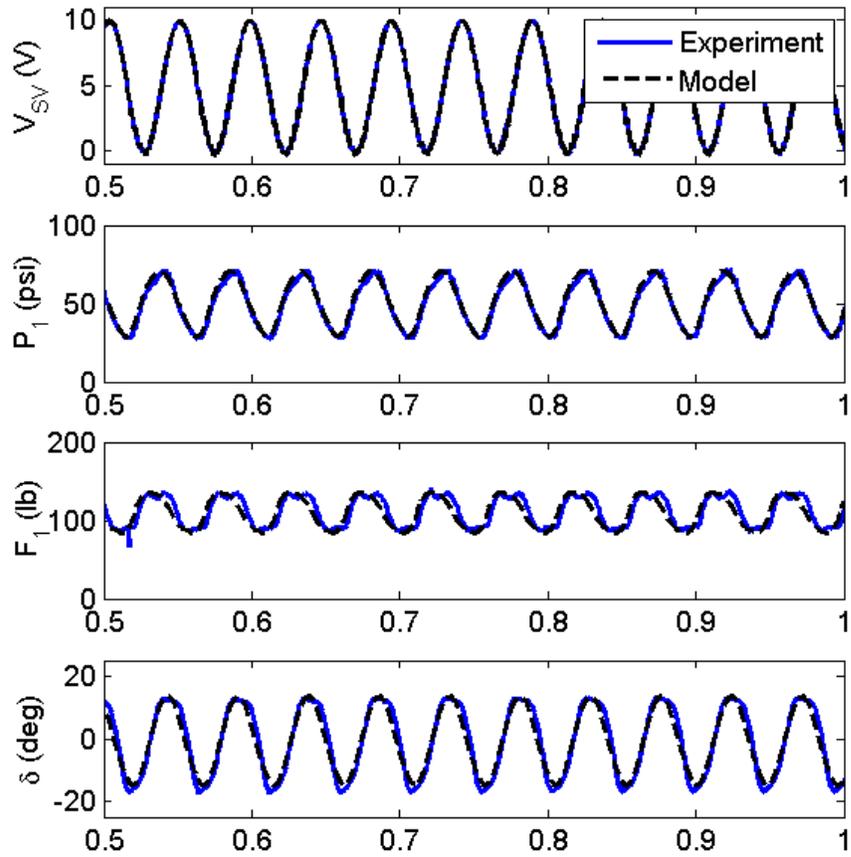
Figure 6.14. Comparison of model and experiment, f_{SV} = 21 Hz, P_{up} = 90 psi
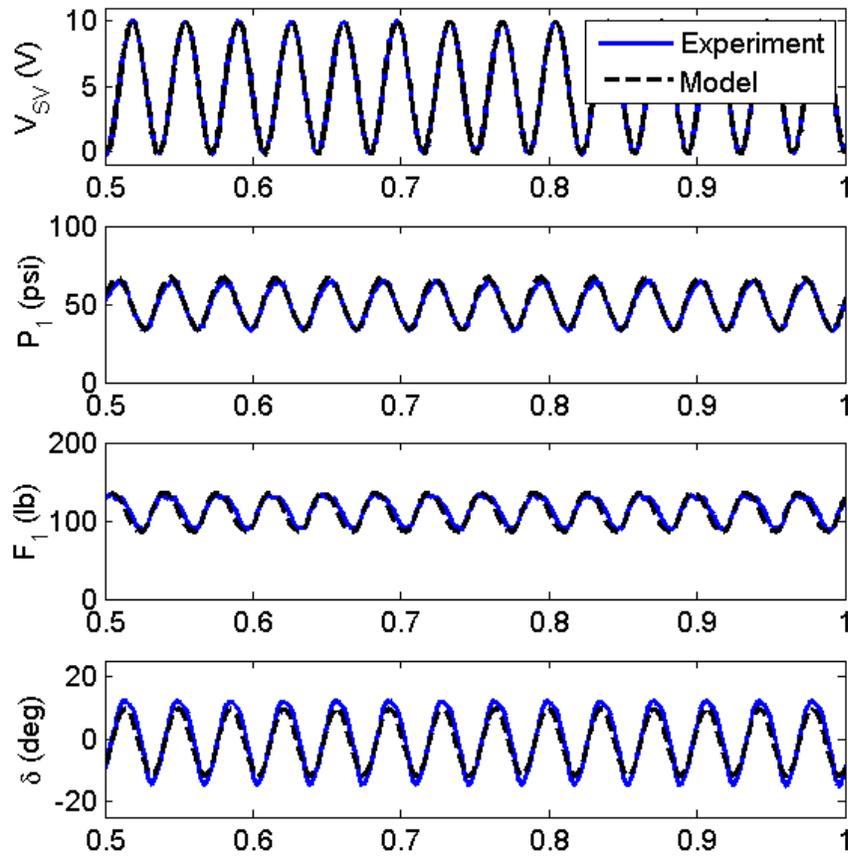
Figure 6.15. Comparison of model and experiment, f_{SV} = **28 Hz,** P_{up} = **90 psi**
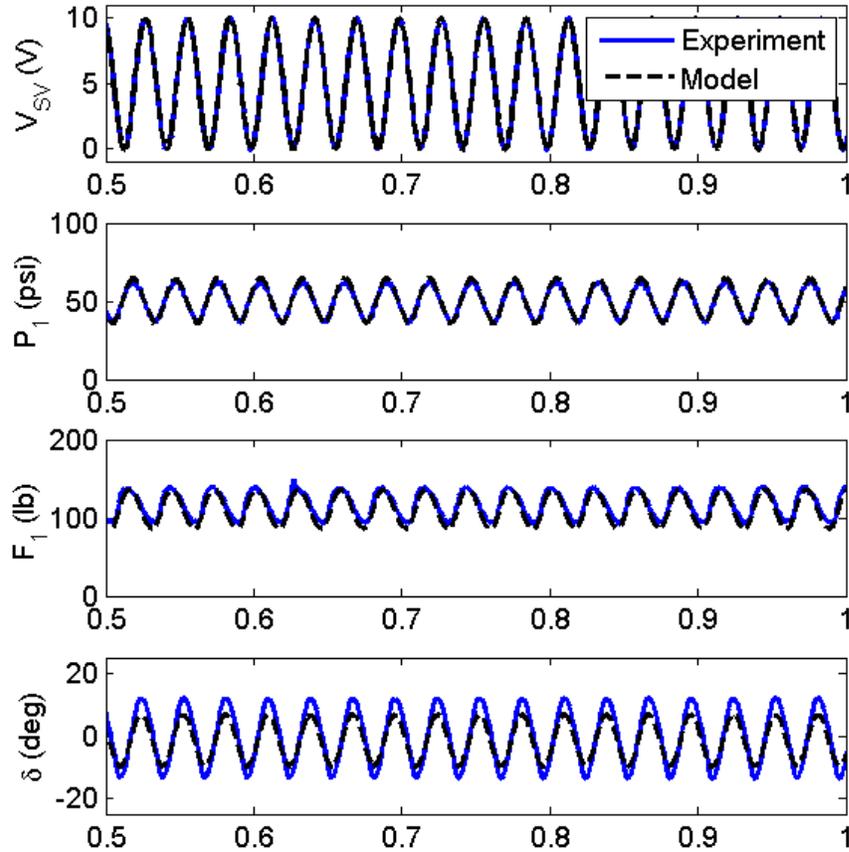
Figure 6.16. Comparison of model and experiment, f_{SV} = 35 Hz, P_{up} = 90 psi

In Figure 6.12 through Figure 6.16 it can be seen that the components of the model which contribute to the estimates of PAM pressure work well over the entire frequency range of interest. While there are some higher frequency dynamics not captured, in general the predictive capability is quite good.

As was the case with the results shown in Figure 6.11, Figure 6.12 through Figure 6.16 show that the force prediction components of the model show good agreement in general, but with significantly more error than is seen in the pressure measurements. Furthermore, the force predictions are significantly better at higher frequencies. This is

somewhat surprising as the PAM force model used is essentially a quasistatic model, and as shown in Chapter 4 the force model produces excellent agreement with quasistatic PAM characterization data. Given this, one might expect better agreement at lower frequencies (which more closely resemble a quasistatic condition) than at higher, but the opposite is true here.

The flap deflection angle results in Figure 6.12 through Figure 6.16 show that at the lower frequencies, particularly 7 and 14 Hz, the model has a tendency to over-predict the achievable flap deflection, whereas at the higher frequencies (28 and 35 Hz) the model under-predicts performance somewhat. It is likely that the over-prediction at lower frequencies is the result of some nonlinearity in the loading applied to the system. The most likely source of this behavior was a mechanical interference present in the bellcrank system. The two bellcranks were constrained in their design by both stress and geometric limitations, with the result being a restricted output range before mechanical interference between the bellcrank and the linkages, the bellcrank and the PAMs, and/or the bellcrank and the control rod would occur. These interferences greatly stiffened the system at its extents. They were not "hard stop" impacts that would prevent deflection above a certain point, but instead a "soft" form of boundary, which effectively acts as an increase in system stiffness once contact has been made. The linkage system was originally designed for a target deflection of $\delta = \pm 20°$, with some margin, but it can be seen that at low frequencies, the predicted performance is above this threshold. It is also possible that, as implemented on the experimental setup, the nonlinear effect of these interferences occurs slightly earlier than intended, with the result being that the experimental output deflections are restrained at low frequencies and high pressures.

Mechanism interference is also a possible cause of the increased discrepancies seen in F_1 at 7 and 14 Hz. Since PAM force is largely dependent on length, and PAM length is linked to the flap deflection angle through the kinematics, collision with other components due to interference would be expected to affect the force measured in the PAMs.

Consideration of other P_{up} values will allow for further consideration of model performance in general, and the question of mechanical interference effects in particular. For the sake of brevity, only low frequency results will be shown for 30, 50, and 70 psi, as the results above establish that the model is generally better at higher frequencies.
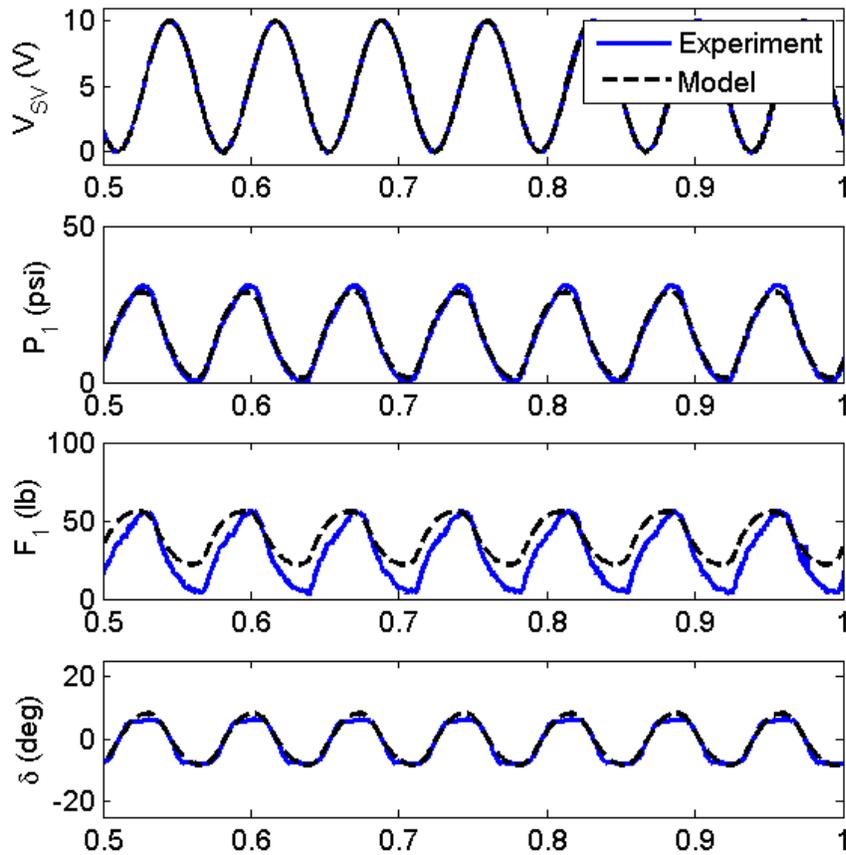
**Figure 6.17. Comparison of model and experiment,** f_{SV} **= 14 Hz,** P_{up} **= 30 psi**
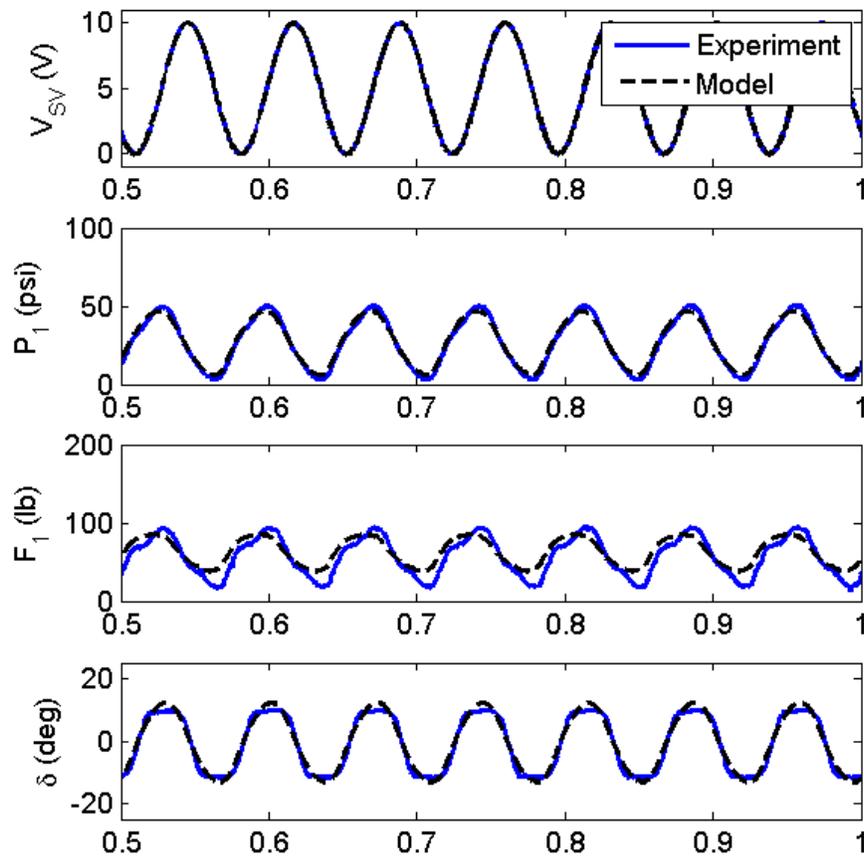
Figure 6.18. Comparison of model and experiment, f_{SV} = 14 Hz, P_{up} = 50 psi
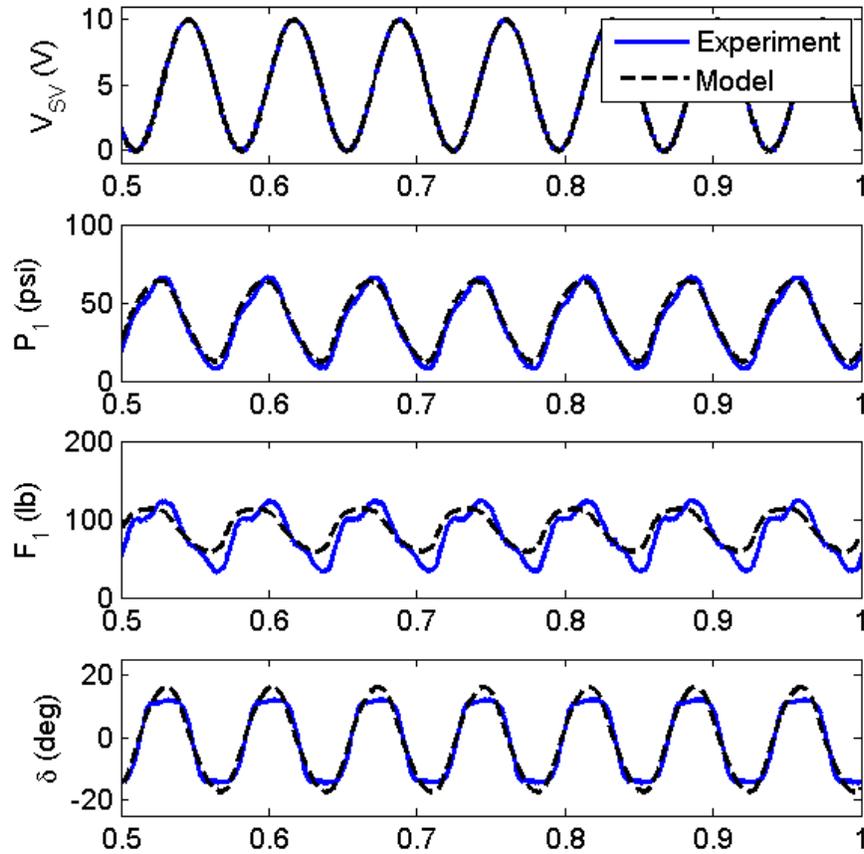
**Figure 6.19. Comparison of model and experiment, $f_{SV} = 14$ Hz, $P_{up} = 70$ psi**

Figure 6.17 through Figure 6.19 show the experimental results and model predictions for $f_{SV} = 14$ Hz and $P_{up} = [30, 50, 70]$ psi. It can be seen that the conclusions made above about the ability of the model to successfully predict pressure are valid across the entire range of pressures tested. The general success of the model in predicting force at lower frequencies also holds true across the various pressures, with again greater discrepancies seen than in the pressure results.

Some further insight into the potential impact of mechanical interferences can be seen by considering Figure 6.17 in particular. Here the operating pressure is low enough that

the maximum flap deflections achieved are significantly below the mechanical limits of the system. We see that the final flap angle is significantly better predicted than it was in Figure 6.13. This could be explained by the lack of mechanical interference and the resulting nonlinearities in the loading.

6.9.   CONCLUSIONS

In summation, the dynamic model of a Pneumatic Artificial Muscle Trailing Edge Flap (PAM TEF) system presented here represents a significant advancement in the state of the art. It incorporates a series of analytical models that describe the various system elements including the spool valve, air tubing, PAM pressure, PAM volume, PAM force, linkage system kinematics, system loading, and flap dynamics. Comparison to experimental data collected on a vacuum chamber whirl rig (non-rotating) showed that the model was able to accurately predict the time evolution of force and pressure in the PAM actuators and the resulting flap deflections, given only the geometric and material parameters of the system, the set point pressure of the regulator, and the control signal sent to the spool valve. It can do so over a broad range of actuation frequencies and pressure settings. More specific conclusions from this work include:

1. The ISO 6358 standard orifice flow model was successfully applied to a FESTO MPYE-5-1/8-HF-010-B proportional spool valve to estimate air mass flow.

2. Spool valve mass flow was combined with a connecting tubing pressure loss, a model governing pressure change in a vessel of changing volume, and an analytical model of PAM volume to very accurately capture the dynamics of the internal PAM pressure over a broad range of operating frequencies and set point pressures.

3. Internal PAM pressure estimates and kinematic relations were fed into a four term quasistatic model of PAM force to produce accurate estimates of the time evolution of force in the PAMs. Some higher order dynamics appear in the experimental results that are not captured in the model, leading to discrepancies between model and experiment. These differences were found to diminish as operating frequency increases.

4. A novel offset bellcrank kinematic system was found to provide significant increases in the amount of quasistatic torque generated by the PAM TEF system, with a 37% increase in torque generated at a flap deflection of 20°.

5. A second order linear model of the flap dynamics that incorporated resultant torque from the actuation system, 2D airfoil theory based aerodynamic hinge moment predictions, linear elastic predictions of torsion rod flexure stiffness, estimates of system inertia derived from component 3D models, and an empirical estimate of system damping successfully predicts the time history of flap deflection angle over a wide range of operating conditions. Accuracy was found to be very good, with the possible exception of high pressure operation at low frequencies.

6. Mechanical interference in the design of the linkage system was identified as one potential source of discrepancies between model and experiment for very high flap deflection angles on the order of 20°. Deflections of this magnitude are achieved only during low frequency operation at high pressures.

6.10. REFERENCES

Ascher, U. and Petzold, L., 1998. *Computer Methods for Ordinary Differential Equations and Differential-algebraic Equations*, Society of Industrial and Applied Mathematics, Philadelphia, PA, pg. 78.

Beater, P., 2007. *Pneumatic Drives: System Design, Modelling, and Control*, Springer, New York, pg. 38.

Bubert, E., 2009. "Highly Extensible Skin for a Variable Wing-Span Morphing Aircraft Utilizing Pneumatic Artificial Muscle Actuation," Master's Thesis, University of Maryland.

Chou, C.P. and Hannaford, B., 1996. "Measurement and Modeling of McKibben Pneumatic Artificial Muscles," *IEEE Trans. Robotics and Automation*, 12(1):90-102.

Colbrunn, R., Nelson, G., and Quinn, R., 2001. "Modeling of Braided Pneumatic Actuators for Robotic Control," *Proceedings of IEEE/RSJ International Conference on Intelligent Robots and Systems*, Maui, HI, Oct. 29 – Nov. 3.

Festo, 2011. "Proportional directional control valves MPYE," Online product documentation, http://www.kiowa.co.uk/static/documents/Festo/MPYE_EN.PDF, accessed 11/11/2011.

Incropera, F., and DeWitt, D., 2006. *Fundamentals of Heat and Mass Transfer*, John Wiley & Sons, New York, New York.

ISO 6358, 1989. "Pneumatic Fluid Power – Components Using Compressible Fluids – Determination of Flow-rate Characteristics."

Pugi, L., Malvezzi, M., Allotta, B., Banci, L., Prescniani, P., 2004. "A Parametric Library for the Simulation of a Union Internationale des Chemins de Fer (UIC) Pneumatic Braking System," *Proc Instn Mech Engrs, Journal of Rail and Rapid Transit*, 218(F):117-132.

Richer, E., and Hurmuzlu, Y., 2000. "A High Performance Pneumatic Force Actuator System: Part I – Nonlinear Mathematical Model," *ASME Journal of Dynamic Systems, Measurement, and Control*, 122(3):416-425.

Sanville, F., 1971. "A New Method of Specifying the Flow Capacity of Pneumatic Fluid Power Valves," *Second International Fluid Power Symposium*, Guildford, England, Paper D3, pp. 37-47.

7. PAM TEF Controller Development

7.1.   PAM CONTROL BACKGROUND

A good overview of control methodologies for PAMs and pneumatic pistons can be found in (Bubert, 2009). The control work reviewed here was performed with either single PAMs acting against a load or with double-acting pneumatic pistons and is similar, but not equivalent, to the current application. A variety of different pneumatic control elements and control algorithms have been employed. It was concluded that the use of a pressure control valve as the driving element provides stable performance with good tracking, but has severely limited bandwidth. Further, Bubert concludes from this review that proportional flow rate control valves show more promise for high frequency control, as they have better response times (Bubert, 2009). Most of the related control work published in the literature has been for robotic applications, so frequencies on the order of only 1 Hz are typical.

One group did investigate higher frequencies, and had success applying a sliding mode controller to a proportional spool valve with a pneumatic piston as the actuator (Richer, and Hurmuzlu, 2000). This system was designed to produce sinusoidal force variations at 20 Hz. Closed-loop frequency response results were shown for frequencies up to 34 Hz, but the phase lag in the response became increasingly large above 12 Hz, and the magnitude response, while good at the 20 Hz design point, deviated substantially at both lower and higher frequencies. This motivates the present study for flap actuation control, which requires accurate wave shape tracking over a much larger frequency band. Moreover, there has been no work published to date on the control of antagonistic PAM

systems in the frequency range of interest for active rotor systems (considered to range from static, or 0 Hz, up to 35 Hz in this study). Given the promising results of previous PAM active flap testing, particularly with regard to flap deflection magnitudes under full-scale loading at both primary control (1/rev) and higher harmonic (N±1/rev) frequencies, there is great potential with these pneumatic devices. Proving their tracking control ability is the remaining hurdle on the actuator level, and hence, is the purpose of this work.

7.2.   EXPERIMENTAL APPARATUS

Controller development work was carried out on a benchtop rig that simulated the full-scale loading (inertia and stiffness) of a representative PAM TEF actuation system. The testing performed here was intended, as much as possible, to show the general controllability of a PAM TEF system under a variety of circumstances. For that reason, the particulars of the design of the PAM system, and of the loading conditions applied, were not intended to be a specific solution to a specific active trailing edge flap system. Instead they were designed to highlight the general controllability of such an actuation system over a broad range of operating conditions.

The agonist/antagonist pair of PAMs was mounted to an aluminum frame. A bellcrank was attached to the moving ends of the PAMs such that torque and rotation outputs were generated from the force and contraction of the PAMs. This arrangement is shown schematically in Figure 7.1a. Unloaded testing was performed with just the two PAMs pulling against each other through the bellcrank. Simulated full-scale loading was

added by attaching an inertial mass and a variable stiffness torsion spring directly to the bellcrank.
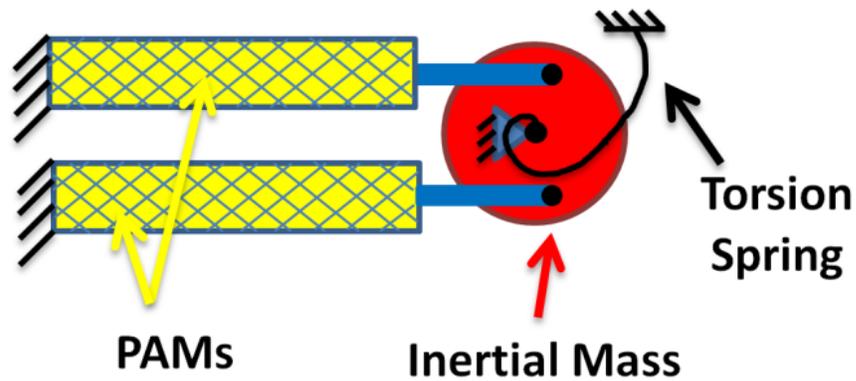
(a.) Test rig schematic
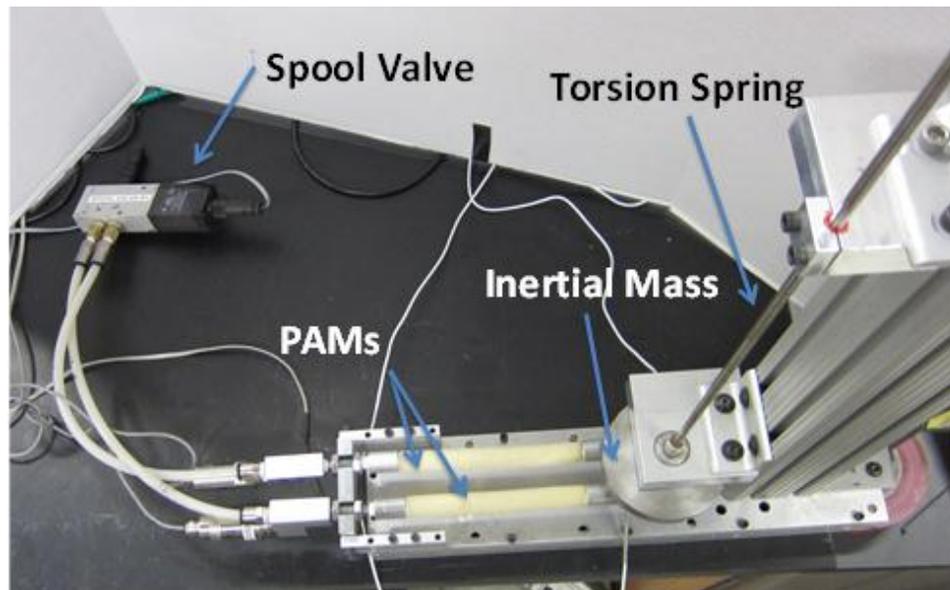
(b.) Test rig as built

Figure 7.1 PAM controller development rig

Pressurization of the two PAM actuators was controlled via a Festo MPYE 5/3-way proportional spool valve, as shown in Figure 7.1**Error! Reference source not found.**b. This device has 5 ports; one for the pressure source, one for each PAM, and

one port for the exhaust from each PAM. These ports are connected in various ways by the movement of the internal spool. The spool is designed such that the inflation and exhaustion of the two PAMs are linked and controlled by the position of the single moving element, which is driven by an electromagnetic actuator. The valve requires an analog control voltage from 0-10 V to set the desired spool location. Control voltages from 0-4.8 V connect the first PAM to the pressure source and the second PAM to atmosphere, and voltages from 4.8-10 V connect the second PAM to the pressure source and the first PAM to atmosphere. The size of the flow orifices increases the farther the control signal is from the center voltage of 4.8 V. At 4.8 V, all flow is nominally blocked, although there is a small leakage flow from the source to the exhaust ports. The supply pressure into the spool valve was nominally set to 90 psi for all of the testing to be shown here. The valve itself is rated up to 150 psi, but the house air system used in this testing was limited to 90 psi. As has been shown in previous work (Woods, Bubert, Kothera, *et al.*, 2007), increasing operating pressure produces larger PAM forces, and therefore larger output torques and deflections in a PAM TEF system. If desired, the system performance could effectively be increased by using a higher pressure pneumatic supply system.

There was 16-in of tubing between the output of the spool valve and the inlet of each PAM, and it had an internal diameter of 0.27-in. This tubing length was determined from preliminary design work for a full-scale PAM TEF system that placed the control valve on top of the rotor hub and the two PAMs internal to the hollow, thickened blade root (Woods, Kothera, and Wereley, 2010).

The PAM actuators used in this experiment were designed to provide large actuation torques and bellcrank deflection outputs up to ±10 deg. It is important to note that in a PAM TEF system, the bellcrank deflection levels do not necessarily have to be the same as the final flap deflection levels. Direct connection of the flap to the bellcrank is feasible (if space permits), but there would likely be some additional mechanism (control rod, linkages, etc.) connecting the bellcrank to the flap. This mechanism, whatever its form, could introduce an amplification or reduction in deflection angle. In other words, the nominal angular deflection of the bellcrank could be scaled up at the expense of torque available, or could be scaled down to increase torque. For this reason, it is useful to consider the deflections achieved in light of the stiffness and inertia against which the system was acting, as this gives a more complete picture of the actuation power output. Details of the design methods used for achieving a certain flap deflection goal have been presented elsewhere (Chapter 4), and so will not be repeated here.

The torsion spring employed was a stainless steel rod rigidly attached to the bellcrank and inertial mass on one end, and clamped at varying effective lengths on the other end via a sliding clamp block. This arrangement allowed for testing at different values of torsional stiffness, from a minimum of 4 in-lb/deg when clamped at its full length, up to a maximum of 11 in-lb/deg. Additionally, the spring was designed to be completely removable such that the unloaded behavior of the system could also be studied.

The inertial mass was constructed from a machined steel disc and provided a total rotational inertia of approximately 5.3 lb-in^2, which was intended to be representative of

a trailing edge flap of substantial chord and span. There is some coupling between the stiffness and inertia in that the amount of torsion spring mass that rotates with the system changes as a function of the effective spring length. The effective rotational inertia of the torsion spring varies from 0.0004 lb-in^2 at its shortest length to 0.001 lb-in^2 at its longest. This change in inertia is only about 0.013% of total inertia however, so this effect is negligible. A summary of the design parameters and possible loading conditions of this PAM TEF system are shown in Table 7.1.

Table 7.1. Actuation system parameters

Parameter	Value	Units
PAM active length	6.1	in
Initial PAM radius	0.625	in
Initial braid angle	73	deg
Initial bellcrank arm	0.8	in
PAM mass (each)	60	g
Operating pressure	90	psi
Loading stiffness	0, 4-11	in-lb/deg
Inertial load	0, 5.3	lb-in^2

The test rig was instrumented with a suite of sensors to track various parameters of system performance. A pressure transducer was installed between the fixed end of each PAM and the tube supplying it with air. This gave as close to a reading of internal PAM pressure as possible without placing a transducer inside of the actual PAM. To record the forces generated by the PAMs, a 1000 lb load cell was installed at the moving end of each PAM, between the end fitting and the bellcrank. Finally, to monitor the output flap deflection angle, a non-contact Hall-effect based sensor was installed on the underside of the bellcrank shaft.

Real-time closed-loop feedback control was implemented on the test rig using a digital signal processing hardware system designed for rapid control prototyping, which ran controller models developed with engineering software. The use of the computer software model allowed for changes in the controller algorithm to be tested quickly. The sensor signals were fed into the analog-to-digital converters of the digital signal processing system and recorded with each data set. The angle sensor signal was used in real-time as the feedback variable.

7.3.   CONTROL SYSTEM DEVELOPMENT

Initial development of the control system began with a proportional-integral-derivative (PID) algorithm, though results with tuned gains showed tracking performance to be benefitted most directly from the proportional term. Integral and derivative control did little to improve tracking, and at times would cause instability. For that reason, further testing used only proportional feedback of the angle error. This simple control algorithm was sufficient for low frequency position tracking, however, significant error developed at higher frequencies. This error was determined to be primarily due to dead-time in the system. Pneumatic fluid control systems generally show a certain dead-time (or transport lag) that comes from delays in the control valve operation and from fluid transport dynamics. The effect of dead-time can be modeled as in Figure 7.2.
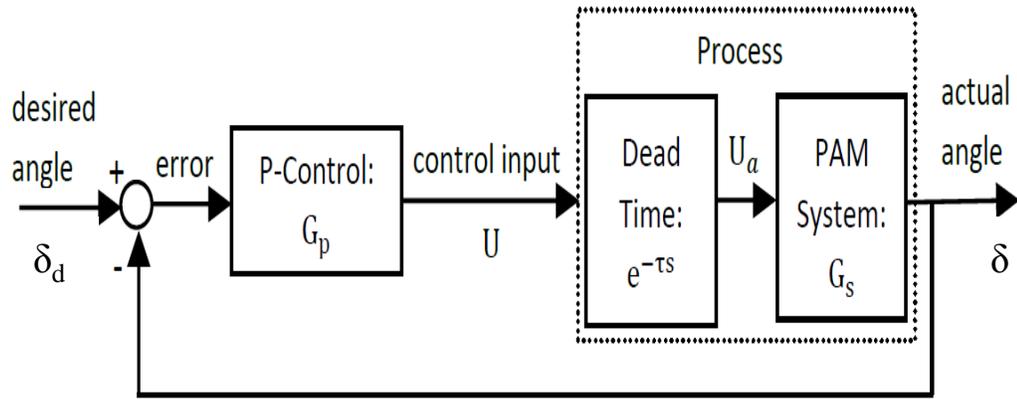
Figure 7.2. Block diagram for system with proportional control and dead-time present in the system

If a proportional controller (P-controller) without dead-time consideration provides the PAM system, G_s, with a control input, U, at current time, t, then the actual control input, U_a, applied to the PAM system will be:

$$U_a = U\,e^{-\tau s} \tag{1}$$

Here, τ is the dead-time of the PAM system. As seen in Eq. (1), the control input, U at current time, t will not affect the PAM system until a later time, $t+\tau$. This delayed control action introduces a time shift in the actual tracking position of the PAM system and increases tracking error significantly, especially at high frequencies. On the other hand, if the desired position (i.e., angle in this study) signal is intentionally shifted by the dead-time, τ of the PAM system, the tracking error due to the dead-time of the PAM system can be minimized. Incorporating such a time shift into the system produces a fixed dead-time compensator (FDTC) and its block diagram is shown in Figure 7.3. As can be seen in Figure 7.3, the error $E(t)$ for the FDTC control algorithm case is given by

$$E(t) = \delta_{d,t-\tilde{\tau}}(t) - \delta(t) \tag{2}$$

Here, $\delta_{d,t-\tilde{\tau}}(t)$ is the desired signal shifted by the estimated dead-time (Horiuchi, Inoue, Konno, *et al.*, 1999; Ahmadizadeh, Mosqueda, and Reinhorn, 2008), $\tilde{\tau}$, of the PAM system at current time, *t*, and is calculated on-line based on Newmark's Beta method (Petyt, 2010) as follows:

$$\dot{\delta}_{d,t-\tilde{\tau}}(t) = \dot{\delta}_{d,t-\tilde{\tau}}(t - \Delta t) + \frac{\Delta t + \tilde{\tau}}{2}\left[\ddot{\delta}_{d,t-\tilde{\tau}}(t - \Delta t) + \ddot{\delta}_{d,t-\tilde{\tau}}(t)\right] \tag{3}$$

$$\delta_{d,t-\tilde{\tau}}(t) = \delta_{d,t-\tilde{\tau}}(t - \Delta t) + (\Delta t + \tilde{\tau})\dot{\delta}_{d,t-\tilde{\tau}}(t - \Delta t) + \frac{1 - 2\beta}{2}(\Delta t + \tilde{\tau})^2\ddot{\delta}_{d,t-\tilde{\tau}}(t - \Delta t)$$

$$+ \beta(\Delta t + \tilde{\tau})^2\ddot{\delta}_{d,t-\tilde{\tau}}(t) \tag{4}$$

Here, Δt is the sampling time and the constant β should satisfy $0 \leq \beta \leq 1$. In this study, the constant $\beta = 0$ was chosen for the calculation of the advance desired signal.
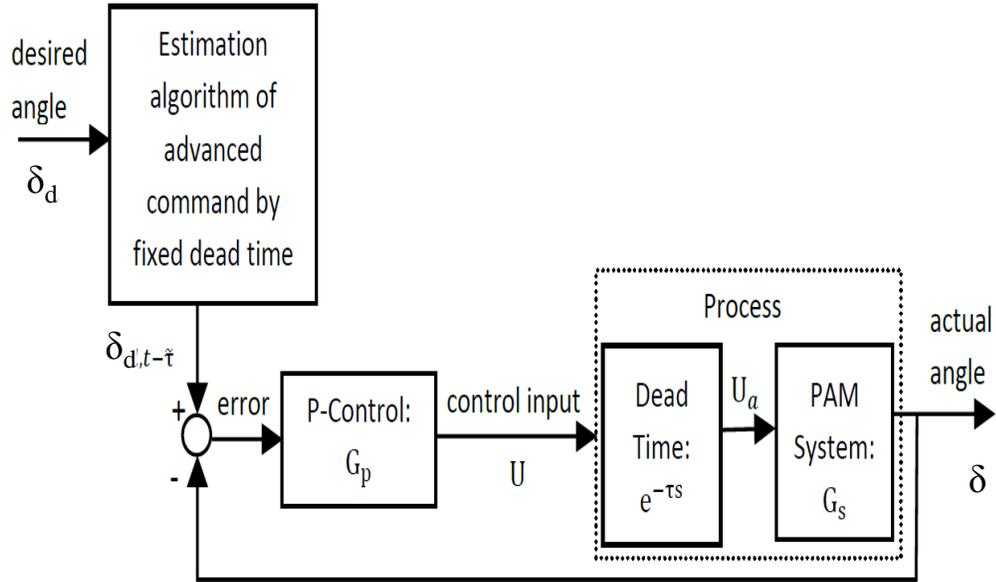
Figure 7.3. Block diagram for system with proportional control and fixed dead-time compensation (FDTC)

Prior accurate estimation of the dead-time of a system is a key factor for successful implementation of the FDTC, but if the dead–time can be estimated on-line during control, there may be an advantage of more robust control performance. Thus, in this study, a variable dead-time compensator (VDTC) was also introduced for comparative evaluations and its block diagram is shown in Figure 7.4. In this case, the estimation of the dead-time τ is calculated using Darby's delay estimation (Darby, Williams, and Blakeborough, 2002) as follows:

$$\tilde{\tau}(t) = \tilde{\tau}(t - \Delta t) + C_p \tanh\{C_v \dot{\delta}_{d,t-\tilde{\tau}}(t)\}\{\delta_{d,t-\tilde{\tau}}(t) - \delta(t)\} \tag{5}$$

In this study, the constants to determine the convergence rate were experimentally chosen to be $C_p = 0.0001$ and $C_v = 0.0003$.
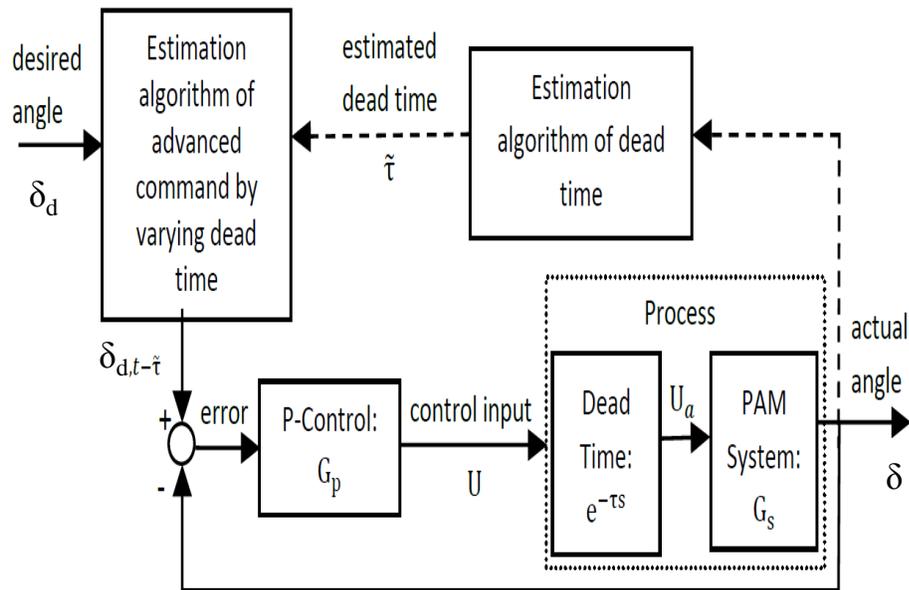
Figure 7.4. Block diagram of a variable dead-time compensating (VDTC) control algorithm

7.4. RESULTS AND DISCUSSION

Results from testing the three controllers on an unloaded system tracking single frequency sine waves will lead to down-selection of the best controller algorithm. This controller will then be used to track both single frequency and complex multiple frequency waveforms under simulated full scale loading.

7.4.1. UNLOADED SINE WAVE TRACKING – CONTROLLER SELECTION

The first round of testing used a classical PID controller, which exhibited good low frequency tracking performance. Gain studies showed that the proportional term was the primary driver of closed-loop tracking performance. The integral and derivative terms were found to have little positive impact on error levels, while leading to instabilities in certain conditions. For this reason, the integral and derivative gains were

set to zero for all further testing. The ability of the proportional controller to track a 1 Hz, ±7° sine wave can be seen in the upper plot of Figure 7.5. The proportional controller suffered from significant phase lag at higher frequencies, however. This can be seen clearly in Figure 7.6 and Figure 7.7.
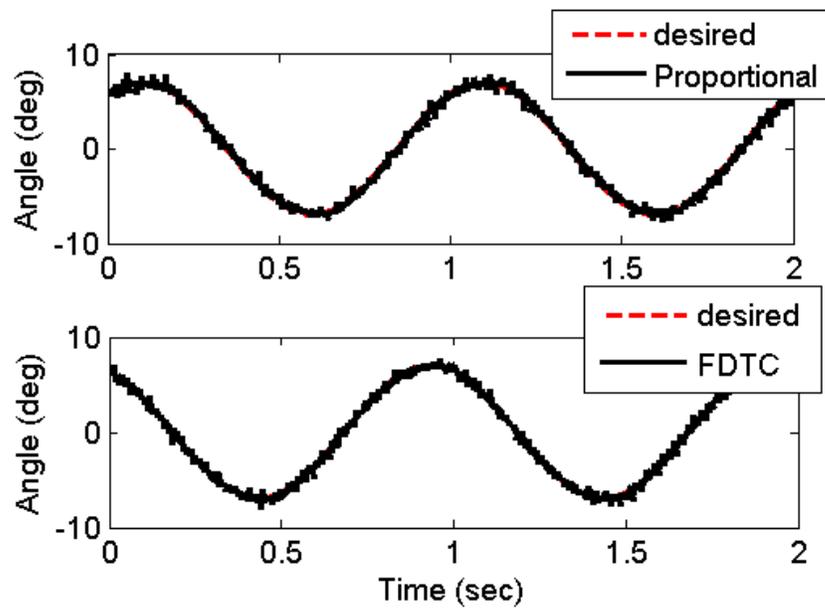
Figure 7.5. Sine wave tracking at 1 Hz, proportional only and fixed dead-time, δ = 7.0°.
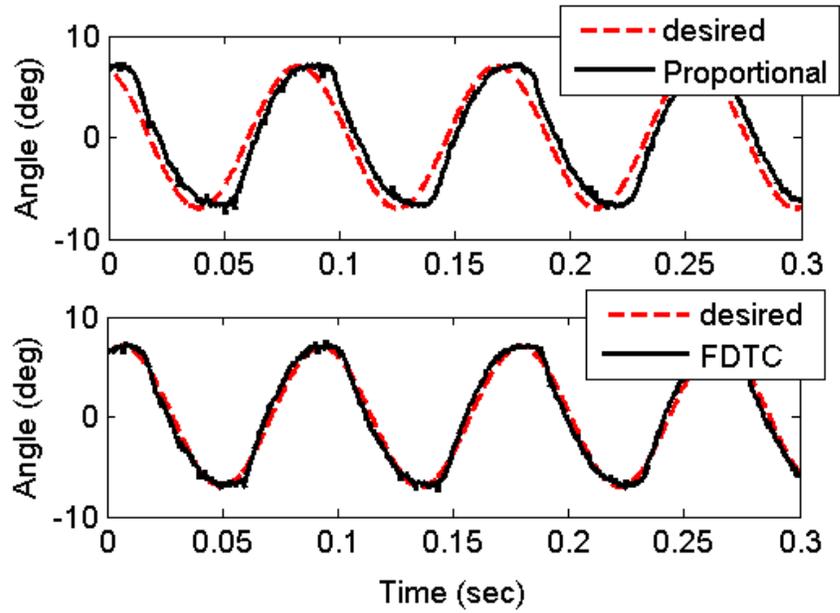
Figure 7.6. Sine wave tracking at 12 Hz, proportional only and fixed dead-time.
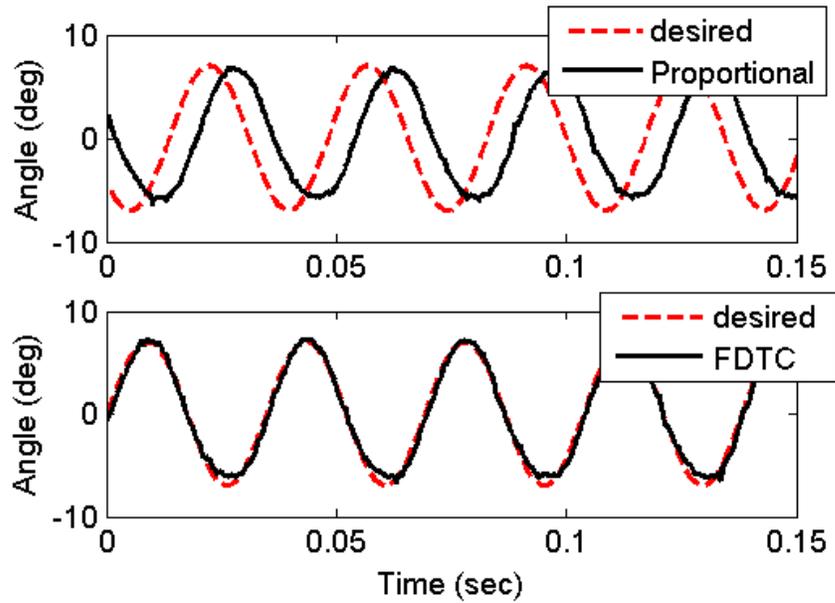
Figure 7.7. Sine wave tracking at 29 Hz, proportional only and fixed dead-time

284
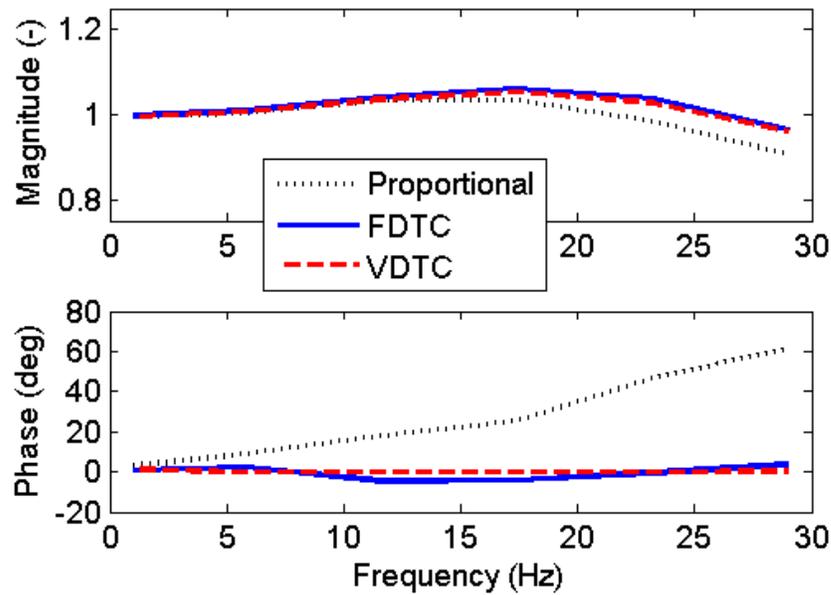
Figure 7.8. Frequency response of unloaded system under different control algorithms

Incorporation of the fixed dead-time compensation (FDTC) into the controller allowed substantial improvement in overall tracking performance. The already good tracking performance at 1 Hz (Figure 7.5) was not significantly improved, but the benefit of the FDTC element is clear at 12 Hz (Figure 7.6), and is even more evident at 29 Hz (Figure 7.7).

It can be seen that the FDTC tracks the changes in direction better than the proportional control. This is because the changes in direction that occur after the peaks and troughs of the sine wave require large control action. When uncompensated, the inherent dead-time in the pneumatic control system does not allow the control action to immediately create the changes in torque and rotation required to track the desired output.

One characteristic of the FDTC algorithm is that it requires an *a priori* estimate of the dead-time in the system. In this study, the dead-time was experimentally estimated by examining the response to a step input. The bellcrank angle would begin to move approximately 7-ms after the command signal. This dead-time is not necessarily constant for a system, however, so tracking errors will occur if the system is operating at conditions different from those used in the experimental estimation.

These shortcomings would be eliminated if the controller was able to estimate the dead-time in real-time and compensate for any changes automatically. This is the concept behind the VDTC controller. The improvement in phase tracking that can be seen in the closed-loop frequency response function shown in Figure 7.8 can be directly attributed to changes in the system dead-time across the bandwidth. Unlike the FDTC, the VDTC controller is able to track these changes and therefore shows very little phase shift across the frequency range of interest.

The improvements in controller tracking performance can also be seen in another quantitative sense by looking at the root mean square (RMS) error calculations of error in the tracking performance over the time period tested. One typical example of this can be seen in Figure 7.9, where the RMS error for a desired single sine wave with $\delta = 7.5°$, K = 9.2 in-lb/deg, and $J = 5.3$ lb-in^2 is shown. It can be seen that there is a significant reduction in error for the FDTC controller as compared to the proportional-only case. It can also be seen that the VDTC provides a further reduction in error across the bandwidth of interest.
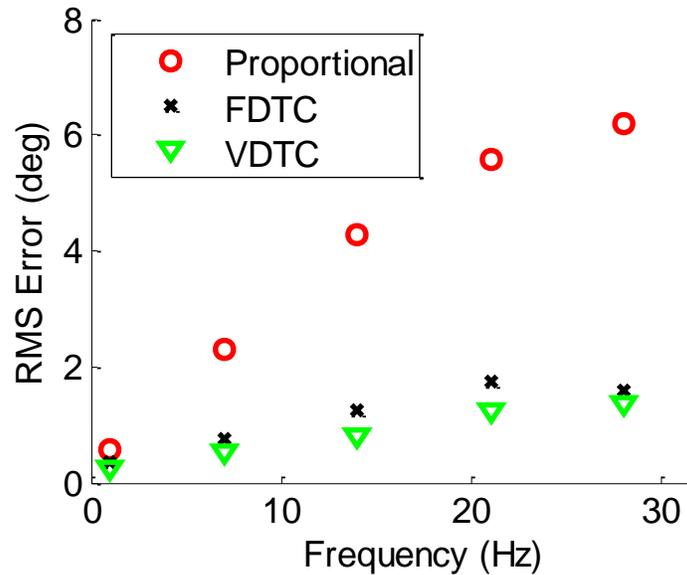
Figure 7.9. Reduction in tracking error with controller changes ($\delta = 7.5°$, $K = 9.2$ in-lb/deg, and $J = 5.3$ lb-in^2).

The VDTC controller was selected as the superior of the three examined due to its better phase and magnitude tracking and lower error levels, and was therefore used for all subsequent testing.

7.4.2. LOADED SINE WAVE TRACKING WITH VDTC CONTROLLER

With the form of the controller having been decided, a series of tests was undertaken to investigate the effects of varying load levels on tracking ability. The parameters studied were flap deflection amplitude, actuation frequency, torsional stiffness, and rotational inertia. Table 7.2 shows the range of variables tested. Figure 7.10 shows the system response to a $\delta = 5°$, $f = 7$ Hz sine wave with $K = 9.2$ in-lb/deg and $J = 5.3$ lb-in^2. While not as smooth or accurate as the unloaded responses shown previously, the tracking capability is still quite good and the error levels are low.

Table 7.2. Sine Wave Tracking Test Parameters

Parameter	Symbol	Values Tested	Units
Amplitude	δ	2.5, 5, 7.5, 10	deg
Frequency	f	7, 14, 21, 28, 35	Hz
Stiffness	K	0, 6, 9.2	in-lb/deg
Inertia	J	0, 5.3	lb-in^2

In order to better understand the response of the system, it is useful to examine the time histories of the pressure and force as well. Figure 7.11 shows this information for the system tracking a $\delta = 5°$, $f = 7$ Hz sine wave with $K = 9.2$ in-lb/deg and $J = 5.3$ lb-in^2. Note that PAM A drives the system to positive deflection angles and PAM B drives the negative deflection angles. This can be seen through comparison of the pressure response to the angle response in Figure 7.10, which has the same time scale and loading conditions. The time histories of pressure show the control action being taken to maintain tracking. The forces in the PAM include the dynamic effects of this pressure and of the stiffness and inertia.

The pressure and force are of particular interest in looking at the behavior of this PAM TEF system because they show key aspects of the chain of events that leads to the final angle output. This chain starts with the controller issuing a command signal to the spool valve based on the error between the desired and actual angle measurements. The valve then responds by changing the orifice area and flow direction to the two PAM actuators. As mentioned previously, the flow ports are linked such that the five different orifice areas are controlled by a single input. This linking forces the two PAMs to fill and exhaust out of phase from each other. Orifice area, combined with existing pressure

differentials, then leads to time-varying mass flow rates of air into and out of the PAMs. As air mass is accumulated in or removed from the PAMs, the internal pressure changes accordingly. This pressure then generates force in the PAM that is also dependent on the current length of the actuator. These forces then resolve through the bellcrank into torques, which act against the inertial and stiffness loading to provide the desired waveform tracking.

With respect to the variable dead-time compensating controller, it is worth noting that the dead-time that is continuously estimated and compensated for is a result of the initial portions of the chain of events described above. The estimated dead-time encompasses the time required by the spool valve to respond to the command signal and change the orifice areas, the time required for the pressure differentials to establish a mass flow rate, and the time required for this mass flow to travel through the fluid tubing and into the PAMs. All three of these phenomena are complex dynamic problems themselves. It is therefore simpler and much faster (from a control perspective) to use a single real-time estimated parameter to account for their combined effects, as opposed to modeling and controlling them all independently.
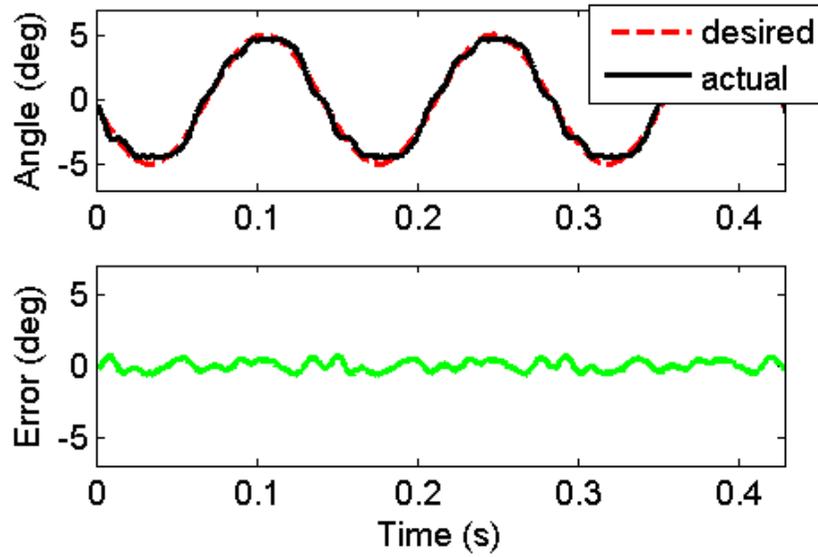
Figure 7.10. VDTC tracking performance with $\delta = 5°, f = 7$ Hz, $K = 9.2$ in-lb/deg, and $J = 5.3$ lb-in^2.
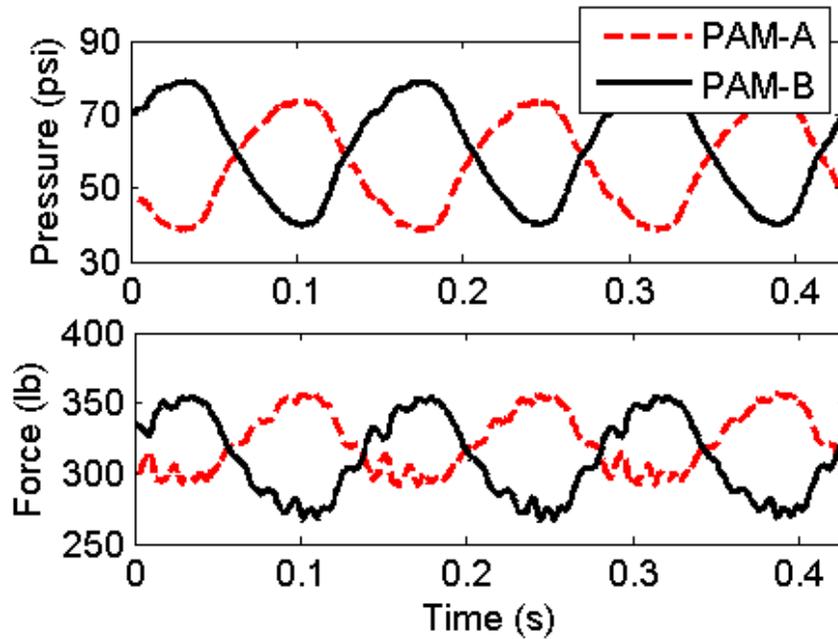
Figure 7.11. Time histories of pressure and force for $\delta = 5°, f = 7$ Hz, $K = 9.2$ in-lb/deg, and $J = 5.3$ lb-in^2.

In Figure 7.12, the tracking performance for a higher frequency sine wave is shown. At 35 Hz under loading of $K = 6$ in-lb/deg and $J = 5.3$ lb-in^2, the system exhibits some overshoot in the amplitude of the deflections. This was not seen in the unloaded testing and is most likely the result of the inertial load restricting the ability of the system to track the change in direction of the sine wave. Lower system inertia or higher PAM torque (which could be obtained by operating at a higher pressure, as discussed previously) would likely mitigate this overshoot. Also note the asymmetry in the overshoot between positive and negative deflections. This is likely the result of either slight differences in the forces generated by the two PAMs due to variances in their manufacturing, or asymmetry in the operation of the spool valve.
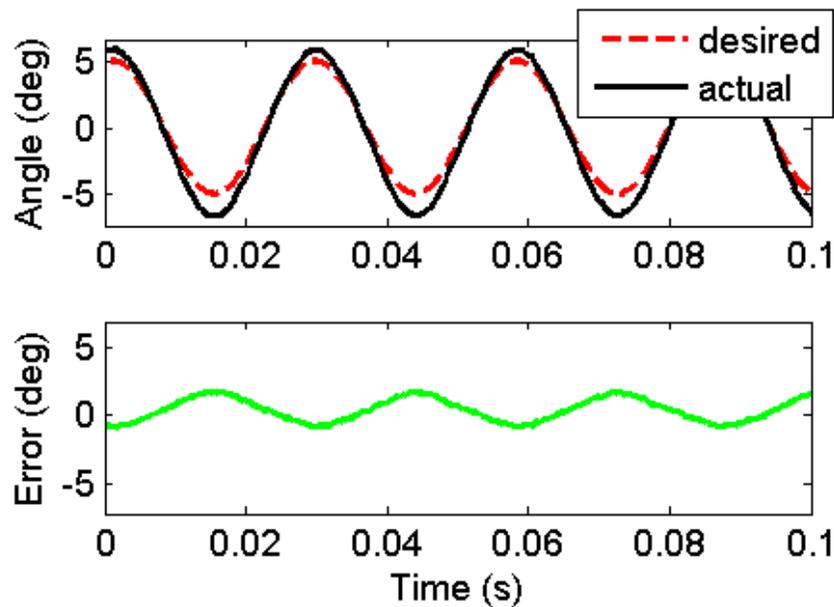
Figure 7.12. VDTC tracking performance with $\delta = 5°$, $f = 35$ Hz, $K = 6$ in-lb/deg, and $J = 5.3$ lb-in2.

The evolution of tracking performance with frequency can be seen in the closed-loop frequency response functions. For example, Figure 7.13 shows the frequency

response for different levels of commanded deflection amplitude. There is an interesting

trend with both the magnitude and phase results. As the deflection amplitude is

increased, the system magnitude response goes from slightly above to slightly below

unity, particularly at the higher frequencies. This is likely a result of the larger torque

levels required to obtain the larger deflections. The phase also goes through a transition

from lagging at low deflections to leading at higher deflections. This being said, it must

also be noted that the magnitudes remain near unity across the entire frequency range of

interest, and the phases remain approximately zero.
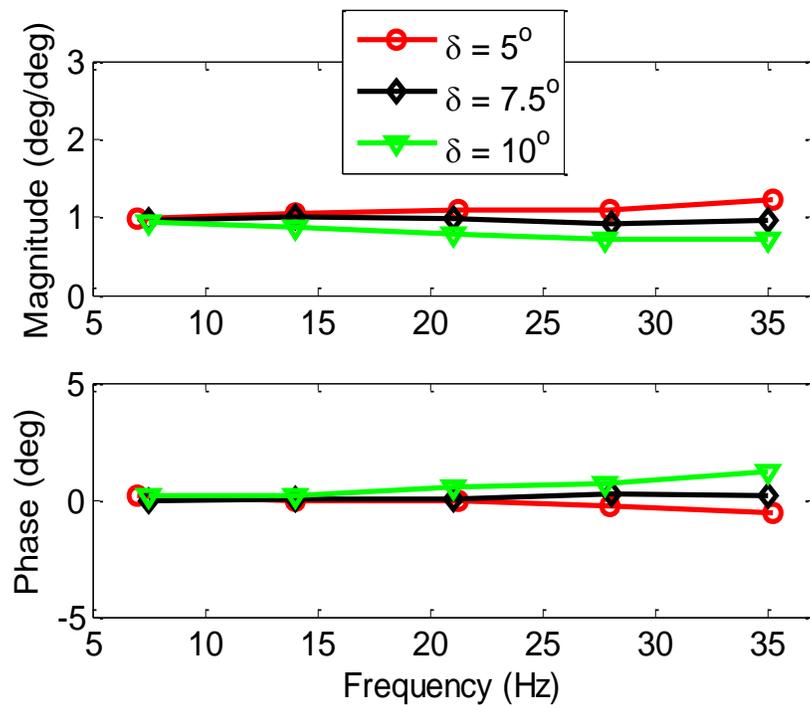
Figure 7.13 Frequency response with deflection amplitude variation, *K* = 9.2 in-lb/deg and J = 5.3 lb-in2
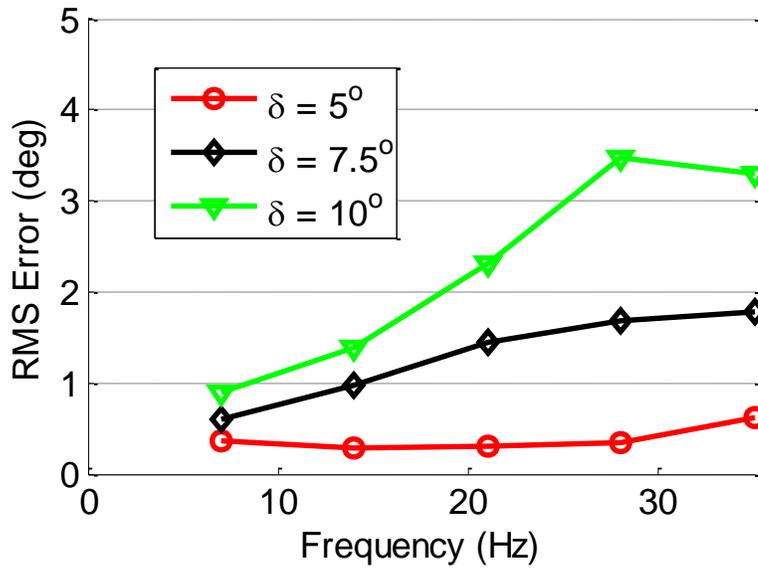
Figure 7.14. RMS tracking error with deflection amplitude variation, K = 9.2 in-lb/deg and J = 5.3 lb-in2

Figure 7.14 shows the effect of different commanded amplitudes on the RMS error. Note that higher deflection levels cause significant increases in the RMS error, as do increases in frequency. The errors shown in Figure 7.14 were the highest seen in this testing as they are for the stiffest spring load and highest inertia.

7.4.3. LOADED SINE WAVE TRACKING WITH VDTC CONTROLLER

With good sine wave tracking capability established, the ability of the VDTC controller to track the more complex waveforms that would be required for an active rotor system were investigated next. A series of waveforms was created to be representative of a four-bladed active rotor tracking a multi-sine wave command signal composed of a large 1/rev primary control component overlaid with smaller components at 3/rev, 4/rev, and 5/rev for vibration control. The vibration control elements were shifted in phase from the 1/rev signal and from each other. The main rotor frequency was

chosen to be 7 Hz, resulting in the representative command signal containing frequency content at 7, 21, 28, and 35 Hz. The waveforms used are detailed in Table 7.3. Note that the amplitudes and phases chosen for the components are arbitrary, but were intended to encompass a large range of possible waveforms, thereby showing the general ability of the PAM actuation system to follow various complex waveforms. Three complex waveforms were created and the ability of the PAM TEF system with VDTC controller to track them was tested against the same loading levels that were used for the single frequency sine waves.

Table 7.3. Composition of complex waveforms tested.

Waveform #	Frequency (Hz)	Amplitude (deg)	Phase (deg)
1			
	7	7	0
	21	2	90
	28	2	240
	35	2	180
2			
	7	6	0
	21	0.5	60
	28	1	120
	35	0.5	30
3			
	7	5	0
	21	3	90
	28	2	240
	35	1	45

The first results shown are for waveform #1 with no inertial or stiffness loading. Figure 7.15 shows that the error in this case is small (RMS error = 0.74 deg) and the tracking performance is good. Adding stiffness to the system without adding the inertial mass causes a reduction in the peak amplitudes obtained when tracking waveform #1. Figure 7.16 shows the response of the system with no inertia and the stiffest spring ($K =$

9.2 in-lb/deg). With an RMS error of 1.38 deg, the error is higher here than that seen with no stiffness. The addition of inertia further degrades the tracking performance. Figure 7.17 shows the system loaded with $K = 9.2$ in-lb/deg and $J = 5.3$ lb-in^2. The RMS error in this instance is 1.51 deg. It can be seen that the addition of this large amount of inertia limits the ability of the system to track the abrupt changes in direction present in this complex waveform.
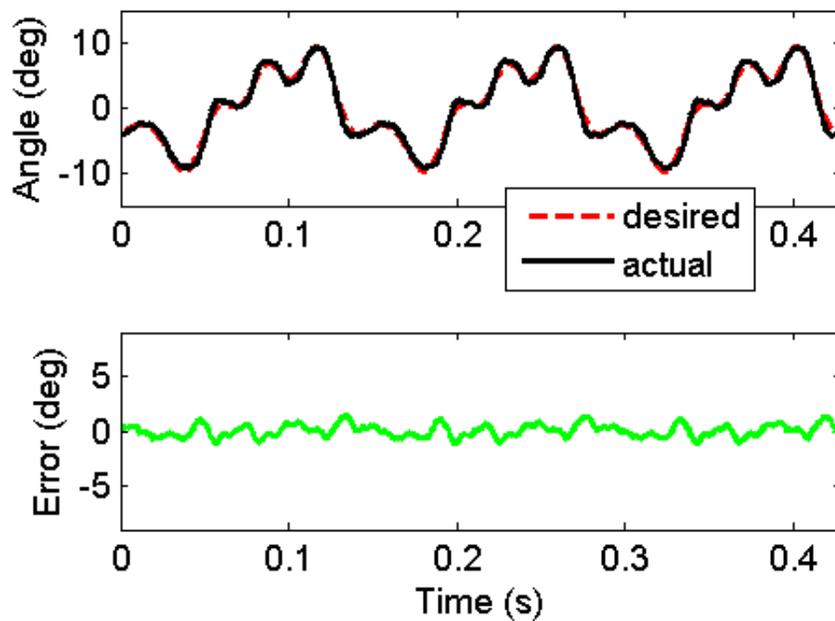
Figure 7.15. Unloaded tracking of complex waveform #1.
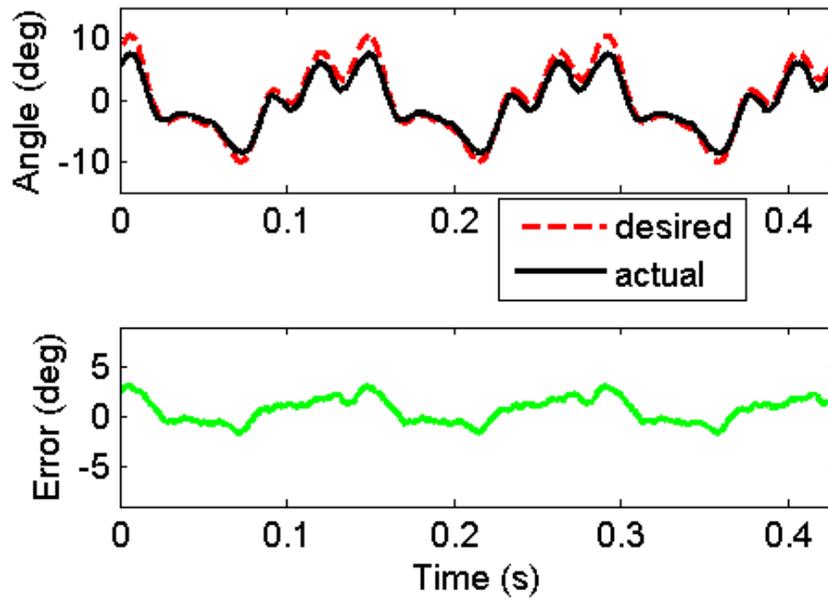
Figure 7.16. Stiffness loaded tracking of complex waveform #1, K = 9.2 in-lb/deg and J = 0 lb-in^2.
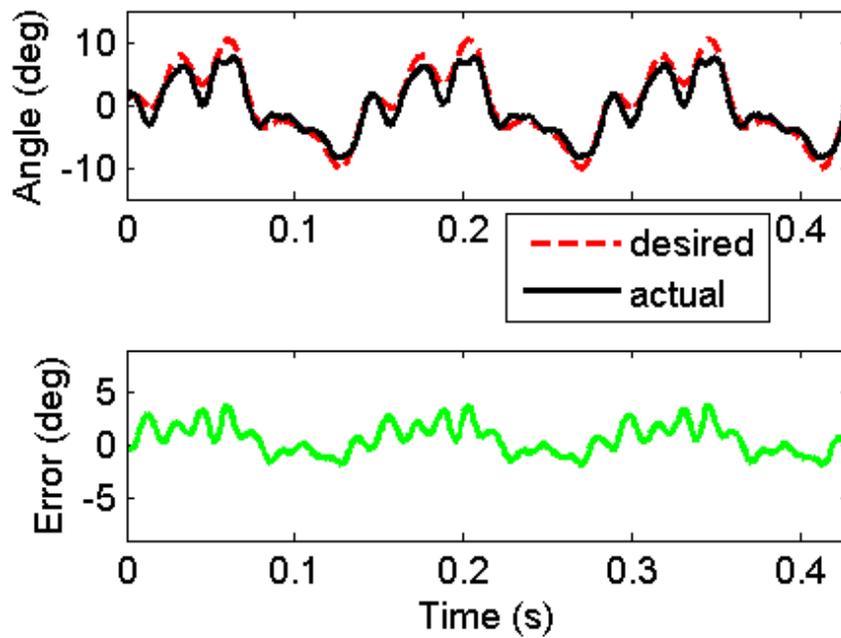
Figure 7.17. Stiffness and inertial loaded tracking of complex waveform #1, K = 9.2 in-lb/deg and J = 5.3 lb-in^2.

Figure 7.18 and Figure 7.19 show the tracking capability of the fully loaded system (K = 9.2 in-lb/deg and J = 5.3 lb-in^2) for complex waveforms #2 and #3. Here, the RMS error levels are 0.68 deg and 0.86 deg, respectively, with the largest diversions from the desired waveform occurring during the most abrupt changes in direction. These three complex waveforms all have the same basic frequency structure, but significantly different amplitude and phase content. They show the generally good tracking capability of this PAM TEF system with a VDTC controller for waveforms featuring frequency, amplitude, and phase content typical of an active rotor flap system.
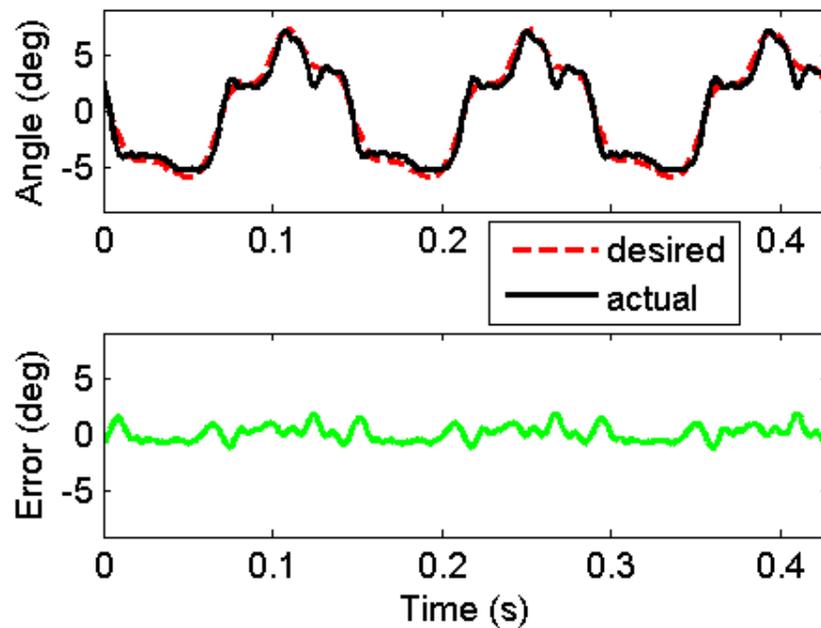
Figure 7.18. Loaded tracking of complex waveform #2, K = 9.2 in-lb/deg and J = 5.3 lb-in^2.
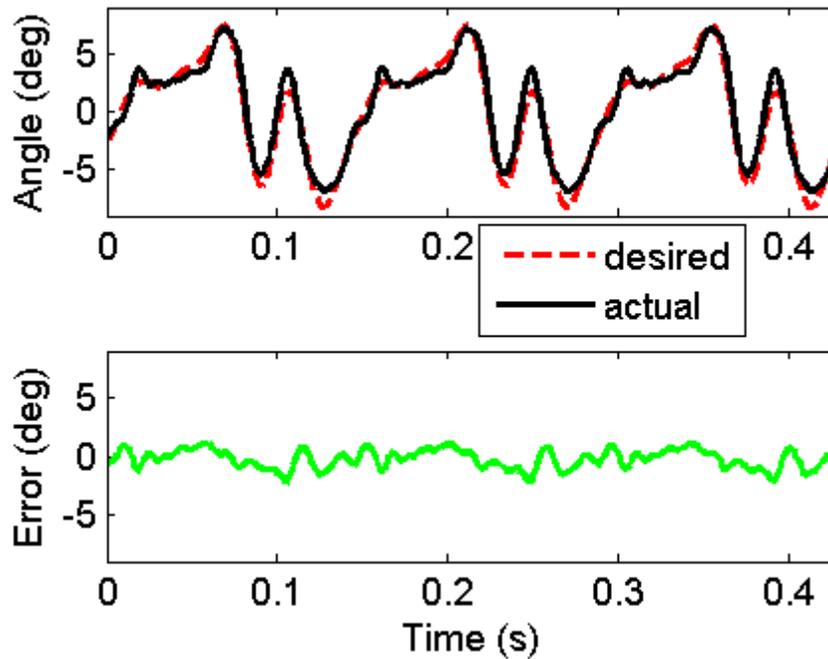
Figure 7.19. Loaded tracking of complex waveform #3, $K = 9.2$ in-lb/deg and $J = 5.3$ lb-in^2.

7.5.   CONCLUSIONS

A proportional closed-loop control system with an integrated variable dead-time compensator has been successfully implemented on a benchtop model of a trailing edge flap system driven by pneumatic artificial muscle actuators. The capability of this system to track single frequency sine waves and complex summed sinusoids over the range of frequencies typical for primary rotor control and on-blade vibration reduction has been shown. Refinement of the control algorithm by incorporating first a fixed dead-time compensator and then a variable dead-time compensator lead to significant reduction in the tracking error. Additionally, testing showed the system to be robust against different levels of simulated aerodynamic loading and rotational inertia. While further reduction of error levels may be desirable, reasonable approaches to improve upon the system

tested, such as operating at higher pressures, changing the PAM geometry or size, and tuning the mechanism kinematics, are all readily available. Overall, the combination of large control authority, high closed-loop bandwidth, and simplicity create strong motivation to pursue pneumatic artificial muscles as the driving actuators for next generation active rotor systems.

7.6.   REFERENCES

Ahmadizadeh, A, Mosqueda, G., and Reinhorn, A.M., 2008. "Compensation of Actuator Delay and Dynamics for Real-Time Hybrid Structural Simulation," *Earthquake Engineering and Structural Dynamics*, Vol. 37, No.1, pp. 21-42. doi: 10.1002/eqe.743

Bubert, E.A., 2009. "Highly Extensible Skin for a Variable Wing-Span Morphing Aircraft Utilizing Pneumatic Artificial Muscle Actuation," Master's Thesis, University of Maryland.

Darby, A.P., Williams, M.S., and Blakeborough, A, 2002. "Stability and Delay Compensation for Real-Time Substructure Testing," *Journal of Engineering Mechanics*, Vol. 128, No. 12, pp. 1276-1284. doi: 10.1061/(ASCE)0733-9399(2002)128:12(1276)

Horiuchi, T., Inoue, M., Konno, T., and Namita, Y., 1999. "Real-Time Hybrid Experimental System with Actuator Delay Compensation and its Application to a Piping System with Energy Absorber," *Earthquake Engineering and Structural Dynamics*, Vol. 28, No. 10, pp. 1121-1141. doi: 10.1002/(SICI)1096-

9845(199910)28:10<1121::AID-EQE858>3.0.CO;2-O

Petyt, M. 2010. *Introduction to Finite Element Vibration Analysis*, Cambridge University Press, Cambridge, UK.

Richer, E., and Hurmuzlu, Y., 2000. "A High Performance Pneumatic Force Actuator System: Part II – Nonlinear Controller Design," *ASME Journal of Dynamic Systems, Measurement, and Control*, Vol. 122, Sept, pp. 426-434. doi: 10.1115/1.1286366

Woods, B., Bubert, E., Kothera, C., and Wereley, N.M., 2007. "Experimental Testing of Pneumatic Artificial Muscles for Trailing Edge Flap Actuation," *AIAA Adaptive Structures Conference*, AIAA-2007-1718, Honolulu, HI, April.

Woods, B.K.S., Kothera, C., and Wereley, N.M., 2010. "Whirl Testing of a Pneumatic Artificial Muscle Actuation System for a Full-Scale Active Rotor" *American Helicopter Society 66th Annual Forum*, Phoenix, Arizona, May.

8. Conclusions

8.1. SUMMARY OF RESEARCH AND KEY CONCLUSIONS

The concept of a Pneumatic Artificial Muscle driven Trailing Edge Flap system for active helicopter rotor control has been given broad and detailed consideration in this dissertation. A novel approach to the long extant problem of active rotor actuation has been pursued and analyzed through a variety of methods, with research focusing on the major challenges and concerns standing in the way of adoption of this actuation technology into the rotorcraft field. Significant inroads have been made into proving the viability, performance, fatigue resistance and controllability of this active rotor concept. The ability to accurately model the behavior of these systems from first principles with a minimal number of empirical parameters has also been shown.

8.1.1. PROOF OF CONCEPT

Initial work focused on the development of a first generation prototype system to show the basic viability of the concept. To gain an understanding of actuator performance, a series of PAM actuators with a range of geometries were manufactured. The best performing of these was then chosen as the basis of a PAM driven TEF system. An antagonistic pair of PAMs was installed into the trailing edge of a UH 60 scale blade model. The PAMs were aligned with the chord of the blade and stacked in the thickness direction. Their moving ends were connected to a plain trailing edge flap through an internal bellcrank. Instrumentation allowed for measurement of actuation pressure, PAM forces, and flap deflection angle. Benchtop testing used spring loading to simulate the aerodynamic hinge moments at $M = 0.3$. Wind tunnel testing of the model took place in

301

an open jet wind tunnel at speeds up to $M = 0.13$. The flap deflection performance of the system was characterized over a wide range of operating pressures, frequencies, wind speeds and angles of attack.

Testing of this proof of concept system successfully showed the viability of the PAM driven TEF. Flap deflections were found to decrease with increasing wind speed and actuation frequency, but significant performance was obtained over the full test range. Deflections of $\pm 20°$ were achieved under $M = 0.13$ loading out to 24 Hz, and deflections of $\pm 4°$ were achieved under $M = 0.3$ loading out to 15 Hz. Flow rate limitations of the pneumatic supply system, which were significant for this first prototype, were identified as the primary cause of reduced performance at higher frequencies.

8.1.2.   ACTUATOR DESIGN AND FATIGUE TESTING

Concerns about the strength, durability and fatigue life of the PAM actuators in the literature were addressed through the development of a new construction method. Review of previous PAM fatigue testing showed low cycles to failure, and identified common failure modes. This informed the design of a new swaging based clamping mechanism. FEM analysis of the end fitting design was used to minimize stress concentrations in the fiber, allowing for multiple design revisions to be made before the start of fatigue testing. Mechanical testing, including both tensile strength and burst pressure, allowed for experimental verification of improvements to the design. The refined actuator design was then evaluated on a fatigue test stand under realistic loading conditions for a PAM TEF system. Intermittent characterization of the actuators during fatigue testing allowed for tracking of performance over the span of the test.

The new swaged PAM actuators showed excellent mechanical properties. Tensile testing of the swaged actuators showed a factor of safety over 5, and burst pressure testing showed a factor of safety of 3. Over 120,000,000 load cycles were applied to the actuators without incident, with testing being stopped due to program time constraints and not actuator failure. Characterization testing before, during, and after the fatigue tests showed no reduction in PAM performance.

8.1.3. WIND TUNNEL TESTING AND QUASISTATIC MODELING

A full-scale PAM TEF system was retrofit into a Bell 407 blade section. This system was designed to produce flap deflection levels well above what has been presented in the literature to date, over a wide bandwidth, under full-scale loading. A quasistatic model of PAM performance incorporating terms to account for the various force generation mechanisms including internal pressure, bladder elasticity, braided sleeve elasticity, and friction was developed. A new length correction term was also included to account for the non-cylindrical shape of the deflected actuator. An aerodynamic model was developed to predict the hinge moments required to deflect the flap to the desired levels; dependent on airfoil properties, flap geometry, wind speed, and blade pitch. By combining the PAM force predictions with the kinematics of the bellcranks and linkages, the torque available was predicted. This was compared to the aerodynamic torques to predict equilibrium flap deflection angles. The outer 5 feet of a Bell 407 blade was cut off such that it could be installed in the Glenn L Martin Wind Tunnel at the University of Maryland. Significant modifications were made to the blade tip to allow for the installation of a trailing edge flap, a linkage and bellcrank system, and an actuator cartridge containing an antagonistic pair of PAM actuators. A structural frame was also

303

clamped onto the end of the blade to allow for mounting into the wind tunnel. Testing was conducted at wind speeds up to the tunnel maximum of $M = 0.3$, which produces 30% of the hinge moment requirement on the actuation system at the $M = 0.56$ design case. To account for this, the PAM operating pressure was derated accordingly. A large matrix of test cases were run over the full bandwidth range of the system, seven blade pitch angles, four pressures, and four wind speeds.

Comparison with experimental PAM characterization data showed that the quasistatic PAM model accurately predicts the force versus deflection behavior over the full range of operating pressures of the PAM TEF systems developed here, including the 0 psi passive PAM stiffness case. Wind tunnel testing of the retrofit blade demonstrated a high degree of control authority over the full bandwidth of interest. At the maximum wind tunnel test speed of $M = 0.3$ and a derated operating pressure of 28 psi, 18.8° half-peak-to-peak flap deflections were achieved at 1/rev (7 Hz), and 17.1° of half-peak-to-peak flap deflection was still available at 5/rev (35 Hz). Quasistatic PAM TEF system performance predictions made using the system model compared well with the experiment.

8.1.4.   WHIRL CHAMBER TESTING

To investigate the effects of centrifugal acceleration on the PAM TEF system under full-scale loading, a vacuum chamber whirl rig was designed, built and tested. A complete sub-span TEF system was built to include all of the major system components mounted into a non-aerodynamic frame, which was spun under vacuum to produce centrifugal acceleration on the system, with a full-scale design point of 843 g at the flap center. An aerodynamic loading of $M = 0.56$ was simulated using linear springs attached to horns on the flap. Full-scale system inertia was also included. A commercially

available pneumatic rotary union was used to transfer air from the fixed to rotating frame. An expansive test matrix characterized system performance over a wide range of operating conditions.

A mechanical failure in the vacuum chamber limited whirl testing to 78% of full-scale *CF* acceleration. At this loading, 17° of half-peak-to-peak flap deflection was achieved at 1/rev (7 Hz), and 8° of half-peak-to-peak flap deflection at 5/rev (35 Hz). Extrapolation of the results to 100% of *CF* acceleration predicts 15.4° of half-peak-to-peak flap deflection at 1/rev (7 Hz), and 7.7° of half-peak-to-peak flap deflection at 5/rev (35 Hz). Thus, a significant level of control authority exists in the system over a broad frequency range in rotation.

8.1.5. DYNAMIC SYSTEM MODELING

A dynamic model of the PAM TEF system was developed. This model coupled the pneumatic, actuation, mechanical, and aerodynamic elements together to allow for accurate time history prediction of system performance. Internal PAM pressure was predicted by combining an ISO 6358 standard model of the spool valve, pressure losses due to tubing friction, and derivations of internal PAM volume into a differential equation describing pressure in a vessel of changing volume. PAM displacement was determined from flap deflection using the kinematics derived for a novel offset bellcrank mechanism. The above mentioned quasistatic PAM force model was used to determine PAM force from internal pressure and displacement. Torque was then determined from PAM force and moment arm. A second order linear equation of motion was used to describe the torsional flap dynamics. This included moment of inertia estimates derived from a system CAD model, an empirical estimate of system damping, torsional stiffness

composed of aerodynamic hinge moments from 2D airfoil theory and linearly elastic torsion rod flexure stiffness, and the net torque generated by the PAMs. The system equations of motion were numerically integrated using the 4th order Runge-Kutta method.

The performance prediction capabilities of the dynamic model were proven in this work. Comparison to experimental results from the vacuum chamber whirl rig showed that the dynamics of all of the various system components were well described. The ISO 6358 standard orifice flow model was successfully adapted to the FESTO spool valve used in these experiments. Internal PAM pressure was well predicted over the entire range of interest, although there are some unmodeled higher order dynamics. PAM force was also well predicted, with some discrepancies that increase at high pressure and low frequency. A novel offset bellcrank design was developed and shown to provide significant increases in output torque, on the order of 37% at 20° of flap deflection. Final flap deflection angles were also well predicted over the entire range. Errors in the force and flap deflection predictions at high pressure and low frequency were partially attributed to mechanical interference in the design of the linkage system. Flap deflection magnitudes were greatest during high pressure, low frequency operation so the effect of the known mechanical interference was greatest at this point.

8.1.6.   PAM TEF CONTROLLER DEVELOPMENT

In order to investigate the commanded waveform tracking capability of PAM TEF systems, a controller development test rig was built. This setup consisted of a pair of PAM actuators connected via a bellcrank to a torsional loading apparatus. This test rig allowed for a wider range of stiffness and inertial loading conditions than the wind tunnel test article or the vacuum chamber test rig. Importantly, it also allowed for elimination of

the mechanical backlash present in the linkage system of the other test rigs. Initial testing with a PID controller identified significant phase and magnitude tracking errors when tracking sinusoidal desired flap deflections under full-scale loading over the bandwidth of interest. A fixed dead-time compensator was added to account for the dead-time present in the system. This dead time compensator was then made variable by including an algorithm to estimate dead-time from current and previous tracking error. Frequency response functions were calculated for all three control algorithms from single frequency sinusoidal command signals over the full bandwidth of interest, under a wide range of torsional inertia and stiffness loading, and with a range of commanded flap magnitudes. Further testing of tracking capability against multi-frequency superimposed complex waveforms representative of an active rotor signal was carried out with the variable delay time compensator controller. Frequency content at 1/rev, 3/rev, 4/rev, and 5/rev was included to simulate a combined primary control and vibration reduction actuation requirement.

The ability of PAM TEF systems to track commanded flap deflection waveforms under full-scale loading conditions was successfully shown. The proportional only control algorithm suffered from significant phase shifting and magnitude loss with increasing frequency. Inclusion of the fixed dead-time compensator greatly reduced phase shift and tracking error, with some improvement in magnitude. However, this algorithm requires an *a priori* estimate of the system dead-time, which is difficult to predict. Furthermore, the dead-time is not constant across all system operating and loading conditions, leading to inconsistencies in the ability to track phase across the desired bandwidth. The variable dead-time compensator directly addressed the short

comings of the fixed compensator, leading to excellent phase tracking capability over the entire bandwidth of interest. Magnitude tracking and tracking error were also improved slightly over the fixed dead-time compensator. The variable dead-time compensator also performed well in tracking representative active rotor waveforms. Increasing torsional stiffness and inertia were both found to increase tracking errors, but even under worst case loading, the tracking capability was generally good for all three of the representative complex waveforms tested.

8.2.   Summary of Research and Key Conclusions

This dissertation covers the first body of work to propose and investigate the use of pneumatic artificial muscle actuators for active rotor applications. It is also the first use of antagonistic PAM systems to drive aerodynamic control surfaces of any type. As such there are several original contributions to the literature contained within.

The initial proof of concept wind tunnel test article is the first use of PAM actuators to drive a trailing edge flap in the literature, for either fixed wing or rotary wing applications. It is also the first wind tunnel test of a PAM driven control surface of any kind.

The swaging construction method developed here is an entirely new approach not seen before in the literature. This design lead to a three orders of magnitude increase in the fatigue life of PAM actuators, and to good operational force and pressure factors of safety. The fatigue testing performed was also the first in the literature to directly simulate a specific operating condition, with much higher actuation frequencies than previous tests. The self-heating present in this test as a result of the higher frequency is

an important factor for creating a representative fatigue test, given the deleterious effect of temperature on the fatigue lives of elastomers.

The PAM force model developed combines model terms existing in the literature with new contributions. A new analytically derived length correction term accounts for the non-cylindrical shape of a deflected PAM without any empirical factors. A new friction term effectively captures PAM hysteresis with a simple direction of motion dependent empirically fit formulation. This model is the first in the literature to be shown to capture the behavior of both active and passive PAMs over a wide pressure range.

The quasistatic model of PAM TEF system performance is the first model in the literature to combine a PAM force model, an aerodynamic model, and system kinematics to predict the performance of a PAM TEF system.

The Bell 407 blade tip with the retrofitted PAM TEF system is also the first of its kind in the literature. Additionally, it is the first wind tunnel test of a trailing edge flap driven by a spanwise oriented pair of PAMs.

The first testing of PAM actuators under rotation was performed as part of this work. The vacuum chamber whirl rig was also used for the first test of a PAM TEF system under full-scale loading; including simulated aerodynamic, inertial, and centrifugal acceleration. The vacuum chamber whirl rig also utilized a commercially available pneumatic rotary union for the first time to supply a PAM system, resolving the question of how to transfer pressurized air from the fixed to rotating frame.

The dynamic system model developed is accurate over a significantly larger bandwidth than other models in the literature. It includes the first published adaptation of

the ISO 6358 standard orifice flow model to a PAM system. It is the first to combine a predominantly deterministic PAM force and volume model with a pneumatic system model, aerodynamic hinge moment predictions and a flap torsional dynamics model. The correlation between experiment and model is significantly better than that seen in other work, particularly at high operating frequencies.

The control algorithm developed here significantly extends the controllable bandwidth of PAM systems beyond what is present in the literature. It is the first controller developed for PAMs to incorporate variable dead-time compensation. It is the highest frequency controller for PAMs, pistons, or any other type of pneumatic actuator known to exist in the literature. It is also the first PAM controller in the literature to be shown to be capable of tracking complex commanded waveforms containing both low frequency and high frequency content.

In summation, the PAM TEF system developed here is the first smart rotor actuation system in the literature to provide the control authority, bandwidth, and tracking accuracy required to simultaneously provide primary control and vibration reduction for full-scale rotorcraft applications.

8.3.   FUTURE WORK

Much work remains before Pneumatic Artificial Muscles are ready for flight. While the initial results are promising and warrant further investigation of the concept, there are several key areas that would benefit from more in-depth research.

The swaged PAM design could benefit from an increased level of environmental protection. A thin elastomeric coating around the braided sleeve is recommended for use

in environments where high levels of exposure to dust, sand, salt, and/or water are expected. The effect of potential coatings on performance and fatigue resistance should be studied as there could be increased friction and self-heating.

Further refinement of the linkage and bellcrank mechanism is desired to remove the mechanical over-travel stop present in the current design. This stop is thought to have contributed significantly to differences between model and experiment in the vacuum chamber whirl rig. Testing with an appropriately modified setup would allow for a better understanding of the accuracy of the quasistatic PAM force model as applied to non-quasistatic operating conditions. Such testing should include a sweep of rotational speeds from non-rotating up to the full-scale CF acceleration matching condition.

It may be desirable to develop a non-empirical formulation to model the friction forces in the PAM. The current approach benefits from simplicity and good accuracy, but the empirically fit friction factor may require re-fitting if another PAM geometry or material is used.

Currently, the effects of CF acceleration on system performance are not modeled. Given the decreasing performance with increasing rotational speed seen in the experiments, some means of including this effect into the dynamic model is desirable. It is believed that frictional forces in the linkage and bellcrank system, which increase with CF loading due to increasing normal forces on the bearings, contribute to losses with increasing rpm. Another potential source of CF induced performance changes are spanwise mass imbalances in the deflected linkage system under a CF gradient. Preliminary analysis indicates that this effect is minor, and should actually lead to larger

311

deflections due to the direction of bellcrank rotation. More detailed modeling of this aspect of the system dynamics would be beneficial.

Once *CF* effects are included, the model should be validated against experimental data from the vacuum chamber whirl rig; either the existing data set or a new data set taken with redesigned linkages/bellcranks and data out to 100+% of the *CF* design point, as described above.

Future whirl chamber testing should also include efforts to reduce the effects of *CF* acceleration on performance, for instance through the use of improved low friction bearings and by ensuring proper alignment of the bellcrank mounting shafts.

Further development of the controller should include consideration of mechanism slop (also known as backlash) in the design of the control algorithm and experimental setup. The test rig used here had minimal backlash due to the direct connection between the PAMs and the inertial and stiffness load. Preliminary testing with a linkage system between actuators and load found that the mechanical slop present in the spherical bearing used to connect the control rod to the flap control horn negatively affected tracking accuracy and stability. Non-bearing based solutions, such as flexures (which have zero backlash), should be used if possible to completely remove this source of non-linearity and potential instability. If that is not feasible due to load or deflection range restrictions, then high precision, wear resistant bearing components should be used as much as possible.

Future work should consider in detail the source of compressed air required for a PAM TEF system. A considerable flow rate of pressurized air would be needed for a

complete multi-bladed active rotor system, and careful design is required to minimize the size, weight, and power consumption of the air compressor needed. Preliminary empirical compressor sizing indicates that with commercially available technologies, a smart rotor system using the PAM TEF system described here would require roughly 10 hp per blade to generate the required mass flow and pressure. Additionally, the energy conversion process should be carefully considered to maximize efficiency. For example, there are at least three potential options: directly using compressor bleed air from the turbine engines, a Shaft Driven Compressor (SDC) attached to the main gearbox, or an electrically powered compressor driven through an alternator on the main gearbox. These three options will have largely different energy efficiencies based on the energy conversion processes required. Shaft driven compressors are a particularly attractive option because there are at least two currently flying rotorcraft, the AH-64A and V-22, which already have significant onboard compressed air capabilities due to high output, high rpm SDCs mounted off of the main gearboxes. The exact capabilities of these systems are proprietary and therefore not available to this author. With all of these compressor options, the temperature of the output air is a concern which must be addressed. Rapid compression of air leads to temperature increases. For instance, the compressor bleed air off of a modern multi-stage gas turbine can be several hundred degrees Fahrenheit, which is above the safe operating temperature of the PAMs used here. Therefore some means of cooling the air will be required. This is a common problem in compressor design, and so many solutions exist. The V-22 SDC, for example, includes a chiller downstream of the compressor, lowering the temperature to the point where the air can be used to cool electronics.

Ultimately, the path forward for PAM TEF active rotor research should lead towards full-scale hover and wind tunnel testing of an entire rotor set. The actuators and flaps could either be retrofit into existing blades, as was done here, or new blades could be designed to properly house them. Retrofitting would likely be the cheaper and faster option, but a new blade design has several advantages. Features such as access hatches and mounting points would be lighter and more structurally efficient if included in the design from the beginning. Instrumentation to track blade response (such as strain gauges and pressure sensors) could be integrated directly into the blade. Finally, and perhaps most significantly, torsional stiffness of the blade could be lowered to provide a more significant servo flap response from the blade. Of course, any significant change to the torsional natural frequencies would require in-depth analysis of the blade dynamics (coupled with trailing edge flap dynamics) before rotational testing to insure that aeroelastic issues are avoided. And so it goes.

9. References

Abbott, I., and Von Doenhoff, 1958. A., *Theory of Wing Sections*, Dover Publications, New York, pp. 190-197.

Abdulrahim, M., and Lind, R., 2006. "Using Avian Morphology to Enhance Aircraft Maneuverability," AIAA Atmospheric Flight Mechanics Conference and Exhibit, Keystone, CO, AIAA 2006-6643.

Ahmadizadeh, A, Mosqueda, G., and Reinhorn, A.M., 2008. "Compensation of Actuator Delay and Dynamics for Real-Time Hybrid Structural Simulation," *Earthquake Engineering and Structural Dynamics*, Vol. 37, No.1, pp. 21-42. doi: 10.1002/eqe.743

Ardelean, E.V., Cole, D.G., and Clark, R.L., 2004. "High performance 'V-stack' Piezoelectric Actuator," *Journal of Intelligent Material Systems and Structures*, Vol. 15, No. 11, pp. 879-889.

Ascher, U. and Petzold, L., 1998. *Computer Methods for Ordinary Differential Equations and Differential-algebraic Equations*, Society of Industrial and Applied Mathematics, Philadelphia, PA, pg. 78.

Austin, F., Siclari, M.J., Kesselman, M., and Weisensel, G.N., 1998. "Smart Terfenol-D-Powered Trailing Edge Experiment," *Proceedings of the SPIE Smart Structures and Materials Conference*, Vol. 3326, San Diego, CA, pp. 282-293.

Beater, P., 2007. *Pneumatic Drives: System Design, Modelling, and Control*, Springer, New York, pg. 38.

Bharadwaj, K., Hollander, K. W., Mathis, C. A. and Sugar, T. G., 2004. "Spring Over Muscle (SOM) Actuator for Rehabilitation Devices," *Engineering in Medicine and Biology Society, 2004. IEMBS '04. 26th Annual International Conference of the IEEE*, 1, 2726-2729.

Blondeau, J. and Pines, D., 2003. "Wind Tunnel Testing of a Morphing Aspect Ratio Wing Using a Pneumatic Telescoping Spar," *Proceedings of the 2nd Unmanned Unlimited Conference and Workshop*, AIAA-2003-6659, San Diego, CA.

Blondeau, J., Richeson, J., and Pines, D., 2003. "Wind Tunnel Testing of a Morphing Aspect Ratio Wing Using a Pneumatic Telescoping Spar," *Proceedings of the AIAA Structures, Structural Dynamics, and Materials Conference*, AIAA-2003-1718, Norfolk, VA.

Brittain Industries, Inc. website, http://www.brittainautopilots.com, accessed 06/08/2011.

Bubert, E.A., 2009. "Highly Extensible Skin for a Variable Wing-Span Morphing Aircraft Utilizing Pneumatic Artificial Muscle Actuation," Master's Thesis, University of Maryland.

Bubert, E.A., Woods, B.K.S., Lee, K., Kothera, C.S., and Wereley, N.M., 2010, "Design and Fabrication of a Passive 1D Morphing Aircraft Skin," *Journal of Intelligent Material Systems and Structures*, 21(17): 1699-1717. DOI: 10.1177/1045389X10378777

Caldwell, D. G., Tsagarakis, N. and Medrano-Cerda, G. A., 2000. "Bio-Mimetic Actuators: Polymeric Pseudo Muscular Actuators and Pneumatic Muscle Actuators for Biological Emulation," *Mechatronics*, 10(4-5):499-530.

Caldwell, D., Medrano-Cerda, G., and Bowler, C., 1997. "Investigation of Bipedal Robot Locomotion Using Pneumatic Muscle Actuators," *Proceedings of the IEEE International Conference on Robotics and Automation*, 799-804.

Caldwell, D., Medrano-Cerda, G., and Goodwin, M., 1995. "Control of Pneumatic Muscle Actuators," *IEEE Journal of Control Systems*, 15(1):40-48.

Casciati, S., and Marzi, A., 2010. "Experimental studies on the fatigue life of shape memory alloy bars," *Smart Structures and Systems*, 6(1):73-85.

Chandra, R., 2001. "Active shape control of composite blades using shape memory actuation," *Smart Materials and Structures*, 10(5):1018.

Chopra, I. 2000. "Status of Application of Smart Structures Technology to Rotorcraft Systems," Journal of the American Helicopter Society, 45(4):228-252.

Chopra, I. 2002. "Review of State of Art of Smart Structures and Integrated Systems," AIAA Journal, 40:2145- 2187.

Chou, A., Philen, M., 2008. "High-Performance Flexible Matrix Composite Actuators for Trailing Edge Flap Control," *Proceedings of Virginia Space Grant Consortium Student Conference*.

Chou, C.P. and Hannaford, B., 1996. "Measurement and Modeling of McKibben Pneumatic Artificial Muscles," *IEEE Trans. Robotics and Automation*, 12(1):90-102.

Colbrunn, R., Nelson, G., and Quinn, R., 2001. "Modeling of Braided Pneumatic Actuators for Robotic Control," *Proceedings of IEEE/RSJ International Conference on Intelligent Robots and Systems*, Maui, HI, Oct. 29 – Nov. 3.

Copp, P., Chopra, I., 2008. "Continued Development of a Mach Scale Swashplateless Rotor with Integrated Trailing Edge Flaps," *American Helicopter Society 64th Annual Forum*, Montreal, Canada, April.

Costa, N. and Caldwell, D. G., 2006. "Control of a Biomimetic "Soft-Actuated" 10 DOF Lower Body Exoskeleton," The First IEEE/RAS-EMBS International Conference on Biomedical Robotics and Biomechatronics, 495-501.

Couch, R.N. 2006. *Development of Magnetic Shape Memory Alloy Actuators for a Swashplateless Helicopter Rotor*. Ph.D. Thesis, Department of Aerospace Engineering, University of Maryland, College Park MD.

Daerden, F. and Lefeber, D. 2002. "Pneumatic Artificial Muscles: Actuators for Robotics and Automation," *European Journal of Mechanical and Environmental Engineering*, 47(1):11-21.

Darby, A.P., Williams, M.S., and Blakeborough, A, 2002. "Stability and Delay Compensation for Real-Time Substructure Testing," *Journal of Engineering*

Mechanics, Vol. 128, No. 12, pp. 1276-1284. doi: 10.1061/(ASCE)0733-9399(2002)128:12(1276)

Davis, S. and Caldwell, D.G. 2006. "Braid Effects on Contractile Range and Friction Modeling in Pneumatic Muscle Actuators," *The International Journal of Robotics Research*, **25**:359-369.

de Marmier, P. and Wereley, N.M. 2003. "Control of Sweep Using Pneumatic Actuators to Morph Wings of Small Scale UAVs," *Proceedings of the AIAA Structures, Structural Dynamics, and Materials Conference*, AIAA-2003-1802, Norfolk, VA.

Dieterich, O., Enenkl, B., and Roth, D. 2006. "Trailing Edge Flaps for Active Rotor Control: Aeroelastic Characteristics of the ADASYS Rotor System," 62th Annual Forum of the American Helicopter Society, Phoenix, Arizona, May 9-11.

Epps, J.J. and Chopra, I., 2001. "In-Flight Tracking of Helicopter Rotor Blades Using Shape Memory Alloy Actuators," *Smart Materials and Structures*, Vol. 10, No. 1, pp. 104-111.

Etkin, B., 1982. *Dynamics of Flight*, 2nd ed., Wiley, New York.

Falls, J., 2008. "Performance Analysis of Trailing-edge Flaps in Helicopter Primary Control," *AHS Specialist's Conference on Aeromechanics*, San Francisco, CA, Jan. 23-25.

Falls, J., Datta, A., and Chopra, I. 2010. "Integrated Trailing-Edge Flaps and Servo-tabs for Helicopter Primary Control," *Journal of the American Helicopter Society,* **55**(3):032005.

Fenn, R.C., Downer, J.R., Bushko, D.A., Gondhalekar, V., and Ham, N.D., 1996. "Terfenol-D Driven Flaps for Helicopter Vibration Reduction," *Smart Materials and Structures*, Vol. 5, No. 1, pp. 49-57.

Ferris, D. P., Czerniecki, J. M. and Hannaford, B., 2005. "An Ankle-Foot Orthosis Powered by Artificial Pneumatic Muscles," Journal of Applied Biomechanics, 21(2):189-197.

Festo, 2006. "Festo Fluidic Muscle DMSP," Product data sheet, URL: www.festo.com [cited 10 August 2006].

Festo, 2006. Humanoid Muscle-Robot, Festo Brochure, [cited 12 June 2006].

Festo, 2009. Air Arm-Robot, Festo Brochure, [cited 20 September 2009].

Festo, 2010, "Fluidic Muscle DMSP," Product data sheet, URL: www.festo.com [cited 21 March 2010].

Festo, 2011. "Proportional directional control valves MPYE," Online product documentation, http://www.kiowa.co.uk/static/documents/Festo/MPYE_EN.PDF, accessed 11/11/2011.

Fink, D. A., Hawkey, T. J., Gaudreau, M. P. J., Wellman, B., and Ormiston, R. A., 2000. "An electromagnetic actuator for individual blade control," *Proceedings of the 56th Annual Forum of the American Helicopter Society*, Virginia Beach, VA, May 2-4, pp 786-797.

Fulton, M., 2000. "Design of the Active Elevon Rotor for Low Vibration," *American Helicopter Society's Aeromechanics Specialists' Meeting*, Atlanta, GA, Nov 13-15.

Gaylord, R. 1955. "Fluid Actuated Motor System and Stroking Device," U.S. Patent No. 2,844,126, Filed: Jan. 20, 1955, Published: July 22, 1958.

Giri, N., and Walker, I., 2010. "Continuum robots and underactuated grasping," *Journal of Mechanical Sciences*, 2:51-58.

Giurgiutiu, V. 2000. "Recent Advances in Smart-Material Rotor Control Actuation," *Proceedings of the AIAA/ASME/ASCE/AHS/ASC 41st Structures, Structural Dynamics and Materials Conference*, AIAA-2000-1709, Atlanta, GA, April 3-6.

Giurgiutiu, V., Chaudhry, Z., and Rogers, C., 1996. "Energy-based Comparison of Solid-state Induced-strain Actuators," *Journal of Intelligent Material Systems and Structures,* 7(1):4-14

Haber, A., Jacklin, S., and deSimone, G., 2002. "Development, manufacturing, and component testing of an individual blade control system for a UH-60 helicopter rotor," *Proceedings of the American Helicopter Society Aerodynamic, Acoustics, and Test and Evaluation Technical Specialists Meeting*, San Fransisco, CA, January 23-25.

Hall, S.R. and Prechtl, E.F. 1996. "Development of Piezoelectric Servoflap for Helicopter Rotor Control," Smart Materials and Structures, 5(1):26-34.

Hall, S.R. and Wereley N.M. 1993. "Performance of Higher Harmonic Control

Algorithms for Helicopter Vibration Reduction," *AIAA Journal of Guidance, Control and Dynamics,* 16(4):794–797.

Hall, S.R., and Spangler Jr., R.L. 1993. "Piezoelectric Helicopter Blade Flap Actuator," U.S. Patent 5,224,826, Filed: Jul. 26, 1989. Published: July 6, 1993.

Ham, N.D. 1987. "Helicopter Individual Blade Control Research at MIT 1977-1985," *Vertica*, **11**(1-2):109-122.

Haven, H. D., 1949. U.S. Patent No. 2483088.

Hinshaw, T., 2009. "Analysis and Design of a Morphing Wing Tip Using Multicellular Flexible Matrix Composite Adaptive Skins," M.S. Thesis, Department of Aerospace Engineering, Virginia Polytechnic Institute and State University, Blacksburg, VA.

Horiuchi, T., Inoue, M., Konno, T., and Namita, Y., 1999. "Real-Time Hybrid Experimental System with Actuator Delay Compensation and its Application to a Piping System with Energy Absorber," *Earthquake Engineering and Structural Dynamics*, Vol. 28, No. 10, pp. 1121-1141. doi: 10.1002/(SICI)1096-9845(199910)28:10<1121::AID-EQE858>3.0.CO;2-O

Huber, J.E., Fleck, N.A., and Ashby, M.F. 1997. "The Selection of Mechanical Actuators Based on Performance Indices," *Proceedings of The Royal Society of London Series A - Mathematical Physical And Engineering Sciences*, **453**(1965):2185-2205.

Incropera, F., and DeWitt, D., 2006. *Fundamentals of Heat and Mass Transfer*, John Wiley & Sons, New York, New York.

ISO 6358, 1989. "Pneumatic Fluid Power − Components Using Compressible Fluids − Determination of Flow-rate Characteristics."

Jacklin, S. A., Nguyen, K. Q., Blaas, A., and Richter, P., 1994. "Full-Scale Wind Tunnel Test of a Helicopter Individual Blade Control System", *Proceedings of the 50th Annual Forum of the American Helicopter Society*, May.

Jacklin, S., Haber, A., de Simone, G., Norman, T., and Shinoda, P., 2002. "Full-scale wind tunnel test of an individual blade control system for a UH-60 Helicopter," *58th Annual Forum of the American Helicopter Society*, Montreal, Canada, June 11-13.

Jacobs, E., and Pinkerton, R. 1931. "Pressure Distribution Over a Symmetrical Airfoil Section with Trailing Edge Flap," NACA Technical Report No. 360.

Johnson, W., 1994. *Helicopter Theory*, Dover Publications, Inc, New York, pg. 331.

Kapadia, A., Walker, I., Dawson, D., and Tatlicioglu, E., 2010. "A model-based sliding mode controller for extensible continuum robots," *Proccedings of the 9th WSEAS International Conference on Signal Processing, Robotics, and Automation*, pp. 113-120.

Kawashima, K., Sasaki, T., Miyata, T., Nakamura, N., Sekiguchi, M., and Kagawa, T., 2004. "Development of Robot Using Pneumatic Artificial Rubber Muscles to

Operate Construction Machinery," *Journal of Robotics and Mechatronics*, 16(1):8-16.

Kennedy, D.K., Straub, F.K., Schtky, L.M., Chaudhry, Z., and Roznoy, R., 2004. "Development of an SMA Actuator for In-flight Rotor Blade Tracking," *Journal of Intelligent Material Systems and Structures*, Vol. 15, No. 4, pp. 235-248.

Kim, J.S., Wang, K.W., Smith, E.C., 2001. "High-authority Piezoelectric Actuation System Synthesis Through Mechanical Resonance and Electrical Tailoring," *Journal of Intelligent Material Systems and Structures*, Vol. 16, No. 1, pp. 21-31.

Kingsley, D. and Quinn, R., 2002. "Fatigue Life and Frequency Response of Braided Pneumatic Actuators," *Robotics and Automation*, 3:2830-2835

Klute, G. and Hannaford, B. 1998. "Fatigue Characteristics of McKibben Artificial Muscle Actuators," *IEEE/RSJ Intl. Conference on Intelligent Robots and Systems*, Victoria, Canada, October 13-17.

Klute, G. K. and Hannaford, B. 2000. "Accounting for Elastic Energy Storage in McKibben Artificial Muscle Actuators," *ASME Journal of Dynamic Systems, Measurement, and Control*, **122**(2):386-388.

Kornbluh, R., Pelrine, R., Eckerle, J., Joseph, J., 1998. "Electrostrictive Polymer Artificial Muscle Actuators," *IEEE International Conference on Robotics and Automation*, Vol. 3, IEEE, pp. 2147-2154.

Kothera, C. S., Woods, B.K.S., Sirohi, J., Wereley, N.M., and Chen, P. C. 2010. "Fluid-Driven Artificial Muscles as Mechanisms for Controlled Actuation," U.S. Patent 7,837,144, Filed: Aug. 11, 2006, Published: Nov. 23, 2010.

Kothera, C., Jangid, M., Sirohi, J. and Wereley, N., 2009. "Experimental Characterization and Static Modeling of McKibben Actuators." *ASME Journal of Mechanical Design*. 131:091010 (10 pp). DOI: 10.1115/1.3158982.

Kothera, C., Wereley, N., Woods, B., and Bubert, E., 2008. "Wind Tunnel Testing of a Trailing-Edge Flap Actuated by Pneumatic Artificial Muscles," *American Helicopter Society 64th Annual Forum*, Montreal, Canada, April.

Kothera, C.S., Woods, B.K.S., and Wereley, N.M. 2010. "Fluidic Artificial Muscle Actuation System for a Helicopter Trailing-Edge Flap," US Patent Pending. Filed: April 29, 2010.

Lee, T. and Chopra, I., 2001. "Design of piezostack-driven trailing-edge flap actuators for helicopter rotors," *Smart Materials and Structures*, Vol. 10, No. 1, pp. 15-24.

Leishman, J. 2000. *Principles of Helicopter Aerodynamics*, Cambridge University Press, New York, 217.

Leishman, J. 2007. *The Helicopter: Thinking Forward, Looking Back*, College Park Press, 101-102.

Liang, C., Davidson, F., Schetky, L., and Straub, F., 1996. "Applications of torsional shape memory alloy actuators for active rotor blade control: opportunities and limitations," *Proceedings of the SPIE,* 2717(91).

Life, 1960. "Artificial Muscle," *Life* magazine, Mar. 14, pp. 87-88.

Lightned, S., and Lincoln, R., 2002. "The Fluidic Muscle: A 'New' Development," *International Journal of Modern Engineering*, 2(2).

Loewy, R. 1997. "Recent Developments in Smart Structures with Aeronautical Applications," *Smart Materials and Structures*, 6:R11 – R42.

Lotfi-Gaskarimahalle, A., and Rahn, C. D., 2009. "Switch Stiffness Vibration Controllers for Fluidic Flexible Matrix Composites," *Proceedings of DETC2009, Design Engineering Technical Conferences*, San Diego, California, USA.

Lotfi-Gaskarimahalle, A., Scarborough, L., Rahn, C., Smith, E., 2009. "Fluidic Composite Tunable Vibration Absorbers," *ASME 2009 Conference on Smart Materials, Adaptive Structures and Intelligent Systems SMASIS 2009*, Philadelphia, Pennsylvania, USA.

Marcinčin, J., and Palko, A., 1993. "Negative pressure artificial muscle—An unconventional drive of robotic and handling systems", *Transactions of the University of Košice*, Riecansky Science Publishing Co, Slovak Republic, pp. 350-354.

McMahan, W., Chitrakaran, V., Csencsits, M., Dawson, D., Walker, I., Jones, B., Pritts, M., Dienno, D., Grissom, M., and Rahn, C., 2006. "Field Trials and Testing of the OctArm Continuum Manipulator," *Proceedings of the 2006 IEEE International Conference on Robotics and Automation*, Orlando, Florida, May 15-19.

Medrano-Cerda, G.A., Bowler, C.J.,Caldwell, D.G., 1995. "Adaptive Position Control of Antagonistic Pneumatic Muscle Actuators," *IEEE Intelligent Robots and Systems Conference*, Vol. 1, IEEE, pp. 378-383

Moog Actuation Technologies, 2011. "Electromechanical Actuators," http://www.moog.com/products/actuators-servoactuators/actuation-technologies/electromechanical/, Accessed July, 21, 2011.

Morin, A. H., 1953. U. S. Patent No. 2642091.

Muirhead Aerospace, 2011. "Actuators," http://www.muirheadaerospace.com/motion-technology/actuators.html #SIngleActuator, Accessed July, 21, 2011.

Mullins, L., 1969. "Softening of Rubber by Deformation," *Rubber Chemistry and Technology*, 42, 339-363.

Neal, D.A., Good, M.G., Johnston, C.O., Robertshaw, H.H., Mason, W.H., and Inman, D.J., 2004. "Design and Wind-tunnel Analysis of a Fully Adaptive Aircraft Configuration," *Proceedings of the AIAA Structures, Structural Dynamics, and Materials Conference*, AIAA-2004-1727, Palm Springs, CA,.

Nelson, C.T. and Rediniotis, O.K., 2004. "An Active Flap Deployment System for Blade-disturbance Interaction Alleviation," *Journal of Fluids Engineering*, Vol. 126, No. 6, pp. 1006-1014.

Niezrecki, C., Brei, D., Balakrishnan, S., and Moskalik, A., 2001. "Piezoelectric Actuation: State of the Art," *The Shock and Vibration Digest*, Vol. 33, 269.

Olsson, H., Astrom, K. J., Canudas de Wit, C., Gafvert, M., Lischinsky, P. 1998. "Friction Models and Friction Compensation," *European Journal of Control*, **4**(3):176-195.

Peel, L., Mejia, J., Narvaez, B., Thompson, K., and Lingala, M., 2009. "Development of a Simple Morphing Wing Using Elastomeric Composites as Skins and Actuators," *Journal of Mechanical Design*, 131(9):091003 (8 pgs).

Petyt, M. 2010. *Introduction to Finite Element Vibration Analysis*, Cambridge University Press, Cambridge, UK.

Philen, M. 2009. "On the Applicability of Fluidic Flexible Matrix Composite Variable Impedance Materials for Prosthetic and Orthotic Devices," *Smart Materials and Structures*, 18:104023. DOI 10.1088/0964-1726/18/10/104023.

Philen, M., 2009. "Semi-Active Vibration Isolation Using Fluidic Flexible Matrix Composite Mounts: Analysis and Experiment," *ASME 2009 Conference on Smart Materials, Adaptive Structures and Intelligent Systems SMASIS 2009*, Philadelphia, Pennsylvania, USA, pp. 463-469.

Philen, M., 2011. "Force Tracking Control Fluidic Flexible Matrix Composite Variable Stiffness Structures," *Journal of Intelligent Material Systems and Structures*, 22:31-43. DOI: 10.1177/1045389X10391498.

Philen, M., Shan, Y., Bakis, C. E., Wang, K. W. and Rahn, D., 2006. "Variable Stiffness Adaptive Structures Utilizing Hydraulically Pressurized Flexible Matrix Composites with Valve Control," *47th AIAA/ASME/ASCE/AHS/ASC Structures, Structural Dynamics and Materials Conference, May 1- 4, 2006*, Newport, RI, United states, American Institute of Aeronautics and Astronautics Inc. 9, 6387-6397.

Pierce, R. C., 1940. U. S. Patent No. 2211478.

Poonsong, P. 2004. "Design and Analysis of a Multi-section Variable Camber Wing," M.S. Thesis, Department of Aerospace Engineering, University of Maryland, College Park, MD.

Pritts, M., and Rahn, C., 2004. "Design of an artificial muscle continuum robot," *Proceedings of the 2004 IEEE International Conference on Robotics and Automation ICRA 04 2004,*, 5(April):4742-4746.

Pugi, L., Malvezzi, M., Allotta, B., Banci, L., Prescniani, P., 2004. "A Parametric Library for the Simulation of a Union Internationale des Chemins de Fer (UIC) Pneumatic Braking System," *Proc Instn Mech Engrs, Journal of Rail and Rapid Transit*, 218(F):117-132.

Richer, E., and Hurmuzlu, Y., 2000. "A High Performance Pneumatic Force Actuator System: Part II – Nonlinear Controller Design," *ASME Journal of Dynamic Systems, Measurement, and Control*, Vol. 122, Sept, pp. 426-434. doi: 10.1115/1.1286366

Robinson, R., Kothera, C., Woods, B. K. S., Vocke, R., and Wereley, N., 2011. "High Specific Power Actuators for Robotic Manipulators," *Journal of Intelligent Materials Systems and Structures*, 22(13):1501-1511

Samuel, J.B., and Pines, D.J. 2007. "Design and Testing of a Pneumatic Telescope-Wing for Unmanned Air Vehicles," AIAA Journal of Aircraft, **44**(4):1088-1099.

Sanville, F., 1971. "A New Method of Specifying the Flow Capacity of Pneumatic Fluid Power Valves," *Second International Fluid Power Symposium*, Guildford, England, Paper D3, pp. 37-47.

Sardellitti, I., Palli, G., Tsagarakis, N. G. and Caldwell, D. G., 2010. "Antagonistically Actuated Compliant Joint: Torque and Stiffness Control," *In: Intelligent Robots and Systems (IROS), 2010 IEEE/RSJ International Conference on*, 1909-1914.

Sawicki, G. S. and Ferris, D. P., 2009. "A Pneumatically Powered Knee-Ankle-Foot Orthosis (KAFO) with Myoelectric Activation and Inhibition," Journal of NeuroEngineering and Rehabilitation, 6(23):1-16.

Schulte, H.F., 1961. "The Characteristics of the McKibben Artificial Muscle," *The Application of External Power in Prosthetics and Orthotics*, Pub. 874, National Academy of Sciences – National Research Council, Washington, DC, App. H, 94-115.

Shan, Y., Philen, M., Amir, L., Bakis, C.E., Rahn, C.D., and Wang, K.W. 2009. "Variable Stiffness Structures Utilizing Fluidic Flexible Matrix Composites," *Journal of Intelligent Material Systems and Structures*, 20:443-456. DOI: 10.1177/1045389X08095270.

Singh, K., Sirohi, J., Chopra, I., 2003. "An Improved Shape Memory Alloy Actuator for Rotor Blade Tracking," *Journal of Intelligent Material Systems and Structures*, 14(12):767-787.

Sofla, A.Y.N., Meguid, S.A., Tan, K.T. and Yeo, W.K. 2010. "Shape Morphing of Aircraft Wing: Status and Challenges," Materials and Design, 31, 1284-1292.

Straub, F., and Merkley, D., 1996. "Design of a Servo-flap Rotor for Reduced Control Loads," *Journal of Smart Materials and Structures*, 5:68-75.

Straub, F., Kennedy, D. K., Stemple, A. D., Anand, V. R., and Birchette, T. S. 2004. "Development and Whirl Tower Test of the SMART Active Flap Rotor," SPIE Smart Structures and Materials, San Diego, CA, March 14-18.

Straub, F.K., Ngo, H.T., Anand, V., and Domzalski, D.B., 2001. "Development of a Piezoelectric Actuator for Trailing Edge Flap Control of Full Scale Rotor Blades," *Smart Materials and Structures,* Vol. 10, No. 1, pp. 25-34.

Strelec, J.K., Lagoudas, D.C., Khan, M.A., and Yen, J., 2003. "Design and Implementation of a Shape Memory Alloy Actuated Reconfigurable Airfoil," *Journal of Intelligent Material Systems and Structures*, Vol. 14, No. 4-5, pp. 257-273.

Takuma, T., Nakajima, S., Hosoda, K., and Asada, M., 2004. "Design of Self-Contained Biped Walker with Pneumatic Actuators," *In: SICE 2004 Annual Conference*, 4-6 Aug. 2004, Piscataway, NJ, USA, 3:2520-4.

Thill, C., Etches, J., Bond, I., Potter, K., and Weaver, P., 2008. "Morphing Skins," *The Aeronautical Journal*, 112(1129): 117-139.

Tondu, B., and Lopez, P. 1997. "The McKibben Muscle and its Use in Actuating Robot-arms Showing Similarities with Human Arm Behaviour," *Industrial Robot*,

24(6):432.

Treloar, L. R. G. 1975. *The Physics of Rubber Elasticity*, Third Edition, Clarendon Press, Oxford, 59-100.

Trivedi, D., Dienno, D., and Rahn, C., 2008. "Optimal, Model-Based Design of Soft Robotic Manipulators," *ASME Journal of Mechanical Design*, 130(091404):9 pages.

Verrelst, B., Ham, R. V., Vanderborght, B., Daerden, F., Lefeber, D. and Vermeulen, J., 2005. "The Pneumatic Biped "Lucy" Actuated with Pleated Pneumatic Artificial Muscles," *Autonomous Robots*, 18(2):201-213.

Walker, I., Dawson, D., Flash, T., Grasso, F., Hanlon, R., Hochner, B., Kier, W., Pagano, C., Rahn, C., and Zhang, Q., 2005. "Continuum Robots Arms inspired by Cephalopods," *Proceedings of SPIE*, 303-314.

Weiss, P. 2003. "Wings of Change: Shape-shifting Aircraft May Ply Future Skyways," *Science News*, 164(23): 359-365.

Woo, C., Kim, W., Lee, S., Choi, B., Park, H., 2009. "Fatigue Life Prediction of Vulcanized Natural Rubber Subjected to Heat-aging," *Procedia Engineering*, 1(1): 9-12.

Wood, R., Steltz, E., and Fearing, R., 2005. "Optimal Energy Density Piezoelectric Bending Actuators," *Sensors and Actuators A: Physical*, 119(2):476-488.

Woods, B. K. S., Kothera, C.S., and Wereley, N.M., 2010. "Whirl Testing of a Pneumatic Artificial Muscle Actuation System for a Full-Scale Active Rotor" *Society 66th Annual Forum of the American Helicopter*, Phoenix, Arizona, May 11-13.

Woods, B. K. S., Bubert, E., Kothera, C., and Wereley, N., 2008. "Design and Testing of a Biologically Inspired Pneumatic Trailing Edge Flap System," Paper No. AIAA-2008-2046, *AIAA Structures, Structural Dynamics, and Materials Conference*, Schaumberg, IL.

Woods, B., Kothera, C., and Wereley, N., 2008. "Whirl Testing of a Pneumatic Artificial Muscle Driven Helicopter Trailing Edge Flap," *American Helicopter Society 64th Annual Forum*, Montreal, Canada, April.

Woods, B.K.S., Bubert, E.A., Kothera, C.S., Sirohi, J., and Wereley, N.M., 2007. "Experimental Testing of Pneumatic Artificial Muscles for Trailing Edge Flap Actuation," April 23 - 26, *AIAA Structures, Structural Dynamics, and Materials Conference*, Waikiki, HI, Paper No. AIAA2007-1718.

Woods, B.K.S., Choi, Y.T., Kothera, C.S., and Wereley, N.M. 2011. "Control System Development for Pneumatic Artificial Muscle Driven Active Rotor Systems," American Helicopter Society 67th Annual Forum, Virginia Beach, VA, May 3-5.

Woods, B.K.S., Gentry, M., Kothera, C., Werleley, N., 2010. "Fatigue Life Testing of Swaged Pneumatic Artificial Muscles as Actuators for Aerospace Applications," *Journal of Intelligent Material Systems and Structure*, Accepted for publication.

Woods, B.K.S., Kothera, C.S., and Wereley, N. M. 2009. "Fluidic Artificial Muscle Actuator and Swaging Process Therefor," U.S. Patent Application No.

12/456,139, Filed: June 11, 2009.

Yenne, B., 2004. *Attack of the Drones: A History of Unmanned Aerial Combat*, Zenith Press, St Paul, MN.

Yu, Y., Gmelin, B., Splettstoesser, W., Philippe, J., Prieur, J., Brooks, T., 1997. "Reduction of Helicopter Blade-Vortex Interaction Noise by Active Rotor Control Technology," *Progress in Aerospace Science*, 33(9):647-687.

Zhang, W., Accorsi, M., and Leonard, W., 2005. "Analysis of Geometrically Nonlinear Anisotropic Membranes: Application to Pneumatic Muscle Actuators," *Finite Elements in Analysis and Desi*gn, 41(9-10):944-962.

Zhang, Z., Philen, M. and Neu, W. 2010. "A Biologically Inspired Artificial Fish Using Flexible Matrix Composite Actuators: Analysis and Experiment," Smart Materials and Structures, 19:094017. DOI: 10.1088/0964-1726/19/9/094017.